

# THESIS REPORT

Ph.D.

## In Process Machine Tool Vibration Cancellation Using Electrostrictive Actuators

*by Z. Eshete*

*Advisors: G. Zhang*

*B. Balachandran*

Ph.D. 96-13



*Sponsored by  
the National Science Foundation  
Engineering Research Center Program,  
the University of Maryland,  
Harvard University,  
and Industry*



## **ABSTRACT**

**Title of Dissertation:           IN-PROCESS MACHINE TOOL VIBRATION  
CANCELLATION USING PMN ACTUATORS**

**Zelalem Eshete, Doctor of Philosophy, 1996**

**Dissertation directed by:   Associate Professor Guangming Zhang, Advisor  
Mechanical Engineering Department, and  
Institute for Systems Research  
Assistant Professor Balakumar Balachandran, Co-advisor  
Mechanical Engineering Department**

At present, the machine tool technology was in the United States is not in the state-of-the-art of leading international competitors. Conventional machine tools under use are being pushed to their machining accuracy limits. Such a pressing need calls for revitalizing the machine tool industry. In this dissertation, a mechatronic system has been proposed and developed for reducing tool vibration during machining. It consists of electrical and mechanical components, and is realized by placing electrically driven electrostrictive (PMN) actuators in a specially designed tool post mechanical structure.

Analytical and experimental investigations are conducted to characterize the performance of the developed system. In the analytical investigation, a mathematical model is developed to describe the turning operation. The control mechanism is identified using experimental testing for the range of the disturbance frequency.

Investigation using computer simulation is carried out in two phases. In phase 1, a linear neural network controller with an adaptive control strategy is examined. In phase 2, a nonlinear neural network with a learning control strategy is explored.

The linear neural networks, namely, digital filters, are implemented using a signal processing board. The experimental investigation is conducted in two stages. In the first stage, a test bed is established to use an electro-magnetic shaker to resemble the excitation of cutting force acting on the tool. In the second stage, experiments were conducted using a lathe on the shop floor.

In the experimental investigation, in-process vibration cancellation observed. In the laboratory experiment, a percent reduction in the 90% was possible using a feedforward scheme. The improvement in surface roughness during the turning operation was confirmed from measurements of surface roughness profiles. A cantilever machining operation gave a percent reduction of 30%.

The main contributions of this thesis research are: 1) a successful implementation of PMN actuators for in-process vibration cancellation in the turning operation; 2) a successful implementation of linear neural network methodology for active machine tool vibration cancellation; 3) development of guidelines for identification of the neural structure for nonlinear neural network control.



**IN PROCESS MACHINE TOOL VIBRATION CANCELLATION  
USING ELECTROSTRICTIVE ACTUATORS**

by

**Zelalem Eshete**

**Thesis submitted to the Faculty of the Graduate School of the  
University of Maryland at College Park in partial fulfillment  
of the requirements for the degree of  
Doctor of Philosophy  
1996**

**Advisory Committee:**

**Associate Professor Guangming Zhang, Chairman/ Advisor  
Assistant Professor Balakumar Balachandran , Co-advisor  
Professor Davinder K. Anand  
Professor Andre Tits  
Professor Jackson Yang**

## **DEDICATION**

**To My Parents**

## ACKNOWLEDGMENTS

The author wishes to express his sincere gratitude to Dr. Guangming Zhang and Dr. Balakumar Balachandran, who have provided technical and moral support throughout his study. The author also would like to thank Dr. Davinder K. Anand, Dr. Andre Tits and Dr. Jackson Yang for serving on his thesis review committee.

The author would like to thank members of Advanced Design and Manufacturing Laboratory for their help in his thesis work. The author is indebted to Mr. Mohammed H. Al-Amoudi, Mr. Dereje Mekonen and his wife Elsa Negash for their support to accomplish his graduate study.

The authors acknowledge the support of the University of Maryland Research Board, the Department of Mechanical Engineering, and the Institute for Systems Research at the University of Maryland under Engineering Research Centers Program: NSFD CDF 8803012. The research is also partially funded by Best Manufacturing Practice Program by the department of Navy.

## TABLE OF CONTENTS

DEDICATION.....	ii
ACKNOWLEDGMENTS.....	iii
LIST OF TABLES .....	vii
LIST OF FIGURES .....	x
NOMENCLATURE .....	xv
CHAPTER 1	
INTRODUCTION	
1.1 Background .....	1
1.2 Motivation .....	2
1.3 Dissertation Objectives .....	5
1.4 Thesis Organization .....	7
CHAPTER 2	
TURNING MACHINING SYSTEMS	
2.1 Introduction .....	9
2.2 Turning Machining System Modeling .....	11
2.2.1 Cutting Process Dynamics .....	13
2.2.2 The Structural Dynamics .....	14
2.2.3 Feedback Paths .....	16
2.3 Machine Tool Vibration .....	17
2.3.1 Random Vibration .....	17
2.3.2 Externally Forced Vibration .....	18
2.3.3 Internally Forced Vibration .....	19
2.3.4 Self-Excited Vibration .....	21
2.4 Machine Tool Vibration Control .....	25
CHAPTER 3	
CONTROL METHODOLOGY	
3.1 Introduction .....	29
3.2 Active Vibration Control Using Smart Material-Made Actuators .....	30
3.3 Adaptive Control Schemes .....	37
3.3.1. Adaptive Feedforward Control .....	38
3.3.2 Adaptive Feedback Control .....	40
3.3.3 Adaptive Hybrid Control .....	40

3.4 Neural Network for Control .....	41
3.4.1 Neural Network Fundamentals .....	41
3.4.2 Linear Neural Network .....	46
3.4.2.1 Nonrecursive Digital Filters .....	47
3.4.2.2 Recursive Digital Filters .....	49
3.4.3 Nonlinear Neural Network .....	52
3.4.3.1 Multilayer Feedforward Neural Network .....	53
3.4.3.2 Nonrecursive Nonlinear Neural Network .....	56
3.4.3.3 Recurrent Nonlinear Neural Network .....	57

## CHAPTER 4

### SYSTEM MODELING AND COMPUTER SIMULATION

4.1 Introduction .....	59
4.2 System Identification of the Control Mechanism .....	62
4.2.1 Design of Experiment .....	63
4.2.2 Experimental Setup .....	64
4.2.3 Identification Procedure .....	67
4.3 System Modeling of the Turning Machining System .....	76
4.4 Computer Simulation of Linear Neural Network Control System .....	81
4.4.1 Linear Emulator Module Development .....	81
4.4.1.1 Design of Experiment .....	83
4.4.1.2 Results and Analysis .....	84
4.4.2 Linear Control Module Development .....	88
4.4.2.1 Design of Experiment .....	91
4.4.2.2 Results and Analysis .....	92
4.5 Computer Simulation of Nonlinear NN Control System .....	104
4.5.1 Neural Structure Identification .....	104
4.5.1.1 Nonlinear Emulator Dynamics .....	108
4.5.1.2 Training Data .....	111
4.5.1.3 Initial Random Weight .....	112
4.5.1.4 Design of Experiment I .....	113
4.5.1.5 Results and Analysis I .....	114
4.5.1.6 Design of Experiment II .....	128
4.5.1.7 Results and Analysis II .....	129
4.5.2 Design of Experiment .....	145
4.5.3 Results and Analysis .....	146

## CHAPTER 5

### EXPERIMENTATION VERIFICATION

5.1 Introduction .....	153
5.2 Laboratory Experiments .....	157
5.2.1 Experimental Setup .....	157
5.2.2. Control with On-Line System identification .....	161
5.2.2.1 Design of Experiment .....	161

5.2.2.2 Results and Analysis .....	167
5.2.3 Control with Off-Line System Identification .....	171
5.2.3.1 Design of Experiment I .....	172
5.2.3.2 Results and Analysis I .....	173
5.2.3.3 Design of Experiment II .....	175
5.2.3.4 Results and Analysis II .....	175
5.2.3.5 Design of Experiment III .....	181
5.2.3.6 Results and Analysis III .....	182
5.2.3.7 Design of Experiment IV .....	187
5.2.3.8 Results and analysis IV .....	187
5.3 Machine Shop Experiment .....	190
5.3.1 Experimental Setup .....	191
5.3.2 Turning Operation with both Ends Supported .....	194
5.3.2.1 System Disturbance Characterization .....	194
5.3.2.2 Design of Experiment .....	201
5.3.2.3 Results and Analysis .....	203
5.3.2.4 Roughness Measurements .....	210
5.3.3. Turning Operation with one End Supported .....	216
5.3.3.1 System Disturbance Characterization .....	217
5.3.3.2 Design of Experiment .....	218
5.3.3.3 Results and Analysis .....	219
 CHAPTER 6	
CONCLUSIONS AND RECOMMENDATIONS	
6.1 Conclusions .....	225
6.2 Recommendations .....	228
 Appendix	
SURFACE PROFILE MEASUREMENT .....	230
 REFERENCES .....	 239

## LIST OF TABLES

Table 3.1	Characteristics of Electrostrictive and Piezoelectric Actuators.....	31
Table 3.2	Typical Actuator Parameters.....	37
Table 4.1	Operation Parameters for PMN Type Actuators.....	62
Table 4.2	Values for Computer Simulations.....	81
Table 4.3	Tap Length Levels.....	83
Table 4.4	Steady State Modeling Error.....	85
Table 4.5	Validation error.....	86
Table 4.6	Disturbance Signal Characteristics.....	92
Table 4.7	Tap Length Levels .....	113
Table 4.8	Weight Parameters .....	114
Table 4.9	Settling Time Parameter .....	115
Table 4.10	Steady State Modeling Error .....	116
Table 4.11	Acceptable Samples .....	117
Table 4.12	Validation Error for Low Case .....	118
Table 4.13	Validation Error for Medium Case .....	119
Table 4.14	AIC Values for Low Case .....	124
Table 4.15	AIC Values for Medium Case .....	124
Table 4.16	Input Neurons .....	128
Table 4.17	Study Cases .....	128

Table 4.18	Weight Structure .....	129
Table 4.19	Statistical Measures of Steady State Modeling Error .....	130
Table 4.20	Settling Time Parameter .....	132
Table 4.21	Steady State Modeling Error .....	136
Table 4.22	Acceptable Samples .....	138
Table 4.23	Validation Error for hl-RN .....	138
Table 4.24	Validation Error for lh-RN .....	139
Table 4.25	AIC Values for hl-RN .....	142
Table 4.26	AIC Values for lh-RN .....	143
Table 4.27	Statistical Measures of AIC .....	143
Table 5.1	Weight Structure Levels .....	172
Table 5.2	Selected Trials .....	173
Table 5.3	Frequencies and Amplitudes of Disturbance Signal .....	175
Table 5.4	Frequencies and Amplitudes of Disturbance Signal .....	182
Table 5.5	Frequencies and Amplitudes of Disturbance Signal .....	187
Table 5.6	Levels for Cutting Conditions .....	194
Table 5.7	Treatment Combinations .....	195
Table 5.8	Cutting Conditions .....	202
Table 5.9	Performance Indices for 16 Samples .....	204
Table 5.10	Statistical Measures of the Performance Indices .....	207
Table 5.11	Selected Trials .....	210



Table 5.12	Roughness Average Measurement .....	210
Table 5.13	Cutting Conditions .....	219
Table A.1	Cutting Conditions .....	230

## LIST OF FIGURES

Figure 2.1	Turning Operation on a Lathe.....	10
Figure 2.2	Block Diagram of Machining System Modeling .....	12
Figure 2.3	Picture of Smart Tool Post Structure .....	14
Figure 2.4	Assembly Drawing of Smart Tool Post Structure .....	15
Figure 2.5	Effect of Built-Up Edge on Rake Angle .....	19
Figure 2.6	Coupling between Cutting Process and Mechanical Structure.....	22
Figure 2.7	Regenerative Effect .....	23
Figure 2.8	Mode Coupling Effect .....	24
Figure 2.9	Typical Stability Chart for a Machine Tool .....	25
Figure 3.1	Actuator Displacement versus Voltage Input .....	32
Figure 3.2	Single Layer and Multilayer Ceramic .....	34
Figure 3.3	Primary Electrostrictive Response Mechanism .....	35
Figure 3.4	Piezoelectric Poling Mechanism .....	36
Figure 3.5	Block Diagram of an Adaptive Control System .....	38
Figure 3.6	Two Biological Neurons in Synaptic Contact .....	42
Figure 3.7	Two Artificial Neurons in Synaptic Contact .....	43
Figure 3.8	Neuron Model .....	43
Figure 3.9	Sigmoid Transfer Function and its Derivative .....	45
Figure 3.10	Neural Architecture of FIR Filter .....	47

Figure 3.11	Neural Architecture of IIR Filter .....	50
Figure 3.12	Meso-Structure of Multilayer Feedforward Neural Network .....	53
Figure 3.13	Nonrecurrent Nonlinear Neural Network .....	57
Figure 3.14	Recurrent Nonlinear Neural Network .....	58
Figure 4.1	Adaptive Type Controllers for Disturbance Attenuation .....	60
Figure 4.2	Learning Type Controller for Disturbance Attenuation .....	60
Figure 4.3	Placement of Actuators in the Smart Tool Post Structure .....	64
Figure 4.4	Block Diagram of Experimental Setup for Identification.....	65
Figure 4.5	Spectral Analysis of Experimental Data .....	66
Figure 4.6	System Identification Cycle.....	68
Figure 4.7	Loss Function of ARX Model.....	70
Figure 4.8	Model Evaluation for SS Models .....	73
Figure 4.9	Experimental and Simulation Outputs.....	74
Figure 4.10	Residuals of the Model.....	74
Figure 4.11	Frequency Response .....	75
Figure 4.12	Model of Smart Tool Post Structure.....	77
Figure 4.13	Block Diagram of the Structural Dynamics of the Tool Post.....	78
Figure 4.14	Steady State Modeling Error.....	85
Figure 4.15	Validation Errors.....	87
Figure 4.16	Final Prediction Error.....	88
Figure 4.17	Adaptation Algorithm.....	90

Figure 4.18	Controller Performance for Harmonic Disturbance.....	94
Figure 4.19	Controller Performance for Multi-Frequency Disturbance, Ex. 1.....	98
Figure 4.20	Percent Tool Displacement Reduction, Example 1 .....	99
Figure 4.21	Controller Performance for Multi-Frequency Disturbance, Ex. 2.....	102
Figure 4.22	Percent Tool Displacement Reduction, Example 2 .....	103
Figure 4.23	Series/Parallel Arrangement .....	105
Figure 4.24	Parallel Arrangement .....	107
Figure 4.25	Statistical Measures of Validation Error for Low Case .....	121
Figure 4.26	Statistical Measures of Validation Error for Medium Case .....	123
Figure 4.27	Statistical Measures of AIC .....	125
Figure 4.28	Validation Errors for Medium Case with 3 Hidden Neurons .....	126
Figure 4.29	Validation Errors for Low Case with 6 Hidden Neurons .....	127
Figure 4.30	Histogram of Settling Time Parameter .....	132
Figure 4.31	Histogram of Steady State Modeling Error .....	134
Figure 4.32	Statistical Measure of Steady State Modeling Error .....	137
Figure 4.33	Statistical Measures of Validation Error for hl-RN .....	141
Figure 4.34	Statistical Measures of Validation Error for lh-RN .....	142
Figure 4.35	Statistical Measures of AIC .....	144
Figure 4.36	Modeling Error .....	148
Figure 4.37	Control Error .....	151
Figure 4.38	Tool Vibration Percent Reduction .....	152

Figure 5.1	Machining Control System .....	154
Figure 5.2	Control System Implementation .....	156
Figure 5.3	Picture of Exciter and Tool Post Arrangement .....	158
Figure 5.4	EZ-ANC Power, Serial and Analogue Signal Connections .....	159
Figure 5.5	Experimental Setup .....	160
Figure 5.6	Control Design Approach .....	162
Figure 5.7	Normalized Tool Displacement with and without Controller .....	169
Figure 5.8	Steady State Percent Tool Vibration Reduction .....	171
Figure 5.9	Machine Tool Vibration Reduction .....	174
Figure 5.10	Spectral Density of Tool Displacement .....	180
Figure 5.11	Spectral Density of Tool Displacement .....	185
Figure 5.12	Transient Response .....	190
Figure 5.13	Shop Floor Experimental Setup .....	193
Figure 5.14	Disturbance Signal Analysis .....	200
Figure 5.15	Statistical Measures of Tool Vibration Reduction .....	209
Figure 5.16	Surface Roughness Measurement Data .....	215
Figure 5.17	Statistical Measures of Tool Vibration Reduction .....	216
Figure 5.18	Disturbance Signal Analysis .....	218
Figure 5.19	Tool Vibration with and without Control .....	223
Figure 5.20	Percent Tool Vibration Reduction .....	223

Figure A.1	Surface Profile for Trial 1 .....	233
Figure A.2	Surface Profile for Trail 2 .....	235
Figure A.3	Surface Profile for Trail 3 .....	236
Figure A.4	Surface Profile for Trail 4 .....	237
Figure A.5	Surface Profile for Trail 5 .....	238

## NOMENCLATURE

$c_1, c_2$	Damping coefficients in smart tool post model
$e$	Output error
$f$	Feed
$f_c$	Frequency of chip segmentation
FPE	Final Prediction Error
$F_c$	Cutting force
$H_i$	Net input signal to the $i^{\text{th}}$ neuron
$k_a$	Spring constant for PMN actuator
$k_c$	Cutting stiffness
$k_{ff}$	Feedforward gain
$k_{fb}$	Feedback gain
$k_u$	Unit cutting force
$k_1, k_2$	Spring constants in smart tool post model
$O_i$	Output of Neuron $i$
$m_1, m_2$	Lumped masses in smart tool post model
$N$	Size of training pattern
$p$	Tap size of input delay for emulator
$q$	Tap size of output delay for emulator
$s$	Variable in Laplace transform
$u_i$	Instantaneous chip thickness
$u_o$	Preset chip thickness
$v$	Cutting speed
$v_c$	Chip velocity
$v_j$	Hidden to output layer weight vector for nonlinear neural network
$w$	Depth of cut
$w_c$	Mean chip thickness
$w_{ij}$	Input to Hidden layer weight matrix for nonlinear neural network
$w_1, w_2$	Natural frequencies of smart tool post model
$y$	Model output
$y_d$	Desired output
$y_m$	Relative machine tool vibration
$\alpha$	Input current and delay weight vector of linear neural network
$\beta$	Output delay weight vector of linear neural network
$\delta$	Gradient error
$\varepsilon$	Average chip segment length
$\eta$	Adaptation coefficient
$\Gamma$	Activation transfer function
$\Gamma^l$	Linear activation transfer function
$\Gamma^s$	Sigmoidal activation transfer function
$\lambda$	Number of hidden neurons
$\mu$	Overlap factor

$v$	Ion function
$\sigma$	Activation function slope
$\tau$	Turning machining delay term



## Chapter 1

### INTRODUCTION

#### 1.1 Background

In the United States, metal cutting is an important and major activity in every industrial sector. Historically, the United States' machine tool industry has maintained its leadership role in the world. The invention of numerical control (NC) machining at the Servomechanisms Laboratory at Massachusetts Institute of Technology in 1961 represented the peak of its development. However, things changed in the 1970s. The downturn of the national economy, the continuous reduction of military spending, and the loss of domestic and world market share of machine tools have placed the industry in a disadvantageous position relative to its major foreign competitors. At present, the state-of-the-art of the manufacturing and production technology of the machine tool industry is significantly below the state-of-the-art that has been attained by leading international competitors. In the United States, conventional machine tools are still extensively used on shop floors. They are being pushed to their machining accuracy limits. There is a pressing need to revitalize the machine tool industry.

Apart from installation of new precision machine tools, the need for enhancing the machining capabilities of the conventional machine tools currently being used on the shop floor is evident. Considerable effort has gone into updating them. In fact, a

significant number of conventional milling machines have been furnished with digital controllers. As a result, the machining accuracy related to tool positioning has been significantly improved. However, the progress in reducing tool vibration that leads to poor surface finish, accelerated tool wear, and even tool breakage has been slow. Process control aimed at reducing tool vibration has been the focus of the entire machine tool industry for decades. But these efforts have met with limited success. The reason for the slow progress can be attributed to the complexity of the machining process and the machine tool dynamics, and the lack of systematic approaches through interdisciplinary research.

## 1.2 Motivation

There are a number of techniques that can be used to design controllers for linear systems with uncertainties. However, few techniques for active control of the machining system are available due to several reasons. First, it is difficult to identify a model structure suitable for describing the system dynamics. At times, it is very difficult if not impossible, to adequately represent system characteristics such as time delay, saturation, time varying parameters, and system complexity in general. The machining systems under study do not behave as their mathematical models describe them to be. As in this research work, when active cancellation is sought through actuators, the actuator dynamics needs to be identified and incorporated into the control algorithms. There are many sources of nonlinearity, uncertainty, and system noise, which cause mathematical models to be poor and control algorithms to be

ineffective. Second, there is lack of standard methodology to generate adaptation laws, which are capable of dealing with uncertainties and nonlinearities in machining systems. These control laws are essential to perform active vibration compensation during machining.

In the past, the techniques developed to control the machine tool vibration have been dominated by passive features with focus on manipulating the cutting parameters such as feed rate, cutting speed, and depth of cut. Therefore, it appears that there is a need for new methods for machining system control. To that end, electroactive actuators and neural network based control algorithms have attributes that make them potentially effective in addressing most of these problems.

The type of actuator implemented in this research is an electroactive device made of the electrostrictive ceramic material; namely, Lead-Magnesium-Niobate (PMN). The actuator produces mechanical displacement by either elongation or contraction in response to an applied electric field. This displacement can serve as a compensation mechanism to cancel the undesirable tool motion, or tool vibration, which is primarily due to the cutting operation.

The control methodology used in this research is based on the requirement that it should produce successful results within the scope of this thesis, and have neural room for future advancements in the area of active vibration compensation for machine tools. To that end neural networks meet the challenging requirements. Neural networks are increasingly being found as effective tools in control problems [Miller, Sutton, and Werbos, 1990; Warwick, Irwin, and Hunt, 1992]. The paramount

difference between the neural networks based controllers and conventional controllers lies in the way the controllers acquire their capabilities. The conventional controllers are programmed to perform a specific control task, whereas, the neurocontrollers are trained to learn the control task. This learning capability is an important attribute in control applications involving neural networks.

The unique learning capabilities of nonlinear neural networks even allows them to mimic highly complex, nonlinear mappings. As a result, the nonlinear neural network are effective for nonlinear control applications. Therefore, the nonlinear neural network is recommended for heavy duty machining where the PMN actuators are also forced to operate in nonlinear region for future work.

They are also adaptive controllers, since they adapt to the changing state of the systems or the changing control requirements through learning. Other advantages of using neural networks over the traditional design and systems tools are also significant. First, neural networks are naturally massively parallel. This suggests that they should be able to make decisions at high speed and be fault tolerant. Second, since the neural networks learn or adapt without time consuming programming, they save additional time and relieve programming loads considerably. Additionally, they produce a more accurate or complete response by utilizing sufficient information extracted from massive training data, therefore, improving their performance with experience. The most significant benefit of neural networks, however, is the fact that they do not require an explicit model or limiting assumptions of linearity. Therefore,

they can solve complex problems that can not be tackled with conventional control schemes.

### 1.3 Dissertation Objectives

In earlier work, at the Advanced Design and Manufacturing Laboratory, a smart tool post has been designed and fabricated with vibration attenuation in mind [Wing, 1995]. The tool post design has fulfilled the design objective of creating a unique testbed to use PMN actuators to compensate for tool vibration during machining. Immediately after the mechanical structural design, a microprocessor based control system was developed and tested for its performance that showed the promise of controlling the tool motion in laboratory experiments [Dold, 1996]. In related efforts at the Vibration Laboratory, digital active control of plate vibrations and enclosed sound fields has been investigated analytically and experimentally [Padmanabhan, 1995; Park, 1995; Sampath and Balachandran, 1996]. The research conducted in this thesis work, building on the previous efforts, characterizes a unique effort in applying the concepts of network control and adaptive filters to compensate for tool vibration in an active manner. A significant accomplishment of this dissertation research is the realization of the “smartness” element in the designed tool post mechanical structure.

The feature that makes the tool post “smart” is the availability of a control strategy that will use the measured information and manipulate the actions of the actuators so that they respond in such a way that they cancel the tool variation away from the equilibrium, or a desired position. This feature characterizes the system

robustness to the primary disturbances. In order to utilize the designed tool post to its full potential, it is necessary to design this type of controller so that it will be effective over a wide range of disturbance frequency bandwidth and also be capable of handling disturbances with multiple frequencies. Also, there is a need to develop an analytical framework to predict the controller performance through computer simulations. Such a virtual environment will be useful for designing similar tool posts in the future. Moreover, an effort should be targeted to cope with the actual machining conditions that include both random disturbances as well as periodic disturbances. The design should also pave a way for future improvement as the need arises.

To meet these challenges, the research in this thesis work has the following objectives:

1. Make a preliminary feasibility study of the control strategy for machine tool vibration cancellation by performing computer simulation.
2. Investigate the performance of the PMN actuators in attenuating tool vibration when the tool tip is excited by a dynamic vibrator in a laboratory. Explore both harmonic and multi-frequency disturbances.
3. Investigate the capability of the PMN actuators to yield better surface finish and maximum throughput by performing an experiment on the shop floor; thus verifying the results obtained from the feasibility study and the experimental work performed in the laboratory.

## 1.4 Thesis Organization

This thesis is organized into six chapters. A summary for each chapter is discussed below.

In Chapter 2, a literature review on machining systems and machine tool vibration control is presented. First, an overview of the turning machining system is presented. Then the different types of machine tool vibration are treated, and finally, a summary of machine tool vibration reduction efforts is provided.

In Chapter 3, different adaptive control methodologies are described. First, the actuator that is used to remedy the vibration problem of the machine tool is discussed. Then the different adaptive control schemes implemented in the research are discussed. Since the control structure implemented in this research is based on neural networks, fundamentals of both linear and nonlinear neural network structures are also discussed.

In Chapter 4, the conducted modeling and computer simulations are presented. The developed mathematical model of the machining system is discussed. Moreover, identification of the control mechanism that is used to cancel the tool vibration is discussed. In computer simulations, the neural controller is designed for the machining system in two steps. First, an emulator is developed to emulate the control mechanism by using a neural network. Then, a neural network based controller is designed to control the machining system. The application of the linear neural network based on adaptive signal processing methods, and the application of a

nonlinear neural network in the form of a multilayer time delay neural network are discussed. Training procedures and results are also detailed.

In Chapter 5, the experimental implementation of adaptive digital filters to compensate the tool vibration is described. The experimental setup used to perform the control tests is illustrated. The EZ-ANC digital signal processing board, a commercially available package from Australia, is discussed and the different design parameters of this system are explained. The experimentation is performed in two phases: a) laboratory experiments and b) machine shop experiments.

In Chapter 6, the results of this thesis work are summarized. The contributions of this research in the areas of machine tool vibration compensation are provided along with the conclusions. Recommendations for future work are also included in this chapter.



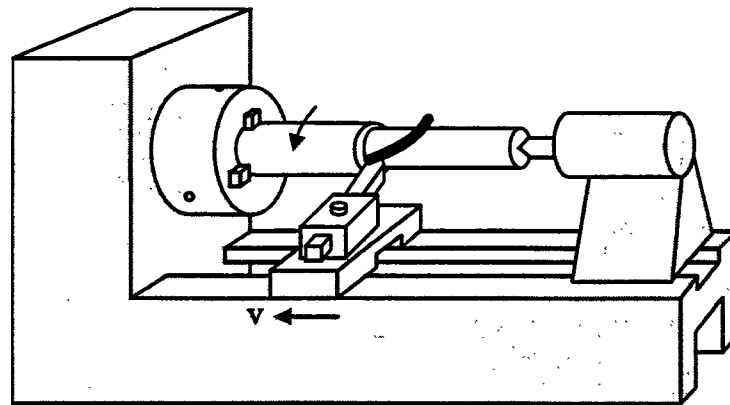
## Chapter 2

### TURNING MACHINING SYSTEMS

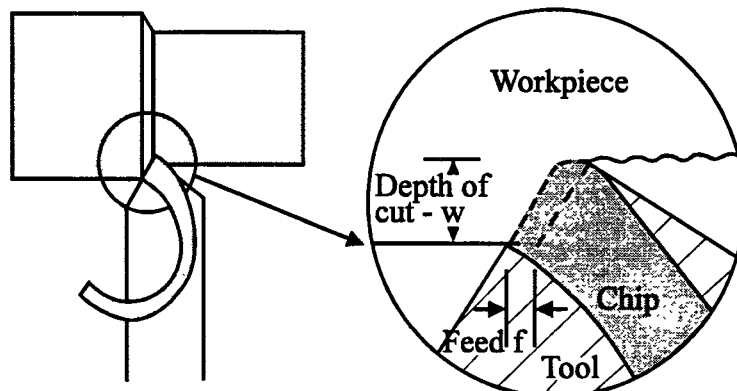
#### 2.1 Introduction

The lathe is probably the oldest machine tool, and possibly the most important ones among all machine tools [Dowyle, 1953]. Basic operations of a lathe include turning, facing, boring, drilling, and threading. Occasionally, a lathe can also be used for milling, shaping, gear cutting, fluting, and grinding. In fact, no other machine tool can be used for such a variety of operations.

In this dissertation research, the turning operation using a lathe is of interest. A turning operation is characterized by the use of single point cutting tool for removal of material from the part being machined. The nature of a single point cutting has made turning the most commonly used operation in experimental work on metal cutting. As illustrated in Figure 2.1, a single cutting edge with specified geometry in constant contact with a workpiece is used to remove material. The workpiece is held in the chuck and it is rotated at a chosen speed. The tool is held rigidly in a tool post and it is moved at a constant feed rate along the axis of the workpiece, cutting away a layer of metal.



(a)



(b)

(c)

Figure 2. 1: Turning Operation on a Lathe

The cutting speed  $v$  is the rate at which the uncut surface of the work passes the shows cutting edge of the tool. The feed  $f$  is the distance through which the tool moves in an axial direction during each revolution of the workpiece. The depth of cut  $w$  is the thickness of metal removed from the workpiece measured in the radial direction.

## 2.2 Turning Machining System Modeling

Merchant proposed the mechanics of the metal cutting process in the 1940s [Merchant, 1940]. His theory indicated that the material removal process can be explained as a process of shearing. Based on his work, models of dynamic chip formation were first established [Merritt, 1965; Tobias, 1965; Kegg, 1965; Koenigsberger and Thusty 1971; Wu and Liu, 1985]. Afterwards, linear force models that relate the inner and outer chip modulations to the dynamic cutting force were proposed and developed empirically [Srinivasan and Nachtigal, 1978; Weck, 1985; Minis, Magrab, and Pandelidis, 1990]. Statistical methods have also been introduced to model machining systems. By fitting linear Auto-Regressive Moving Average (ARMA) models to cutting force and workpiece acceleration data, statistics-based models were capable of predicting not only the deterministic part, but also the stochastic part of the cutting force [Pandit, Subramanian, and Wu, 1975; Eman and Wu, 1980].

There is an on-going research on machine tool dynamics at the Mechanical Engineering Department, University of Maryland at College Park. Berger, Minis and Rokni [1993], established the complex dynamics in orthogonal cutting through the analysis of experimental cutting data. They developed nonlinear cutting equations combined with linear structural models resulting in systems which exhibit chaotic oscillations [Berger, Rokni, and Minis, 1993].

The turning machining system model proposed by Meritt [1965] is based on control theory. This modeling process gives significant insight into the underlying

dynamics of the machining process. The modeling strategy adopted in this thesis work is mainly based on his approach. The machining system modeled by Merritt consists of three components. These components are the cutting process, structural dynamics, and a set of feedback paths that represent the interactions between the cutting process and structural dynamics. In Figure 2.2, the block diagram for the machining system model is shown.

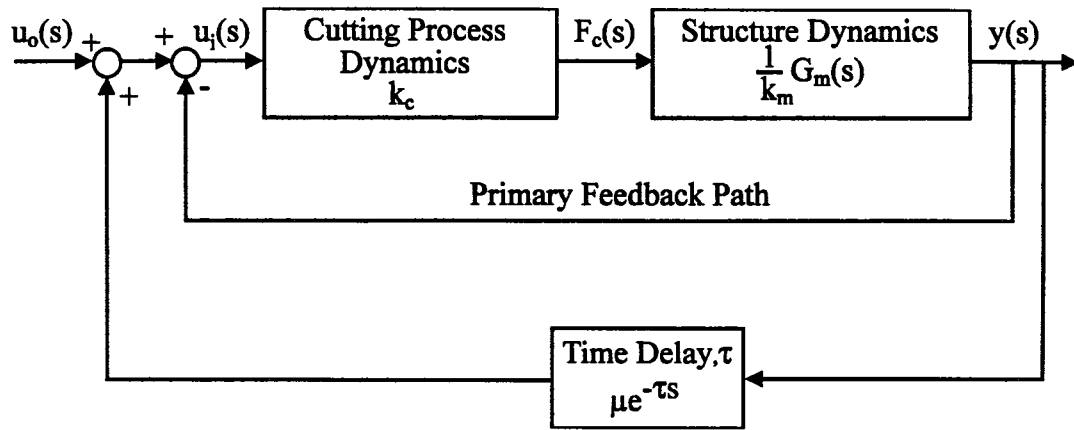


Figure 2. 2: Block Diagram of Machining System Model

As illustrated, the input to the cutting process or the machining system is the chip load. The output of the cutting process is the cutting force, which serves as an input to the machine tool structure. The output of the machine tool structure, when subjected to the cutting force, is the tool vibratory motion. The feedback paths modify the nominal chip load instantly by sending the tool motion back to the system input. Next, the three components of the machining system are discussed in detail.

### 2.2.1 Cutting Process Dynamics

Merchant [1940] suggested that a steady state cutting process could be characterized by a parameter to represent the proportionality between the cutting force and the chip load. This parameter was later called the unit cutting force  $k_u$ . The nominal chip load is given using the previously defined parameters for feed and depth of cut as

$$\text{nominal chip load} = f * w \quad \text{Eq. 2.1}$$

The instantaneous chip load, which is an input to the machining system, is defined as the area being removed during machining. The cutting force  $F_c$  is related to the instantaneous uncut chip thickness  $u_i$  as shown below.

$$F_c(t) = k_c * u_i(t) \quad \text{Eq. 2.2}$$

$$k_c = k_u * w \quad \text{Eq. 2.3}$$

where the parameter  $k_c$  is the cutting stiffness. The unit cutting force for a given workpiece material under certain machining conditions can be found either in machining data handbooks or experimentally determined [Kalpakjian, 1991].

This cutting process model has been widely accepted by the machine tool industry despite its limitations in characterizing the machining process due to the assumption of the linear proportionality. The model's deviation from accurately depicting the cutting process is due to the following:

1. The uncut chip thickness depends on the cutting dynamics.
2. The cutting stiffness does not remain constant at varying speeds.

Nevertheless, these factors do not significantly weaken the ability of the model to characterize the cutting process. Rather, it does a fairly good job with acceptable accuracy. After all, there are very few alternative models that have been developed from the physics of metal cutting process, nor is there a definitive experimental validation to prove its superior working accuracy.

### 2.2.2 The Structural Dynamics

The structural dynamics of the machine tool plays a significant role in the machine tool vibration. The structural dynamics consists of the lathe machine base and the tool post which holds the cutting tool. The tool post used in this research is shown in Figure 2.3.

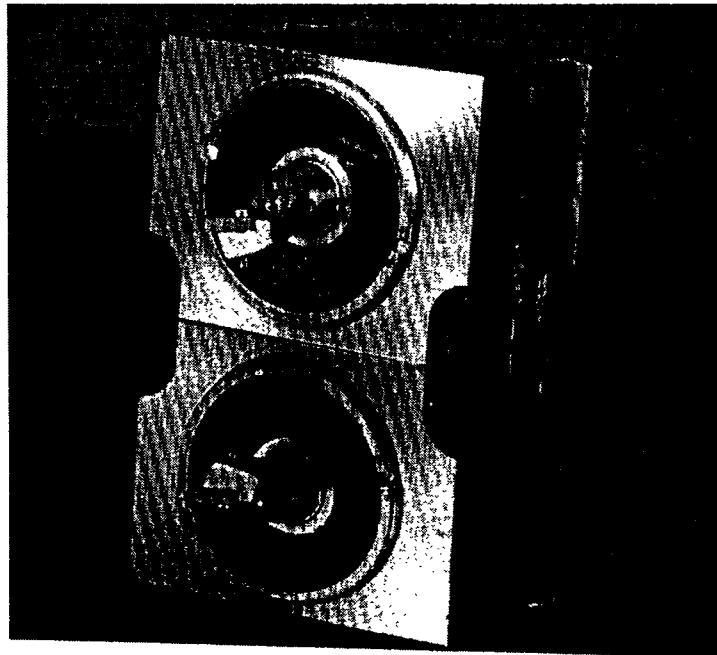


Figure 2.3: Smart Tool Post Structure

The tool post under study consists of four main parts: a cutting tool, a vibration absorber, membranes, and a case. Figure 2.4 is an assembly drawing of the smart tool post mechanical structure showing all these components of the tool post mechanical structure along with the actuators and sensor.

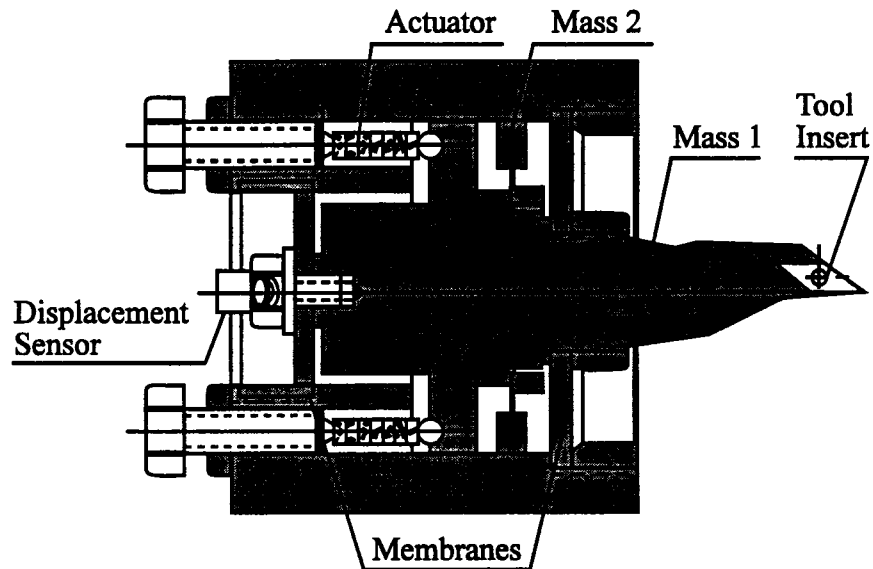


Figure 2.4: Assembly Drawing of Smart Tool Post Structure

The cutting force acts on the workpiece so as to displace it as well as the structure of the machine itself due to the reaction force. Therefore, the structural dynamics is of interest from the viewpoint of machine tool vibration. As a result, it is necessary to model the structural dynamics that relates the cutting force to the machine tool displacement. This dynamic model should include the following three important parameters: inertia, stiffness, and damping coefficients. The mathematical modeling of the tool post is covered in Chapter 4.

### 2.2.3 Feedback Paths

The two feedback paths shown in Figure 2.2 describe the interaction between the structural dynamics and the cutting process, thereby a model for the instantaneous chip thickness can be constructed. The first feedback path is called the primary feedback path, and it characterizes the relative position of the tool with respect to the workpiece being machined. Intuitively, the instantaneous thickness of the cut decreases as the cutting tool moves away from the preset depth of cut relative to the workpiece.

The second feedback path is called the regenerative path, and it represents how much material was left over from the previous cutting action. The effective residual material from the previous action is the product of the percentage of overlap between two consecutive actions and the amount of residual material left from the first action. This concept is consistent with the fact that there is no residual material from the previous revolution in machining a thread. The instantaneous uncut chip thickness is related to the preset thickness  $u_o$  by using the following relation.

$$u_i(t) = \mu y_m(t-\tau) - y_m(t) + u_o(t) \quad \text{Eq. 2.4}$$

The above expression states that the chip thickness that produces the feeding force is due to undulations on the free surface of the chip formed on the previous revolution, undulations on the workpiece surface being generated, and the programmed feed. Therefore, the momentary uncut chip thickness is the sum of three components. The first component  $\mu[y_m(t-\tau)]$  is the amount of residual material from



$\tau$  units of time ago. The second term  $y_m(t)$  is the current position of the cutting tool, and the third term  $u_o(t)$  is the preset feed.

## 2.3 Machine Tool Vibration

In a perfectly rigid body, the distance between any two points remains constant in time. In other words, the size and the shape of the body does not change when the body is subjected to dynamic and/or static forces. If all of the elements of the system are mounted together to form an ideal rigid body, the different elements will not move relative to each other and the system performance will not be impaired due to vibration. However, a turning machine can be represented as a vibrating system made up of spatially continuous springs, masses, and dampers. Since components of the machine tool and the workpiece are elastic bodies, they undergo deformation when they are subjected to static forces. When the acting force varies as a function of time, the structural dynamics of the machine tool and the workpiece characterize a physical phenomenon observed during machining known as vibration. Machine tool vibration may be classified as random, externally forced vibrations, internally forced vibrations, and self-excited or self-induced vibrations.

### 2.3.1 Random Vibration

Random vibration is caused by excitations that are characterized by uncertainty, such as irregular impulsive loading of the machine tool. Random vibration can happen when a non-deterministic loading is transmitted through the

machine foundation. The process of tool wear changes the tool geometry. Such a change can be another source of random vibration. As the tool wears, the cutting force changes accordingly. The random nature of tool wear results in a random excitation to the machine tool structure.

Nonhomogenous distribution of the hardness in the workpiece in micro-scale is another source of random vibration. Due to the nonhomogenous distribution in micro-hardness, the cutting forces produced during machining vary instantaneously.

### 2.3.2 Externally Forced Vibration

Forced vibration from sources other than cutting originates from external forces coming either via the foundations or from acoustic coupling, or resulting from defective mechanical parts, such as bearings, gearbox, or unbalanced rotating members like gear drives, motors, or machine tool components. Such forced vibration causes the machine to vibrate at the excitation frequency, a typical characteristic of forced vibration.

The amplitude of tool vibration depends on the compliance of the machine at that particular frequency of the disturbance force. Usually, the externally forced vibration is periodic because the source is often due to a rotating component of the machine tool. As a result, the frequency is usually an integer multiple of the rotational frequency of a drive or a spindle.

Compared with random vibration, it is relatively easy to influence externally forced vibration. Factors such as faulty machine elements or unbalanced rotating parts can be eliminated by undertaking well known steps. Strict machine maintenance, on-

machine diagnostics, and good machine tool or component design are the ways that this source of vibration can be eliminated.

### 2.3.3 Internally Forced Vibration

Externally forced vibrations can occur when a machine is not removing material, whereas internally forced vibrations occur only during the material removal process. Under certain conditions, the cutting process becomes periodic in character because of the chip making process.

The first cause of internally forced vibration is built-up edge (BUE). The presence of BUE changes the effective cutting geometry. In general, the effective rake angle increases as the BUE develops and grows as shown in Figure 2.5. It can be seen that the longer the height of BUE the larger the effective rake angle, and the smaller the height of the BUE, the smaller the effective rake angle. An increase in the effective rake angle reduces the cutting force generated during machining. As a result, a variation in the effective rake angle produces a variation in the cutting force.

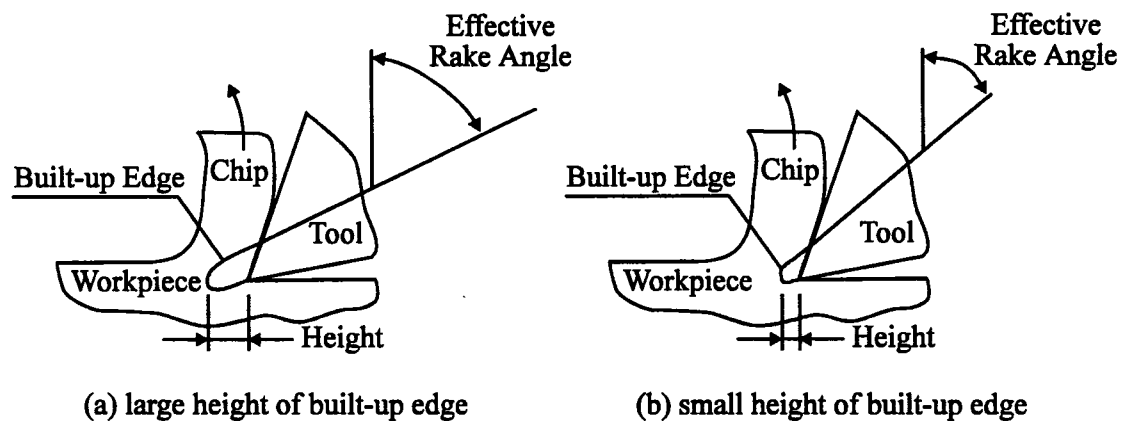


Figure 2.5 Effect of Built-Up Edge on Rake Angle

Kuznetsov [1966] in a discussion of the work of Shteinberg [1947] showed that the frequency of vibration, as measured by recording force on the tool, was essentially the same as the frequency of BUE fracture determined by counting BUE particles on the chip. Kuznetsov suggested that fracture of the BUE be controlled by the friction force between the tool and the BUE and the forces applied by the chip and the workpiece to BUE. The rate of growth of the built-up layers will be approximately constant. Thus there will be a natural frequency for BUE formation. This frequency can be a forcing frequency for the machine system.

The second source of internally forced vibrations is chip segmentation. Landberg [1956] experimentally investigated the segmentation of the chip and found that for low speeds the frequency fluctuations in the measured cutting force corresponded with the frequency of formation of chip segments. The frequency of chip segments was determined by counting the segments on a measured length of chip. From this he obtained the average chip segment length  $\epsilon$ . The chip velocity  $v_c$  in terms of the mean chip thickness  $w_c$  is given by

$$v_c = \frac{vw}{w_c} \quad \text{Eq. 2.5}$$

where  $v$  is the cutting speed in ft/min and  $w$  is the depth of cut in inch. The frequency of chip segmentation in Hertz is thus

$$f_c = \frac{12v_c}{60\epsilon} = \frac{12vw}{60w_c\epsilon} \quad \text{Eq. 2.6}$$

Ferraresi [1960] carried out an investigation similar to Landberg's investigation. In order to examine the effect of machine stiffness he performed comparative experiments on two different lathes. His results showed that the machine had no effect on chip segmentation.

The third cause of internally forced vibration is discontinuous-chip formation. An explanation for the physical phenomena of discontinuous-chip formation based on cutting at very low speeds were presented [Field and Merchant, 1949; Cook, Finnie, and Shaw, 1954]. In the early stages of chip formation, the chip slides up the tool face creating a shear zone. Then the chip ceases to flow up the tool face and the plastic zone spreads ahead of the tool. At this stage a fissure opens up at the tool point. Later the fissure swings up and meets the free surface to form a free chip particle. The tool then moves forward to initiate a new cut in the inclined plane left from the previous chip formation.

The cyclic frequency due to discontinuous-chip formation appears to be largely determined by cutting conditions, particularly the properties of the work material. The characteristics of discontinuous-chip formation influence tool vibration amplitudes significantly when resonance occurs.

#### 2.3.4 Self-Excited Vibration

The last form of machine tool vibration is self-induced vibration. Doi was one of the first researchers to consider the cutting process as an energy transferring

mechanism capable of establishing a self-excited system [Doi, 1937]. Such vibration is caused, built up, and sustained by the interaction or coupling inherent between the cutting process and the machine tool. Figure 2.6 illustrates the process of self-excited vibration in turning. It shows that the cutting process and the vibrating system comprising the machine, the machine tool and the workpiece form a closed loop. The vibration between the machine tool and the workpiece influences the cutting process so as to cause a variation of the cutting force. This force in turn acts on the machine structure, resulting in vibration. Under some conditions, the coupling between the mechanical structure and the cutting process becomes such that the vibration once started due to any random cause does not die down; it may even build up into a severe state of vibration called chatter.

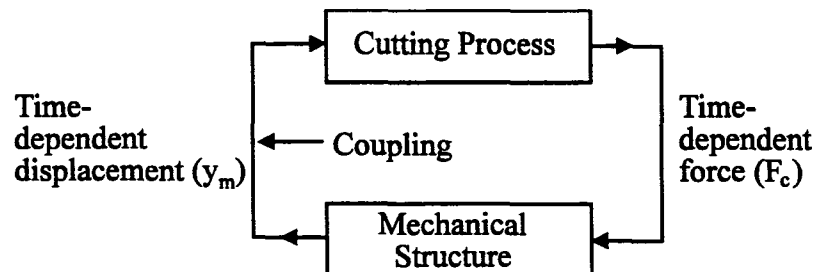


Figure 2.6: Coupling between the Cutting Process and the Mechanical Structure

Self-excited vibrations represent unstable events in a system of the workpiece-tool-machine-turning process. The main distinguishing feature between self-excited and forced vibration is time dependency. In case of self-excited vibration, there is a relationship between the machining time and the development of tool vibration amplitude. In the case of forced vibration, the amplitudes are more or less

independent of the machining time. The most important causes of self-excited vibration are the regenerative effect and the mode coupling effect [Juneja, and Sekhon, 1987].

The regenerative effect can be best depicted as in Figure 2.7. The turning process produces a new surface by removing material from a surface generated during a previous workpiece rotation. The surface modulation produced during the previous revolution is added to the cutting action in such a way that self-excited vibration or chatter occurs.

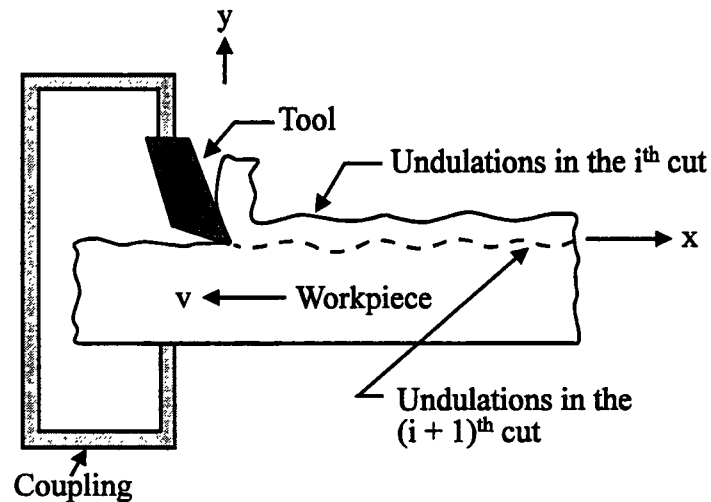


Figure 2.7: Regenerative Effect

The energy imparted by the fluctuating force caused by the variation of uncut chip thickness to the vibratory system may be sufficient to cover the loss of energy due to friction and damping present in the system. In this case, vibration in the subsequent passes does not die out, on the contrary, it may actually increase.

The mode coupling effect can produce chatter only when the vibratory system possesses at least two degrees of freedom and can simultaneously vibrate in two opposing directions as shown in Figure 2.8. In this case, the cutting force opposes the motion of the vibrating mass in the first half-cycle and assists it in the other half-cycle. Since the uncut chip thickness is greater in magnitude in the second half-cycle, the addition of energy is more than its expenditure. This surplus energy may be sufficient to overcome the damping losses and create a chatter phenomenon.

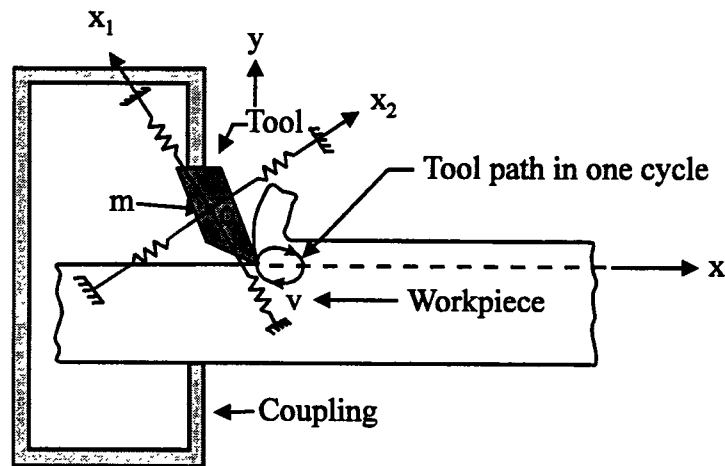


Figure 2.8: Mode Coupling Effect

The problem caused by vibration and chatter introduces the question of stability in the machining system. Figure 2.9 the stability chart used by many researchers when dealing with machining stability. There are three borderlines of stability in the figure: lobed, tangent, and asymptotic. The lobed borderline of stability is the exact borderline and may be approximated with the asymptotic borderline or more closely with the tangent borderline. The three borderlines of



stability are progressively more difficult to compute. Nevertheless, they are perceived to be progressively less important from a practical viewpoint.

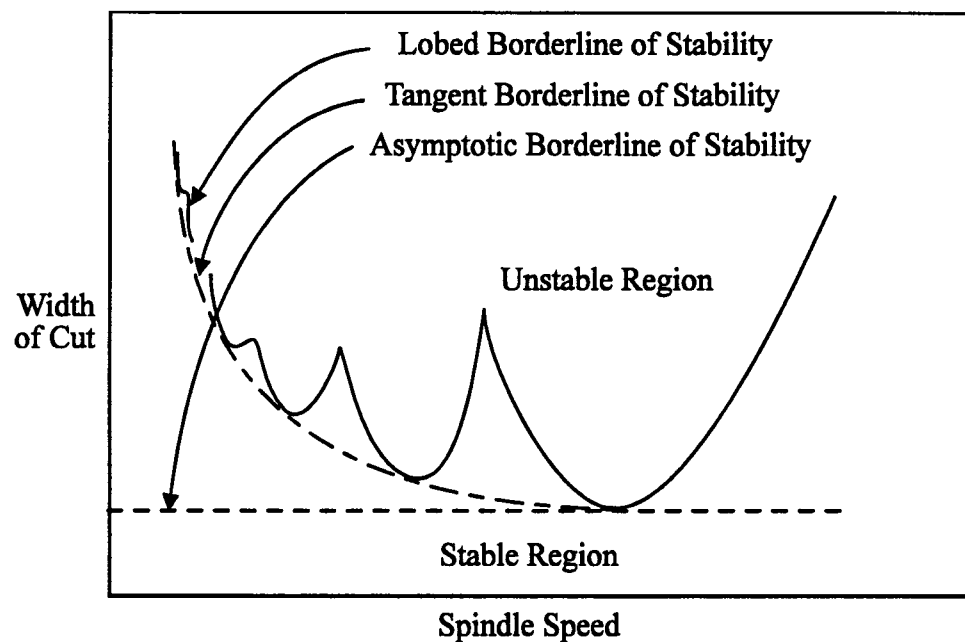


Figure 2.9: Typical Stability Chart for a Machine Tool

## 2.4 Machine Tool Vibration Control

Since the full potential of turning machines often cannot be utilized due to the occurrence of vibration, it is very desirable to eliminate chatter by taking steps to reduce its incidence. Since it is not possible to completely eliminate the sources of vibrational disturbances, the goal is to reduce relative motion between the machine

tool and the workpiece. The steps the machining industry has taken to reduce or eliminate tool vibration include the following:

1. Adding stiffness and/or damping to the setup. This is a passive means to tackle machine tool vibration. All the critical elements should be connected together to form a dynamically rigid structure that is designed to have resonance frequencies far removed from the operating frequencies and/or significant damping at resonance frequencies.
2. Isolating the system from vibration by operating at speeds that do not cause cyclical forces whose frequency approaches a resonance of the machine tool system.
3. Changing the cutting conditions, for example, by reducing the feed rate and the depth of cut and increasing the rake angle.
4. Changing the design and geometry of the machine tool and changing the method of clamping the workpiece.

There has been considerable research in the development of adaptive controllers for machining systems. The main problem addressed in the area of the manufacturing community is that of controlling the cutting force in metal cutting operation by controlling the feed rate. The term “adaptive control” is used in machining literature in a rather misleading way when applied to the control of machine tools. Adaptive control for machine tools is used to describe a system that employs feedback from the cutting process to alter cutting conditions. Hence adaptive machine

tool controller does not have an adaptive control scheme in the control engineering sense.

Even though adaptive control of machine tools has attracted much academic and industrial interest for decades, very little progress has been achieved.

Conventional linear control schemes have been shown to be inadequate for regulation of variables in metal cutting, such as the cutting force generated during machining.

Several ad hoc schemes have been developed [Bedini and Pinotti, 1982; Wilson and Wilkinson, 1981]. A commercially available adaptive control system is reported to use gain scheduling, based on measurement of oscillations [Koren and Masory, 1981]. They implemented parameter Adaptive Control Constraint (ACC) of cutting force in turning using a microprocessor, neglecting the process time-constant and without the use of any formal adaptive control design techniques. Ulsoy, Koren, and Rasmussen [1983] presented simulation results of the same scheme. Stute and Goetz [1975] used a hardwired model reference adaptive system, based on estimation of gain and relating time-constant to spindle rpm, for regulating spindle power by varying feed rate.

Spiewak and Szafarczyk [1978] carried out an analysis of the control of cutting force using feed as the control input. They judged that the on-line estimation of process gain was too complex for implementation. Tomizuka, Oh, and Dornfeld [1983] provided the first comprehensive analysis of parameter adaptive control for a machine tool based on the theory of adaptive control systems.

The target of this research is active vibration cancellation using smart material-made actuators. Here, we explore the possibility of active cancellation of the vibration using actuators. In this scheme, displacement sensors deliver information concerning the relative displacements between workpiece and machine tool. This information is used by the adaptive controller to develop adjusting signals for the actuators. The actuator forces in turn produce displacements opposing the primary disturbance, thus canceling the vibration.

## Chapter 3

### CONTROL METHODOLOGY

#### 3.1 Introduction

In this chapter, the focus is on active vibration control. The cutting action generates a primary disturbance to the tool, which results in tool vibration. The secondary disturbance which is generated by using “smart” material-made actuators is used to cancel the unwanted tool vibration. Specifically, these actuators are Lead-Magnesium-Niobate (PMN) actuators.

As stated in Chapter 2, there are a variety of sources of process variations in machining operations. The machining process is rather complex, and not well understood; it is neither possible nor economical to make a through investigation of all the causes of the process variations. Therefore, an adaptive control strategy is a good candidate to cancel machine tool vibrations. In this thesis research, a pragmatic definition is taken in which an adaptive controller is defined as a controller with adjustable parameters and a mechanism for adjusting the control system parameters.

### 3.2 Active Vibration Control Using Smart Material-Made Actuators

The active vibration control implemented in this research employs an external device to produce a secondary disturbance to cancel the unwanted primary disturbance. A complete active control system includes actuators to produce and apply forces to the structure, sensors to measure the response of the system and to deliver the information to the control circuitry, and a controller to deliver the appropriate control signals to the actuators so as to achieve the desired system response. This desired response corresponds to near zero machine tool vibration. The device employed to serve such a purpose in this research is called a smart tool post because it has the ability to sense and react to its environment. The actuators are electroactive devices made of the electrostrictive ceramic material Lead-Magnesium-Niobate (PMN).

An electroactive device is broadly defined as a device that produces a non-electrical output, given an electrical input, or vice versa. An electromechanical device produces mechanical displacement by either elongation or contraction in response to an applied voltage. The two basic categories of electromechanical devices are electrostrictive and piezoelectric devices. In Table 3.1, the characteristics materials for these two actuator types are provided.

Table 3.1 Characteristics of Electrostrictive and Piezoelectric Actuators

	<b>Electrostrictive [Lead Magnesium Niobate (PMN)]</b>	<b>Piezoelectric [Lead Zirconate Titanate (PZT)]</b>
Unit Cell's Microstructure	Perovskite Structure; Centro-Symmetric	Perovskite Structure; Non Centro-Symmetric.
Net Material Polarization	Before Usage, No During Usage, Yes After Usage, No	Yes All the Time.
Poling before Service	No	Yes. Electric field is applied to the heated sample. Domains are realigned from relocation of cell ions.
Operating Principle	The cations and anions are displaced in the electric field. The net result is a distortion of the unit cell with an unbalanced charge distribution.	Application of an electric field of the same polarity as the poling field will increase domain alignment. It causes a physical elongation. Contraction can be caused by applying opposite polarity.
Displacement vs. Applied Field	Quadratic	Linear
Displacement Resolution	High Precision	Low Precision
Hysteresis*	Prominent	Not Serious
Creep*	Insignificant	Significant
Operating Temp.	Narrow range	Wide range
Capacitance	High	Low
Force	High	Low

\*Note: **Hysteresis** is defined as the difference in device output resulting from different input conditions.

**Creep** is defined as the change in displacement over time under constant electric field.

Although not all devices can operate bi-directionally, the type of PMN actuators is a special kind of electromechanical device that can convert the energy in both directions. In Figure 3.1, the actuator strains for both electrostrictive and piezoelectric devices are shown.

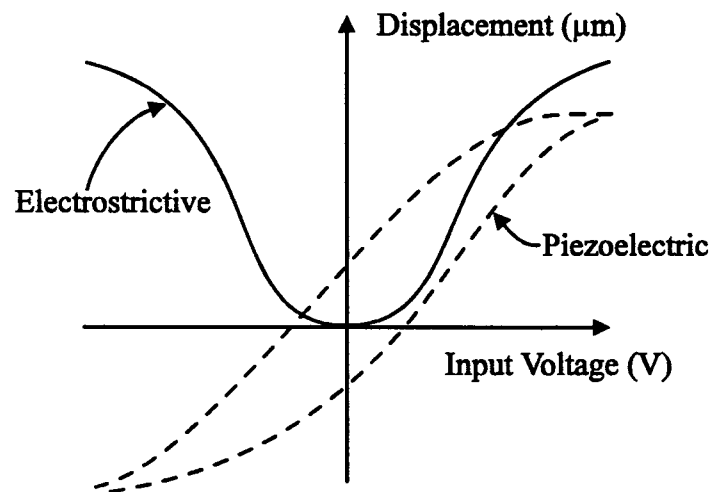


Figure 3. 1: Actuator Displacement versus Voltage Input

The actuators used to actively control the tool vibration must fulfill various requirements among which the following are cited:

1. Displacement resolution with high precision.
2. High mechanical rigidity
3. Compact setup
4. Amenable to control using an electric field
5. Production of large forces



The actuators based on conventional mechanical and/or hydraulic methods are not suited because of the time delay in the system response and the low efficiency of energy conversion. For these reasons, efforts have been made to find new types of actuators. Certainly, PMN actuators deserve special attention because they have wider operational range by producing high forces and display precise displacement capabilities.

An actuator can be either a single-layer device or a multilayer device. The amount of displacement an actuator can achieve is proportional to the voltage per unit length of the material, which is expressed as the electric field with the unit of Volts/micro-meter. For a given actuator length and actuator input voltage, it is preferable to have an actuator consisting of many thin layers rather than a single thick layer actuator to realize a large displacement. Therefore, lower voltage operations are possible with multilayer actuators for a chosen displacement. In order to maximize total displacement and minimize operating voltage, many single layer devices are usually stacked together to produce a multilayer device as shown in Figure 3.2. Hence, the PMN actuators used in this thesis work are in the form of multilayer ceramic actuators (MCA) .

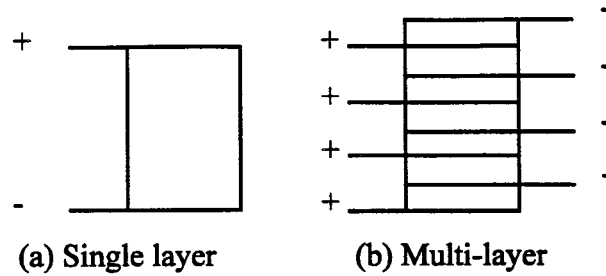


Figure 3. 2: Single Layer and Multi-layer Ceramic

The primary physical phenomenon that causes an electromechanical device to increase in length when an electric field is applied is different for electrostrictive and piezoelectric materials. The displacement in the ceramic electrostrictive material used in this research is caused by the elongation of the individual atomic cells as shown in Figure 3.3. As illustrated, in part (a), the structure is shown before the application of an electric field, and in part (b), the structure is shown when subjected to an electric field. The unit cells are made up of positively and negatively charged ions. When subjected to an electric field, the positively and negatively charged ions are forced in opposite directions. The net result of this is a distortion of the previously symmetric unit cell into a nonsymmetric shape with an unbalanced charge distribution called electric dipole.

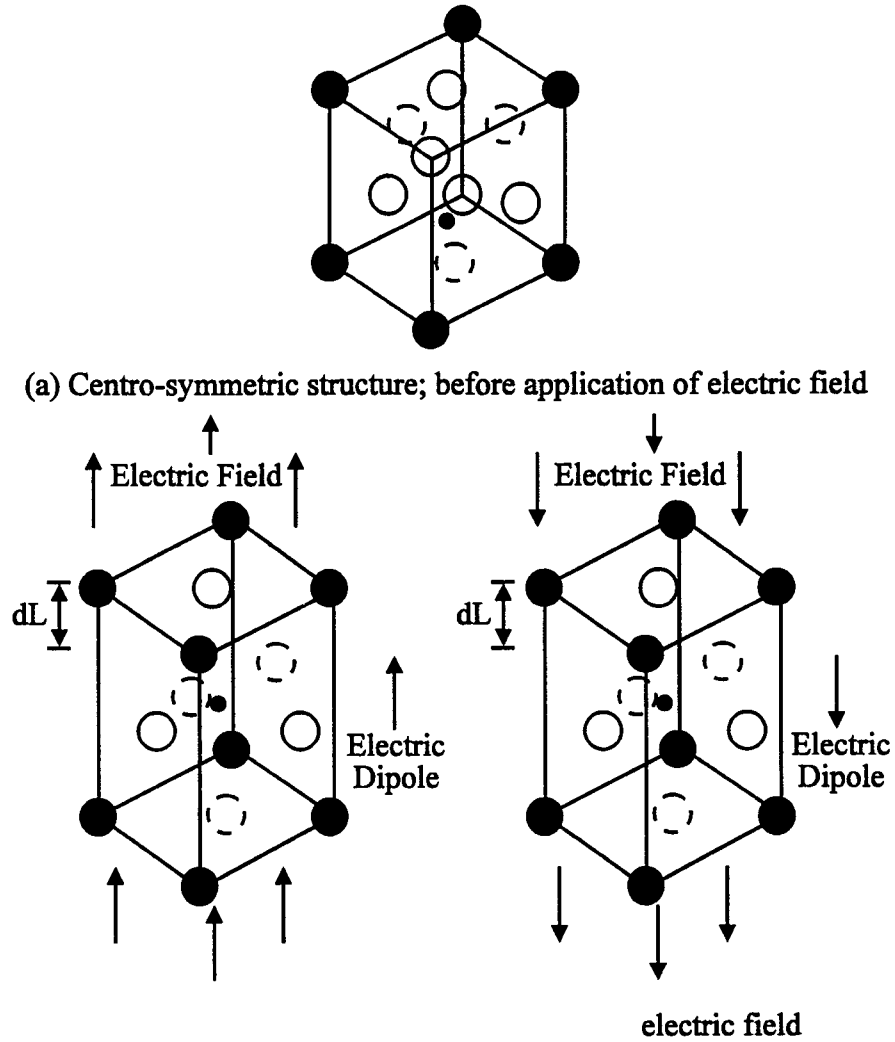
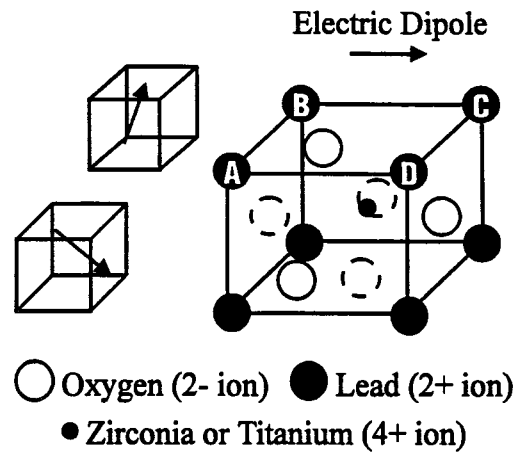


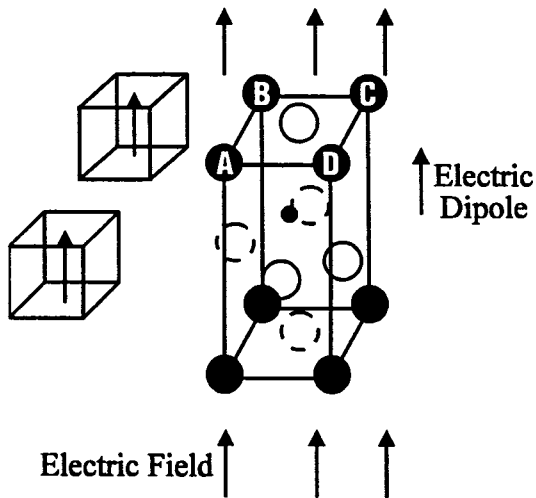
Figure 3. 3: Primary Electrostrictive Response Mechanism

However, the piezoelectric materials have nonsymmetric unit cells in the unperturbed state to begin with. Therefore, the unbalanced charge distribution results in an electric dipole or polarization. Unit cells are grouped in regions of similarly oriented dipoles called domains. Since the domains are randomly oriented for kinetic and thermodynamic reasons, it results in no net material polarization.

During the poling process, the piezoelectric material is heated to facilitate domain realignment. When an electric field is applied it causes the dipoles in the nonsymmetric unit cells and the domains to align, resulting in net electrical polarization of the material as shown in Figure 3.4.



(a) Before application of electric field



(b) Under electric field

Figure 3. 4: Piezoelectric Poling Mechanisms

Typical parameters and specifications for a 6 mm diameter, 20 mm length, cylindrical actuator stack are shown in Table 3.2 [SMS News, 1993].

Table 3.2 Typical Actuator Parameters

	<b>Electrostrictive</b>	<b>Piezoelectric</b>
Maximum Displacement ( $\mu\text{m}$ )	18	16
Capacitance ( $\mu\text{F}$ )	6	1
Dissipation Factor (%)	4.5	3
Force (N)	3,000	1,300
Hysteresis (%)	2	15
Creep (Max. after 24 hours)	2%	15%
Operating Temperature ( $^{\circ}\text{C}$ )	10 to 50	-20 to 80
Thermal Coeff. of Expansion	<1 ppm/ $^{\circ}\text{C}$	<2 ppm/ $^{\circ}\text{C}$
Modulus (N/m <sup>2</sup> )	9.6e10.	6.0e10.
Response Time	<100 $\mu\text{s}$	<10 $\mu\text{s}$

### 3.3 Adaptive Control Schemes

The adaptive control architecture implemented in this research for a single-input single-output is shown in Figure 3.5. The architecture has three components: emulator, controller, and adaptation algorithm. The emulator is used to emulate the control mechanism. The controller provides control signals for the actuators, and the adaptation algorithm is used to adjust the weights of the controller for maximum disturbance attenuation. The adaptive control strategy of machine tool vibration compensation can take the form of a feedforward scheme, a feedback scheme, or a hybrid implementation of both schemes. These three schemes are realized by assigning appropriate values to the forward gain and feedback gain represented in Figure 3.5 by  $k_{ff}$  and  $k_{fb}$ , respectively.

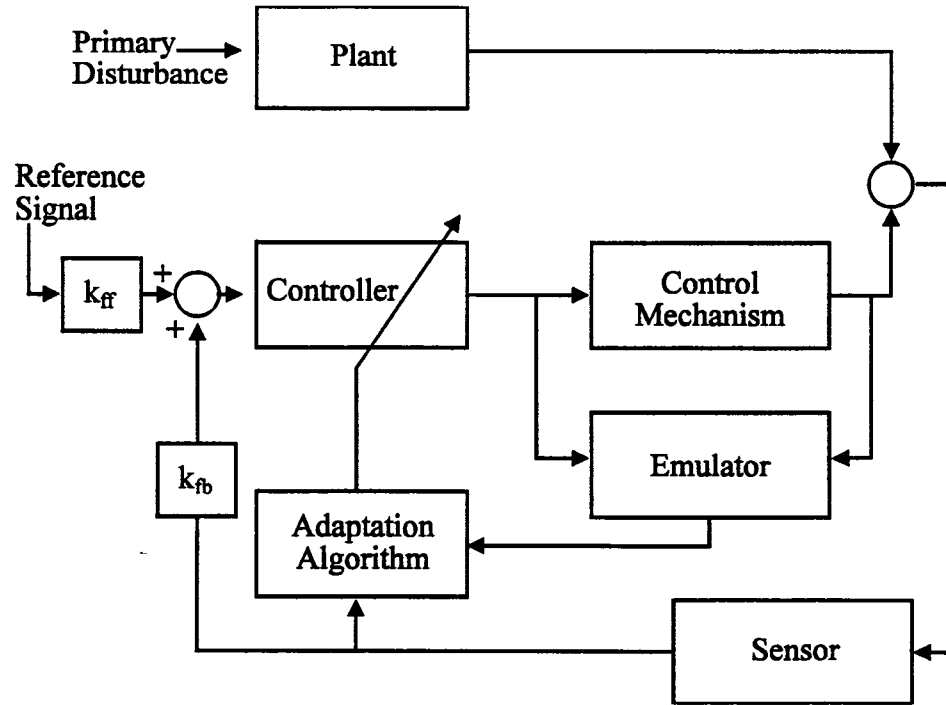


Figure 3. 5: Block Diagram of an Adaptive Control System

### 3.3.1 Adaptive Feedforward Control

The application of adaptive feedforward control for active vibration and noise cancellation problems has been well explored over the past decade [Widrow, 1971; Nelson and Elliott, 1994]. It is usually implemented through digital finite impulse response (FIR) filters or infinite impulse response (IIR) filters whose coefficients are updated by using gradient algorithms.

The adaptive feedforward architecture for vibration compensation takes a form given by block diagram shown in Figure 3.5 with the feedback gain set to zero. Here, a measure of the primary disturbance is available to the controller in the form of a reference signal. The control signal is obtained by systematic modification of the

weights of the controller. A feedforward control scheme performs well as long as the reference signal is partially coherent with the primary disturbance, and the controller causality is ensured.

For a persistent tonal disturbance or a bandlimited disturbance, feedforward control systems often offer the potential for greater disturbance attenuation than feedback control systems. In order to implement a feedforward control system, the disturbance needs to be known a priori. It is also robust in the sense that uncertain systems or those that have been modeled inaccurately can be handled to some extent.

There is an important difference in the control strategy between the feedforward and feedback control systems. Heuristically, the feedforward control system can be viewed as offering prevention of the disturbance, producing an output to counteract the disturbance upon its arrival, while feedback control systems must wait until the disturbance has occurred and has been measured by the output sensor before the controller can use it as a reference signal.

In general both kinds of forced vibration, internal and external vibrations of the machining system, are excited by a particular harmonic disturbance. Frequency components of the machine tool vibration are likely to be at the excitation frequency. Therefore, it is possible to determine the sources of forced vibrations by examining the tool vibration signal. This way a suitable reference signal can be identified for the machining operation.

### 3.3.2 Adaptive Feedback Control

An adaptive feedback control system is a closed loop control system where the output is measured and compared to a desired value, and the resulting error is used to adjust parameters of the controller, thus affecting the output of the entire system. The classical approach involves feedback of either the system states or system outputs. The feedback gains can be designed by using methods such as pole-zero placement and root locus analysis in frequency domain or linear optimal quadratic regulation in time domain [Kwakernaak and Sivan, 1972; Ogata, 1990]. The most intuitive approach is feedback of algebraically negative values of position and/or velocities of the system. In Figure 3.5, if the feedforward gain is set to zero, the resulting block diagram is for a feedback control scheme.

This control strategy is well suited for the control of transient disturbances, whereas in the presence of persistent disturbances, an adaptive feedback control scheme is not as appropriate as a feedforward scheme [Padmanabhan, 1995]. Therefore, it is necessary to combine both schemes to create a hybrid control system to take advantage of the features of both schemes..

### 3.3.3 Adaptive Hybrid Control

It is apparent that either a feedback control scheme or a feedforward control scheme by itself has certain limitations and advantages. An extension of these schemes, where the benefits of both may be used to full advantage, is a hybrid control



scheme. Here, both feedforward and feedback control schemes are implemented in an integrated form to produce a control system that will effectively attenuate the referenced disturbance to the degree maximally possible, and also provide some attenuation of the unreferenced component of the disturbance. While the feedback scheme provides robust disturbance compensation, the feedforward control provides active vibration cancellation. In Figure 3.5, when the gains are nonzero, the resulting block diagram is for a hybrid control scheme.

### 3.4 Neural Network for Control

The study of neural networks in control systems can be seen as a natural step in the evolution of control methodology to meet new challenges due to the need to address challenging problems effectively. There is a renewed interest to exploit neural networks for control applications [Narendra & Mukhopadhyay, 1994; White & Sofge, 1992; Hunt & Sbarbaro, 1991; Levin, Gewirtzman & Inbar, 1991; Miller, Sutton & Werbos, 1990; Psaltis, Sideris & Yamamura, 1987].

#### 3.4.1 Neural Network Fundamentals

Research has been done in the field of artificial neural networks since the early 1940s. The early neural network research was motivated by the observation that the human brain can perform very complicated tasks and yet is made of “simple” processing elements called the neurons, as shown in Figure 3.6 [Hebb, 1949].

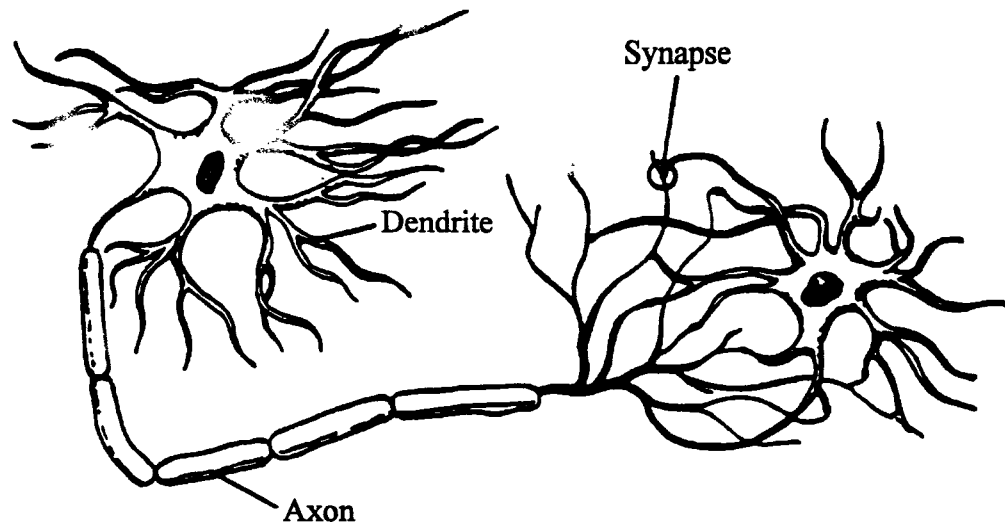


Figure 3. 6: Two Biological Neurons in Synaptic Contact

The soma or nerve cell is the large round central body of the neuron which is approximately 100 microns in diameter. The axon is attached to the soma and is electrically active producing the pulse which is emitted by the neuron. Synapse is a specialized contact that occurs where the dendrites of two different nerve cells meet. There, the electrically passive dendrites receive inputs from other neurons.

Artificial neurons are analogous to their biological counterparts, as illustrated in Figure 3.7. Here, the axons and dendrites are in the form of wires, the neurons are in the form of processing elements, and the synapses take the form of variable resistors carrying weighted inputs that represent data.

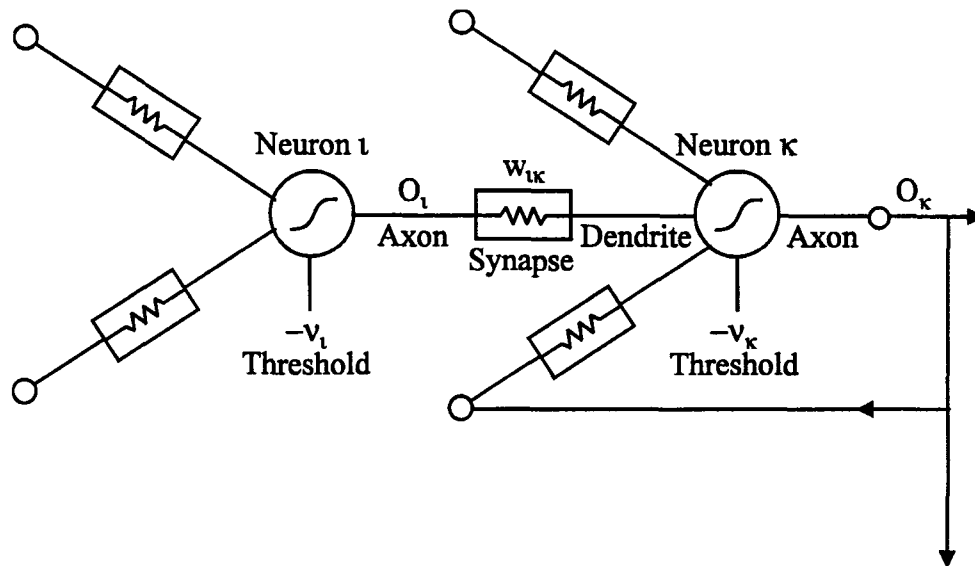


Figure 3. 7: Two Artificial Neurons in Synaptic Contact

The basic node elements employed in neural networks differ in terms of the type of network considered. Here, the commonly encountered model, a form of the McCulloch and Pitts neuron, is employed [Aleksander, 1991]. In Figure 3.8, a typical model of a neuron is illustrated. Each input connection to the neuron unit has a weighting value associated with it, and the unit produces a single output.

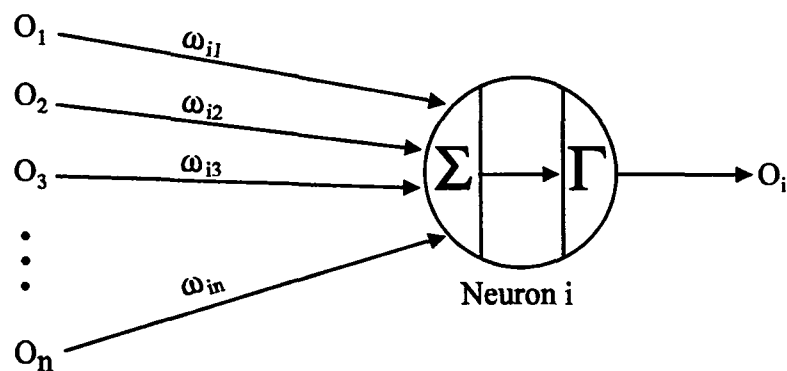


Figure 3. 8: Neuron Model

The input computation for each unit  $i$  in the network at time  $t$  is given by

$$H_i(t) = \sum_{j=1}^n w_{ij}(t) O_j(t) \quad \text{Eq. 3.1}$$

where the term  $H_i(t)$  represents the net input signal to the  $i$ th unit in the network,  $O_j(t)$  represents the output from the  $j$ th unit in the network, the term  $w_{ij}(t)$  represents the weighting value associated with the connection that runs from the  $j$ th unit to the  $i$ th unit, and the value  $n$  represents the number of other units that are connected to the input of the  $i$ th unit.

The output computation for each unit  $i$  in the network at time  $t$  is given by

$$O_i(t) = \Gamma(H_i(t)) \quad \text{Eq. 3.2}$$

where  $\Gamma$  is the activation function of the unit. The activation of a unit is analogous to the degree of excitation of the unit. The output signal is related to its activation by a transfer function known as the activation function.

The first activation function employed in this research is the linear function.

The derivative of this transfer function is 1 and it is independent of  $H$ . The linear activation function  $\Gamma'$  can be expressed mathematically as

$$\Gamma'(H_i(t)) = H_i(t) \quad \text{Eq. 3.3}$$

The second activation function is a sigmoidal unit. The sigmoidal unit produces an output signal that has two stable states and a transition region. The sigmoidal unit used in this research is given by

$$\Gamma^s[H(t)] = \tanh(\sigma H(t)) = \frac{e^{\sigma H(t)} - e^{-\sigma H(t)}}{e^{\sigma H(t)} + e^{-\sigma H(t)}} \quad \text{Eq. 3.4}$$

A sigmoid unit is defined by a continuous function and it is asymptotic for both infinitely large positive and negative values of the input sum of each node. This nonlinear transfer function allows for more complex pattern recognition and for capturing nonlinearities in the system. The function takes values between -1 and 1. If the parameter  $\sigma$  is made large, then most of the outputs, will come close to the limiting values of  $\pm 1$ . The derivative of the function is always positive, and it is close to zero for either large positive values of  $H$  or large negative values of  $H$ . In Figure 3.9, the sigmoid function and its derivative for  $\sigma = 1$  are illustrated. As shown in Figure 3.9, the derivative attains its maximum value at  $H$  equal to zero.

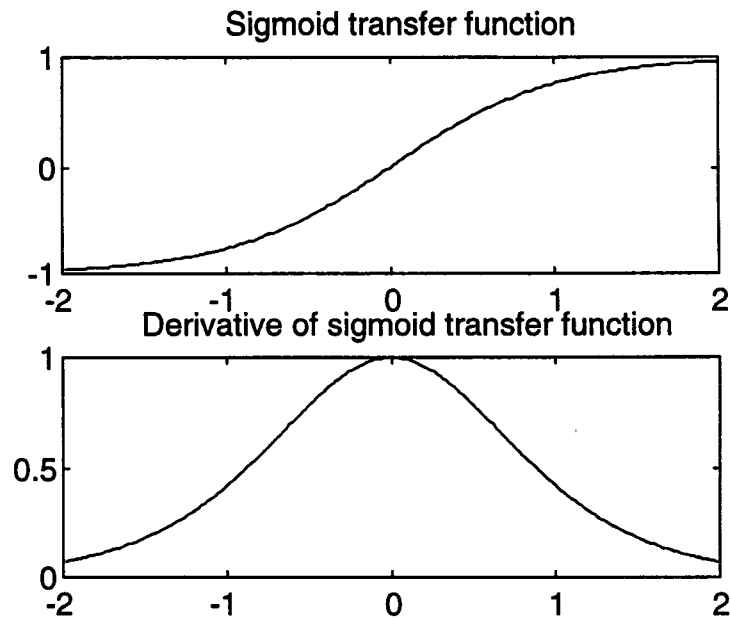


Figure 3. 9: Sigmoid Transfer Function and its Derivative

The linear and nonlinear neural dynamic models are used for system identification and control purposes. In system identification applications, it has been shown that a feedforward network of the multilayer perceptron type can approximate any continuous function [Cybenko, 1988; Cybenko, 1989; Funahashi, 1989; Hornik, Stinchcombe, and White, 1989].

The linear neural network is implemented as a two layer feedforward neural network with a linear activation function and tapped delay inputs. This arrangement takes the form of the well known recursive filters and nonrecursive filters. For modeling and controlling complex systems, linear models are extended to nonlinear dynamic models. The nonlinear neural network is implemented by using a multilayer feedforward neural network with sigmoidal activation functions and tapped delay inputs. This includes time-delay neural networks (TDNN), and recurrent neural networks (RNN). In this research work, the linear models are implemented in both computer simulations and experiments while the nonlinear models are implemented only in computer simulations.

### 3.4.2 Linear Neural Network

The linear neural networks implemented in this research are linear temporal dynamic models. These dynamic models can be classified into nonrecursive digital filters and recursive digital filters [Kung, 1993]. They are also referred to as finite impulse response (FIR) filters and infinite impulse response (IIR) filters, respectively.

### 3.4.2.1 Nonrecursive Digital Filters

The nonrecursive digital filters are discrete linear time-invariant systems in which an output number, representing a sample of the filtered signal, is obtained by weighted summation of a finite set of input numbers, representing samples of the signal to be filtered. In Figure 3.10, the neural architecture of nonrecursive digital filters is shown.

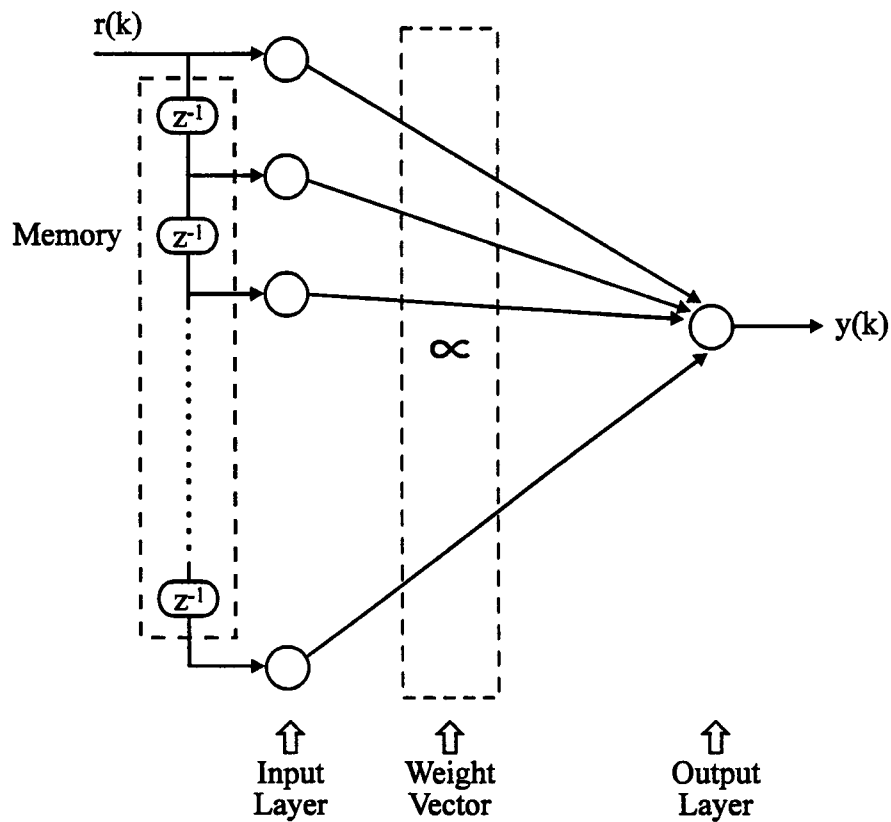


Figure 3. 10: Neural Architecture of FIR Filter

It is a two layer feedforward time delay linear neural network. The first layer is called an input layer. Here, the current input signal and time delayed input signals

are applied. The time delay function in all dynamic neural network structures is performed through the use variables stored in memory. The second layer is called the output layer with a single neuron representing a single output. In between the two layers there is a vector of weights  $\alpha$  connecting the input neurons with the output neurons. The activation function is linear.

The net input to the output neuron is given by

$$H(k) = \sum_{i=0}^p \alpha_i(k) r(k-i) \quad \text{Eq. 3.5}$$

where  $\alpha_i$  is the weight parameter for the connection of the  $i$ th input neuron to the output neuron,  $(p+1)$  is the size of the weight vector, and  $r(k)$  is the input signal at instant  $k$ . The network has  $(p+1)$  input neurons with the first neuron for the current input signal value, and  $p$  neurons for the delayed input signal values.

The output of the network is given by

$$y(k) = \Gamma^t[H(k)] = H(k) \quad \text{Eq. 3.6}$$

For a FIR filter, thus the defining relation between the input set  $r(k)$  and output set  $y(k)$  is given by

$$y(k) = \sum_{i=0}^p \alpha_i(k) r(k-i) \quad \text{Eq. 3.7}$$

Using matrix notation, the relation can be written in the form

$$y(k) = \alpha^T(k) R(k) \quad \text{Eq. 3.8}$$

where

$$\alpha(k) = [\alpha_0(k) \quad \alpha_1(k) \quad \dots \quad \alpha_p(k)]^T \text{ and } R(k) = [r(k) \quad r(k-1) \quad \dots \quad r(k-p)]^T$$



The training algorithm generally adapted is the least mean square (LMS) algorithm developed by Widrow [Widrow, 1971; Widrow and Stearns, 1985]. The filter weights are updated with the objective of minimizing an error energy function. This error can be defined as

$$e(k) = y_d(k) - y(k) \quad \text{Eq. 3.9}$$

where  $y_d$  is the desired output and  $y$  is the model output. The objective error energy function at instant  $k$  is given by

$$J(k) = \frac{1}{2} e^2(k) = \frac{1}{2} [y_d(k) - y(k)]^2 \quad \text{Eq. 3.10}$$

Since the desired signal does not depend on the weight structure, the gradient of the error energy function with respect to the filter weights is given by

$$\frac{\partial J(k)}{\partial \alpha(k)} = -e(k) \frac{\partial y(k)}{\partial \alpha(k)} \quad \text{Eq. 3.11}$$

The gradient of the model output is given by

$$\frac{\partial y(k)}{\partial \alpha(k)} = R(k) \quad \text{Eq. 3.12}$$

Therefore, the weight updating equation can be written as

$$\alpha(k+1) = \alpha(k) - \eta e(k) R(k) \quad \text{Eq. 3.13}$$

where  $\alpha(k+1)$  is the new weight vector,  $\alpha(k)$  is the old weight vector, and  $\eta$  is the adaptation coefficient.

#### 3.4.2.2 Recursive Digital Filters

Digital filters with an infinite impulse response are discrete linear systems that are governed by a convolution equation based on an infinite number of terms. In

principle, they have an infinite memory. This memory is achieved by feeding the output back to the input.

The neural architecture for recursive digital filters can be realized by applying delayed output signals and delayed input signals to the input neurons of a two layer feedforward neural network. The activation function is still a linear function. In Figure 3.11, the neural architecture of such a filter is illustrated.

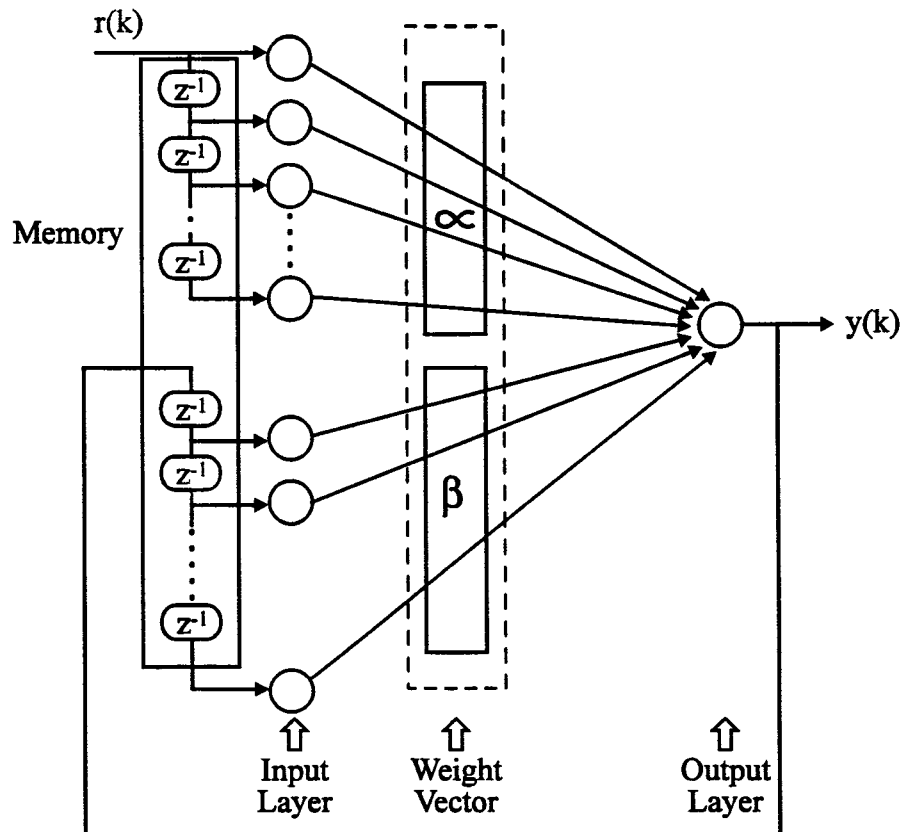


Figure 3. 11: Neural Architecture of IIR filter

The weight vector can be partitioned into two parts. The first subset  $\alpha$  consists of weights for the connections of the input neurons (with the current and delayed input

signal values) to the output neuron. The second subset  $\beta$  consists of weights for the connections of input neurons (with delayed recurrent output signal values) to that of the output neuron.

The net input to the output neuron is given by

$$H(k) = \sum_{i=0}^p \alpha_i r(k-i) + \sum_{j=1}^q \beta_j y(k-j) \quad \text{Eq. 3.14}$$

The output of the output neuron and hence the network is given by

$$y(k) = \Gamma'[H(k)] = H(k) \quad \text{Eq. 3.15}$$

Therefore, the dynamic equation that relates the input signal  $r(k)$  to the output signal  $y(k)$  is given by

$$y(k) = \sum_{i=0}^p \alpha_i r(k-i) + \sum_{j=1}^q \beta_j y(k-j) \quad \text{Eq. 3.16}$$

Equation 3.16 can be written in terms of delay operators as

$$y(k) = \alpha(D)r(k) + \beta(D)y(k) \quad \text{Eq. 3.17}$$

where the delay operators are defined by

$$\alpha(D) = \sum_{i=0}^p \alpha_i D^i \quad \beta(D) = \sum_{j=1}^q \beta_j D^j \quad D^i y(k) = y(k-i).$$

In general, a gradient type algorithm is adopted as a training algorithm. The filter weights are updated with the objective of minimizing the error energy function  $J$  defined by Equation 3.10.

Thus the gradient of the error energy function is given by

$$\frac{\partial J}{\partial \alpha_i} = -e(k) y'_{\alpha_i}(k) \quad \text{Eq. 3.18}$$

$$\frac{\partial J}{\partial \beta_j} = -e(k) y'_{\beta_j}(k) \quad \text{Eq. 3.19}$$

where the Jacobians are defined by

$$\begin{aligned} y'_{\alpha_i}(k) &= \frac{\partial y(k)}{\partial \alpha_i} \\ y'_{\beta_j}(k) &= \frac{\partial y(k)}{\partial \beta_j} \end{aligned} \quad \text{Eq. 3.20}$$

The Jacobians may be derived directly taking gradients on Eq. 3.17

$$\begin{aligned} y'_{\alpha_i}(k) &= D^i r(k) + \beta(D) y'_{\alpha_i}(k) \\ y'_{\beta_j}(k) &= D^j y(k) + \beta(D) y'_{\beta_j}(k) \end{aligned} \quad \text{Eq. 3.21}$$

The initial conditions for calculating the gradients are assumed to be zero.

Equation 3.21 can be written in a conventional notation as

$$\begin{aligned} y'_{\alpha_i}(k) &= r(k-i) + \sum_{n=1}^q \beta_n y'_{\alpha_i}(k-n) \\ y'_{\beta_j}(k) &= y(k-j) + \sum_{n=1}^q \beta_n y'_{\beta_j}(k-n) \end{aligned} \quad \text{Eq. 3.22}$$

### 3.4.3 Nonlinear Neural Network

Linear filters have limited applications. Most real world applications need nonlinear dynamic models. Therefore, nonlinear temporal dynamic models are also investigated in this research. These nonlinear dynamic models are also divided into two categories. Similar to the nonrecursive filters, there are time delay neural networks (TDNNs), and similar to the recursive filters, there are recurrent neural networks (RNNs). These nonlinear models are derived by modifying the standard multilayer feedforward neural network.

### 3.4.3.1 Multilayer Feedforward Neural Network

A multilayer feedforward neural network consists of multiple layers of neurons. The first layer is the input layer where the external input signals are applied. The last layer is the output layer that produces the output signals, and the other layers in between are called the hidden layers. In Figure 3.12, the meso-structure of a four layers feedforward neural network is shown.

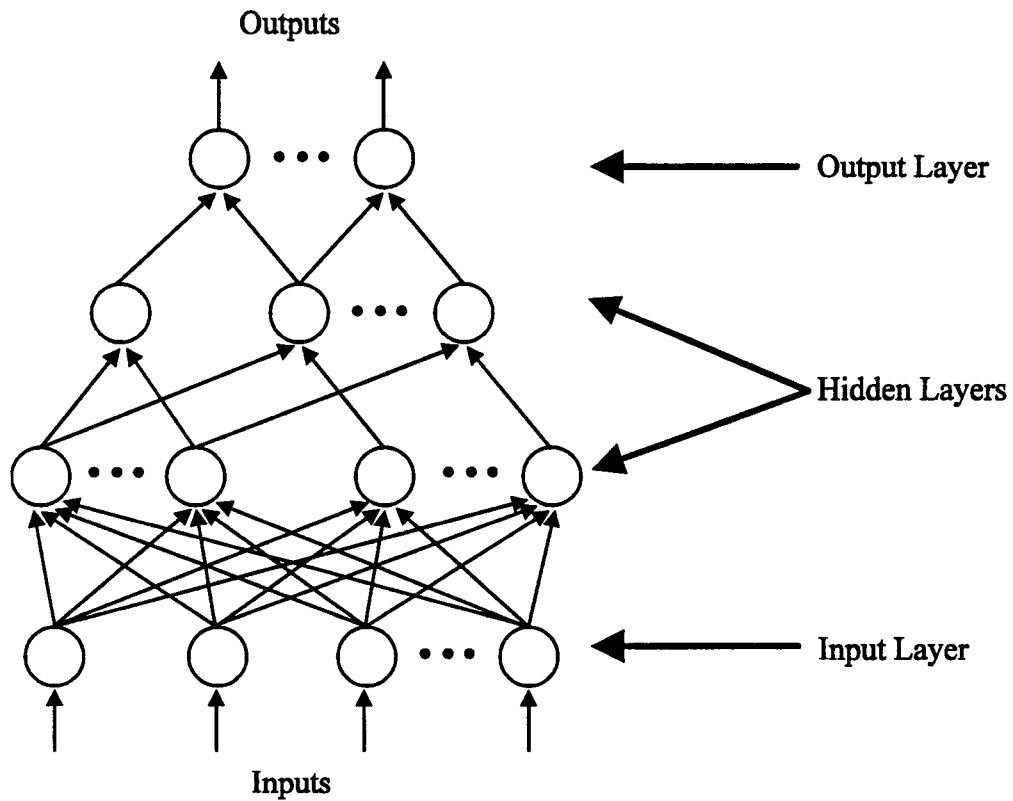


Figure 3. 12: Meso-Structure of Multilayer Feedforward Neural Network

It is crucial to build a neural network that provides a good dynamic representation of a system to be controlled. A modification of a feedforward neural network is devised for system identification and control purposes. A feedforward

neural network is characterized by layered architectures with the following advantages:

- 1) They can be used for optimization and control.
- 2) Unlike conventional batch algorithms, they are incremental learning algorithms.
- 3) The update rule of back propagation for the network is local; that is, the weight change for a given connection is computed based on quantities available. This makes the back propagation rule appropriate for parallel computation and the network best suited for fast computations on parallel architectures.
- 4) They do not require an a priori knowledge of a mathematical function. Training of the network is accomplished using data that can be obtained through experimentation.
- 5) They have good generalization capabilities.
- 6) The hidden layers perform feature extraction so as to find a correct fit of output space for the given input space.
- 7) They can learn from experience and give acceptable results from noisy and incomplete data.

Here, the algorithm used for training the nonlinear network is the back propagation algorithm. The back propagation algorithm was invented independently several times by Bryson and Ho [1969], Werbos [1974], Parker [1985] and Rumelhart, Hinton, and Williams [1986 a, b]. It lends itself to an efficient computational scheme for training multilayer networks. The objective of the algorithm is to adjust the weights in such a way so as to minimize the error energy function.

Consider a network with  $L$  layers  $l=1,2,\dots,L$ , let  $O_i^l$  be the output of the  $i^{\text{th}}$  neuron in the  $l^{\text{th}}$  layer and let  $O_i^0$  be a synonym for the  $i^{\text{th}}$  input,  $I_i$ . Let  $W_{ij}^l$  be a notation for the weight connection from  $O_j^{l-1}$  to  $O_i^l$ . Then, the back propagation algorithm can be implemented by carrying out the following sequential steps:

1. Initialization of the weights using random numbers.
2. Application of the input signals to the input layer ( $l=0$ ) so that

$$O_k^0 = I_k \text{ for all } k \quad \text{Eq. 3.23}$$

3. Forward signal propagation through the network using

$$O_i^l = \Gamma[H_i^l] = \Gamma\left[\sum_j W_{ij}^l O_j^{l-1}\right] \quad \text{Eq. 3.24}$$

for each  $i$  and  $l$  until the final outputs  $y_i = O_i^L$  have been calculated.

4. Computation of deltas for the output layer

$$\delta_i^L = \Gamma'[H_i^L](y_{di} - y_i) \quad \text{Eq. 3.25}$$

by comparing the actual outputs  $y_i$  with the desired outputs  $y_{di}$ .

5. Computation of deltas for the preceding layers by propagating the error backwards

$$\delta_j^{l-1} = \Gamma'[H_j^{l-1}] \sum_i W_{ji}^l \delta_i^l \quad \text{Eq. 3.26}$$

for  $l=L, L-1, \dots, 2$

6. Weight adaptation according to

$$W_{ij}^{\text{new}} = W_{ij}^{\text{old}} + \Delta W_{ij} \quad \text{Eq. 3.27}$$

where

$$\Delta W_{ij}^l = \eta \delta_i^l O_j^{l-1} \quad \text{Eq. 3.28}$$

7. Return to step 2 and repeat the sequence until the error tolerance is achieved.

The drawbacks of a feedforward network is due to the back propagation algorithm that is used to train the network. The drawbacks of the algorithm are convergence and existence of local minima. As a result, the algorithm will get stuck in a local minima and may not reach the global minima. Therefore, proper training is needed to overcome these drawbacks.

The feedforward neural network structure can take two different forms: static and dynamic. The static feedforward network discussed so far is best suited for pattern recognition purposes. In this research work, a dynamic neural network is implemented for the system under consideration, because the system is dynamic in nature.

#### 3.4.3.2 Nonrecurrent Nonlinear Neural Network

In the case of dynamic systems, the system outputs depend on the system inputs through a time-integration rather than a one-to-one instantaneous correspondence. As a result, the dynamic nonrecurrent nonlinear neural network, namely, Time Delay Neural Network structure, is preferred to the static one for control system implementation. In Figure 3.13, the mechanics of time delay nonlinear neural networks is shown.



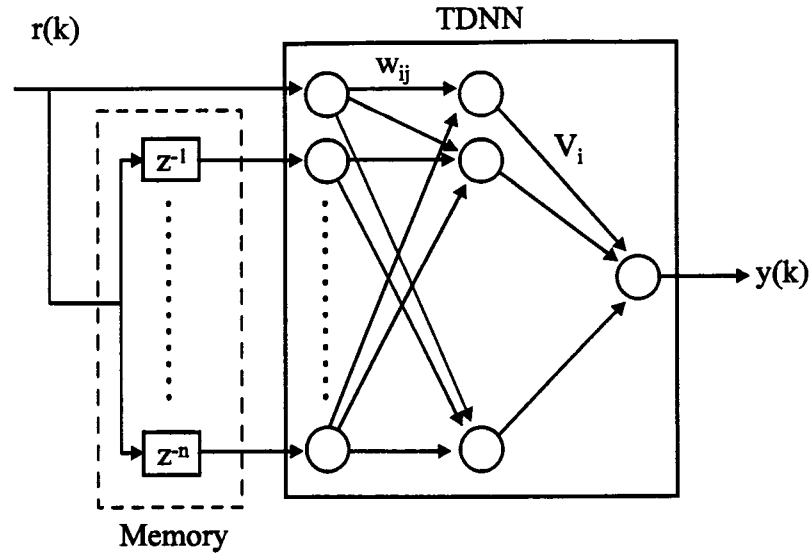


Figure 3. 13: Nonrecurrent Nonlinear Neural Network

The input structure of the time delay nonlinear neural network is similar to that of FIR filters. However, here nonlinearity is incorporated through multilayer connections and also through nonlinear activation functions.

#### 3.4.3.3 Recurrent Nonlinear Neural Network

The dynamics of the system can better be realized by using an outer recurrent feedback loop with a time delay operator. In Figure 3.14, the structure for a recurrent dynamic neural network is shown. By feeding back past information of the plant states or outputs, the neural network is expected to better realize the dynamics of linear or nonlinear systems.

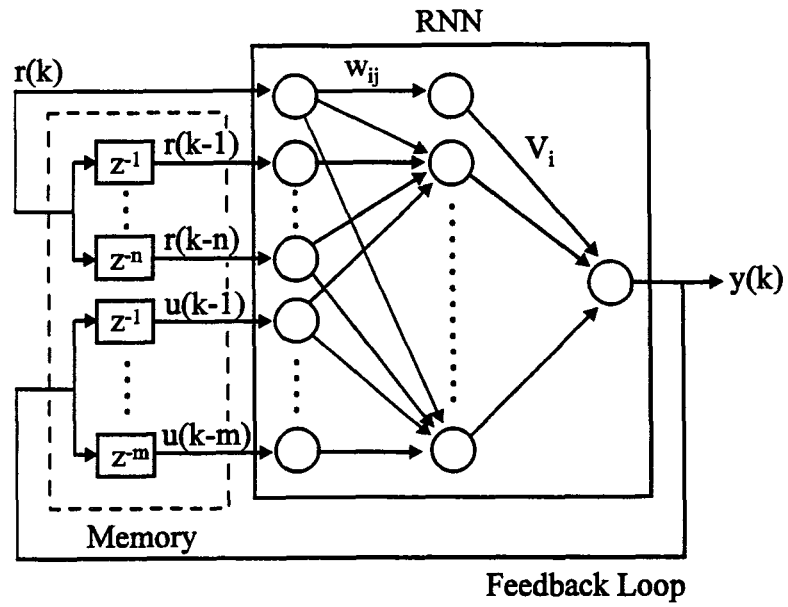


Figure 3. 14: Recurrent Nonlinear Neural Network

## Chapter 4

### SYSTEM MODELING AND COMPUTER SIMULATION

#### 4.1 Introduction

In this thesis work, computer simulation is performed in order to make a preliminary feasibility study of the control strategy. Tool vibration compensation has been a challenge to the machine tool industry for decades. Efforts made during the past have consumed materialized wealth which can be measured in million dollars. Developing a model that accounts for regeneration phenomenon, and intrinsic uncertainties in the values of the cutting process parameters is expensive. The intrinsic uncertainties in the cutting process parameters alone depend on the geometry of the tool, the properties of the material being cut and the cutting conditions. Therefore, the Meritt model is found to serve the purpose in creating the primary path. The mathematical model for the control mechanism is derived through experimental testing for the secondary path. Using these mathematical models, the feasibility of the control strategy is ascertained by performing computer simulation.

In this thesis work, the linear neural network is designed to be an adaptive type controller, and the nonlinear neural network is designed to be a learning type controller. The learning methods determine the classification of controllers as adaptive type or learning type [Yabutta and Yamada, 1990]. The adaptive type is depicted in Figure 4.1 for a disturbance attenuation application. This type of controller learns at every sampling cycle. The plant output converges on-line to the

desired value. As a result, rapid learning convergence is required in order to ensure that the controller is capable of carrying out the control action in real time. It should be pointed out that the effect of plant dynamics on the learning rule should be taken into consideration in advance when the adaptive type neural controllers are realized.

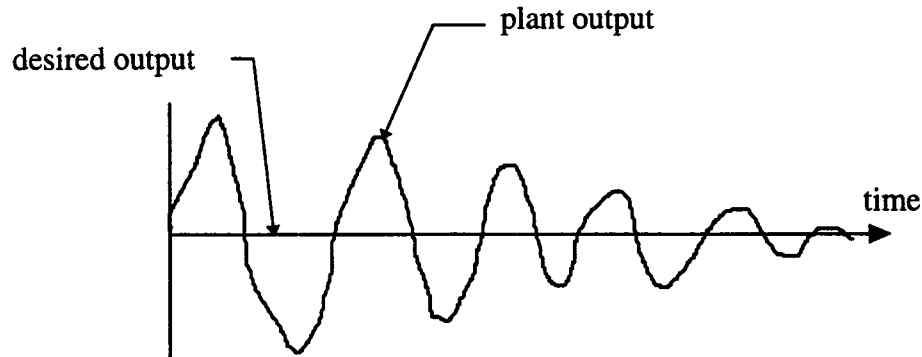


Figure 4.1: Adaptive Type Controllers for Disturbance Attenuation

The learning type controller is depicted in Figure 4.2 for disturbance attenuation applications. This type of controller learns after several trial periods. The training is performed off-line. Therefore, it is not necessary to know in advance the effect of plant dynamics on the learning rule since it can be estimated during the trial process.

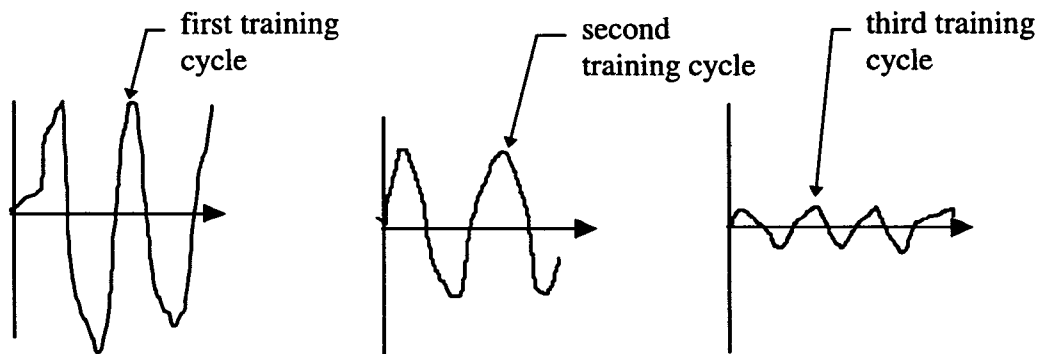


Figure 4.2: Learning Type Controller for Disturbance Attenuation

The performance of the system identification and control system in computer simulations and experiments is evaluated using the following performance indices.

#### 1. Arithmetic Average [AA]

The arithmetic average (AA) is the form of a  $l_1$  norm and it is defined as

$$AA = \frac{1}{N} \cdot \sum_{i=1}^N |z_i| \quad \text{Eq. 4.1}$$

where  $z_i$  is the  $i^{\text{th}}$  value of the variable for which the norm is sought, and  $N$  is the total number of sampled points. Numerical values of AA characterize the variation relative to its mean value. For example, in system identification application,  $z$  can take the value of the error between the output predicted by the developed model and the output actually measured from the experiments. The concept of AA values can also be applied to characterize the magnitude of tool vibration about the equilibrium position during machining. Measurements of surface profiles taken from the machined surface are typical examples where the concept of AA values is applied. The AA profile measurement is excellent for data that have a small number of isolated wild points and tends to ignore such isolated wild points.

#### 2. Root Mean Square [RMS]

The root mean square (RMS) performance index is the form of a  $l_2$  norm that is defined as

$$RMS = \sqrt{\frac{\sum_{i=1}^N z_i^2}{N}} \quad \text{Eq. 4.2}$$

This performance index gives large weighting factors to large deviations. Consequently, this performance index is best suited to data with errors in a normal or statistically related distribution where the standard deviation in the error is not large, and where approximations of the data require at-best comparable accuracy.

### 3. Peak To Valley [PTV]

The Peak-To-Valley (PTV) performance index is defined as

$$PTV = \max(z_i) - \min(z_i) \quad \text{Eq. 4.3}$$

This profile measurement is ideal for data that are exact and accurate or have errors in a uniform distribution such as data that have been rounded. The PTV performance index suffers from a limitation because only two data points are used for evaluation while the other data are ignored.

a long string of data, the sampled data are divided into sections, and for each section the performance indices are calculated. The mean and the standard deviation of the performance indices are then used to evaluate the performance of a network.

## 4.2 System Identification of the Control Mechanism

The key operation parameters for a typical 6 mm diameter, 20 mm long PMN type actuator is shown in Table 4.1.

Table 4. 1: Operation Parameters for the PMN Type Actuators

Bias Voltage	53 V (DC)
Control Voltage	-53V to 101 V (AC)
Linearized Transductance	0.179 $\mu\text{m/V}$
Actuator Stroke Limit	+/- 9.25 $\mu\text{m}$

The actuators are pre-stressed using a DC voltage. Attention has been paid to avoid saturation and to avoid reversal stroke that may be caused by large voltage inputs. Although the dynamic behavior of the actuator is not linear over its entire operation range, the effect of nonlinearities is not pronounced below saturation, especially for a small voltage variation range. A simple (tangent) linearization is effective for up to 80% stroke [Wing, 1995]. However, the slope of the linearization varies with frequency of operation; this fact necessitates system identification. The system identification process will be discussed in detail in the following sections.

#### 4.2.1 Design of Experiment

A successful identification application requires that the measurement data contain significant information about the system behavior under excitation. It is therefore necessary for the data acquisition to be well planned. The experiment is designed to make it similar to the actual case as much as possible.

The actuators are implemented in place with a series connection and with a biased DC electric voltage of 26 V. A known magnitude of AC voltage at a certain frequency is applied to the actuator, and the displacement sensor is used to capture the displacement of the tool tip. The data are collected first, and a system identification procedure is performed off-line to get a reliable model for later use in the computer simulations.

The sampling interval is coupled to the time constants of the system. Sampling that is considerably faster than the system dynamics leads to data redundancy. Sampling that is considerably slower than the system dynamics leads to serious

difficulties in determining the parameters that describe the dynamics. Therefore, the Nyquist frequency is used as a basis, and the selected sampling frequency is selected to be 2.5 times the bandwidth of the system. The sampling rate is 1 kHz, assuming that the upper limit of the frequency range is 400 Hz.

The input signal needs to be rich in spectral content within the working range of operation. As a result, a pseudo random signal is selected because this type of signal contains all frequencies within the specified range. The frequency range of the pseudo random signal generator is limited to vary from 0 to 400 Hz. The amplifier for the PMN actuators is set in such a way that the input signal amplitude in the neighborhood of  $[-1, 1]$  volt range produces a tool displacement amplitude in the neighborhood of  $[-1, 1]$  micrometer range.

#### 4.2.2 Experimental Setup

Three actuators are arranged in the smart tool post structure so that the loading produced by the actuators are distributed uniformly along a concentric circle about the center of the tool. In Figure 4.3, the placement of the three actuators in the smart tool post structure is shown. The three actuators are connected to each other in series.

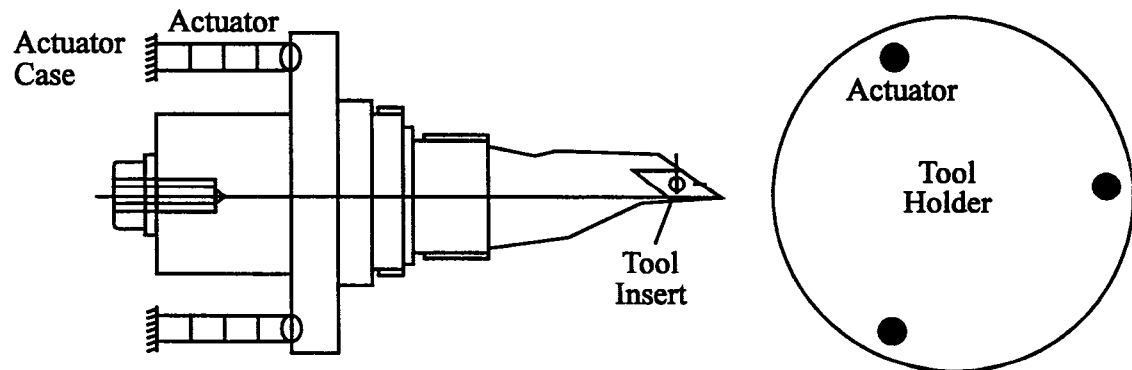


Figure 4.3: Placement of Actuators in the Smart Tool Post Structure



The machine tool motion in axial direction is the one that is of concern in this thesis work. In order to capture the relationship between the voltage input and the displacement of the tool, voltage input is applied to the actuators, and the displacement of the tool is recorded through the usage of a sensor. A signal generator is used to generate the random voltage signal. The tool tip is free to vibrate so that the displacement due to the applied voltage can be identified. The non-contact position measuring system, namely, a variable impedance transducer, is used as a displacement sensor. In Figure 4.4, the block diagram of the experimental setup is shown.

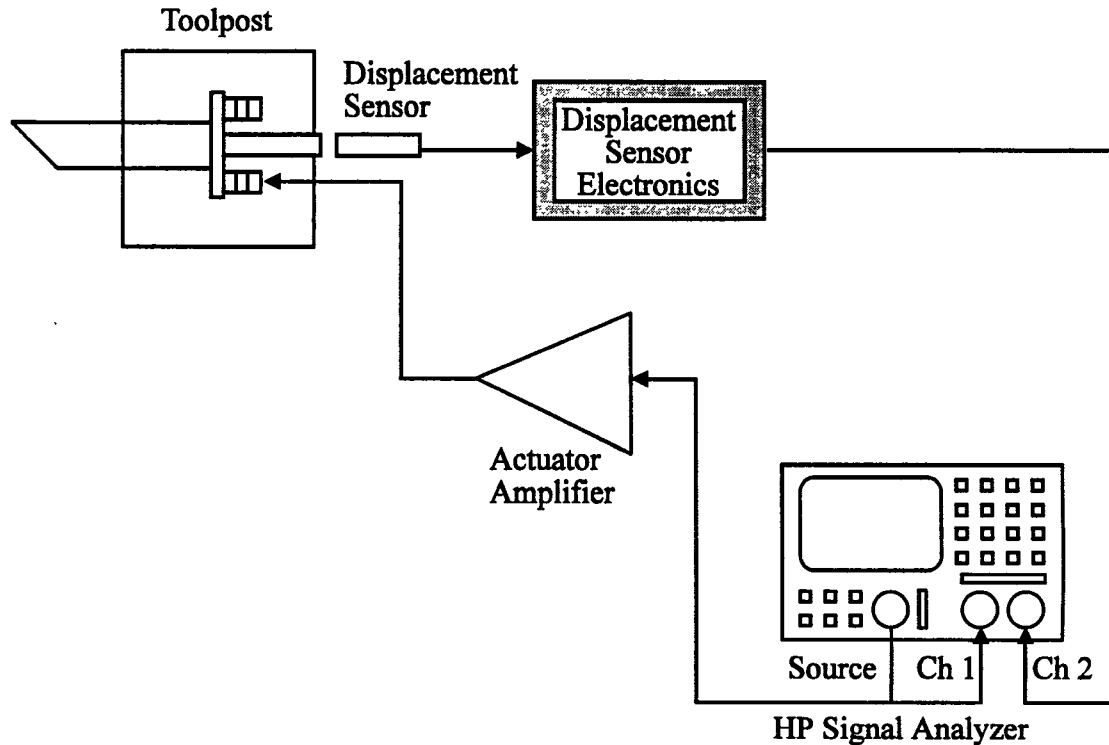
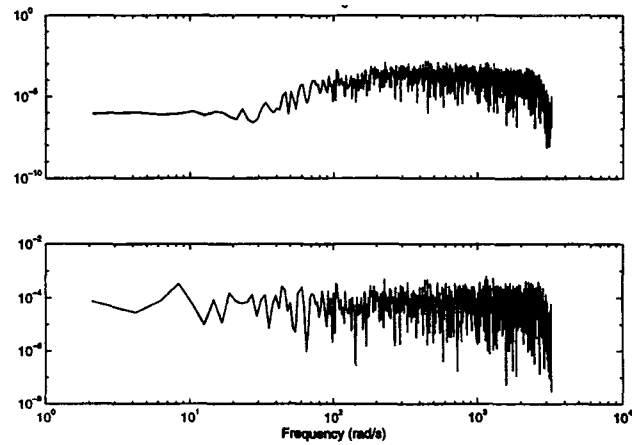


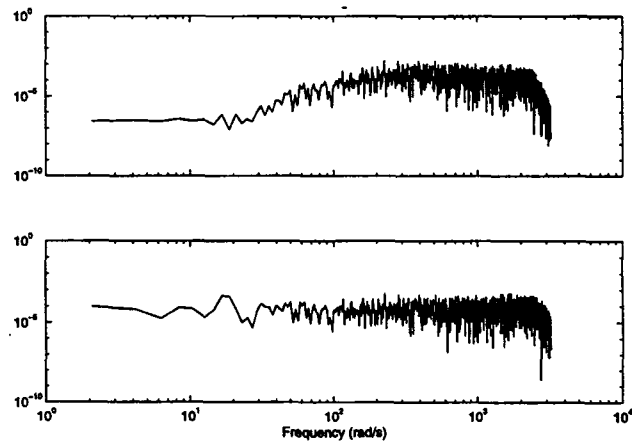
Figure 4.4: Block Diagram of Experimental Setup for Identification

A series of experiments were conducted and two sets of data were selected after evaluating the data. The spectral content of the two sets of data is shown in

Figure 4.5. As shown in the figure, the data is rich in spectral content within the specified bandwidth. One set of data is used for modeling purpose, while the other set is used for validating the model.



a) Modeling Signal; Top: output signal, Bottom: input signal



b) Validating Signal, Top: output signal, Bottom: input signal

Figure 4.5: Spectral Analysis of Experimental Data

#### 4.2.3 Identification Procedure

The models structures chosen for identification purposes in this thesis research include Auto Regressive X (ARX) model, Output-Error (OE) model, Auto Regressive and Moving Average X (ARMAX) model, Box-Jenkins (BJ) model, and State Space (SS) model. In order to identify an appropriate model structure that best describes the control mechanism, MathWorks SYSTEM IDENTIFICATION TOOLBOX (SITB) is used. The software package is one of the most used packages in system identification [Ljung and Glad, 1994]. The identification procedure to produce a model is summarized in the following sequence.

1. Specification of a model structure.
2. Determination of an appropriate model of this structure.
3. Evaluation of the properties of the established model.
4. Acceptance of the evaluated model structure if meeting specifications.
5. Iteration of the above four steps to test a new structure if not accepted.

In Figure 4.6, a flow chart illustrating these steps involved in the identification procedure is shown. The experimental data are presented to the algorithm. The computer algorithm then determines the best model structure. The model is evaluated through a validation technique. The process is repeated for all of the five models. The model which shows the best match is selected to serve as the model of the control mechanism in the computer simulations of the control system.

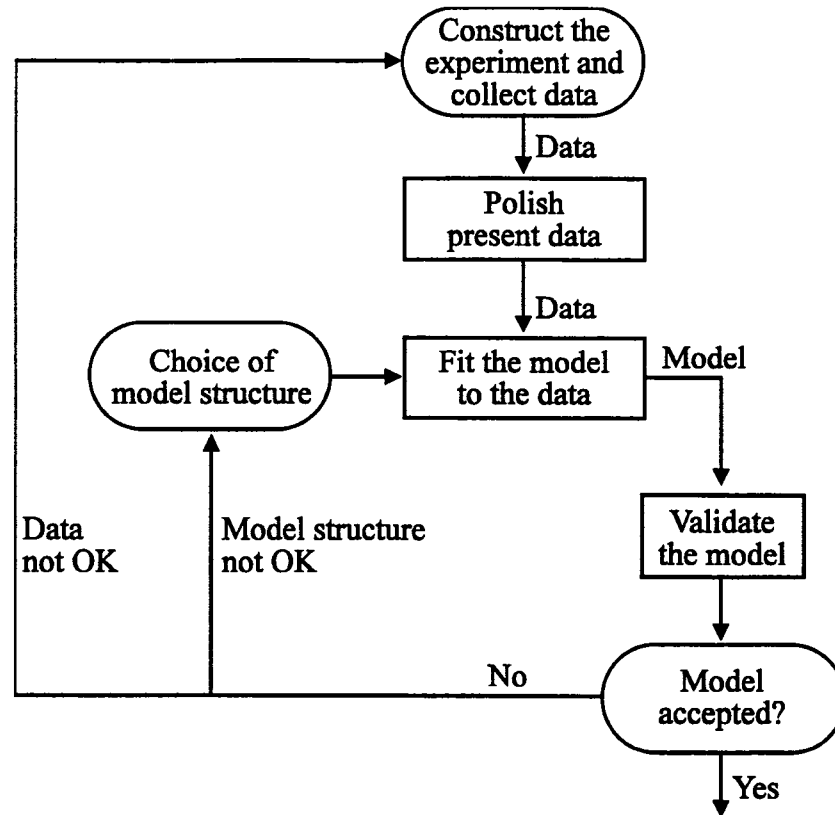


Figure 4.6: System Identification Cycle

The criterion used to select the best model from the five model structures is the variance of the prediction error for each of the five model structures using the recorded new data sequences. In statistical terms, this is referred to as cross validation. Cross validation is preferred to a method that bases the comparison on data used for modeling. The use of old data is not sufficient because the performance of a higher order model in general gives a lower value of the criterion function since it has been obtained by minimizing over more parameters. Moreover, the limitation of cross validation is alleviated due to the fact that experimental data measurements are not scarce.

The model can exhibit overfit when a number of excessive parameters are used wazzu to fit the model to the specific disturbance signals in the present data set. This should be avoided because the model will be used when other disturbances affect the system. The transition from relevant model fit to over fit is studied. The models are compared based on criterion that balance between model fit and the number of parameters using prediction variances produced by the models. Since cross validation is performed, the most well-known Final Prediction Error (FPE) is used for a statistical estimate of the prediction error variance as stated by:

$$FPE = \min_{size(\theta)} \frac{1 + \frac{size(\theta)}{N}}{1 - \frac{size(\theta)}{N}} \bullet V \text{ For} \quad \text{Eq. 4.4}$$

where  $V$  is the loss function for the structure in question and  $\theta$  is the weight parameter.

The loss function is given by the quadratic fit as

$$V = \frac{1}{N} \sum_{i=1}^N e^2(i) \quad \text{Eq. 4.5}$$

where  $e(i)$  is the modeling error at instant  $i$ .

The first parametric model tested is ARX model that corresponds to the following equation

$$A(q)y(t) = B(q)u(t - nk) + e(t) \quad \text{Eq. 4.6a}$$

where  $B$  and  $A$  are polynomials in the delay operator  $q^{-1}$  given by

$$A(q) = 1 + a_1 q^{-1} + \dots + a_{na} q^{-na} \quad \text{Eq. 4.6b}$$

$$B(q) = b_1 + b_2 q^{-1} + \dots + b_{nb} q^{-nb+1} \quad \text{Eq. 4.6c}$$

The parameters  $na$  and  $nb$  are the orders of the respective polynomials. The parameter  $nk$  is the number of delays from input to output.

First, a suitable value of the delay  $nk$  is established by testing a second order model with delays between 1 and 10. For this structure, a delay  $nk=3$  gives the smallest loss function. Around this chosen value all combinations of ARX models with up to 10  $na$  and 10  $nb$  parameters are tested. In Figure 4.7, the loss function as a function of the number of parameters is shown. From the figure there is no significant improvement in the loss function beyond 13 parameters. The best fit for the 13 parameters yields  $na=6$ ,  $nb=7$ , and  $nk=2$ .

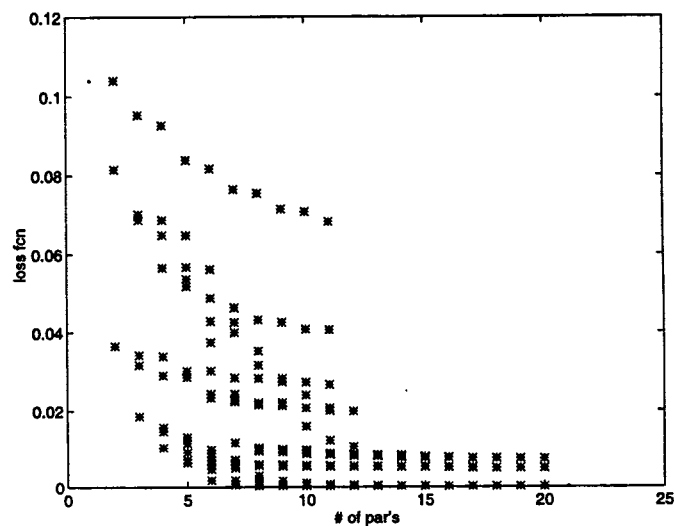


Figure 4.7: Loss function of ARX model

These selected model parameters are used to model the control mechanism. The residuals associated with the data and the ARX model is found by evaluating the

auto-correlation function of the errors and the cross correlation function between the errors and the input signals. Since the residual is too large, the model is rejected.

The second model structure test is OE structure that corresponds to the following equation

$$y(t) = \frac{B(q)}{F(q)} u(t - nk) + e(t) \quad \text{Eq. 4.7a}$$

where the polynomial  $F(q)$  is given by

$$F(q) = 1 + f_1 q^{-1} + \dots + f_{nf} q^{-nf} \quad \text{Eq. 4.7b}$$

where  $nf$  is the order of the polynomial.

Around the chosen delay parameter, all combinations of OE models with up to 10  $nb$  and 10  $nf$  parameters are tested. All OE models are tested but yielded higher FPE, loss function, and residuals than ARX models. Therefore, this model structure is also rejected.

The third model structure tested is the ARMAX structure that corresponds to the equation given by

$$A(q)y(t) = B(q)u(t - nk) + C(q)e(t) \quad \text{Eq. 4.8a}$$

where the polynomial  $C(q)$  of order  $nc$  is given by

$$C(q) = 1 + c_1 q^{-1} + \dots + c_{nc} q^{-nc} \quad \text{Eq. 4.8b}$$

A series of trials are performed with different values of parameters with the order ranging from 1 to 10. Even though some ARMAX models give smaller values of loss function and smaller values of FPE than those obtained from the previous two models, the residuals remain large. Therefore, this model is also rejected.

The fourth model structure tested is the Box-Jenkins (BJ) model structure that corresponds to the equation given by

$$A(q)y(t) = \frac{B(q)}{F(q)} u(t-nk) + \frac{C(q)}{D(q)} e(t) \quad \text{Eq. 4.9a}$$

where the polynomial  $D(q)$  of order  $nd$  is given by

$$D(q) = 1 + d_1 q^{-1} + \dots + d_{nd} q^{-nd} \quad \text{Eq. 4.9b}$$

A series of trials are performed with different values of parameters within the range specified before. Again, a smaller value of the loss function and a smaller value of FPE were found for some of the BJ models. However, the residual analysis results in the rejection of this model.

The last model structure tried out is the State Space model; this model gave the best results. The model structure is given by

$$\begin{aligned} x(t+1) &= Ax(t) + Bu(t) \\ y(t) &= Cx(t) + Du(t) + e(t) \end{aligned} \quad \text{Eq. 4.10a}$$

Here, the relationship between the input  $u(t)$  and the output  $y(t)$  is defined by the  $nx$ -dimensional state vector  $x(t)$ . In the transfer function form, the above equation can be given by

$$G(q) = C(qI_{nx} - A)^{-1} B + D \quad \text{Eq. 4.10b}$$

where  $I_{nx}$  is  $nx$  by  $nx$  identity matrix, and  $A$ ,  $B$ ,  $C$ ,  $D$  are matrices defining the model.



The SS model structure is tested for orders that range from 1 to 10. The best model structure found by the algorithm of the computer is of the order 6 as shown in Figure 4. 8.

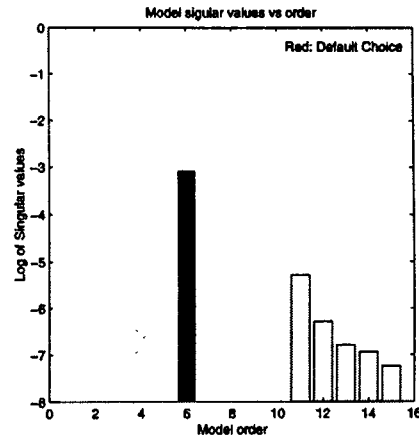
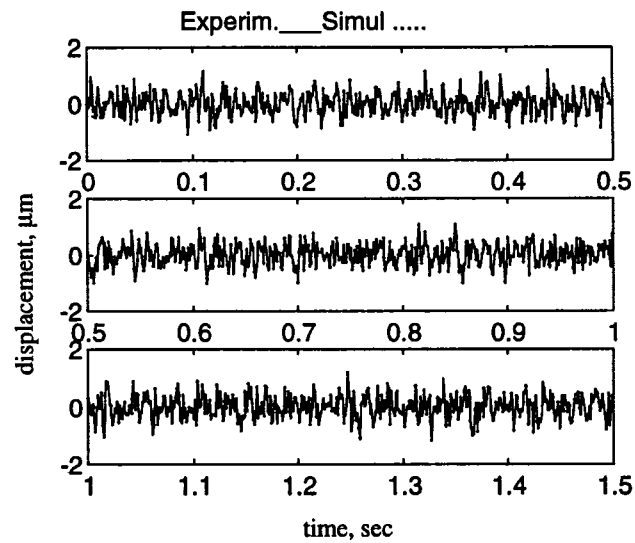


Fig. 4.8: Model Evaluation for SS Models

In Figure 4.9, the output of the model and the actual validation data is shown. It shows that the model is in agreement with the experimental data.



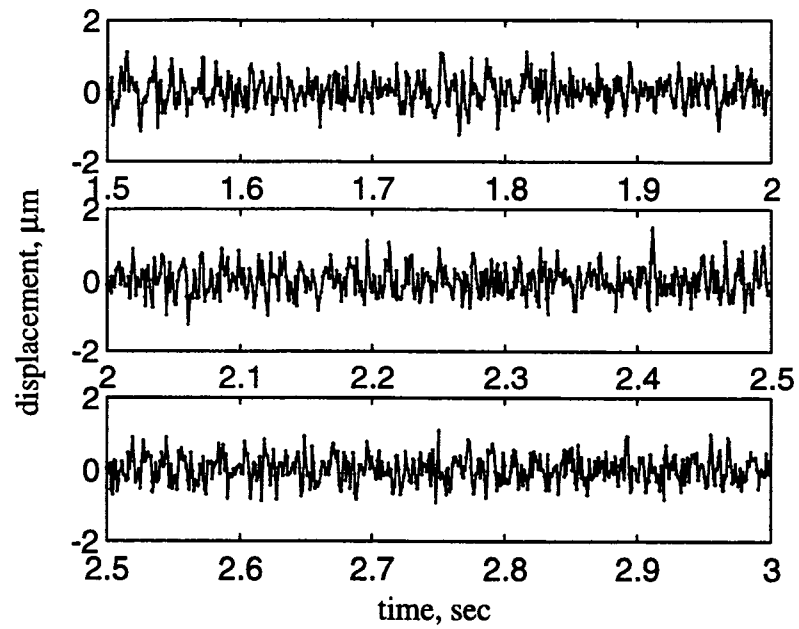


Figure 4.9: Experimental and Simulation Outputs

The residuals obtained for the model is depicted in Figure 4.10.

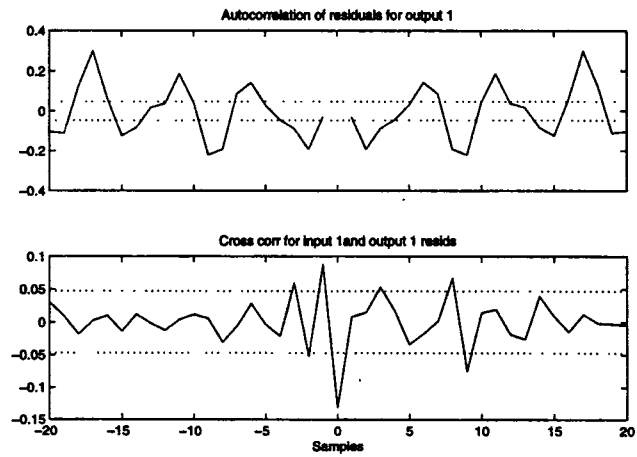


Figure 4.10: Residuals of the Model

The frequency response of the state space Model is shown in Figure 4.11.

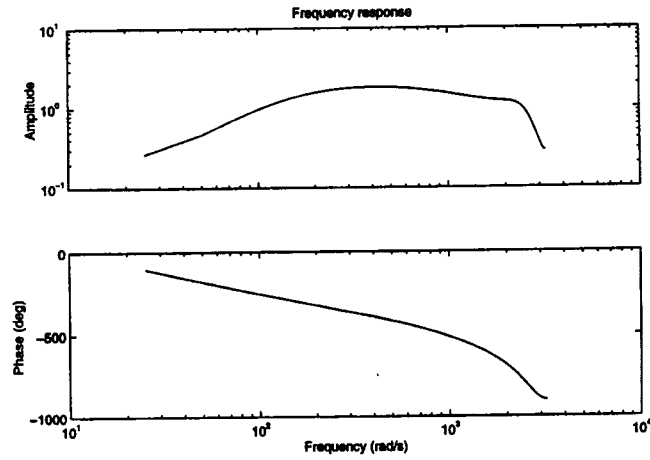


Figure 4.11: Frequency Response

The continuous state space model of the control mechanism model found from the discrete state space model is in the following form:

$$\begin{aligned}\dot{\bar{x}}(t) &= A_c \bar{x}(t) + b_c u(t) \\ y(t) &= C_c \bar{x}(t) + d_c u(t)\end{aligned}\tag{Eq. 4.11}$$

where the  $A_c$ ,  $b_c$ ,  $C_c$ , and  $d_c$  matrices are given by

$$A_c = \begin{bmatrix} 111.4 & 240.4 & 199.5 & -242.8 & -82.9 & 706 \\ -196.6 & -200.8 & -214.9 & 187.4 & 109.8 & -839.9 \\ -137.5 & -179.6 & -194.1 & 173.6 & 107.6 & -745.3 \\ -131.2 & -126.5 & -137 & 307.4 & 41.3 & -1274.8 \\ -29.4 & -43.2 & -46 & -89.6 & 20.8 & -230.1 \\ -64.6 & -94.6 & -97.4 & 225.7 & 51.5 & -513.3 \end{bmatrix} \quad b_c = \begin{bmatrix} 3576.2 \\ -5283.8 \\ -4631.2 \\ -4282.8 \\ -1074.6 \\ -2409.5 \end{bmatrix}$$

$$C_c = [-0.5172 \quad 0.5062 \quad 0.4984 \quad 0.4478 \quad 0.0802 \quad 0.1442] \quad d_c = 0$$

where the  $A_c$ ,  $b_c$ ,  $C_c$ , and  $d_c$  matrices are given by

$$A_c = \begin{bmatrix} 111.4 & 240.4 & 199.5 & -242.8 & -82.9 & 706 \\ -196.6 & -200.8 & -214.9 & 187.4 & 109.8 & -839.9 \\ -137.5 & -179.6 & -194.1 & 173.6 & 107.6 & -745.3 \\ -131.2 & -126.5 & -137 & 307.4 & 41.3 & -1274.8 \\ -29.4 & -43.2 & -46 & -89.6 & 20.8 & -230.1 \\ -64.6 & -94.6 & -97.4 & 225.7 & 51.5 & -513.3 \end{bmatrix} \quad b_c = \begin{pmatrix} 3576.2 \\ -5283.8 \\ -4631.2 \\ -4282.8 \\ -1074.6 \\ -2409.5 \end{pmatrix}$$

$$C_c = [-0.5172 \quad 0.5062 \quad 0.4984 \quad 0.4478 \quad 0.0802 \quad 0.1442] \quad d_c = 0$$

### 4.3 System Modeling of the Machining System

The machine tool structure is a vibratory system with a large number, if not infinite, of degrees of freedom. Mass and flexibility are distributed over the structure of the machine tool continuously but nonuniformly. From a practical point of view, it is sufficient to consider a limited number of degrees of freedom corresponding to the lower modes of natural vibrations that are known to dominate the tool motion during machining. Therefore, the vibration analysis is performed with the assumption that the lathe machine is rigid along with the tool post case. As a result, the vibratory system is limited to a finite number of degrees of freedom of the machine tool with respect to the tool post case.

The mathematical model of the tool post is formulated based on physical insights [Wing, 1995]. Machine tool structures are spatially continuous systems, which can be described by models using partial differential equations. The boundary conditions and constraints for the machine tool are quite complex. For the feasibility

study, a lumped-parameter model with concentrated masses and springs is used in this thesis research. To account for the energy dissipation, viscous dashpots are included. The actuator stiffness is represented by  $k_a$ . In Figure 4.12, the schematic drawing of the model of the smart tool post structure is shown.

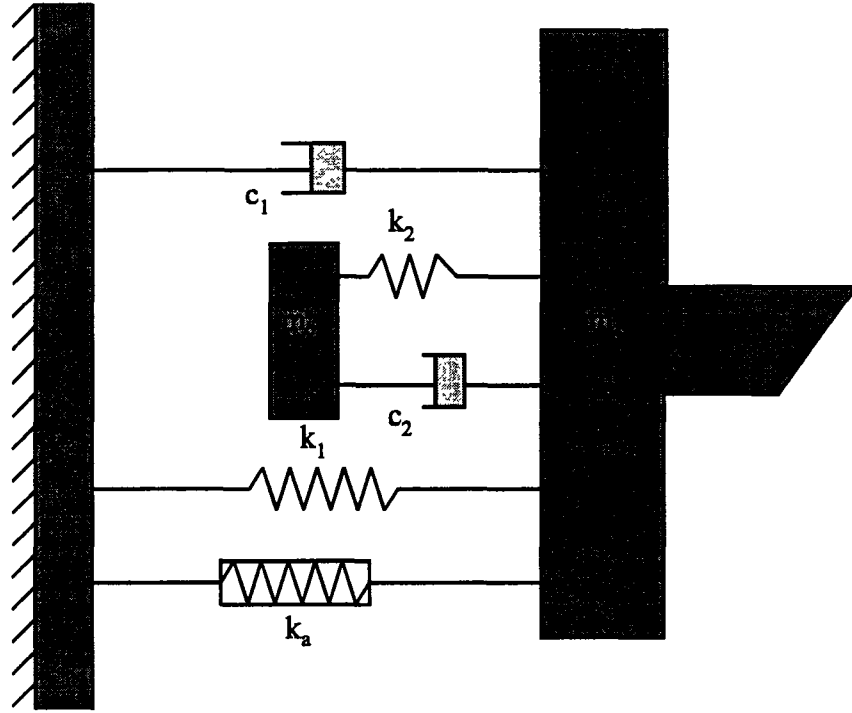


Figure 4.12: Model of Smart Tool Post Structure

The two differential equations of motion for the smart tool post structure can be derived to be

$$\begin{aligned} m_1 \ddot{x}_1 + (c_1 + c_2) \dot{x}_1 + (k_1 + k_2 + k_a) x_1 - c_2 \dot{x}_2 - k_2 x_2 &= F_c \\ m_2 \ddot{x}_2 + c_2 \dot{x}_2 + k_2 x_2 - c_2 \dot{x}_1 - k_2 x_1 &= 0 \end{aligned} \quad \text{Eq. 4.12}$$

where  $F_c$  is the cutting force. The matrix form of the above set of differential equations of motion is given by

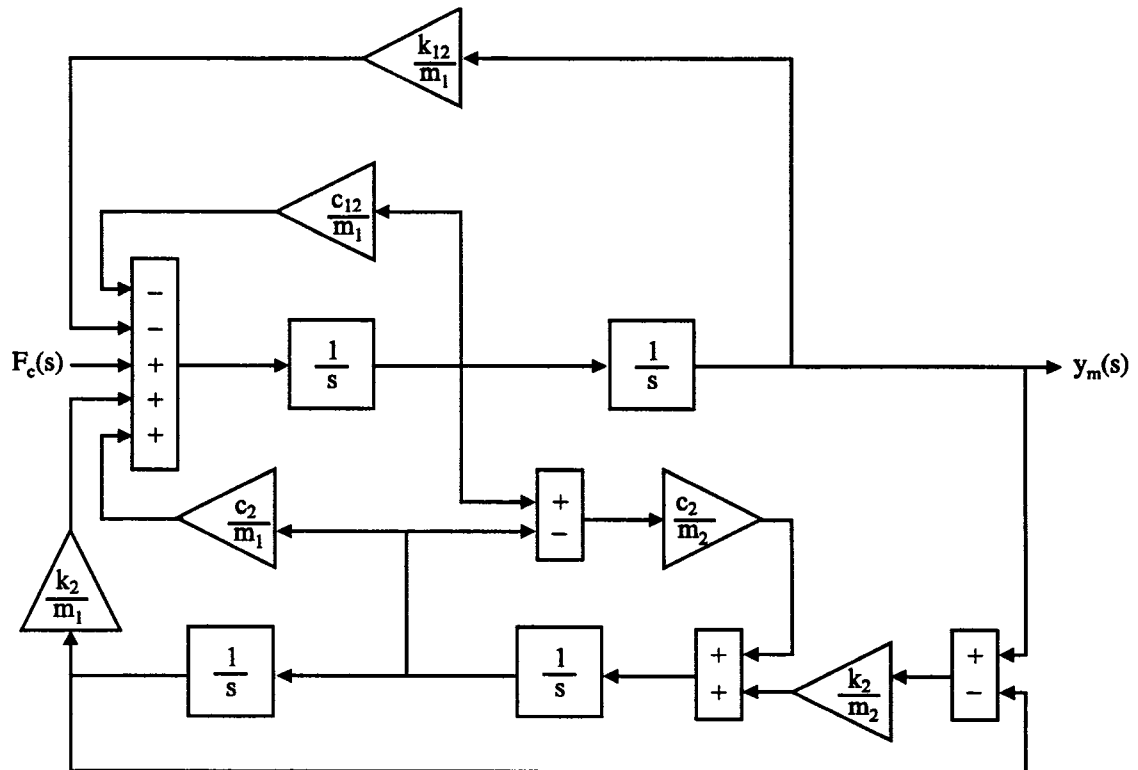
$$M\ddot{\bar{x}} + C\dot{\bar{x}} + K\bar{x} = \bar{b}F_c \quad \text{Eq. 4.13}$$

where,

$$M = \begin{bmatrix} m_1 & 0 \\ 0 & m_2 \end{bmatrix} \quad C = \begin{bmatrix} c_1 + c_2 & -c_2 \\ -c_2 & c_2 \end{bmatrix} \quad K = \begin{bmatrix} k_1 + k_2 + k_a & -k_2 \\ -k_2 & k_2 \end{bmatrix}$$

$$\bar{b} = \begin{pmatrix} 1 \\ 0 \end{pmatrix} \quad \bar{x} = \begin{pmatrix} x_1 \\ x_2 \end{pmatrix}$$

In Figure 4.13, the block diagram of the structural dynamics of the smart tool post, the signal flow graph, is shown.



**Figure 4.13: Block Diagram of the Structural Dynamics of the Tool Post**

The transfer function of the system which relates the input cutting force to the machine tool displacement is given by

$$\frac{x_1(s)}{F_c(s)} = \frac{m_2 s^2 + c_2 s + k_2}{[m_1 s^2 + (c_1 + c_2)s + (k_1 + k_2 + k_a)][m_2 s^2 + c_2 s + k_2] - (c_2 s + k_2)^2} \quad \text{Eq. 4.14}$$

After some manipulation and substitution of

$$w_1^2 = \frac{k_1}{m_1}, w_2^2 = \frac{k_2}{m_2}, w_a^2 = \frac{k_a}{m_1}, \zeta_1 = \frac{1}{2} \frac{c_1}{m_1 w_1}, \zeta_2 = \frac{1}{2} \frac{c_2}{m_2 w_2}$$

the transfer function can be expressed in terms of damping coefficients and natural frequencies

$$\frac{x_1(s)}{F_c(s)} = \frac{s^2 + 2\zeta_2 w_2 s + w_2^2}{m_1 m_2 (s^2 + 2\zeta_1 w_1 s + w_1^2 + w_a^2)(s^2 + 2\zeta_2 w_2 s + w_2^2) + m_2^2 (2\zeta_2 w_2 s + w_2^2) s^2}$$

Eq.4.15

The state space equations of the system are of the form

$$\begin{aligned}\dot{\bar{x}} &= A\bar{x} + \bar{b}F_c \\ \bar{y} &= C\bar{x} + \bar{d}F_c\end{aligned}$$

Eq. 4.16

where

$$A = \begin{bmatrix} 0 & 0 & 1 & 0 \\ 0 & 0 & 0 & 1 \\ -\frac{k_1+k_2+k_a}{m_1} & \frac{k_2}{m_1} & \frac{c_1+c_2}{m_1} & \frac{c_2}{m_1} \\ \frac{k_2}{m_2} & -\frac{k_2}{m_2} & \frac{c_2}{m_2} & -\frac{c_2}{m_2} \end{bmatrix} \quad \bar{b} = \begin{pmatrix} 0 \\ 0 \\ 1 \\ \frac{1}{m_1} \\ 0 \end{pmatrix}$$

$$C = \begin{bmatrix} 1 & 0 & 0 & 0 \\ 0 & 0 & 1 & 0 \\ -\frac{k_1+k_2+k_a}{m_1} & \frac{k_2}{m_1} & \frac{c_1+c_2}{m_1} & \frac{c_2}{m_1} \end{bmatrix} \quad d = \begin{pmatrix} 0 \\ 0 \\ 1 \\ \frac{1}{m_1} \end{pmatrix}$$

$$\bar{x} = \begin{pmatrix} x_1 \\ x_2 \\ \dot{x}_1 \\ \dot{x}_2 \end{pmatrix} \quad \bar{y} = \begin{pmatrix} x_1 \\ \dot{x}_1 \\ \ddot{x}_1 \end{pmatrix}$$

Based on equations (2.2) and (2.4), the cutting force is relating to the preset chip thickness by

$$F_c(t) = k_c [u_o - y(t) + \mu y(t - \mu)] \quad \text{Eq.4.17}$$

Using Matlab, the third order pade approximation of the delay term is given by

$$\begin{aligned} \dot{\bar{x}}_d &= A_d \bar{x}_d + \bar{b}_d y(t) \\ y(t - \tau) &= C_d \bar{x}_d + \bar{d}_d y(t) \end{aligned} \quad \text{Eq. 4.18}$$

Finally, integration of the equations for the tool post, the cutting process and the delay term approximation gives a state space equation of the machining system relating the preset chip thickness  $u_o$  to the machine tool displacement  $y_m$  as:

$$\begin{aligned} \dot{\bar{x}}_m(t) &= A_m \bar{x}_m(t) + b u_o(t) \\ y_m(t) &= C_m \bar{x}_m(t) + d_m u_o(t) \end{aligned} \quad \text{Eq. 4.19}$$

where the matrices are given by the following equation

$$\begin{aligned} A_m &= A_0 + A_1 + A_2 + A_3 \\ C_m &= [1 \ 0 \ 0 \ 0 \ 0 \ 0 \ 0] \\ b_m &= \begin{bmatrix} \bar{b} \\ \bar{O}_3 \end{bmatrix} \\ d_m &= 0 \end{aligned}$$

and the variables in the above equations are given by

$$\begin{aligned} A_0 &= \begin{bmatrix} A & O_{43} \\ S_{34} & A_d \end{bmatrix} & A_1 &= \begin{bmatrix} \bar{b} \\ \bar{O}_3 \end{bmatrix} \begin{bmatrix} -1 & 0 & 0 & 0 & 0 & 0 & 0 \end{bmatrix} \\ A_2 &= \mu k_c \begin{bmatrix} \bar{b} \\ \bar{O}_3 \end{bmatrix} \begin{bmatrix} \bar{O}_4 & C_d \end{bmatrix} & A_3 &= \mu k_c \begin{bmatrix} \bar{b} \\ \bar{O}_3 \end{bmatrix} \begin{bmatrix} d_d & 0 & 0 & 0 & 0 & 0 & 0 \end{bmatrix} \end{aligned}$$



and  $O_{ij}$  is a zero matrix with  $i$  number of rows and  $j$  number of columns, whereas  $\vec{O}_i$  is a zero vector with  $i$  number of rows.

The set of values that is shown in Table 4.2 is used here in the computer simulations.

Table 4.2: Values for Computer Simulations

<u>Variable</u>	<u>Value</u>
Preset chip load	0.0001 m
Mass 1	0.9 kg
Mass 2	0.1 kg
Stiffness 1	$1 \times 10^8$ N/m
Stiffness 2	$1 \times 10^6$ N/m
Damping factor	0.09
Cutting stiffness	$1 \times 10^6$ N/m
Time delay	0.001 sec
Overlap factor	0.8

#### 4.4 Computer Simulation of Linear Neural Network Control System

The architecture of the linear NN controller has the following two components:

a) an emulator to emulate the control mechanism and b) a controller with a built-in adaptive algorithm. During an operation, the controller drives the control signal and an adaptive algorithm adjusts the controller parameter values via the emulator. The two modules in this control system are discussed in the following sections.

##### 4.4.1 Linear Emulator Module Development

An emulator is a model representing the control mechanism that is later used by the adaptation algorithm to update the control weights. The nonrecurrent network

is used in the linear NN system control application, since is found sufficient in this thesis work.

In the hardware realization, the emulator is derived from the control mechanism. For the computer simulations, the parametric model of the control mechanism identified in Section 4.2 replaces the actual plant.

The NN identification procedure is performed in two phases. First, training data are collected. The data consists of system inputs and outputs for one second of time with 10,000 data points collected at 10 kHz. In order to capture the full spectrum content, the input signal used to excite the control mechanism is a random signal. The input signal is delayed successively according to the tap length, and a matrix of input data is stored in an input file. In a similar manner, the corresponding output is stored in an output file.

Second, the data are used on the corresponding weight structure of the NN, and the errors between the output of the control mechanism and the emulator are minimized. The least-mean square (LMS) algorithm that was discussed in Chapter 3 is used. Using this algorithm, the weights of the emulator are adjusted in such a way that the modeling errors between the control mechanism and the model are minimized. The basic principle of the LMS algorithm is a gradient descent algorithm. The algorithm attempts to arrive at a calculation of the optimum set of filter weights by adding to the present estimate of the optimum weight vector a portion of the negative gradient of the error surface at the location defined by this estimate. The magnitude of the portion is governed by a scalar called the adaptation coefficient. In this manner,

the current value of the mean square error descends down the sides of the error surface which is a function of the weight vectors.

#### 4.4.1.1 Design of Experiment

Since nonlinear systems cannot be represented by a linear network, using a linear network to represent nonlinear systems would be valid only for making linear approximations in a small region. By creating a delayed tap line on the inputs, the approximation can be as close to a solution as possible for a given structure. The parameters under investigation during system identification include the tap length that represents the weight size and the adaptation coefficient in the adaptation algorithm. A series of levels of tap lengths that are multiples of 20 are investigated in this research. In order to determine the sufficient tap length for the emulator five levels of tap lengths are studied, as shown in Table 4.3.

Table 4. 3: Tap Length Levels

Levels	Tap Length
1	20
2	40
3	60
4	80
5	100

The identification process is governed by two factors that are regulated by the adaptation coefficient. A low adaptation coefficient ensures stability but the rate of convergence is very slow. On the other hand, a high adaptation coefficient can increase the convergence rate, but would also make the system unstable. Therefore, a low value is taken as a starting point for the adaptation coefficient. By gradually

increasing the adaptation coefficient, the maximum value, at which the identification process is stable, is obtained. The steady state value of the residual error is considered to ascertain the steady state performance of the structure for a given adaptation coefficient, whereas the number of epochs or number of batches it takes to attain the steady state would be used to ascertain the transient performance of the training process.

#### 4.4.1.2 Results and Analysis

The emulator evaluation process consists of two factors that correspond to the two types of residual errors. The first type of residual error is determined by finding the difference between the outputs of the control mechanism when subjected to modeling input signals and the modeling output signals. The second type of residual error is determined by finding the difference between the outputs of the control mechanism when subjected to validating input signals and the validating output signals. Since a linear network only has a global minima, a series of trials would give the same results regardless of different initial weights derived from a random number within  $[-1,1]$  range as expected. Therefore, it is not necessary to make statistical analysis to account for the random nature of the initial weights.

After making several trials, the adaptation coefficient for all the levels was found to be 0.0001, and in all the cases the steady state was obtained at about 20 epochs.

The steady state modeling performance of the emulator is evaluated by calculating the modeling error after the training process settles down. The steady state

modeling error values for the five levels in terms of the three performance indices are listed in Table 4.4.

Table 4. 4: Steady State Modeling Error

Level	AA	RMS	PTV
1	.0700	.0885	.6110
2	.0596	.0753	.5553
3	.0313	.0395	.3077
4	.0108	.0136	.1045
5	.0024	.0032	.0948

In order to visualize the effect of tap length on the modeling error, the modeling error is plotted as a function of the levels using the three performance indices as shown in Figure 4.14.

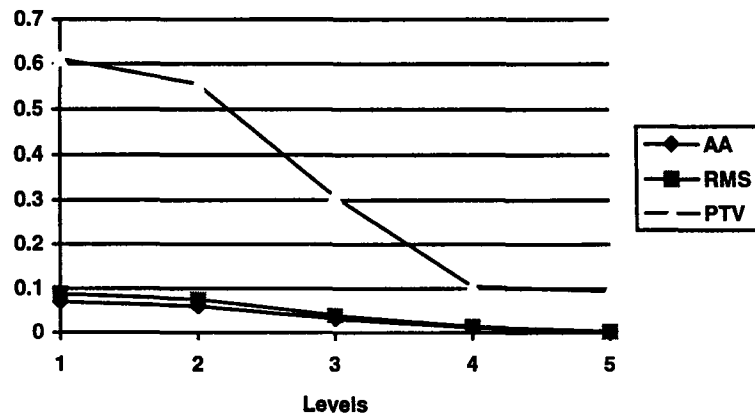


Figure 4. 14: Steady State Modeling Error

As seen from the above figure, the rate of error reduction with respect to the increments in tap length is higher for tap length 40 to 80 than for tap length 20 to 40

and 80 to 100. The variation of the RMS and AA performance indices with respect to the tap length is lower than for PTV index. This is understandable because few points are used in calculation of the PTV index unlike the calculation for AA and RMS indices, which make use of all of the evaluation data.

The five emulator structures are further analyzed for validation error. An input of the following is used as a source of excitation:

$$u(t) = \frac{1}{3} \sum_{i=1}^3 \sin(2\pi f_i t) \quad \text{Eq. 4.20}$$

where  $f_1=100$  Hz,  $f_2=200$  Hz, and  $f_3=300$  Hz.

Using the modeled weight structures, the outputs of the control mechanism and the emulator are noted for this input excitation. The difference between the two yields the validation error. The validation errors calculated using the three performance indices for the five levels of emulator are tabulated in Table 4.5.

Table 4. 5: Validation Error

Tap length	AA	RMS	PTV
20	.1263	.1494	.6011
40	.1132	.1393	.5794
60	.0643	.0806	.3315
80	.0246	.0303	.1164
100	.0059	.0071	.0269

In order to visualize the effect of tap length on the validation error, the validation error is plotted as a function of the tap length for the three performance indices as shown in Figure 4.15.

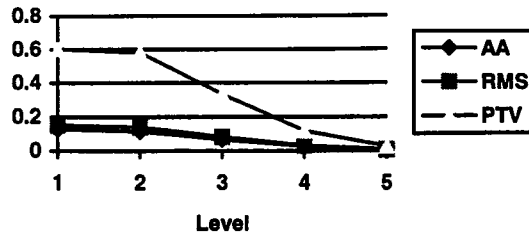


Figure 4. 15: Validation Error

The same conclusion can be reached for the validation error as in the case of the modeling error. The consistency of the model is not unusual because the modeling signal used is a band limited random signal that has a wide frequency range. Moreover, the format for the arrangement of nonrecurrent models is in the same for both modeling process and validation process unlike the format for the arrangement of recurrent networks.

The required size of the emulator is defined as the minimum size in which the weights between the neurons are such that the neural network output matches the output of the control mechanism. The degree to which the network should match the control mechanism depends on the application.

In order to balance the number of parameters and model fit, the previously used FPE criterion is applied here. The FPE values for the five levels are shown in Figure 4.16. From the figure, it is clear that the increase of tap length from level 1 to level 2 results in small performance improvement which is a reduction of the error

level by 0.0014. When the increase of tap length reaches level 3, the improvement in system performance is significant. The error level reduction (.0145) is more than the previous reduction by 90%. Further error reductions are possible with respect to increases in tap length levels, but they are in lower magnitudes (0.007, 0.002). Therefore, level 3 is selected as the optimal tap length for the emulator in this thesis research.

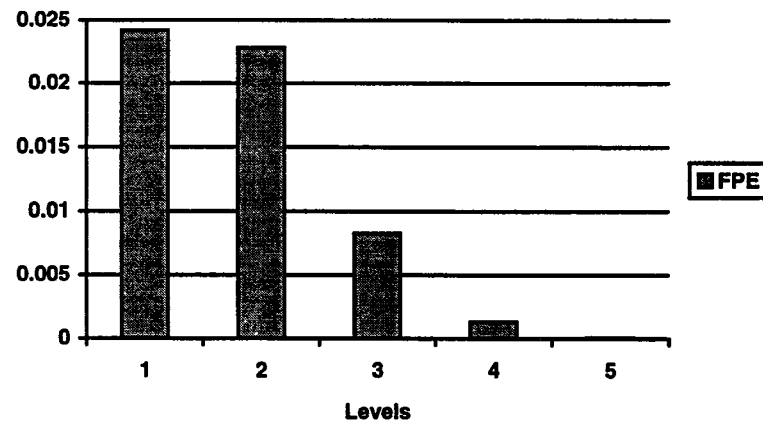


Figure 4.16: Final Prediction Error

#### 4.4.2 Linear Control Module Development

The controller is also a nonrecurrent linear NN like the emulator. The controller is responsible for producing control signals that drive the control mechanism. Unlike the emulator, the weights of the controller are tuned on-line. The control weights are adjusted through the adaptation algorithm that attempts to minimize the displacement of the tool.



The adaptation schemes developed for an emulator cannot be directly used for adaptation of the controller weights because there is a transfer function between the controller and the performance signal. This transfer function is the control mechanism. Therefore, the basic LMS adaptive filter needs to be modified by adding a transfer function of the control mechanism, which is actually the emulator. The complete development was presented independently by Widrow and Burgess and has come to be known as the filtered-X algorithm [Widrow, Shur, and Shaffer, 1982; Burgess, 1981]. In Figure 4.17, the block diagram of the adaptation algorithm as it is implemented in the SIMULINK program is shown.

At the start of the system operation, the switch assigns random values within the range of  $[-1,1]$  to the controller weights. When the reference signal is propagated through the delay tap of the controller, a vector of reference data is created at each instant. The dot product of the initial weight vector and the reference data vector produces the control signal. The control signal in turn excites the control mechanism to produce a secondary disturbance.



At the subsequent steps, the reference signal that is filtered through the emulator is used in calculating new weight values for the controller. The delay tap of the controller is used to create a vector of data of this filtered signal at each instant corresponding to the control weight vector. An appropriate value is assigned to the adaptation coefficient. The product of the filtered reference data vector, adaptation coefficient and the negative of the error signal at each instant produces the corrections of the weight values for the controller. The switch assigns these corrections of weight values instead of the initial weights at this point. The previous weight values of the controller were stored in the memory. Therefore, the summation of the corrections of weight values and the old weight values in the memory gives the new weight vector. The dot product of the reference data vector and the new weight vector produces the control signal. The control signal produced by the controller excites the control mechanism in such a way that the primary disturbance is attenuated.

#### 4.4.2.1 Design of Experiment

Here, the effect of the size of the control weight structures on the performance of the system is investigated. In order to analyze the effect of the size of the control structure, the five levels listed in Table 4.3 are used.

Two types of disturbance signals are considered for analysis. The first type is a harmonic disturbance with frequencies within the range of the cutting operation while the second type is a multi-frequency disturbance. The multi-frequency disturbance components are chosen with one dominant frequency. The amplitudes and frequencies of the disturbance signal are listed in Table 4.6.

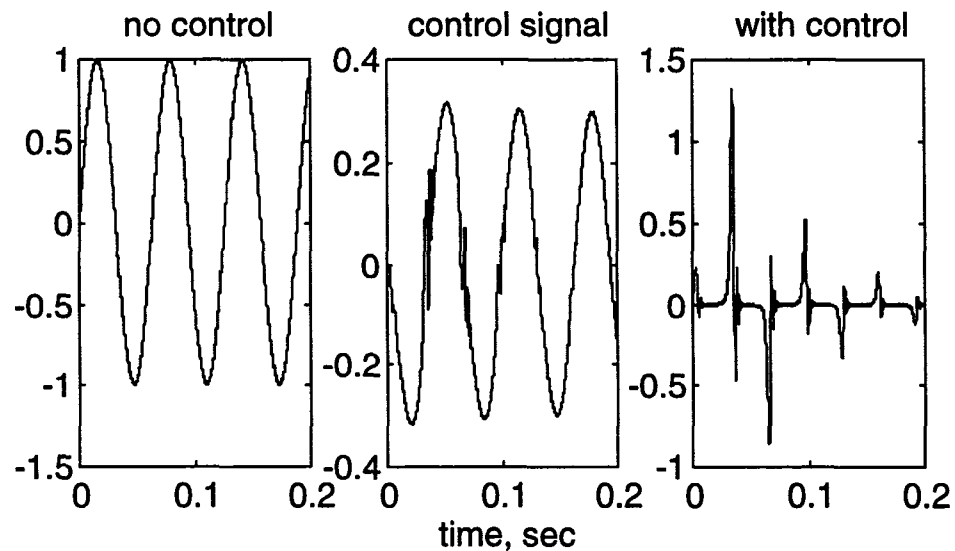
Table 4.6 Disturbance Signal Characteristics

	frequency, Hz	amplitude, V
Non dominant	300	.2
Dominant	200	.5
Non dominant	100	.3

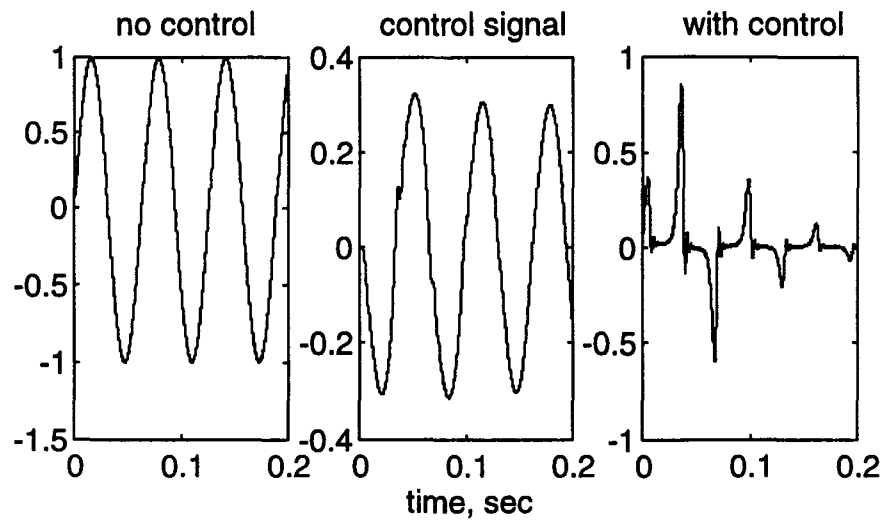
#### 4.4.2.2 Results and Analysis

##### 1. Harmonic Disturbance.

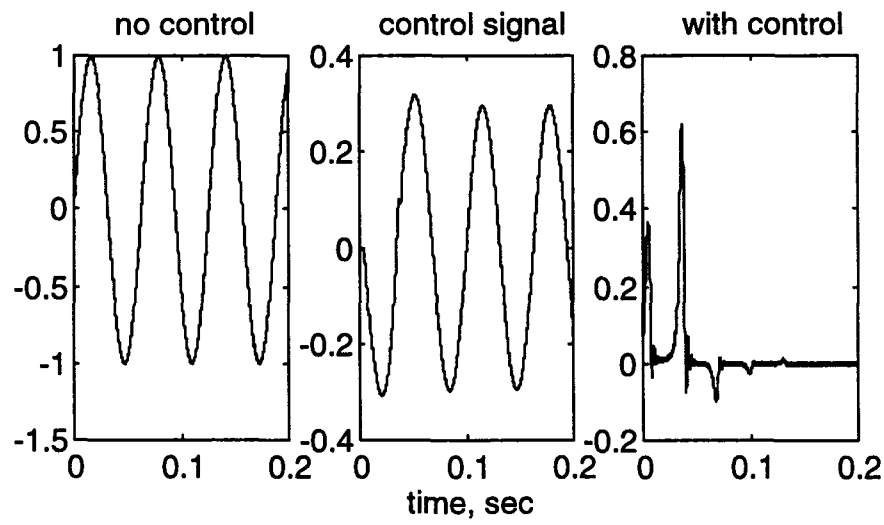
The harmonic disturbance is assumed to be known for simulation of the feedforward control scheme. The tool displacement without the controller, the control signal, and the tool displacement with the feedforward controller for each level of the controller structure at one of trial frequencies is shown in Figure 4.18.



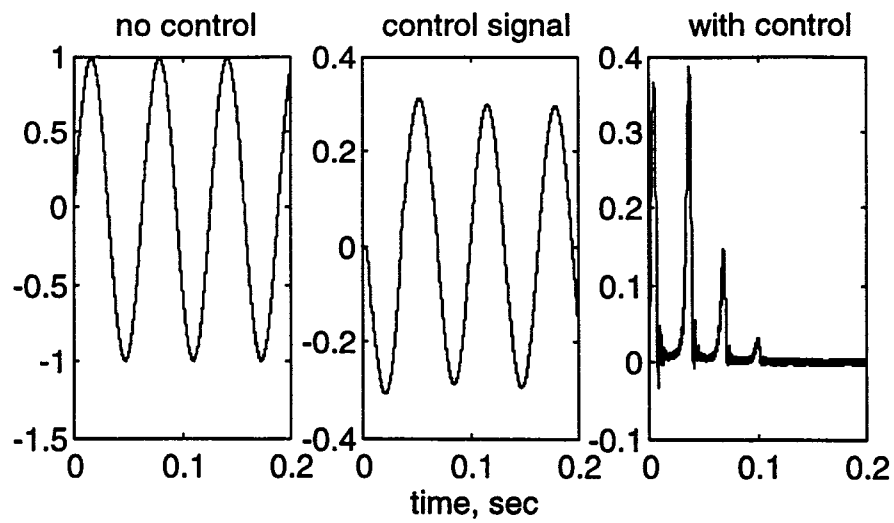
a) Level 1, tap length=20



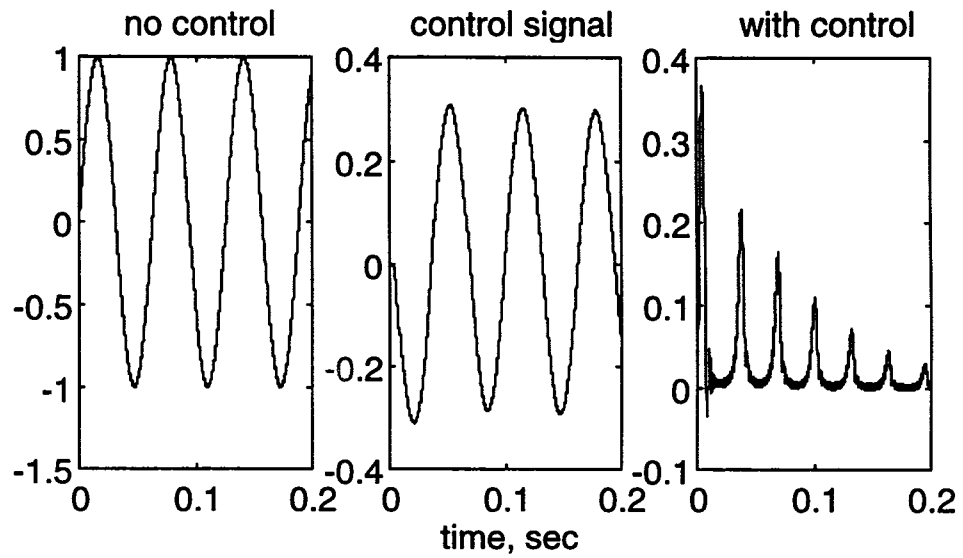
b) Level 2, tap length=40



c) Level 3, tap length=60



d) Level 4, tap length=80



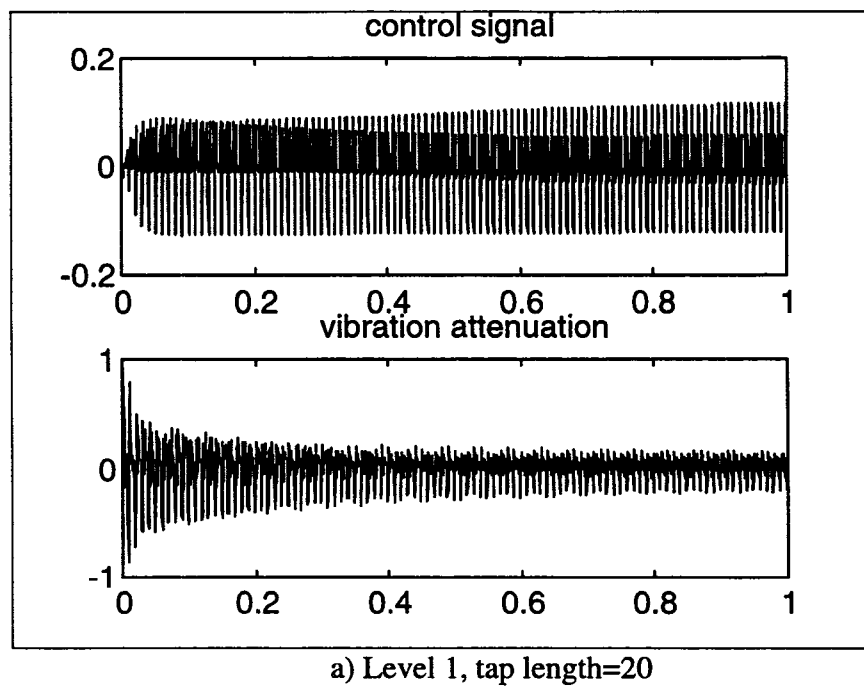
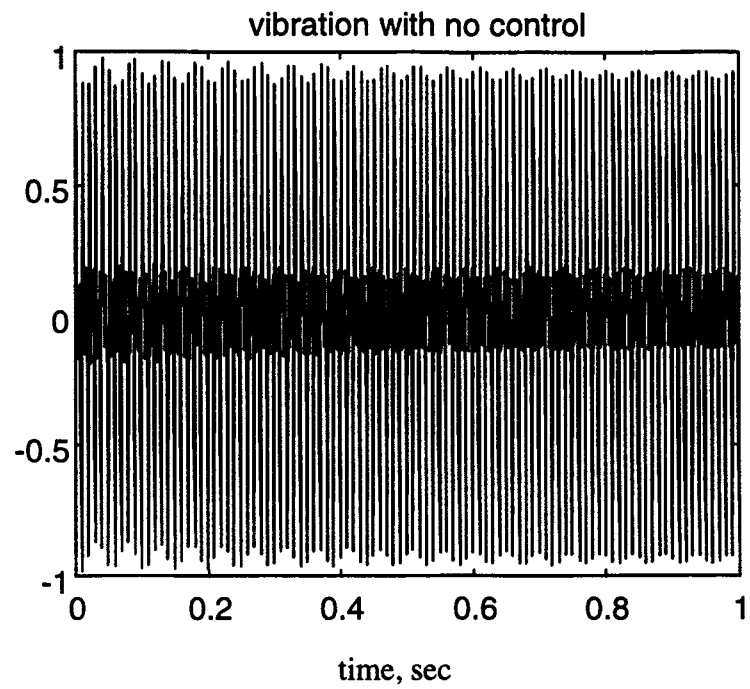
e) Level 5, tap length=100

Figure 4.18: Controller Performance for a Harmonic Disturbance

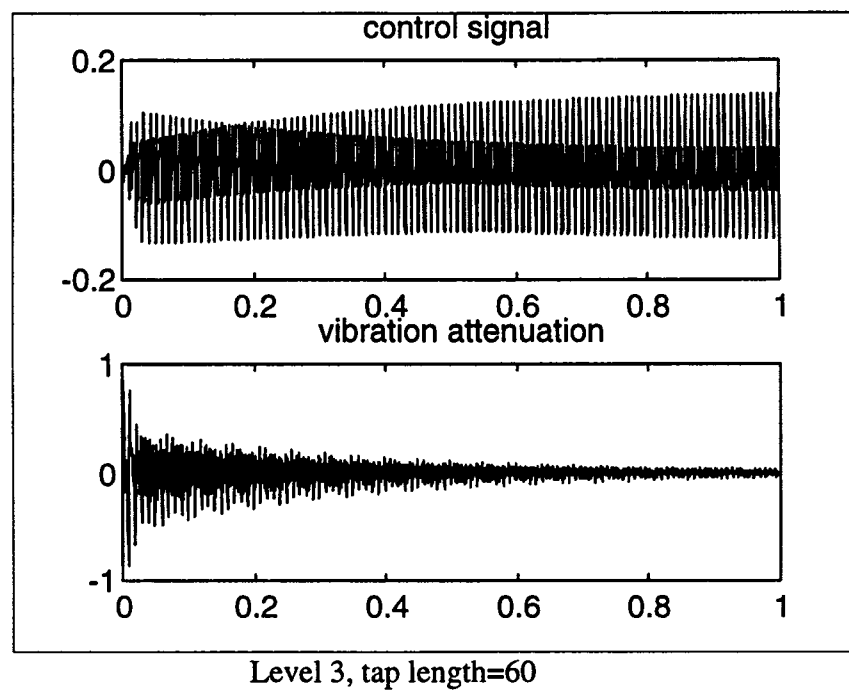
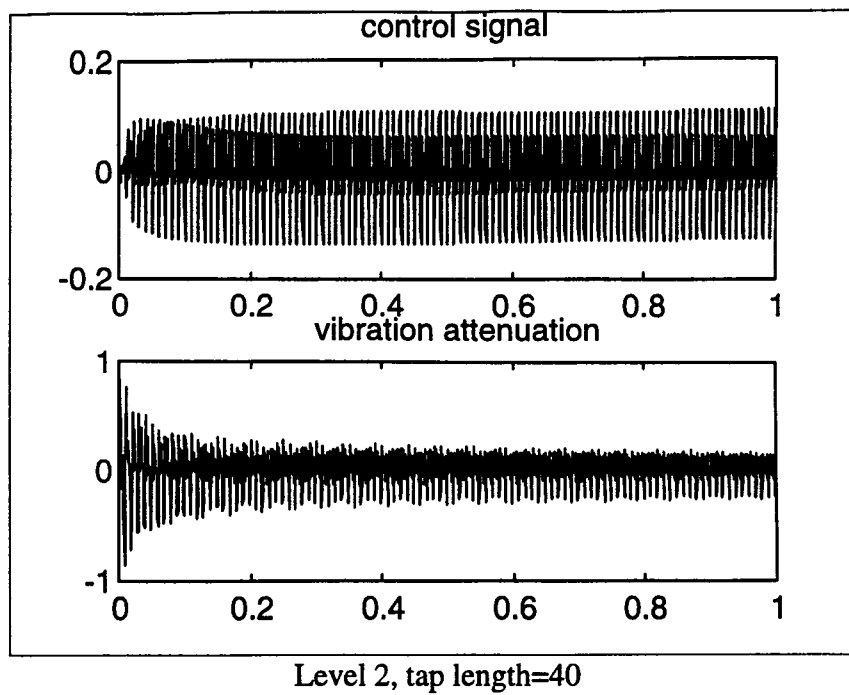
A convergence coefficient of 0.001 is used for the 100,80,60, and 40 weight structures while such a convergence coefficient did not result in a stable scheme for the 20 weight structure. The convergence coefficient for this case was set at 0.01. As the weight structure of the controller is increased, the negative part of the disturbance, or the disturbance leading the tool away from its equilibrium and reducing the depth of cut, is attenuated more than the positive part of the disturbance. The rate of attenuation was better for larger control weight structures. The 80 weight structure was slow in reducing the vibration at the initial cycle compared to the 100 weight structure; but yielded better attenuation rate after the second cycle.

## 2. Multi-Frequency Disturbance

Next, a multi-frequency disturbance is simulated. In this category, two examples are used for demonstration. The first example is to demonstrate the effect on the system response when a reference signal is correlated to the primary disturbance. Therefore, an identical signal is used as both the primary signal and the reference signal. The performance of the controller for the five levels of the control weight structures is shown in Figure 4.19. First, the tool displacement without the controller for one second time period is shown. Then the control signal and the vibration attenuation for the five levels for one second period are shown.







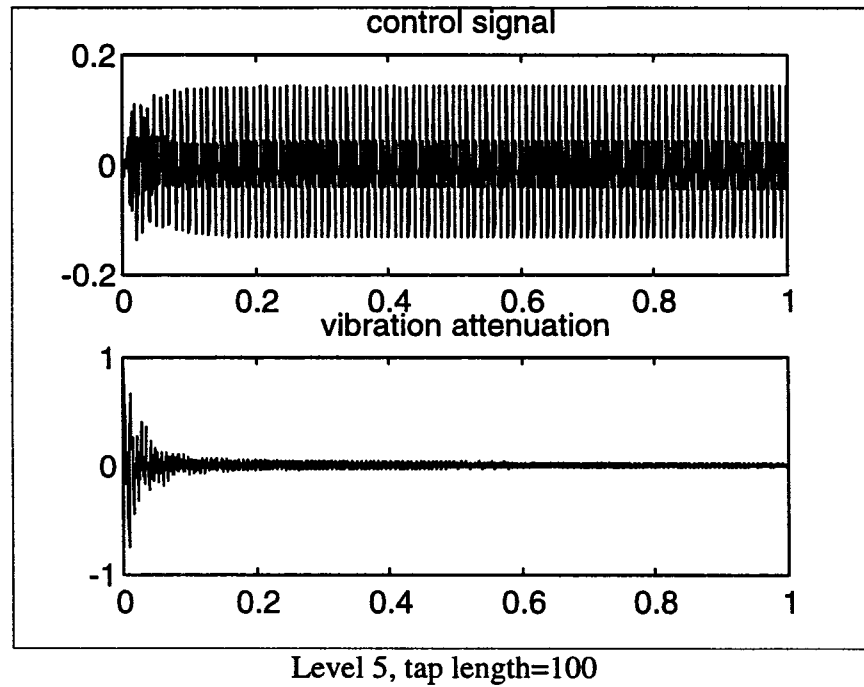
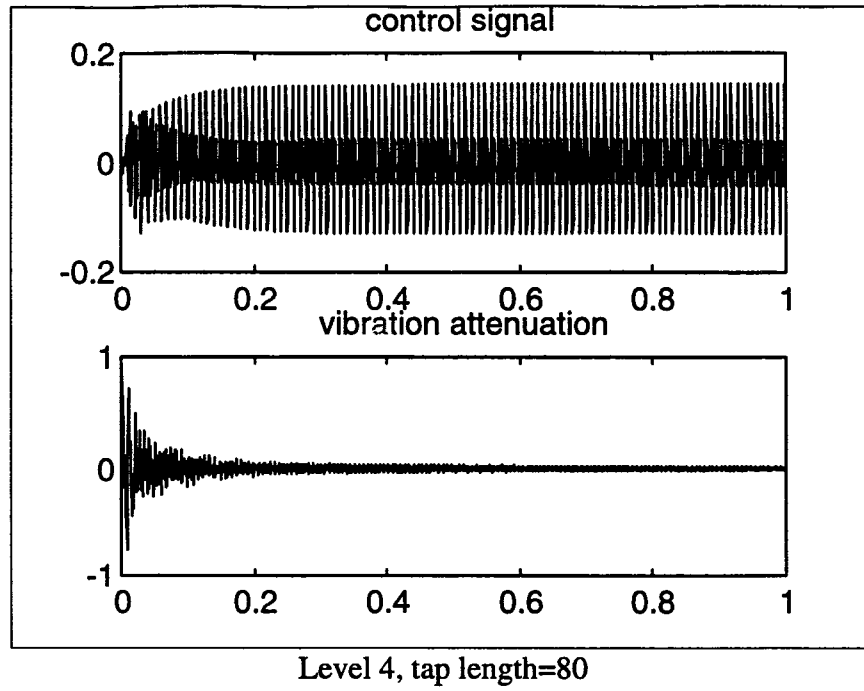


Figure 4.19: Controller Performance for a Multi-Frequency Disturbance, Example 1

A look at the transient response shows that tap lengths of 80 and 100 outperform the other three. The vibration settles to near the 0 value after a 0.2 second time period. The steady state performance can be evaluated by calculating the performance measurement indices on the last 0.1 second of the transient response data. The percent reduction in machine tool vibration is shown in Figure 4.20.

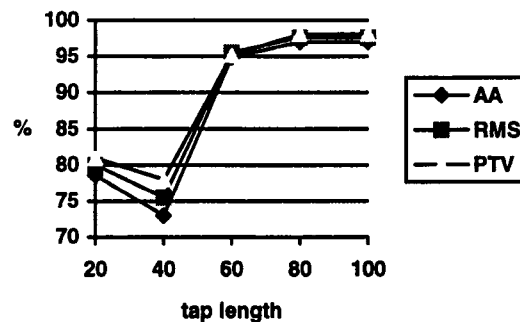
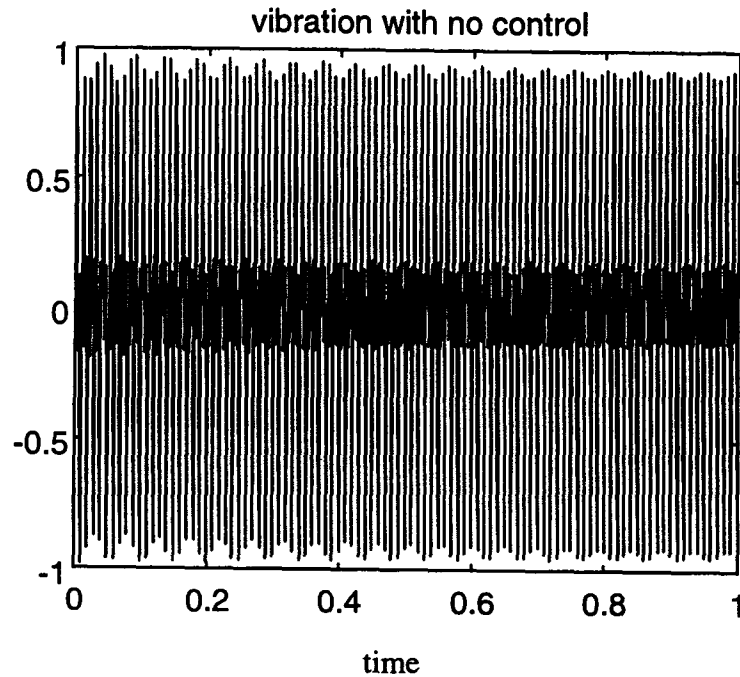


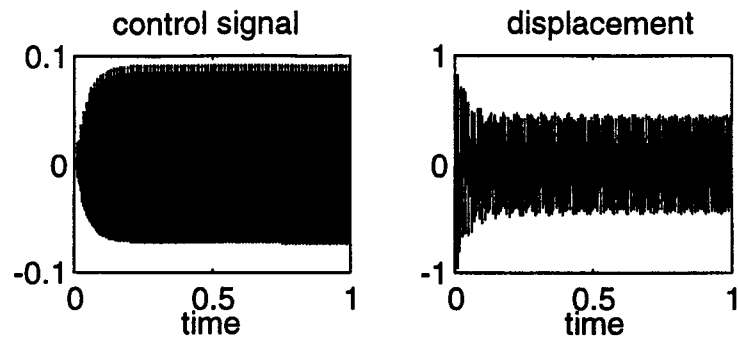
Fig. 4.20: Percent Tool Displacement Reduction

As shown in the figure, all structures were able to give percent reduction for the three profile measurement indices in the order of more than 70%. The weight structures associated with tap lengths of 60 to 100 in particular show the best performance; the reduction is in the 90% adaptation percentage range. The control structure with 40 tap lengths has lower performance indices when compared to the weight structure with 20 tap lengths. The reason for such a poor performance in reduction is due to the fact that the process was not yet complete.

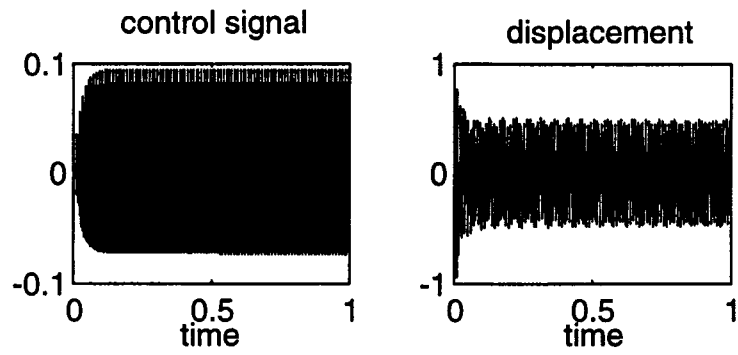
The second example is to demonstrate the performance of the controller when only the dominant frequency signal of the reference signal is available. The control

weight structure is varied and five levels are considered as before. The adaptation coefficient for each case is varied and the one which gives maximum convergence for a stable system is noted. The performance of the controller for the five levels of control structure is shown in Figure 4.21. First, the tool displacement without the controller for one second time period is shown. Then the control signal and the vibration attenuation for the five levels for one second period are shown.

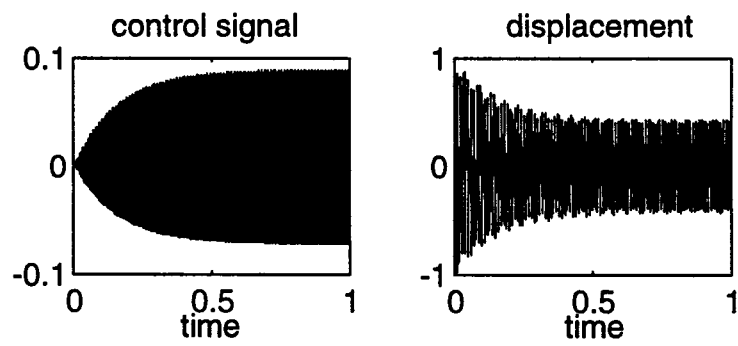




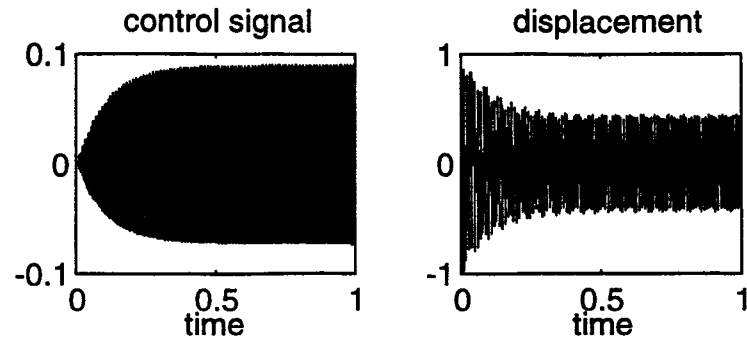
a) Level 1, tap length=20



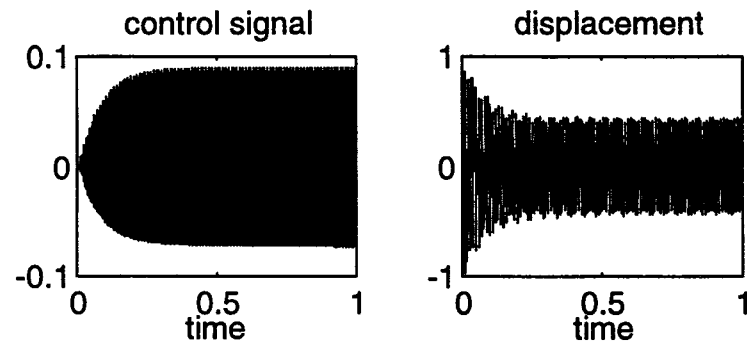
b) Level 2, tap length=40



c) Level 3, tap length=60



d) Level 4, tap length=80



e) Level 5, tap length=100

Fig. 4.21: Controller Performance for a Multi-Frequency Disturbance, Example 2

The effect on the rate of convergence due to change of convergence coefficient is observable for the order of 10. Therefore, the increment of the convergence coefficient is taken as a multiple of 10. A convergence coefficient of 1.0 brings instability, 0.1 assures stability, and 0.01 brings about the best performance for the level 1 control structure

The convergence coefficient for level 2 is the same as that of level 1. Unlike the first two levels, for level 3, the point of instability is lowered to 0.1 for the

convergence coefficient. This shows that as the control structure size increases, the convergence coefficient needs to decrease. Similar to the previous cases, a convergence coefficient of 0.01 ensures stability, but the best performance is obtained at a value of 0.001.

The same convergence coefficients that were employed for level 3 are also the appropriate values for levels 4 and 5. Therefore, the weight structures with tap length 20 and 40 fall in one class, whereas, the ones with tap lengths 60, 80, and 100 fall in another class.

In order to evaluate the steady state performance quantitatively, data collected in the final 0.1 seconds are used for calculating the AA, RMS, and PTV indices to evaluate the vibration levels with and without the controller. The percent reduction in vibration as a function of the control structure is shown in Figure 4.22.

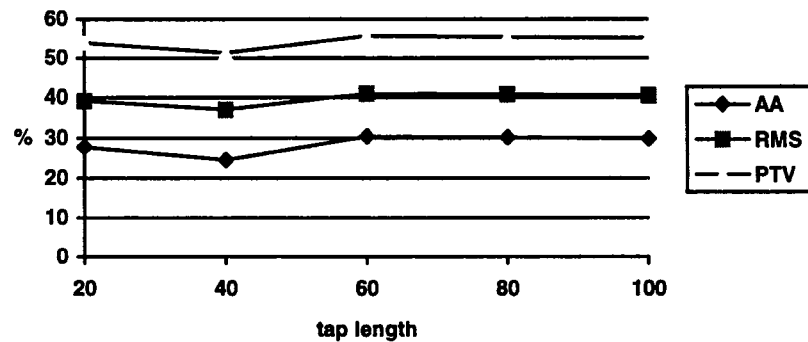


Fig. 4.22: Percent Tool Displacement Reduction

The performance of the controller for tap length 40 drops in similar fashion to the first example. Since the amplitude of the dominant frequency that is used as a

The performance of the controller for tap length 40 drops in similar fashion to the first example. Since the amplitude of the dominant frequency that is used as a reference signal is one half of the amplitude of the disturbance signal, the vibration reduction is reduced by half when compared to what was obtained in first example. This is because the feedforward control scheme compensates only the dominant frequency that is referenced by a reference signal. Once this frequency component is compensated quickly, then the scheme makes no effort to compensate for the unaccounted frequency components.

#### 4.5 Computer Simulation of Nonlinear NN Control System

The nonlinear NN control system is composed of two modules, the emulator and the controller, which resemble the linear counter part. Similar to the linear NN control system, the emulator is derived off-line. Unlike the linear NN control system, the nonlinear NN controller is a learning type controller. The training process is performed in an off-line fashion. Hardware implementation of the nonlinear NN controller is left for future work.

##### 4.5.1 Neural Architecture Identification

First, neural architecture for the emulator and controller is identified. In this thesis work, both recurrent and nonrecurrent nonlinear NN structures are investigated for the neural architecture identification. The identification process is conducted using the simpler module, the emulator.



In the hardware realization, the emulator is derived from the actual plant, namely, the control mechanism. For computer simulation investigation, the parameteric model of the control mechanism identified in Section 4.2 replaces the actual plant. Depending on the recurrent signals, the nonlinear recurrent emulator is capable of taking two different formats as series/parallel and parallel [Narendra, and Parthasarathy, 1990]. The series/parallel format is where recurrent signals are obtained from the output of the system, which is the control mechanism, as shown in Figure 4.23. This arrangement has several advantages over the other format. Since the plant is assumed to be bounded-input bounded-output (BIBO) stable, all the input signals to the neural networks are assumed to be bounded. Moreover, since no feedback loop exists in this arrangement from itself, static back propagation can be used to adjust the parameters reducing the computational overhead substantially. As a result, this arrangement, known as series/parallel, is best suited for training the emulator off-line.

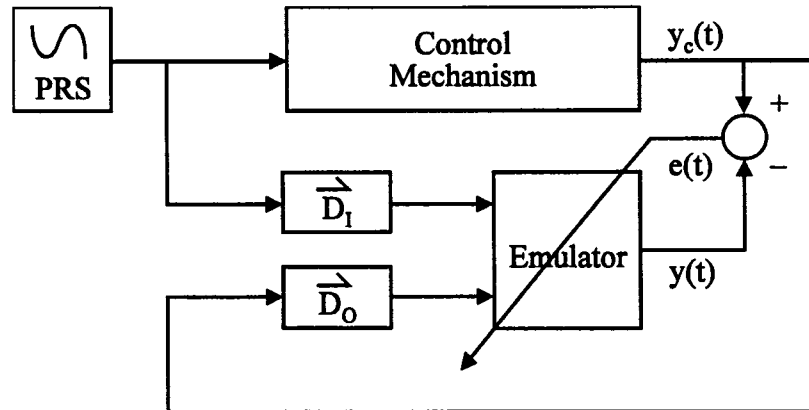


Figure 4.23: Series/Parallel Arrangement

The delay vectors for the input and output signals shown in Figure 4.23 and Figure 4.24 are given by

$$\bar{D}_I = \begin{Bmatrix} 1 \\ z^{-1} \\ z^{-2} \\ . \\ . \\ z^{-p} \end{Bmatrix} \quad \bar{D}_O = \begin{Bmatrix} z^{-1} \\ z^{-2} \\ . \\ . \\ . \\ z^{-q} \end{Bmatrix} \quad \text{Eq. 4.21}$$

When training the controller, the recurrent signals from the control mechanism are no longer available for the emulator because they are contaminated with the primary disturbances. Therefore, recurrent signals from the emulator outputs should be used, instead of the outputs of the control mechanism. This arrangement is known as the parallel arrangement as shown in Figure 4.24. Assuming that the output error tends to be reduced to a small value asymptotically so that  $y_c(k) \approx y(k)$ , the series/parallel model can be replaced by a parallel model with accuracy. Since the emulator is a model of the control mechanism, the output of the emulator is supposed to match the output of the control mechanism. The difference between the output of the emulator in parallel format after being trained in series/parallel format and the output of the control mechanism, is referred to as validation error. Back propagation of this validation error in the recurrent signals can pose serious problems in the performance of the control system. Therefore, the emulator that is trained with the series/parallel arrangement needs to be checked for its performance in parallel arrangement. As a result, there are two factors to govern the performance of an emulator. These factors are modeling error based on the series/parallel arrangement in

the modeling mode, and validating error based on parallel arrangement in the functional mode.

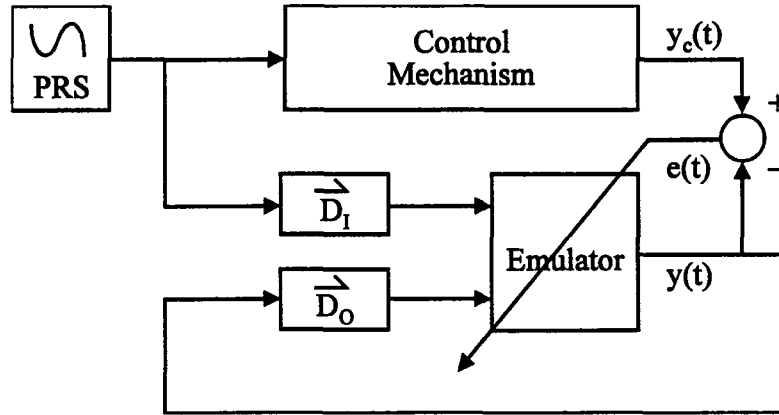


Figure 4. 24: Parallel Arrangement

The nonlinear emulator has three layers. The nonrecurrent nonlinear network is a TDNN as shown in Figure 3.13. The recurrent nonlinear network is a RNN as shown in Figure 3.14 in Chapter 3. Both networks have three layers; namely, an input layer, a hidden layer, and an output layer. The input layer of the nonrecurrent emulator has one neuron for the current input signal,  $p$  neurons for the delayed input signals, while the recurrent emulator has, in addition,  $q$  neurons for the delayed recurrent output signals. Therefore, the total number of the input neurons in the input layer is  $p+1$  for the nonrecurrent emulator and  $p+q+1$  for the recurrent emulator. The hidden layer has a  $\lambda$  number of neurons, while the output layer has only 1 neuron corresponding to the output of the emulator.

#### 4.5.1.1 Nonlinear Emulator Dynamics

At time  $k$ , a hidden neuron  $j$  receives a net input given by

$$H_j^h(k) = \sum_{i=0}^{p+q} (w_{ji} \bullet I(i, k)) + v_j^h \quad \text{Eq. 4.22}$$

where

$v_j^h$  are biases [threshold] for hidden neurons.

$w_{ji}$  is the weight connecting the  $j^{\text{th}}$  hidden neuron to the  $i^{\text{th}}$  input neuron

$$I(:, k) = [u(k) \ u(k-1) \ \dots \ u(k-p) \ z(k-1) \ \dots \ z(k-q)]^T$$

$u(k)$  is the control signal at instant  $t=k$

$z(k)=y(k)$  for parallel emulator arrangement.

$z(k)=y_c(k)$  for series/parallel emulator arrangement.

$y(k)$  is the output of the emulator

$y_c(k)$  is the tool displacement due to the control signal.

The hidden neuron  $j$  produces an output which is given by

$$O_j^h(k) = \Gamma^s[H_j^h(k)] = \Gamma^s\left[\sum_{i=0}^{p+q} (w_{ji} \bullet I(i, k)) + v_j^h\right] \quad \text{Eq. 4.23}$$

where  $\Gamma^s$  is a sigmoidal processing function of the hidden neuron. The output neuron

thus receives a net input which is given by

$$H^o(k) = \sum_{j=1}^{\lambda} v_j O_j^h(k) + v^o = \sum_{j=1}^{\lambda} v_j \Gamma^s\left[\sum_{i=0}^{p+q} (w_{ji} \bullet I(i, k)) + v_j^h\right] + v^o \quad \text{Eq. 4.24}$$

where

$v_j$  is the weight connecting the  $j^{\text{th}}$  hidden neuron to the output neuron,

$\lambda$  is the number of hidden neurons,

$v^o$  are biases [threshold] for output neuron.

Finally, the output neuron produces the final output which is given by

$$y(t) = \Gamma' [H^o(k)] = \Gamma' \left\{ \sum_{j=1}^{\lambda} v_j \Gamma^s \left[ \sum_{i=0}^{p+q} (w_{ji} \bullet I(i, k)) + v_j^h \right] + v^o \right\} \quad \text{Eq. 4.25}$$

where

$\Gamma'$  is a linear processing function of the outer neuron.

The processing function selected for the first layer is the nonlinear sigmoidal function which maps  $\psi[-\infty, \infty] \Rightarrow h[-1, 1]$ . This function is chosen to take advantage of the nonlinear capabilities of the neural network, and also to capture the vibrational displacement which varies around zero, or the equilibrium position. In order to retain the mapping capability of any input value to any output value, the pure linear function is chosen to map  $h[-1, 1] \Rightarrow y[-\infty, \infty]$ . Moreover, the complexity of the network reduces by limiting the nonlinear sigmoid transfer function to one set of the weight structure.

The modeling error of the NN model can be found by evaluating the difference of the outputs of the control mechanism and the emulator.

$$e(k) = y_c(k) - y(k) \quad \text{Eq. 4.26}$$

The error energy function is given by

$$J(k) = \frac{1}{2} \{e^2(k)\} \quad \text{Eq. 4.27}$$

The gradient of the error energy function with respect to the weight is back propagated through the network to modify the weight parameters so as to reduce the

error energy function of the emulator. The Levenberg-Marquardt Method is implemented in this research to adapt the weights of the emulator. This method balances between the extremes of the inverse-Hessian method and the steepest descent method.

Let the parameter  $\theta$  be used for all the weight structures  $\{w_{ji}\}$  and  $\{v_j\}$  arranged in an array. The weight updating equation is thus given by

$$[\Phi^T \Phi + \eta I] \delta\theta = -\Phi^T e \quad \text{Eq. 4.28}$$

where  $\eta$  is adaptation coefficient and  $\Phi$  is the Jacobian that is defined as  $\Phi = \frac{\partial J(\theta)}{\partial \theta}$ .

Given an initial random guess for the set of fitted weight parameters  $\theta$ , the recipe used in emulator training is given as follows [Press, Teukolsky, Vetterling, and Flannery, 1992]

1. Computing of the performance index  $J(\theta)$ .
2. Picking of a modest value for  $\eta$ , say  $\eta=0.001$
3. Evaluating Eq. 4.28 for  $\delta\theta$  and evaluation of  $J(\theta+\delta\theta)$
4. Incrementing of  $\eta$  by a factor of 10 if  $J(\theta + \delta\theta) \geq J(\theta)$ , and returning back to step 3.
5. Decrementing of  $\eta$  by a factor of 10, if  $J(\theta+\delta\theta) < J(\theta)$ , updating the trial solution  $\theta \leftarrow \theta + \delta\theta$ , and returning back to step 3.

Also it is necessary a condition for stopping the scheme be defined. Iterating to convergence (to machine accuracy or to the round-off limit) is generally wasteful and unnecessary since the minimum is at best only a statistical estimate of the

parameters  $\theta$ . Otherwise, the parameters wander around near the minimum in a flat valley of complicated topology. Outright failure by a zero pivot when solving for  $\delta\theta$  is possible, but unlikely, because more often a small pivot will generate a large correction which is then rejected, the value of  $\eta$  being then increased. For sufficiently large  $\eta$ , the matrix  $[ \varphi^T \varphi + \eta I ]$  is positive definite and can have no small pivots. Thus the method does tend to stay away from zero pivots, but at a cost of a tendency to wander around doing the steepest descent in very unsteep valleys. These considerations suggested in actual training to stop iterating on the first occasion that  $J$  decreases by machine accuracy.

#### 4.5.1.2 Training Data

The identification procedure is performed in two phases as before. First, training data that represent system input and system output for a duration of one second of time are collected that because the collected data of 1 second can contain frequency content as low as 1 Hz. In order to capture the full spectrum content, the input signal used to excite the control mechanism is chosen to be a random signal. The input signal is delayed according to the tap length of the NN and a matrix of input signals is stored in an input file. The corresponding array of output signals is stored in an output file. The memory block size is a function of the tap length.

The devised neural network structure can handle both inputs and outputs in the range of  $(-\infty, +\infty)$ . In order to create an environment that best suits the comparison of different models, a scaling process is performed on both the inputs and outputs so that

the magnitudes of both signals would lie in the  $[-1,1]$  interval. The time step of the simulation is maintained constant and is set to 0.0001 seconds. That yields a sampling frequency of 10 kHz.

#### 4.5.1.3 Initial Random Weight

The size of the initial random weights is important. If they are too large, the sigmoidal transfer function will saturate from the beginning, and the system will become stuck in a local minimum (or very flat plateau) near the starting point. The strategy taken to tackle this problem is to choose random weights so that the magnitude of the typical net input to the hidden neuron  $H_j^h$  is a little less than unity to avoid initial saturation. Since the inputs are limited to lie within  $[-1,1]$  range, the initial weights accordingly need to fall in the same range. As a result, the initial weight is derived using a random number generator within  $[-1,1]$  range. Though the activation function of the output neuron is linear, the same range of values are used for all network weights in order to make a fair comparison among the different neural structures.

Unlike the linear neural network, the initial weights play a role in arriving at the global or local minima. The randomness of initial weights for different neural structures makes it difficult to make comparisons among the different neural structures. Therefore, a statistical approach is devised to control the performance variation due to this uncontrollable variable. As a result, twenty sets of training data are collected for each control structure from which a mean and a standard deviation can be evaluated.



The required size of a neural network that suites the application needs to be defined. In order to define the required neural network structure, the nonlinear emulator has limitations compared to the linear emulator. First, the linear emulator can be found easily for there is global minima in the case of linear networks. Second, the nonrecurrent network was sufficient in this thesis research work for the linear case while recurrent network were required for the nonlinear counterpart. The recurrent networks introduce two different arrangements for modeling and functional modes and thereby, increases the complexity. Therefore, the following design of experiments in two stages are devised to tackle this problem.

#### 4.5.1.4 Design of Experiment I

The design parameters for the chosen neural structure include the input delay tap length  $p$ , the output recurrent delay tap length  $q$ , and the number of hidden neurons  $\lambda$ .

The first factor that is analyzed is the required tap length of the network for the emulator. The levels for the study are tabulated in Table 4.7.

Table 4.7: Tap Length Levels

Cases	input delay tap	recurrent delay tap
Low	4	4
Medium	9	9
High	19	19

The variation in the weight structure of the emulator is monitored by the total number of weight parameters. After many initial trials, total weight parameters that range from 10 to 80 are selected for analysis. The total number of the total weight parameters is a function of the tap length levels and the number of hidden neurons.

The number of hidden neuron is varied in such a way that the total number of weight parameters remains within the range of 10 to 80. The total number of weight parameters for the three cases as a function of hidden neurons are listed in Table 4.8. Note that the matches, in total number of parameters, among these cases are shown by bold figures.

Table 4.8: Weight Parameters

<b>Hidden Neuron</b>	<b>Low</b>	<b>Medium</b>	<b>High</b>
<b>1</b>	10	<b>20</b>	<b>40</b>
<b>2</b>	<b>20</b>	<b>40</b>	<b>80</b>
<b>3</b>	30	<b>60</b>	
<b>4</b>	<b>40</b>	<b>80</b>	
<b>5</b>	50		
<b>6</b>	<b>60</b>		
<b>7</b>	70		
<b>8</b>	<b>80</b>		

#### 4.5.1.5 Results and Analysis I

The transient response of the training response is evaluated by noting the number of epochs, or the settling time, required to reach a training error tolerance of 0.1. The maximum number of epochs is selected in such a way that all the neural structures reach a steady state. A total number of epochs of 20 is found to be sufficient for all neural structures to reach the steady state. The statistical parameters calculated based on the 20 samples include the mean, the standard deviation, the maximum, and the minimum values. In Table 4.9a, the number of epochs, or the settling time, for Low [L] case is provided, and in Table 4.9b, the number of epochs for Medium [M] case is provided, and in Table 4.9c, the number of epochs for High [H] case is provided.

Table 4.9: Settling Time Parameter

$\lambda$	1*	2	3	4	5	6	7	8
<b>Mean</b>	13.6	10.9	8.4	8.4	8.2	7.3	7.5	7.7
<b>S. D.</b>	3.7	4.5	2.01	2.04	2.1	2.0	1.5	1.1
<b>Max</b>	19	20	12	13	16	13	10	10
<b>Min</b>	7	6	6	6	6	5	5	6

a) Low case

$\lambda$	1*	2	3	4
<b>Mean</b>	11.5	8.6	7.5	7.8
<b>S. D.</b>	3.7	3.7	2.3	2.7
<b>Max</b>	19	20	14	18
<b>Min</b>	6	5	5	6

b) Medium case

$\lambda$	1*	2
<b>Mean</b>	15.94	12.35
<b>S. D.</b>	4.5	5.3
<b>Max</b>	20	20
<b>Min</b>	6	5

c) High case

Note: Number of samples that didn't meet the specification: \*=one, +=three

The mean of the epochs required to attain the error goal for the Low case stabilizes at the third hidden neuron while for the Medium case the mean stabilizes at the second hidden neuron. When a comparison is made between the Low and Medium cases, there is a slight improvement in the Low case for the same weight structures. The worst case is seen in the High case. Based on the transient response of the modeling error, the Low and Medium cases give similar results for the same total number of weight parameters.

The steady state parameter for the modeling process can be evaluated from the modeling error where the training process reaches steady state. Since the maximum number of epochs, 20, is used for training, the modeling error at the 20<sup>th</sup> epoch is used as the steady state error. The statistical parameters are calculated for the three cases and they are listed in Table 4.10.

Table 4.10: Steady State Modeling Error

$\lambda$	1	2	3	4	5	6	7	8
<b>Mean</b>	0.413	0.236	0.086	0.048	0.037	0.041	0.037	0.0137
<b>S. D.</b>	0.276	0.211	0.155	0.067	0.085	0.083	0.059	0.007
<b>Max</b>	1.394	0.829	0.662	0.262	0.394	0.317	0.229	0.034
<b>Min</b>	0.059	0.008	0.008	0.008	0.008	0.008	0.008	0.008

a) Low case

$\lambda$	1	2	3	4
<b>Mean</b>	.3686	.1458	.0825	.0402
<b>S. D.</b>	.4197	.1735	.0865	.0989
<b>Max</b>	1.9901	.6766	.2553	.457
<b>Min</b>	.0082	.0082	.0092	.0082

b) Medium case

$\lambda$	1	2
<b>Mean</b>	0.6739	0.4555
<b>S. D.</b>	0.5485	0.5215
<b>Max</b>	1.8347	1.7145
<b>Min</b>	0.0219	0.0082

c) High case

The High case again shows in the worst performance. When the other two cases are compared under the condition of keeping the total weight parameters constant, the Low case gives much better performance. It yields lower mean values coupled with lower standard deviations. In almost all cases, the performance improves

with an additional number of hidden neurons. Before a final decision is made on the performances of the different cases, the validation error has to be checked.

There is a great discrepancy when it comes to validation error. The validation error can go beyond the working range of the emulator since the arrangement for the validation error is different from the modeling error. Since the validation arrangement is in the format for a control application, the model can be rejected though it appears to have acceptable modeling errors. Therefore, it is crucial to evaluate the validation error using the previously identified models.

Since the emulator is identified off-line in this thesis application, a working model can be found after many trials. Among the twenty samples, a sample is said to be acceptable if at any time the validation error is bounded below 2. Since the control mechanism and the emulator have inputs in the range of  $[-1, 1]$ , the maximum error at any instant should be below 2. The number of samples accepted for further analysis are listed in Table 4.11.

**Table 4.11: Acceptable Samples**

<b>Cases</b>	<b>Hidden Neurons</b>	<b>Accepted # of samples</b>
<b>Low</b>	1	11
	2	11
	3	12
	4	12
	5	12
	6	13
	7	15
	8	15
<b>Medium</b>	1	10
	2	10
	3	17
	4	13
<b>High</b>	1	3
	2	6

Here, among the twenty samples, the best ten are selected for evaluation. From previous discussion, the High case yields the worst performance. Moreover, the High case has fewer number of acceptable samples. Therefore, the High case is excluded from further investigation. The validation errors are evaluated using the three performance indices. The performance indices of the ten selected samples for the Low case are listed in Table 4.12 and those for the Medium case are listed in Table 4.13.

Table 4.12: Validation Error for Low Case

Hidden Neuron = 1			Hidden Neuron = 2		
RMS	AA	PTV	RMS	AA	PTV
0.1439	0.0938	0.6191	0.0658	0.0488	0.1721
0.0796	0.0542	0.1932	0.0937	0.0728	0.3078
0.0409	0.0231	0.1691	0.0205	0.0122	0.0706
0.0168	0.0109	0.0614	0.0881	0.0527	0.3763
0.1045	0.0778	0.3321	0.0939	0.0523	0.3946
0.1529	0.1026	0.6561	0.0493	0.0273	0.1658
0.0899	0.0552	0.3734	0.0587	0.0207	0.2529
0.1738	0.1362	0.5410	0.0378	0.0112	0.1937
0.2078	0.1590	0.7294	0.0904	0.0501	0.3181
0.2289	0.1713	0.6855	0.1066	0.0683	0.4532

Hidden Neuron = 3			Hidden Neuron = 4		
RMS	AA	PTV	RMS	AA	PTV
0.0362	0.0216	0.1471	0.0273	0.0146	0.1043
0.0409	0.0193	0.1874	0.0384	0.0117	0.1958
0.0387	0.0116	0.1965	0.0366	0.0112	0.1929
0.0332	0.0194	0.1377	0.0469	0.0270	0.1806
0.0311	0.0135	0.1478	0.0104	0.0068	0.0361
0.0322	0.0116	0.1526	0.0364	0.0108	0.1879
0.0366	0.0108	0.1893	0.0318	0.0187	0.0956
0.0449	0.0148	0.2046	0.0442	0.0258	0.1383
0.0386	0.0116	0.1965	0.0390	0.0119	0.1990
0.0309	0.0173	0.1080	0.0385	0.0117	0.1959

Hidden Neuron = 5			Hidden Neuron = 6		
RMS	AA	PTV	RMS	AA	PTV
0.0529	0.0185	0.2474	0.0379	0.0113	0.1942
0.0382	0.0113	0.1934	0.0378	0.0113	0.1938
0.0342	0.0101	0.1774	0.0370	0.0110	0.1911
0.0388	0.0118	0.1973	0.0311	0.0108	0.1380
0.0489	0.0279	0.1971	0.0194	0.0063	0.0923
0.0376	0.0112	0.1926	0.0230	0.0068	0.1093
0.0343	0.0138	0.1474	0.0457	0.0200	0.2009
0.0286	0.0160	0.1190	0.0135	0.0084	0.0447
0.0390	0.0121	0.1954	0.0383	0.0115	0.1904
0.0373	0.0111	0.1917	0.0370	0.0106	0.2020

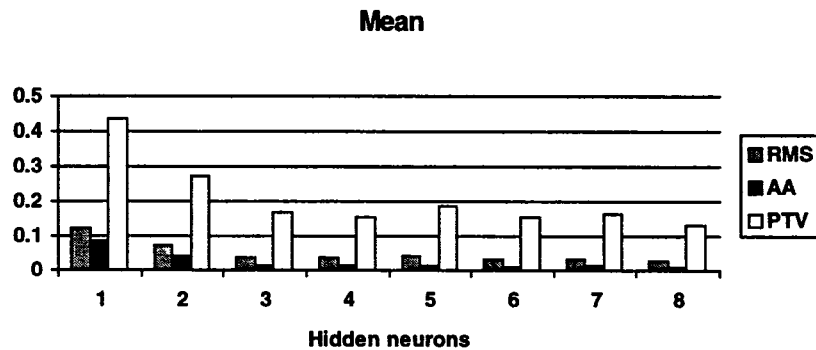
Hidden Neuron = 7			Hidden Neuron = 8		
RMS	AA	PTV	RMS	AA	PTV
0.0377	0.0112	0.1899	0.0348	0.0103	0.1732
0.0386	0.0117	0.1964	0.0279	0.0095	0.1253
0.0333	0.0133	0.1478	0.0136	0.0076	0.0519
0.0297	0.0144	0.1203	0.0038	0.0014	0.0173
0.0375	0.0111	0.1922	0.0348	0.0099	0.1939
0.0396	0.0118	0.1999	0.0383	0.0115	0.1974
0.0224	0.0138	0.0673	0.0377	0.0113	0.1890
0.0253	0.0094	0.1180	0.0321	0.0166	0.1134
0.0390	0.0117	0.1974	0.0141	0.0049	0.0653
0.0369	0.0109	0.1922	0.0373	0.0110	0.1925

Table 4.13: Validation Error for Medium Case

Hidden Neuron = 1			Hidden Neuron = 2		
RMS	AA	PTV	RMS	AA	PTV
0.0038	0.0024	0.0171	0.0591	0.0339	0.2005
0.0835	0.0507	0.3528	0.0070	0.0028	0.0328
0.0011	0.0007	0.0041	0.0100	0.0032	0.0493
0.0736	0.0540	0.2413	0.0498	0.0149	0.2333
0.0489	0.0272	0.2088	0.0053	0.0020	0.0267
0.0642	0.0357	0.2646	0.0111	0.0077	0.0358
0.0058	0.0037	0.0161	0.1503	0.0968	0.6826
0.0244	0.0158	0.0869	0.0650	0.0354	0.2700
0.2182	0.1198	1.1593	0.1310	0.0650	0.7612
0.0110	0.0074	0.0337	0.0128	0.0068	0.0502

Hidden Neuron = 3			Hidden Neuron = 4		
RMS	AA	PTV	RMS	AA	PTV
0.0087	0.0055	0.0292	0.0064	0.0024	0.0296
0.0091	0.0030	0.0464	0.0175	0.0058	0.0798
0.0128	0.0061	0.0537	0.0034	0.0023	0.0093
0.0053	0.0021	0.0243	0.0029	0.0009	0.0139
0.0115	0.0040	0.0534	0.0079	0.0026	0.0396
0.0045	0.0030	0.0127	0.0103	0.0045	0.0418
0.0086	0.0053	0.0384	0.0129	0.0044	0.0590
0.0017	0.0006	0.0098	0.0034	0.0019	0.0130
0.0087	0.0032	0.0433	0.0037	0.0021	0.0173
0.0033	0.0015	0.0175	0.0081	0.0024	0.0420

For the ten samples, values of the mean and standard deviation, the maximum, and the minimum are calculated for the three performance indices. In Figure 4.25, the statistical measures of the validation errors for the Low case are illustrated.





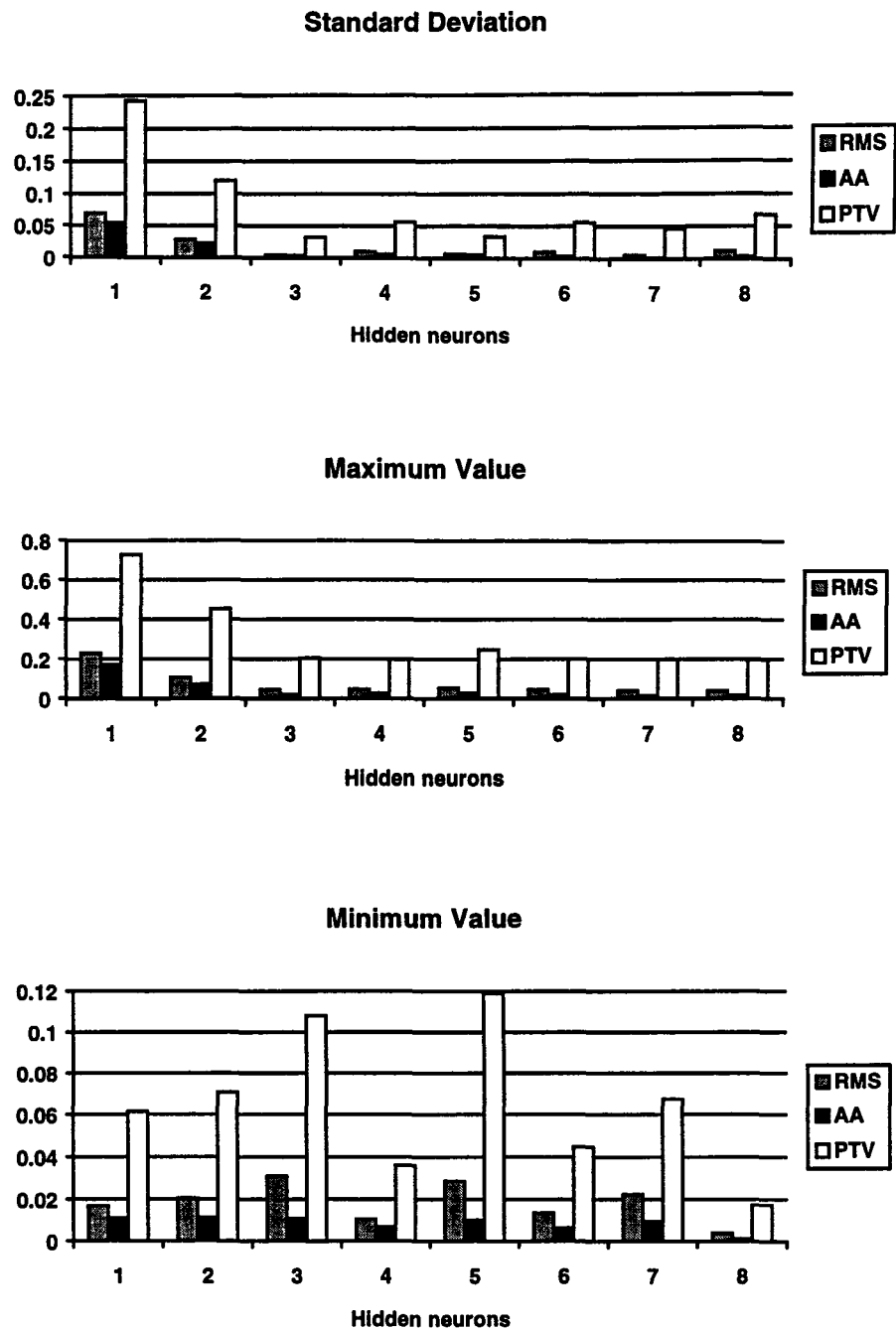
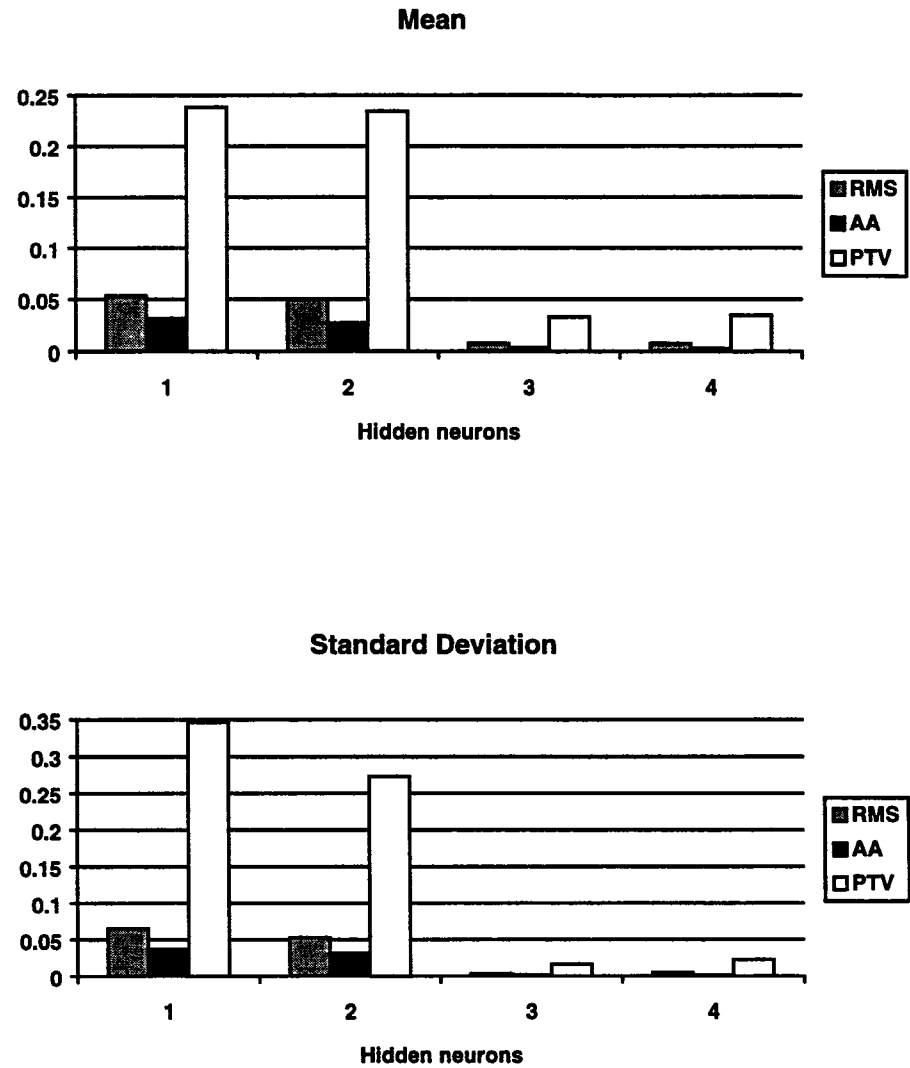


Figure 4.25: Statistical Measures of Validation Error for Low Case

Statistical measures of the validation error for the Medium case are given in

Figure 4.26.



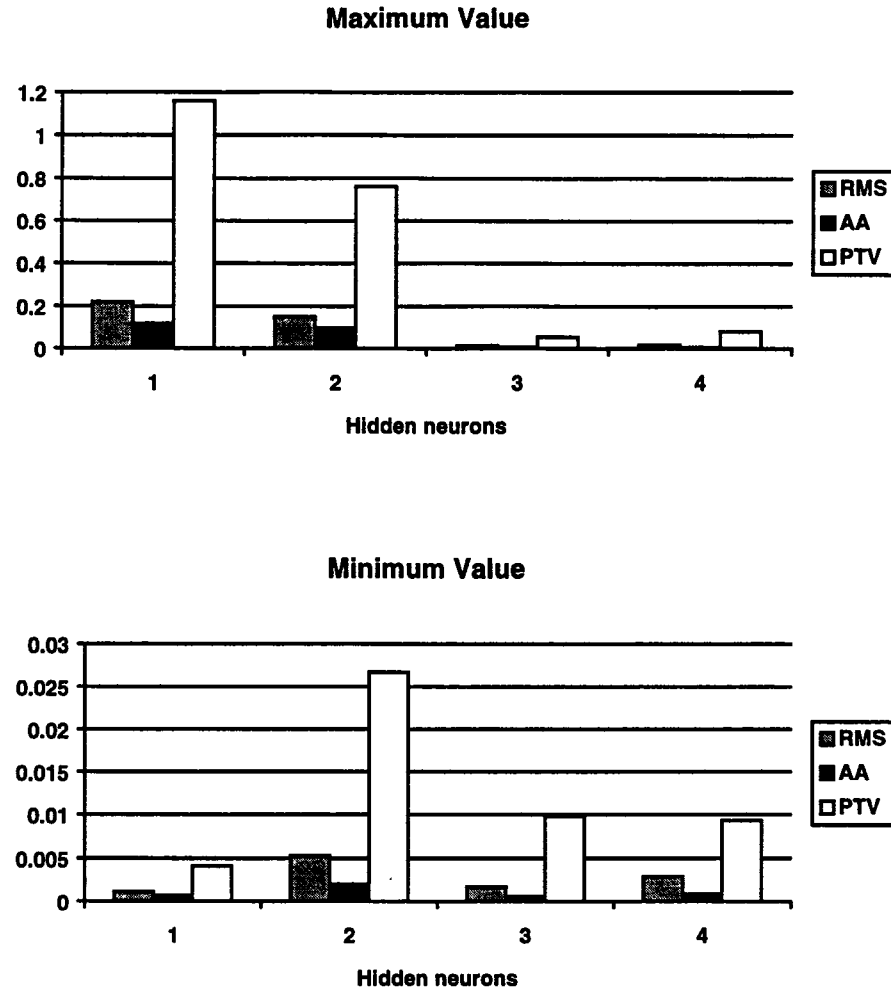


Figure 4.26: Statistical Measures of Validation Error for Medium Case

In order to select the best model, a criterion that balances model fit and the number of weight parameters is needed. As a result, the Akaike's information criterion (AIC), is used. The AIC criterion is defined by

$$AIC = \min_{\theta} \left( 1 + \frac{2 \text{size}(\theta)}{N} \right) \sum_{k=1}^N e^2(k, \theta) \quad \text{Eq. 4.29}$$

where  $e$  is the validation error.

The AIC is calculated for the ten samples of the Low case. The results are tabulated in Table 4.14. For the Medium case, the results are tabulated in Table 4.15.

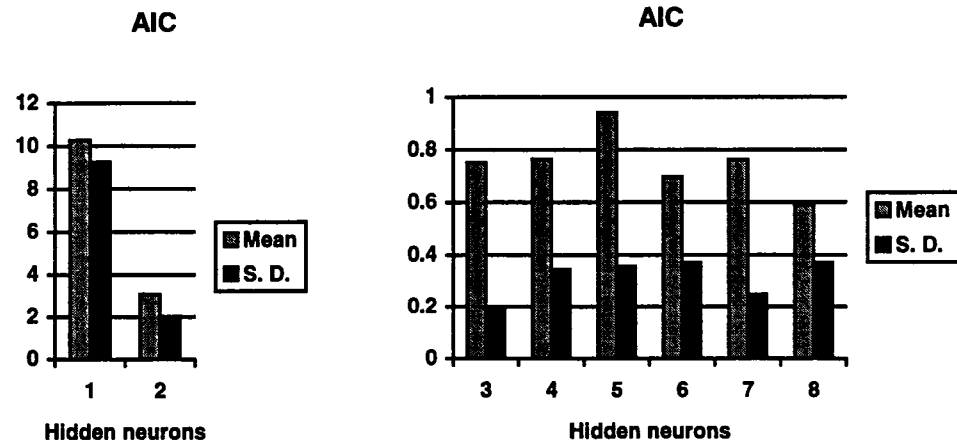
Table 4.14: AIC Values for Low Case.

$\lambda=1$	$\lambda=2$	$\lambda=3$	$\lambda=4$	$\lambda=5$	$\lambda=6$	$\lambda=7$	$\lambda=8$
10.7824	2.3406	0.7345	0.4345	1.6802	0.8904	0.9111	0.8004
3.2992	4.7479	0.9395	0.8577	0.8777	0.8883	0.9565	0.5162
0.8712	0.2277	0.8383	0.7774	0.7035	0.8510	0.7123	0.1223
0.1467	4.2020	0.6181	1.2771	0.9041	0.6003	0.5657	0.0095
5.6866	4.7707	0.5432	0.0626	1.4384	0.2328	0.9023	0.8003
12.1832	1.3143	0.5829	0.7691	0.8485	0.3280	1.0028	0.9692
4.2150	1.8659	0.7532	0.5857	0.7051	1.2991	0.3212	0.9389
15.7366	0.7722	1.1323	1.1342	0.4901	0.1129	0.4118	0.6814
22.5003	4.4175	0.8376	0.8849	0.9132	0.9095	0.9736	0.1306
27.2980	6.1510	0.5359	0.8604	0.8365	0.8503	0.8735	0.9188

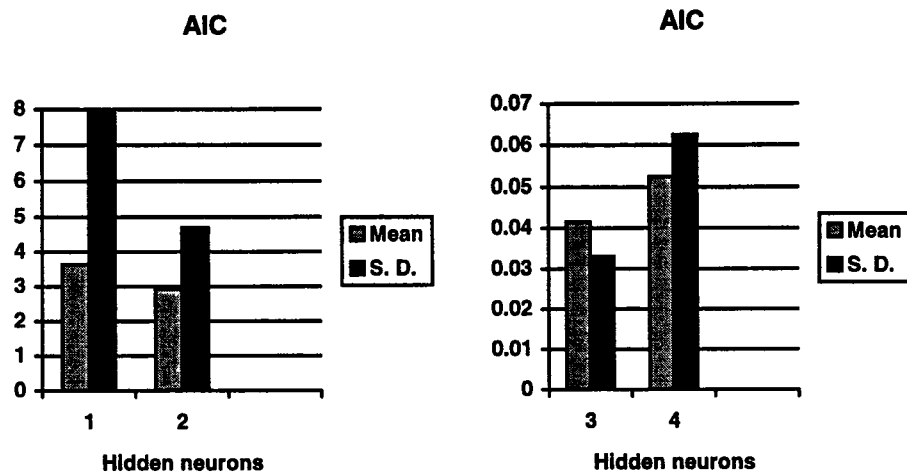
Table 4.15: AIC Values for Medium Case.

$\lambda=1$	$\lambda=2$	$\lambda=3$	$\lambda=4$
0.0076	2.0327	0.0470	0.0268
3.7683	0.0283	0.0517	0.2023
0.0006	0.0586	0.1025	0.0075
2.9268	1.4427	0.0174	0.0057
1.2957	0.0161	0.0826	0.0409
2.2317	0.0717	0.0126	0.0705
0.0181	13.1192	0.0462	0.1105
0.3212	2.4552	0.0017	0.0074
25.7523	9.9665	0.0473	0.0091
0.6600	0.0959	0.0066	0.0437

The mean and standard deviation of the AIC values of the ten samples for both cases are shown in Figure 4.27.



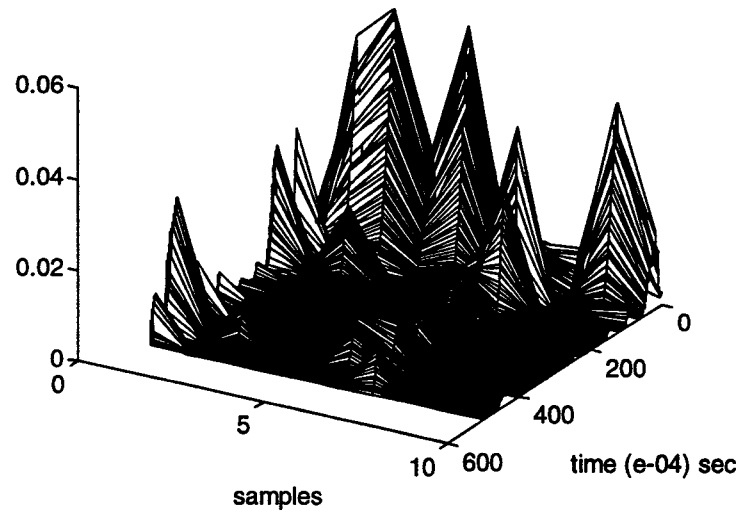
a) Low Case



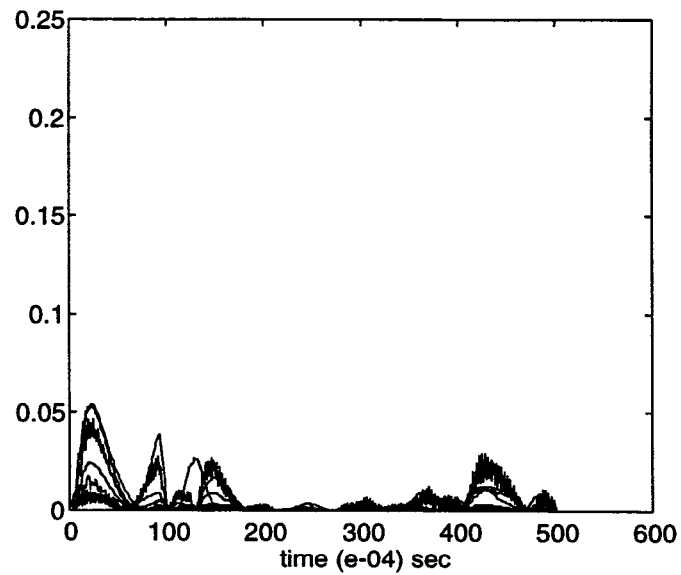
b) Medium Case

Figure 4.27: Statistical Measures of AIC

For the same total number of weight parameters of 60, the Medium case with 3 hidden neurons yields much better performance than the Low case with 6 neurons. The discrepancy occurs mainly at the initial time as shown in Figure 4.28 and Figure 4.29.

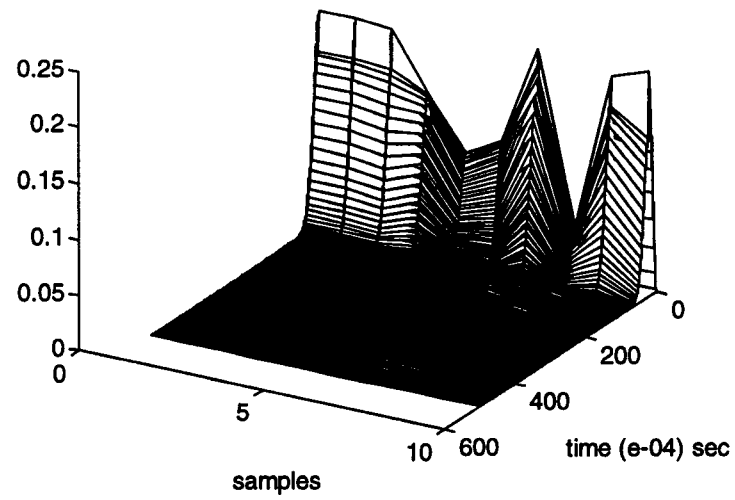


a) Validation Error

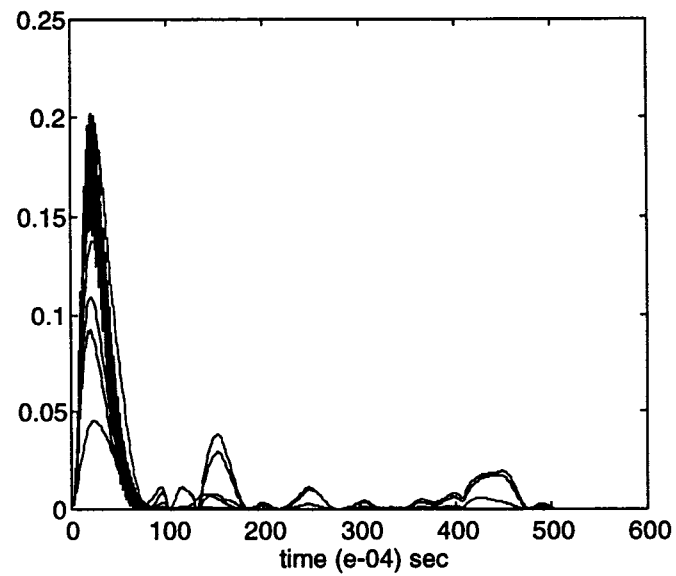


b) Projection on x-z Plane

Figure 4.28: Validation Error for Medium Case with 3 Hidden Neurons



a) Validation Error



b) Projection on x-z Plane

Figure 4.29: Validation Error for Low Case with 6 Hidden Neurons

From the results shown in Figures above, the Medium case with 3 hidden neurons outperforms the other neuron structures. The Medium case is further analyzed in the next experimental design, before reaching a conclusion on the emulator selection.

#### 4.5.1.6 Design of Experiment II

Here, the effect of delay variation among the input taps and recurrent taps is investigated. The nonrecurrent network represents the case where the recurrent tap is zero. To make the comparisons possible between the different structures, the input layer is maintained to have 18 neurons as before. The levels listed in Table 4.16 are designed for recurrent NN models in such a way that the total input neurons is equal to 18.

Table 4.16: Input Neurons

Level	Number of Neurons
Low [L]	6
Medium [M]	9
High [H]	12

Accordingly, the study cases listed in Table 4.17 are derived to study the effect of the forward taps and backward taps on system performance of the recurrent network.

Table 4.17: Study Cases

Cases	forward tap	backward tap
lh-RN	<b>L</b>	<b>H</b>
hl-RN	<b>H</b>	<b>L</b>
mm-RN	<b>M</b>	<b>M</b>



The case corresponding to the nonrecurrent network is given with 18 forward taps and zero backward tap represented by TDNN. The five levels corresponding to the number of hidden neurons determine the total number of weight elements in the emulator structure as shown in Table 4.18. Accordingly, the weight structure for the four cases is maintained constant at multiples of 20.

Table 4.18: Weight Structure

$\lambda$	Weight Elements
1	20
2	40
3	60
4	80

In order to study the learning curve of each treatment combination for each level of hidden neuron, a sample of twenty simulations was considered since each training is started , with a random weight values between  $[-1, 1]$  as before. Data collected over 1 second at a sampling frequency of 10 kHz is used for the analysis.

#### 4.5.1.7 Results and Analysis II

While the performance index of the recurrent networks at the steady state is less than 1, which is in the same order of the linear network discussed, the TDNN case has the order of 100. In Table 4.19, the meanstandard deviation, maximum and minimum values of the steady state error for the twenty samples of a TDNN neural structure are listed.

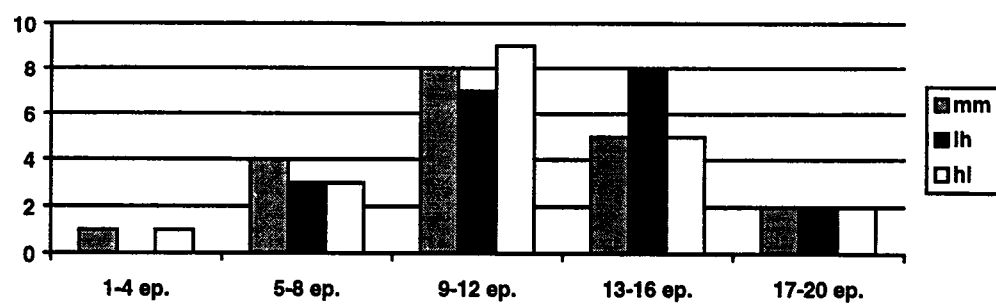
Table 4.19 Statistical Measures of Steady State Modeling Error

	$\lambda=1$	$\lambda=2$	$\lambda=3$	$\lambda=4$
Mean	127.7539	98.0132	96.4429	92.9822
S.D.	109.7069	3.5218	0.8389	22.9974
Max.	591.1292	109.4338	99.156	127.5784
Min	96.4142	96.0343	95.7002	95.3493

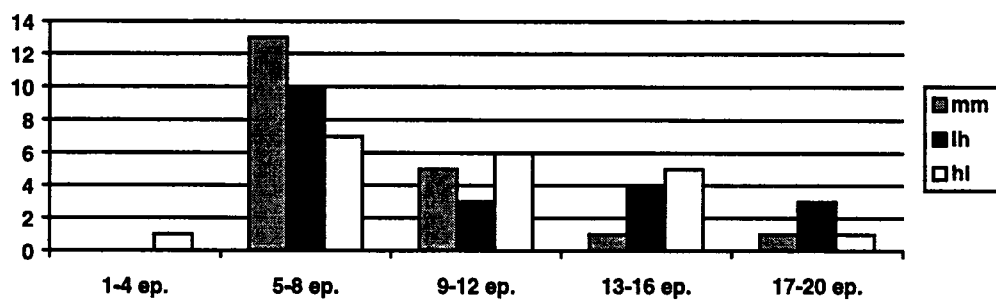
It is evident that the nonlinear nonrecurrent networks does not perform as well if compared to the linear counterpart for the same magnitude of weight parameters. Therefore, in the rest of discussion, we will focus on the recurrent networks.

The first system performance evaluation is the transient response of the modeling process. An error tolerance of 1.0 is used within the steady state regions of all the cases to mark the transient response. Such an error tolerance is also used as the criterion to determine the settling time . The number of maximum epochs, or the settling time, required to attain this bench mark is what determines the transient response of the modeling process. The histogram characterizing the settling time for the modeling error is shown in Figure 4.30. This histogram is useful in determining the maximum number of epochs to set in training the network for the specified error tolerance.

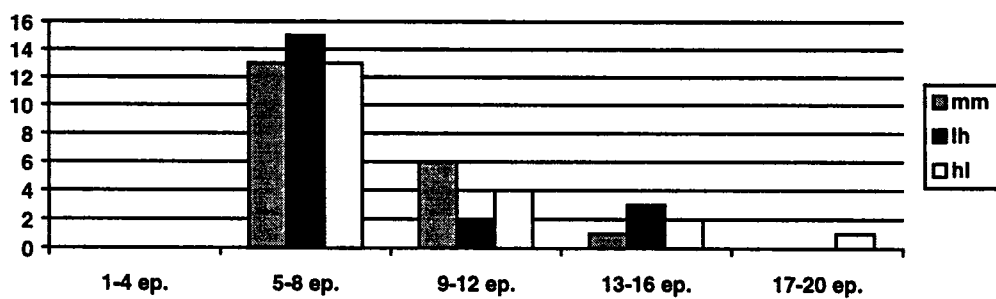
hidden neuron = 1



hidden neuron = 2



hidden neuron = 3



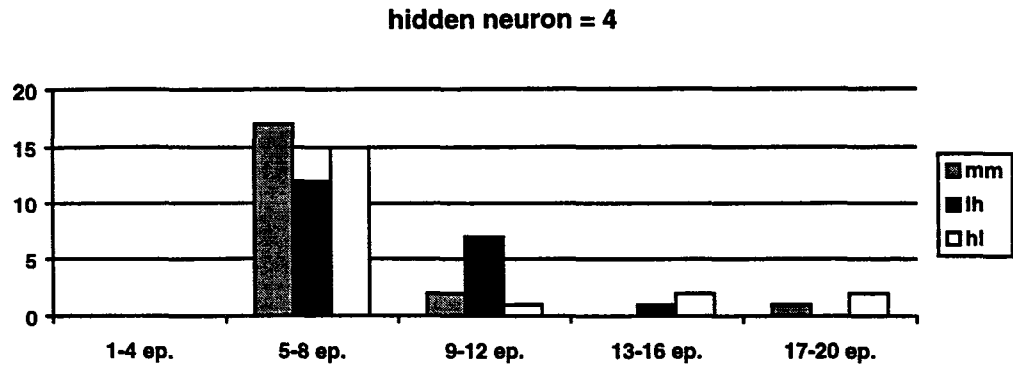


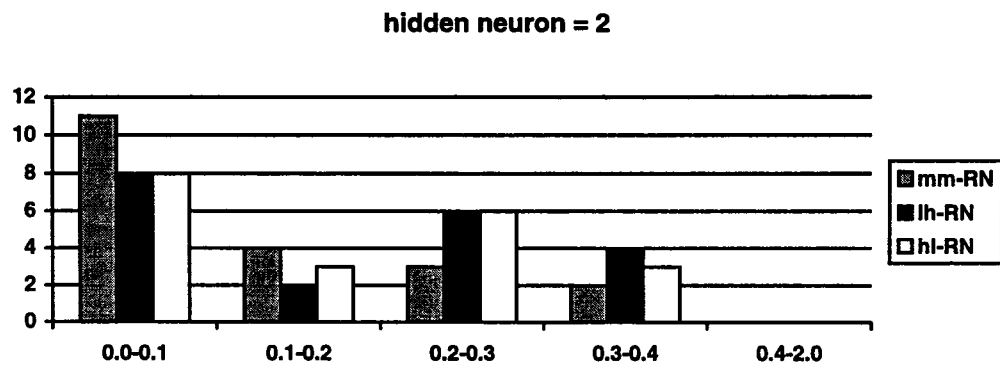
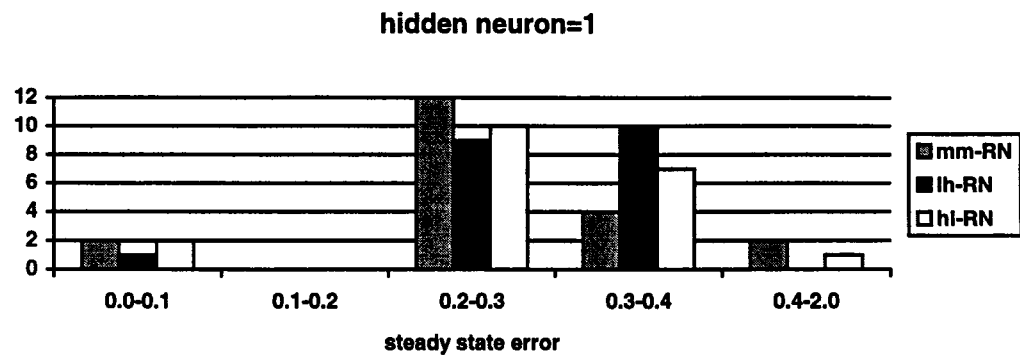
Figure 4. 30: Histogram of Settling Time Parameter

The statistical parameters of the settling time of the modeling error of the twenty samples are given in Table 4.20. The listed values are at different hidden neurons for the three cases.

Table 4. 20: Settling Time Parameter

		$\lambda=1$	$\lambda=2$	$\lambda=3$	$\lambda=4$
mm-RN	Mean	11.5	8.6	7.5	7.8
	S. D.	3.7	3.7	2.3	2.7
	Max.	19	20	14	18
	Min.	6	5	5	6
lh-RN	Not achieved	once	-	-	-
	Mean	12.6	10.6	8.1	8.1
	S. D.	3.4	4.5	2.6	1.9
	Max.	17	20	14	13
hl-RN	Min.	5	5	5	5
	Not achieved	-	-	-	-
	Mean	11.9	10.6	8.6	9.2
	S. D.	3.1	4.0	3.3	3.8
hl-RN	Max.	17	17	17	17
	Min.	6	4	5	7
	Not achieved	-	-	-	-

The characterization parameters of the modeling error at the steady state are calculated next. The steady state modeling error is defined as the modeling errors of the maximum epoch, the 20<sup>th</sup> epoch because all the emulator structures reach steady state at this point. The histogram of modeling errors for the twenty samples at the steady state is shown in Figure 4.31. This histogram is useful in determining the maximum error tolerance value to set in training the given network.



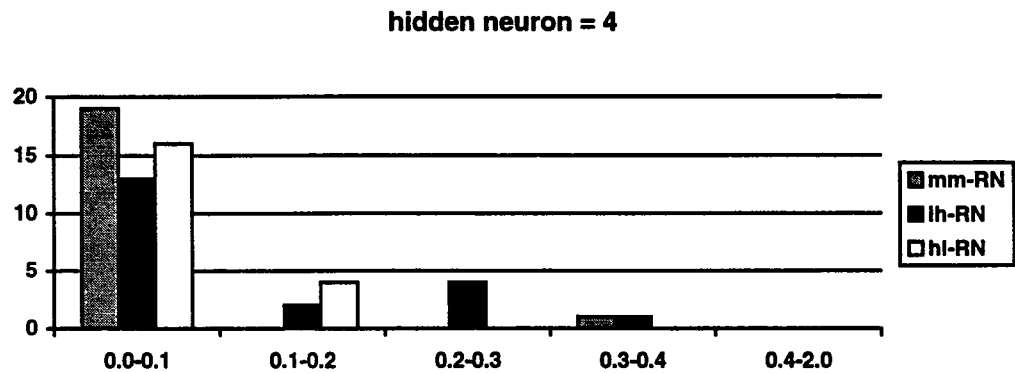
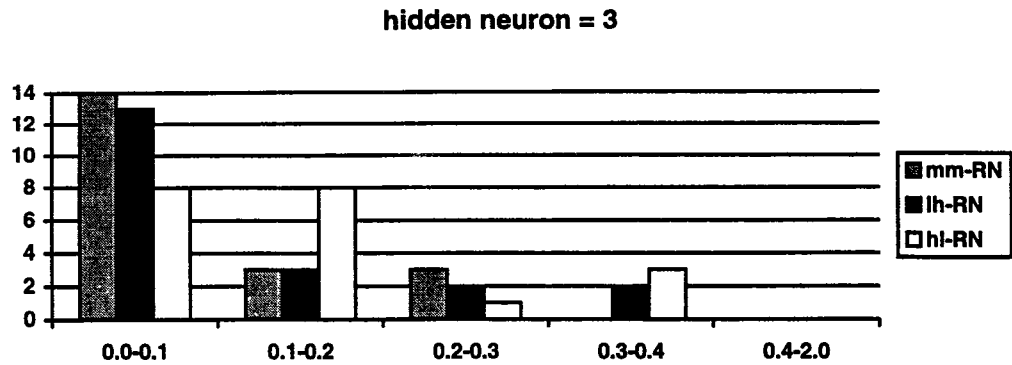


Figure 4. 31: Histogram of Steady State Modeling Error

The statistical measures of the steady state modeling error are listed in Table 4.21. When the number of neurons in a hidden layer is equal to one, data flow has to pass the sole neuron. Consequently, a hidden layer structure with neuron equal to 1 is the poorest in approximating the system. The results indicate, for example, that the steady state error of mm-RN and hl-RN falls below 0.2 for 10% of the samples and that of lh-RN for 5% of the samples. The lh-RN structure gives the lowest mean modeling error with the lowest standard deviation for 1 hidden neuron. It also

consistently gives the lowest maximum modeling error. Additionally, it has been shown that lh-RN yields the highest percentage of samples to attain a steady state modeling error in 0.2 - 0.4 range.

For a hidden layer with two hidden neurons, the steady state modeling error below 0.2 is achieved by a higher percentage of samples. The improvement for mm-RN is from 10% to 75%, for lh-RN is from 5% to 50%, for hl-RN is from 10% to 55%, respectively. That makes the mm-RN achieve the lowest mean value of steady state modeling errors, but with the highest standard deviation. The hl-RN yields the minimum values of mean and standard deviation when compared with lh-RN.

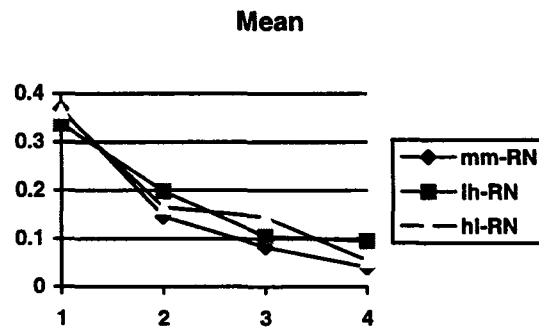
For 3 hidden neurons, mm-RN can achieve a steady state modeling error less than 0.2 for 85% samples. For the same error range, lh-RN can achieve for 80% samples while hl-RN achieves for 80% samples. This time, the mm-RN yields the minimum standard deviation on top of the minimum mean modeling error. It also produces the minimum maximum modeling error.

For 4 hidden neurons, the percent of samples that attain less than 0.2 steady state modeling error improves for mm-RN to 95%, for lh-RN to 75%, and for hl-RN to 100%. Although the mean error is further reduced for mm-RN, the standard deviation is increased when the hidden neuron increases from 3 to 4.

Table 4. 21: Steady State Modeling Error

		$\lambda=1$	$\lambda=2$	$\lambda=3$	$\lambda=4$
<b>mm-RN</b>	Mean	.3686	.1458	.0825	.0402
	S.D.	.4197	.1735	.0865	.0989
	Max	1.9901	.6766	.2553	.457
	Min	.0082	.0082	.0092	.0082
<b>lh-RN</b>	Mean	.3376	.1978	.1047	.0948
	S.D.	.1341	.1625	.1253	.1136
	Max	.6461	.5901	.3688	.3292
	Min.	.0512	.0082	.0085	.0085
<b>hl-RN</b>	Mean	.3634	.1647	.1444	.0551
	S.D.	.359	.134	.1195	.0643
	Max.	1.8298	.4047	.4172	.1815
	Min.	.0531	.0082	.0084	.0082

The plots of the statistical measures of the steady state modeling error for each hidden neuron are given in Figure 4.32. The standard deviation, maximum value, and minimum value all settle at about the second hidden neuron for the three cases.





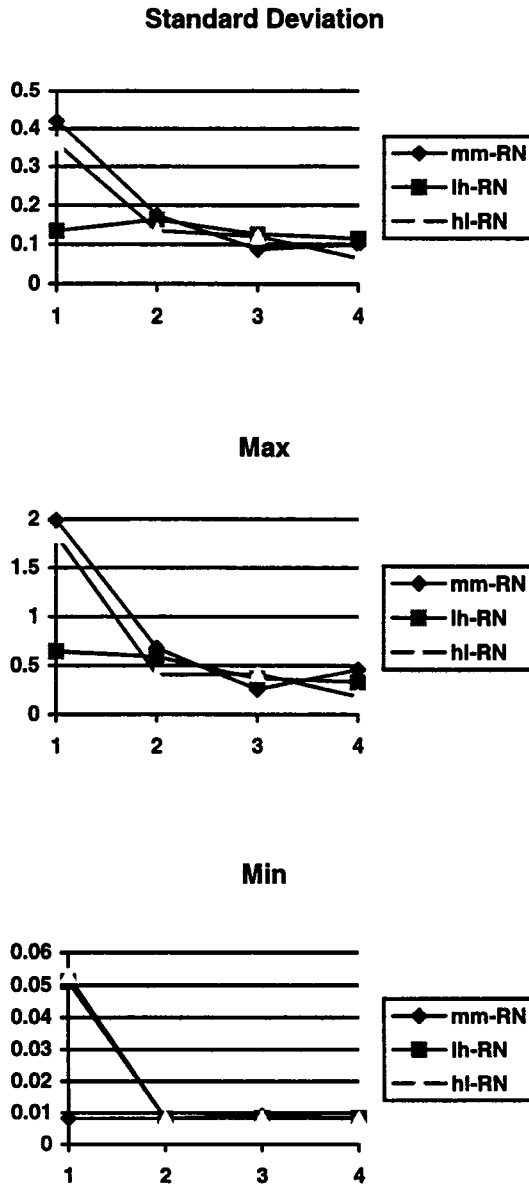


Figure 4. 32: Statistical Measures of Steady State Modeling Error

Once the emulator is modeled, it is used in a different arrangement in the control architecture. The performance of the emulator in this arrangement is characterized by the validation error. In a similar manner to the first design of

experiment, ten best samples that meet the requirement of being bounded below 2 are selected. In Table 4.22, the number of acceptable samples from the twenty samples are listed. Since the mm-RN case is discussed in the first design of experiment, it is not repeated here.

Table 4.22: Acceptable Samples

Cases	Hidden Neurons	Accepted # of samples
lh-RN	1	13
	2	11
	3	13
	4	13
hl-RN	1	16
	2	16
	3	18
	4	8

The RMS, PTV, and AA for the best ten of the twenty samples of hl-RN case are listed in Table 4.23 and those for the lh-RN case are listed in Table 4.24. Only hl-RN case with 4 hidden neurons fails to meet the challenge, and this case is excluded from analysis.

Table 4.23: Validation Error for hl-RN

Hidden neuron=1			Hidden neuron=2		
RMS	AA	PTV	RMS	AA	PTV
0.0350	0.0229	0.1174	0.0355	0.0234	0.1246
0.0468	0.0261	0.1903	0.0018	0.0006	0.0081
0.0538	0.0271	0.2319	0.0568	0.0305	0.2416
0.0197	0.0108	0.0762	0.0644	0.0367	0.2651
0.0477	0.0271	0.1938	0.0128	0.0061	0.0564
0.0483	0.0289	0.1940	0.0222	0.0131	0.0870
0.0804	0.0596	0.2175	0.0370	0.0238	0.1301
0.0548	0.0325	0.2203	0.0067	0.0046	0.0192
0.0228	0.0142	0.0865	0.0158	0.0048	0.0754
0.0322	0.0189	0.1287	0.0309	0.0122	0.1365

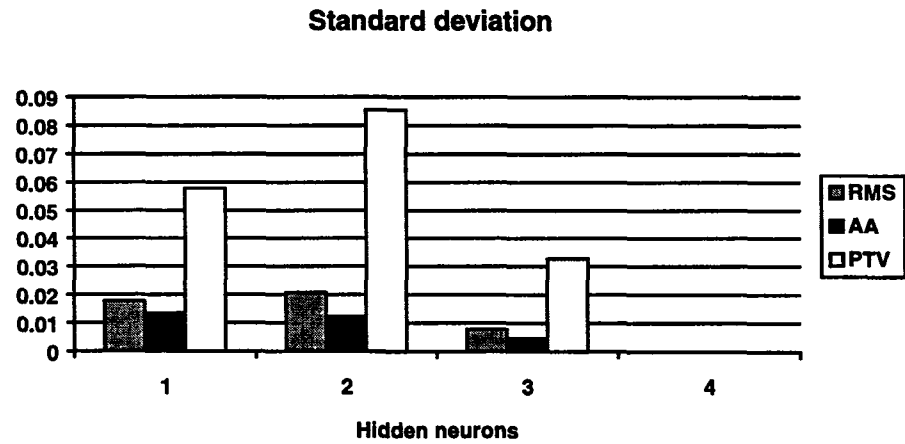
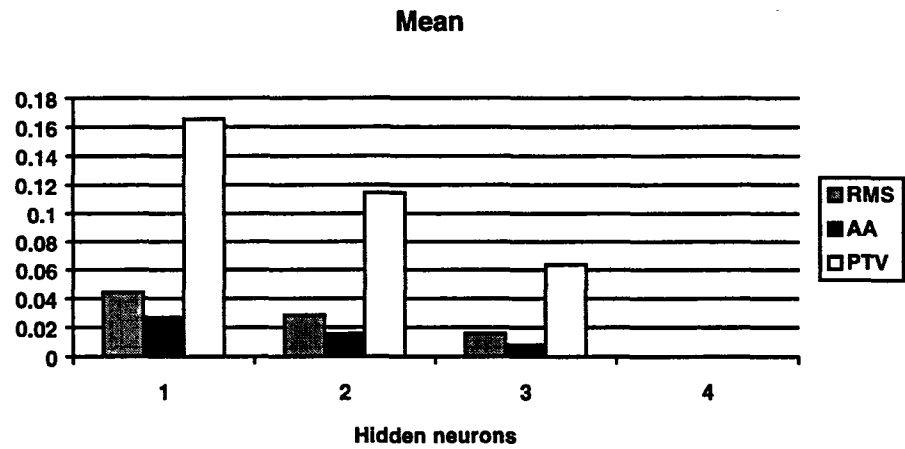
Hidden neuron=3		
RMS	AA	PTV
0.0140	0.0065	0.0708
0.0094	0.0028	0.0469
0.0154	0.0071	0.0657
0.0197	0.0137	0.0486
0.0072	0.0025	0.0349
0.0309	0.0164	0.1262
0.0248	0.0077	0.1136
0.0092	0.0062	0.0285
0.0081	0.0040	0.0391
0.0185	0.0124	0.0633

Table 4.24: Validation Error for lh-RN

Hidden neuron=1			Hidden neuron=2		
RMS	AA	PTV	RMS	AA	PTV
0.0343	0.0134	0.1358	0.0148	0.0253	0.0517
0.0212	0.0134	0.0782	0.0408	0.0253	0.1601
0.0547	0.0318	0.2215	0.0232	0.0139	0.0882
0.0345	0.0213	0.1349	0.0241	0.0143	0.0912
0.0771	0.0484	0.3012	0.0147	0.0075	0.0685
0.0626	0.0343	0.2597	0.0575	0.0339	0.2297
0.0444	0.0256	0.1791	0.0288	0.0131	0.1299
0.0381	0.0224	0.1497	0.0154	0.0093	0.0477
0.0807	0.0556	0.2828	0.0220	0.0115	0.0895
0.0205	0.0124	0.0757	0.0256	0.0153	0.0977

Hidden neuron=3			Hidden neuron=4		
RMS	AA	PTV	RMS	AA	PTV
0.0256	0.0084	0.1155	0.0154	0.0053	0.0705
0.0156	0.0050	0.0750	0.0233	0.0159	0.0787
0.0277	0.0153	0.0853	0.0307	0.0093	0.1443
0.0300	0.0106	0.1349	0.0096	0.0030	0.0446
0.0256	0.0084	0.1155	0.0312	0.0175	0.1116
0.0156	0.0050	0.0750	0.0252	0.0111	0.1293
0.0277	0.0153	0.0853	0.0263	0.0085	0.1182
0.0300	0.0106	0.1349	0.0320	0.0106	0.1438
0.0026	0.0016	0.0145	0.0079	0.0025	0.0406
0.0253	0.0162	0.0776	0.0124	0.0041	0.0587

The statistical measures are evaluated for the samples. The plots for hl-RN and lh-RN cases are shown in Figure 4.33 and Figure 4.34, respectively. The values for mm-RN cases are discussed before, and hence, they are not repeated here.



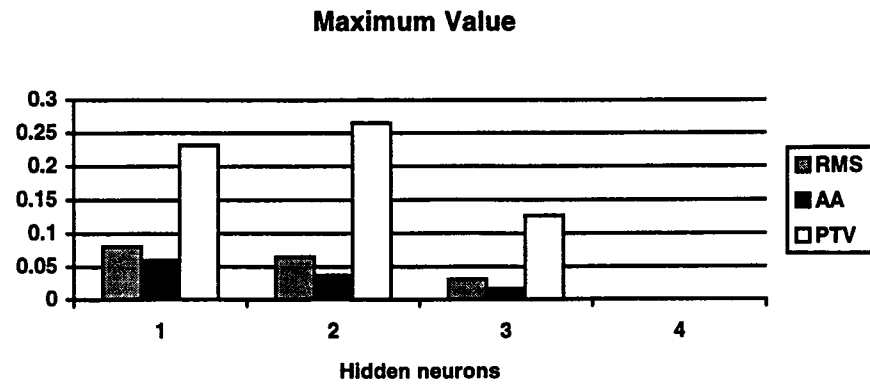
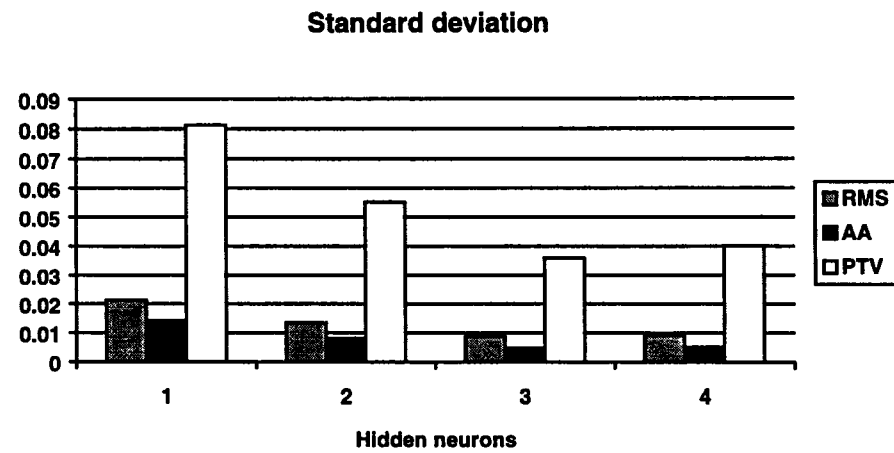
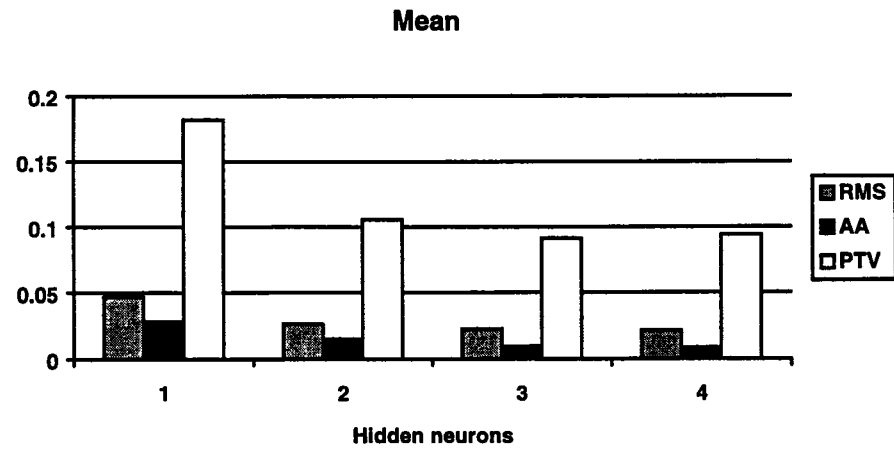


Figure 4.33: Statistical Measures of Validation Error for hl-RN



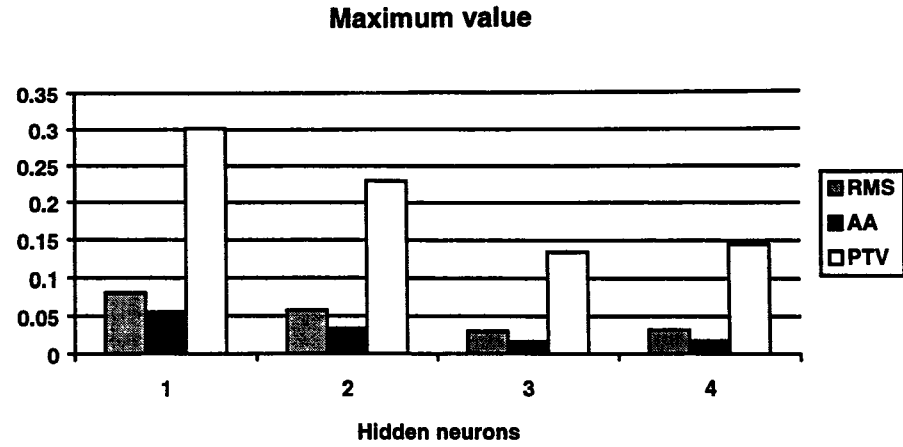


Figure 4.34: Statistical Measures of Validation Error for lh-RN

In order to be able to decide on the neural architecture of the emulator, Akaike's information criterion *AIC* is used. The *AIC* values for the hl-RN case are listed in Table 4.25 and those of the lh-RN case are listed in Table 4.26. The statistical measures of *AIC* are listed in Figure 4.27

Table 4.25: *AIC* Values for hl-RN

$\lambda=1$	$\lambda=2$	$\lambda=3$
0.6642	0.7330	0.1213
1.1837	0.0018	0.0552
1.5649	1.8735	0.1476
0.2110	2.4085	0.2407
1.2299	0.0950	0.0320
1.2634	0.2855	0.5915
3.4985	0.7946	0.3808
1.6271	0.0259	0.0530
0.2816	0.1455	0.0406
0.5626	0.5534	0.2134

Table 4.26: AIC Values for lh-RN

$\lambda=1$	$\lambda=2$	$\lambda=3$	$\lambda=4$
0.6383	0.1267	0.4076	0.1573
0.2435	0.9654	0.1506	0.3599
1.6164	0.3133	0.4760	0.6210
0.6454	0.3365	0.5590	0.0608
3.2188	0.1263	0.4076	0.6434
2.1229	1.9201	0.1506	0.4203
1.0675	0.4823	0.4760	0.4562
0.7843	0.1371	0.5590	0.6751
3.5257	0.2824	0.0041	0.0415
0.2267	0.3797	0.3987	0.1023

Table 4.27: Statistical Measures of AIC

Cases	Mean	S.D.	Max.	Min.
lh-RN				
$\lambda=1$	1.40089	1.1902	3.5257	0.2267
$\lambda=2$	0.5070	0.5545	1.9201	0.1263
$\lambda=3$	0.3589	0.1905	0.5590	0.0041
$\lambda=4$	0.3538	0.2491	0.6751	0.0415
hl-RN				
$\lambda=1$	1.2087	0.9497	3.4985	0.2110
$\lambda=2$	0.6917	0.8242	2.4085	0.0018
$\lambda=3$	0.1876	0.1799	0.5915	0.0320

The mean and standard deviation of the AIC are shown in Figure 4.35.

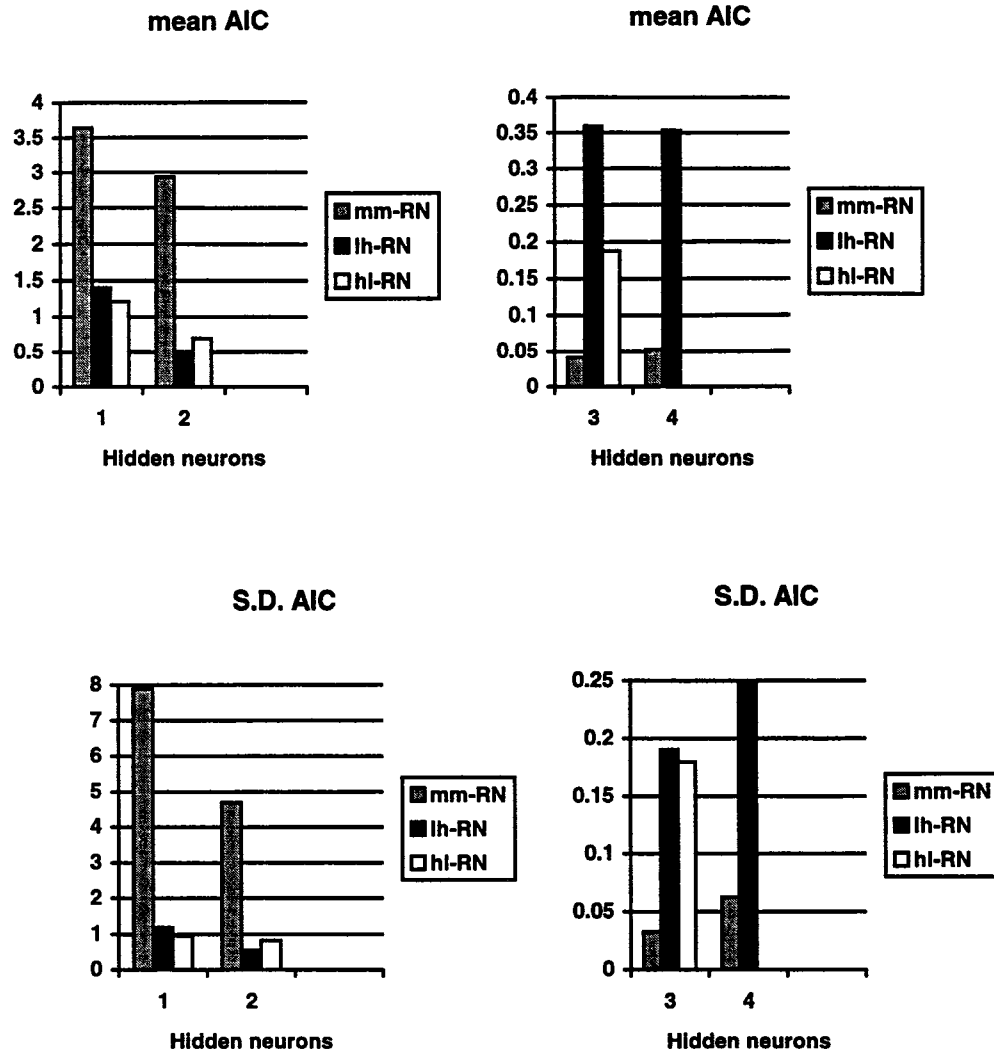


Figure 4.35: Statistical Measures of AIC

From Figure 4.35, it is clear that both the lh-RN and hl-RN cases perform better for number of hidden neurons equal to 1 and 2. When the number of hidden neuron is increased to 3 and 4, the mm-RN case performs much better than the other two neural structures. In the previous analysis, the mm-RN case is found to be the best. In this second analysis, it is confirmed that an even split of feedforward taps and



backward taps at the middle level with three hidden neuron is the best candidate for emulator. Moreover, the general structure of the controller is set as an mm-RN case. From the discussed analysis, it is apparent that statistical measures of AIC based on validation error gives more insight into model selection process than any of the previously attempted methods.

#### 4.5.2 Design of Experiment

Like the linear control module, the adaptation schemes developed for emulator cannot be directly used for adaptation of the controller weights. This is because there is a transfer function between the output of wazzu the controller and the performance criteria formulated as the square of the error at the output of the control mechanism. Therefore, the error is back propagated through the emulator without adapting the weights of the emulator. The back propagated error only alter the weights of the controller.

The emulator used in this study is a mm-RN case with 3 hidden neurons. The controller is assumed to be a mm-RN case with the number of hidden neurons varying between 1 and 4. Here a 0.05 second time period is used to train the controller off-line. Then the controller is used to perform tool vibration cancellation for a long period of time to test stability. The controller is trained for a harmonic signal at one of the trial frequencies. When the training period is over, the controller weights are frozen.

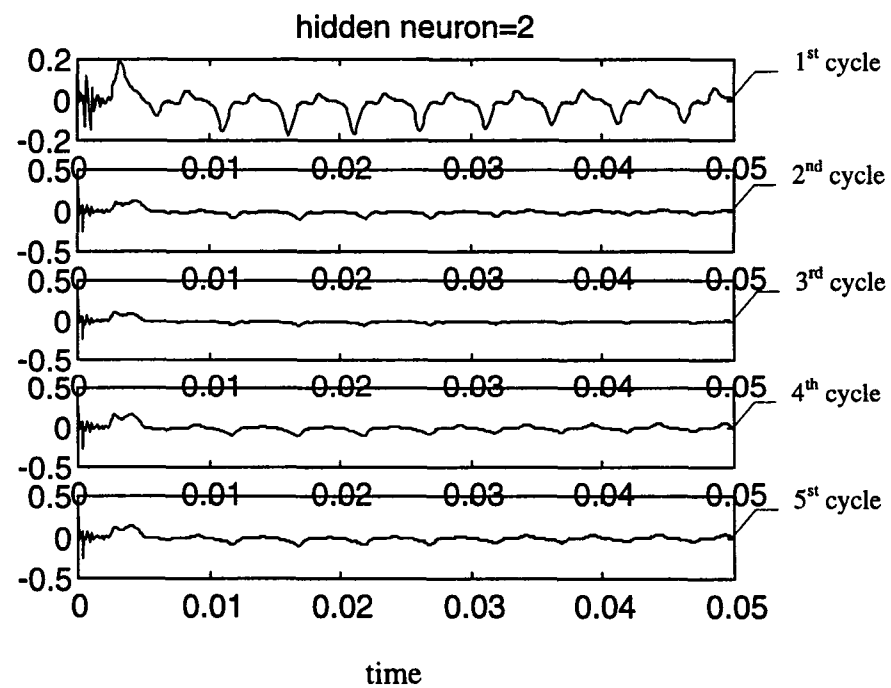
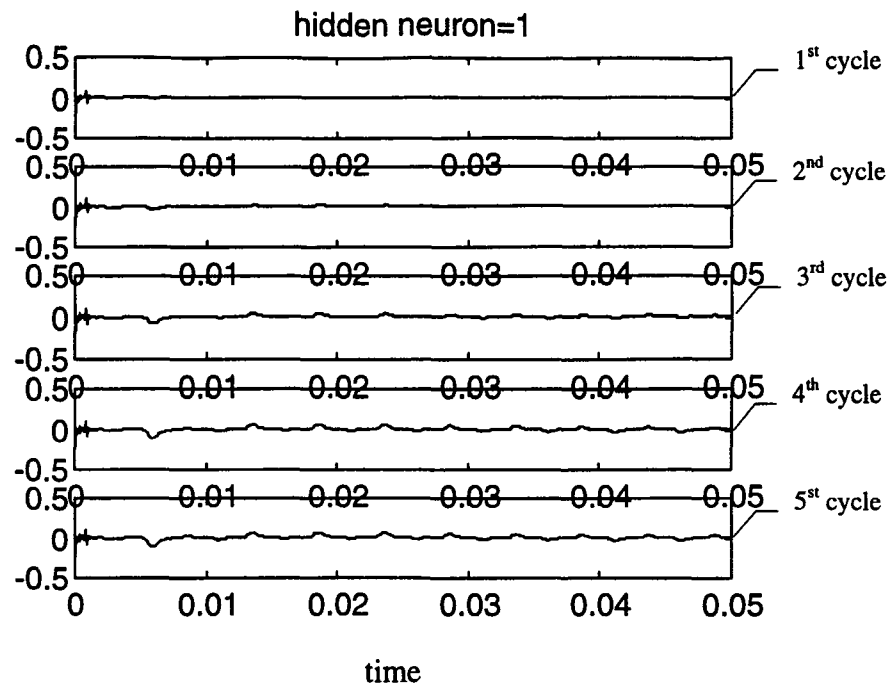
#### 4.5.3 Results and Analysis

The two parameters that need to be studied are the modeling error, and the control error. The modeling error signal is the error of the emulator in emulating the control mechanism. It is found by determining the difference in the outputs of the control mechanism and its emulator. The control error is the tool vibration after the application of the controller. Since the goal of the controller is zero tool vibration, any tool vibration with the controller is termed as the controller error.

##### 1. Modeling Error

The modeling error discussed here is the error of the emulator after it is trained off-line and placed in the control architecture. The modeling error for the five learning cycles for each of the control weight levels is shown in Figure 4.36.

For the control weight level 1, the modeling error remains the same in all the learning cycles. The same can be said for control weight level 2. A significant change appears in the modeling error when the weight structure is increased to level 3. For level 3, the initial two cycles are dominated by a modeling error at high frequency. Afterwards, the high frequency component of the error is limited to the initial period of time. The same condition is observed when the control weight structure is increased to level 4. Therefore, a low-end weight structure gives desirable modeling error characteristics.



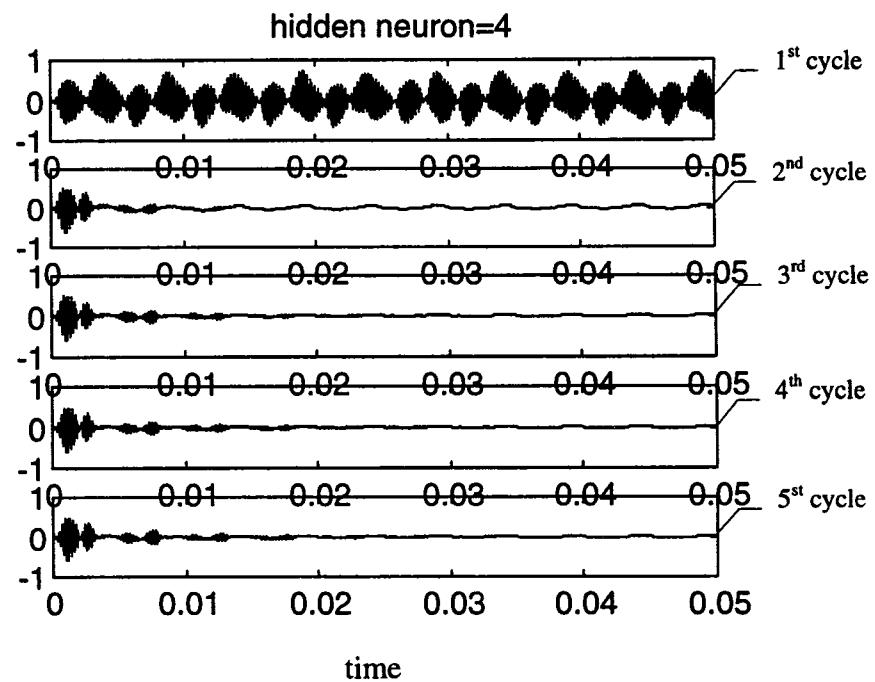
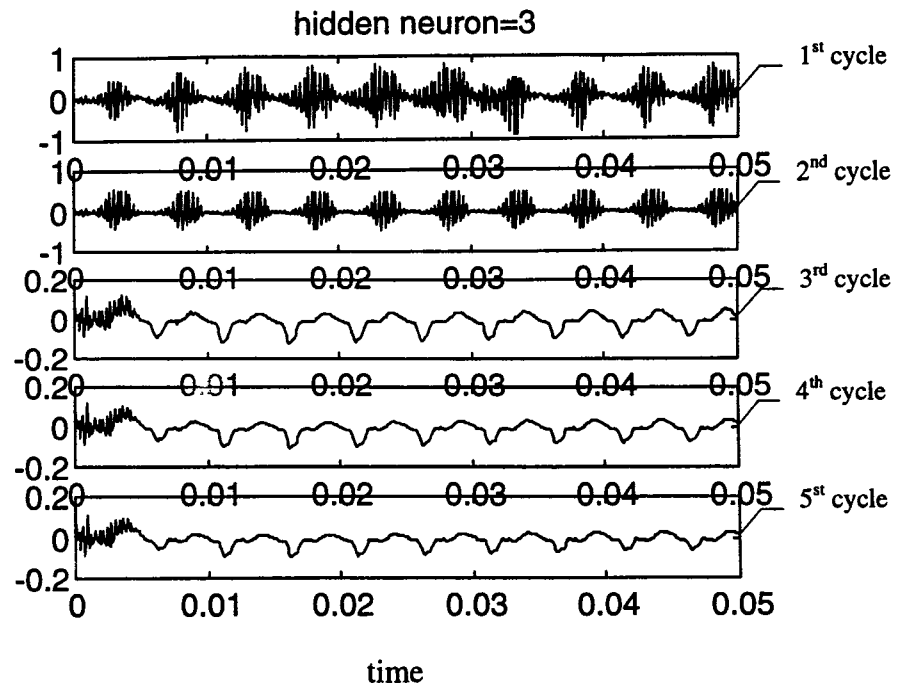
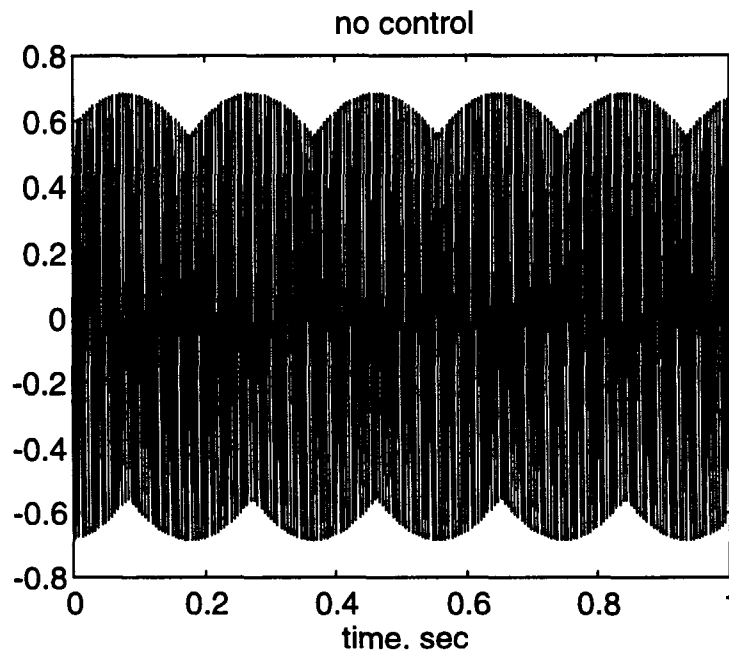
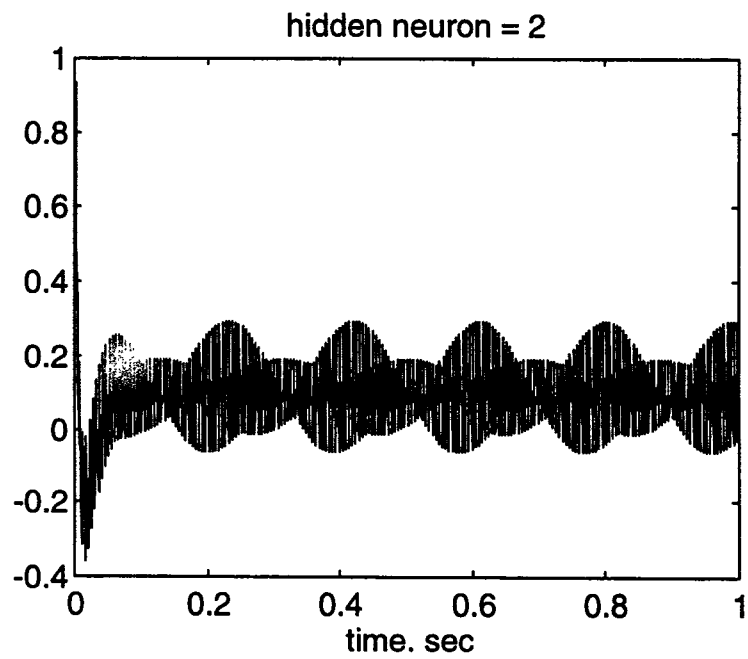
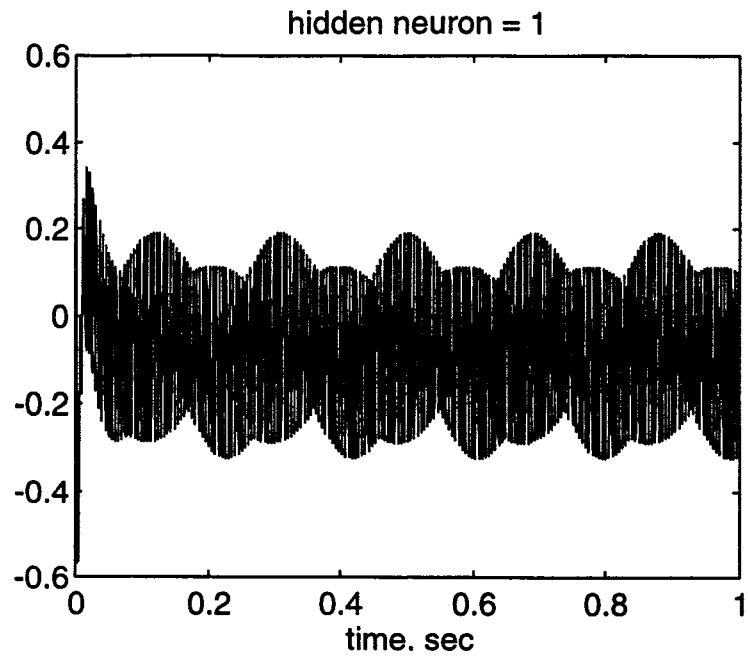


Figure 4.36: Modeling Error

## 2. Control Error.

Finally, the performance of the controller is governed by its ability to attenuate the disturbance. Therefore, the machine tool vibration with and without the controller is studied. After five training cycles for which the modeling error is discussed, the controller weights are frozen. In order to check system stability, the controller is run for one second period of time. First, the tool vibration without the controller is shown in Figure 4.37. Then the control error, the tool vibration with the controller, is shown in Figure 4.37 for the four levels of the controller weight structures. The level of the controller weight structures is governed by the number of hidden neurons.





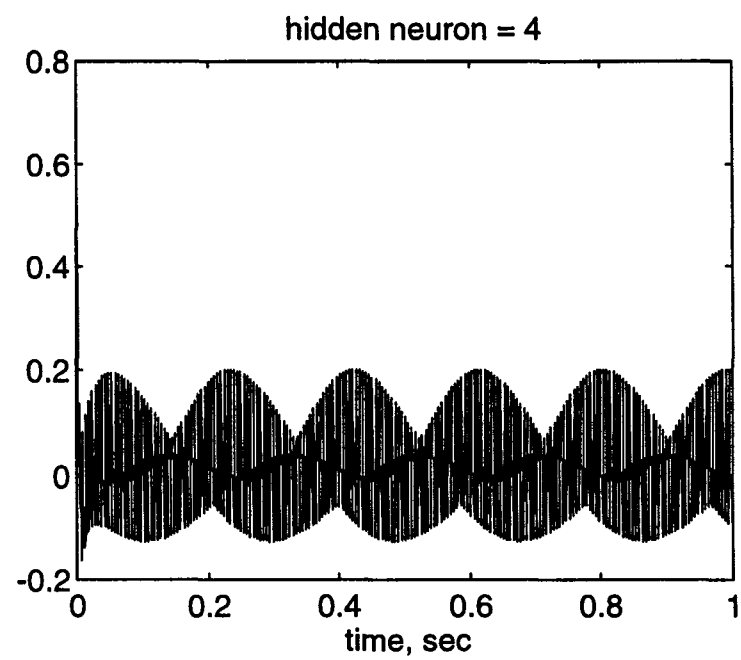
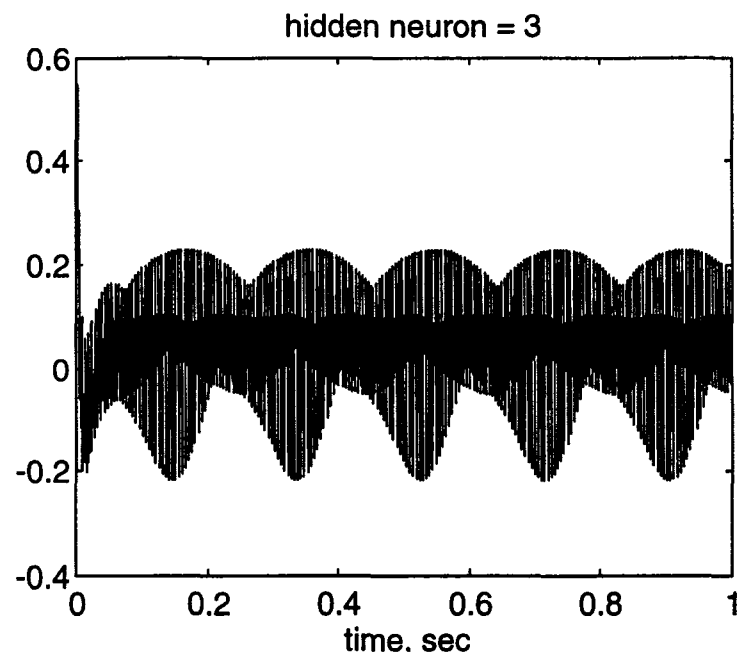


Figure 4.38: Control Error

The second half of the collected data is used to calculate the RMS, PTV, and AA for the five levels of the control weights. The percentage reduction in these performance indices due to the controller is shown in Figure 4.38. As seen in the figures, the percentage reduction improves when the tap length is increased from level 1 to level 2. When the level is further increased, the percentage reduction drops. Further increase in the level of the control weights doesn't improve the performance significantly. Such significant performance is obtained after training the controller over only five cycles.

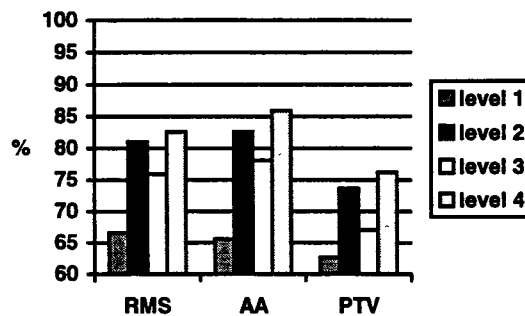


Figure 4.38 Tool Vibration Percent Reduction



## Chapter 5

### EXPERIMENTATION VERIFICATION

#### 5.1 Introduction

The machining system under investigation can be viewed as an integration of four components. These four components are the plant, control mechanism, system disturbance, and controller. Each of these components in turn can be decomposed into two parts. The plant system comprises the cutting process along with the tool post mechanical structure. The control mechanism comprises the PMN actuator along with the tool post mechanical structure. The system disturbance, or the dynamic chip load generation, consists of the nominal chip load and the two feedback paths (the primary and regenerative feedback paths). The controller comprises the sensor and the control circuitry. The block diagram illustrating this system architecture is presented in Figure 5.1.

This system decomposition is devised in order to follow the logic of controller development in this experimentation verification. The verification is performed in two phases. In the first phase, which is the laboratory experimentation, the system disturbance considered is limited to the nominal chip load, with the feedback path being omitted. To resemble the feedback subsystem, which is absent during the laboratory experimentation, a signal representing the dynamic chip load is fed directly

to the plant using a signal generator. Such a case corresponds to tapping in the machining operation. Thus, tool vibration is noted. Then an effort is made to cancel the observed vibration using the control mechanism driven by the controller. The design parameters of the controller are used for the second phase application. In the second phase, the system disturbance is an integral part in the actual machining operation.

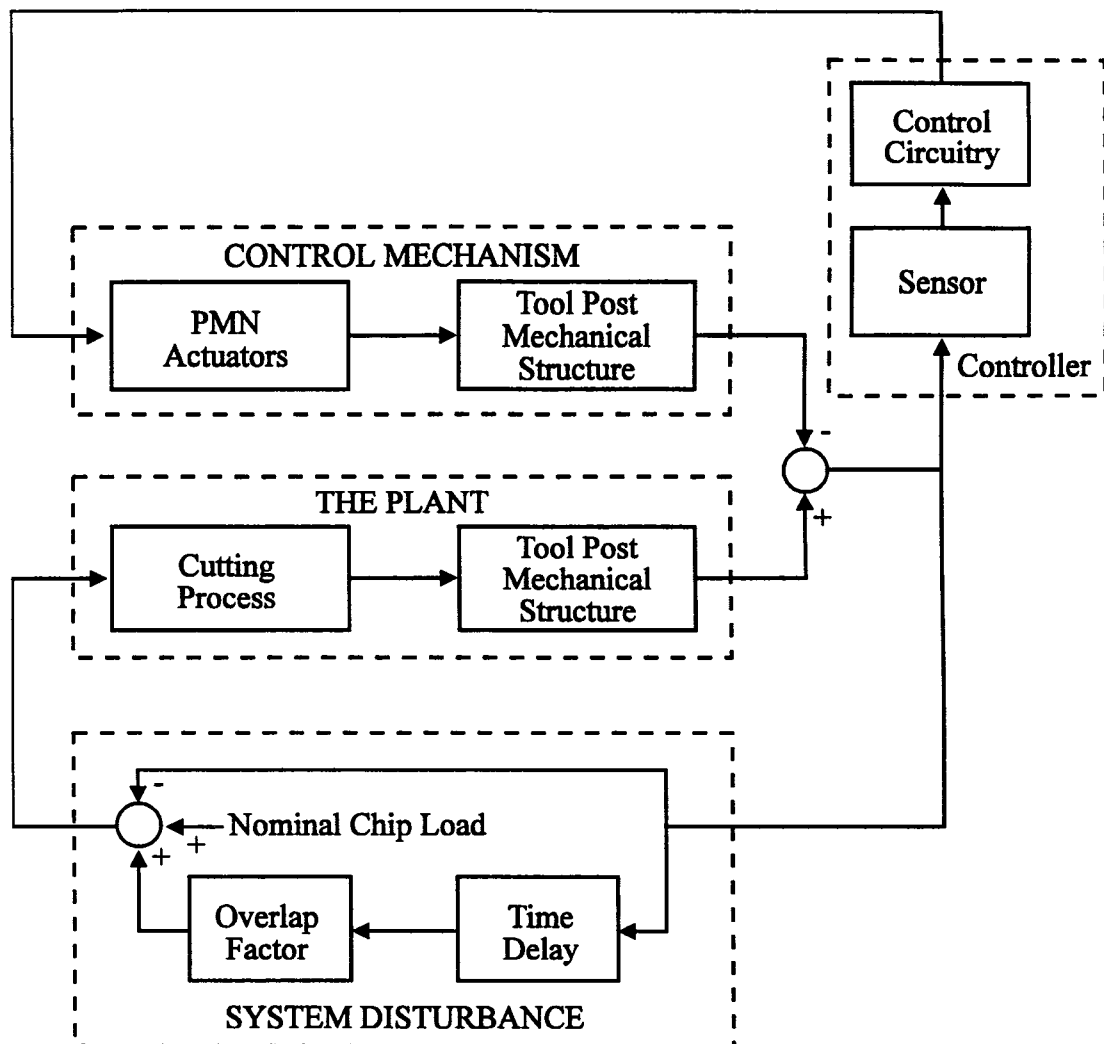


Figure 5.1: Machining Control System

Hardware implementation of the active control system is realized by using digital electronics. The linear neural network control system designed in the computer simulation is implemented in the experiments by using a digital signal processing circuit board.

The control system implementation is composed of several parts. The controller consists of the control filter, adaptive algorithm, and system identification. The interface part includes sample rate selection, input gains and output attenuations. The control schemes part includes feedforward, feedback and hybrid schemes. Sensors and amplifiers make up part of the data collection and conditioning setup. The smart tool post part consists of the mechanical structure and the actuators that make up the control mechanism. The integration shown in Figure 5.2 is used in both laboratory and machine floor experiments. The two phases of experiments will be discussed in detail in the sections to follow.

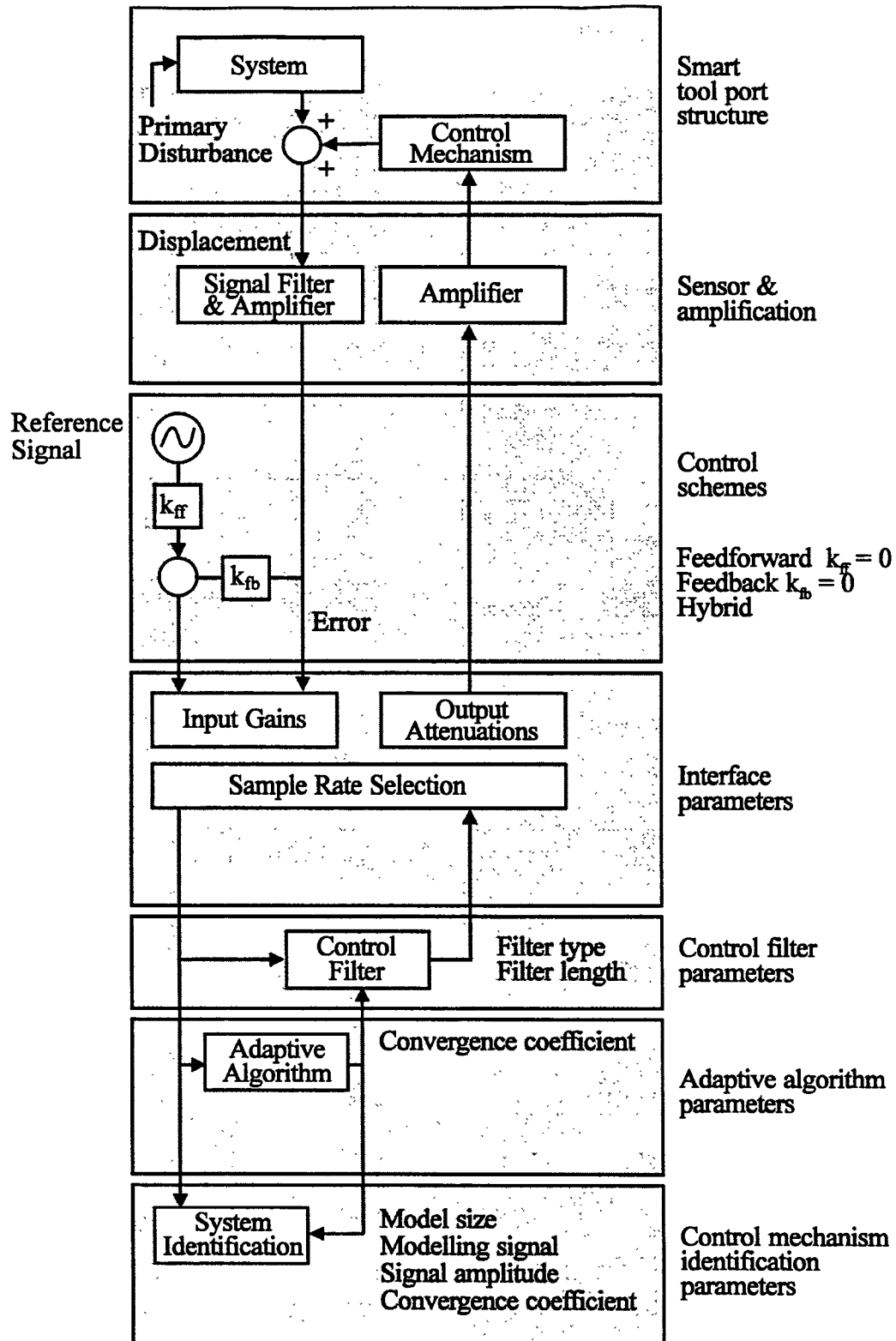


Fig. 5.2: Control System Implementation

## 5.2 Laboratory Experiments

In the first phase, the machine tool vibration compensation is studied in a laboratory environment [Luu, 1996]. There are two main goals to be measuring achieved. First, the performance of the feedforward control system studied through computer simulations is compared with the results obtained from the lab experiments. Second, the design parameters used in the laboratory experiments are validated through the machine shop experiments.

### 5.2.1 Experimental Setup

The cutting force is simulated in the lab using a vibration exciter. In this thesis study, the exciter is a LDS Vibration Generator 400 Series, Model V411. The exciter is used to excite the tool post. In Figure 5.3, the setup with the exciter and tool post is illustrated. The tip of the tool and the exciter are connected in a horizontal plane. Such a setup assures that the force transmitted to and from the tool post is in one direction; that the axial direction only. The exciter is capable of generating a force with magnitude of 97.9 N peak to peak. Therefore, the maximum force that can be generated ranges up to 50 N. To detect the motion of the tool tip during the experiment, a variable impedance transducer, Kaman Smpu-9100 with an output of zero to one volt over a 25.4  $\mu\text{m}$  range, is attached to the tool housing. Therefore, the sensing system is a precision noncontact position system.

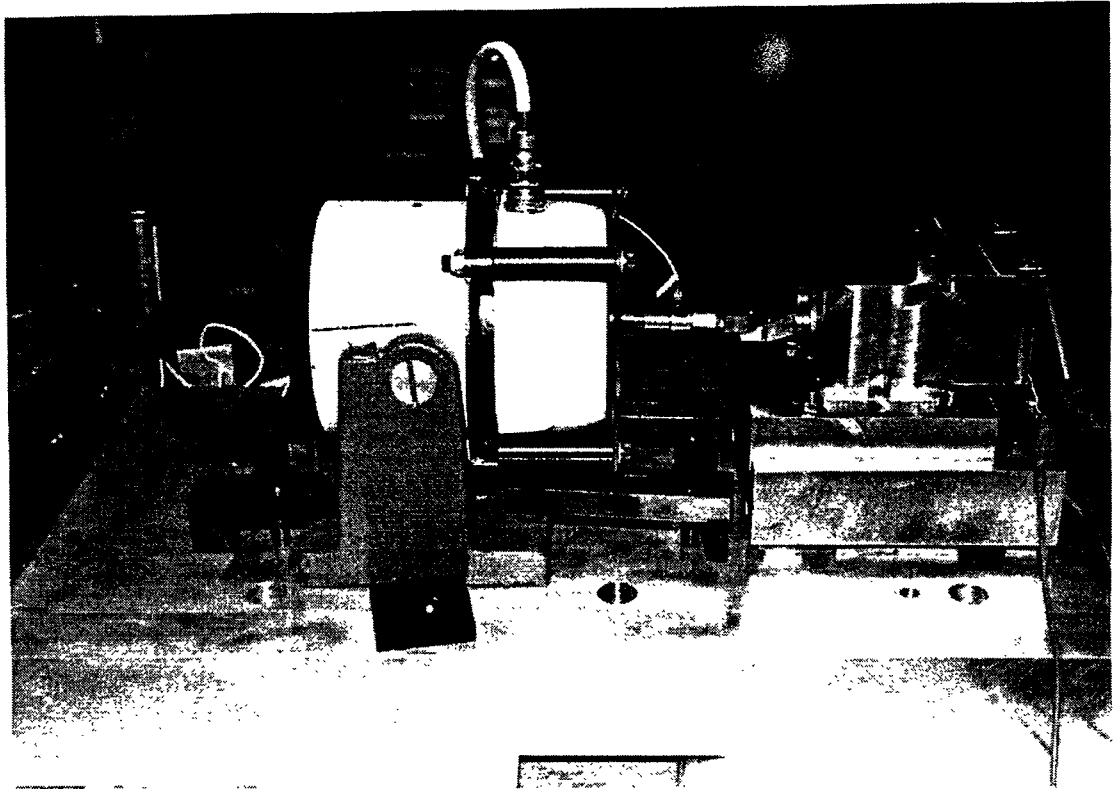


Figure 5.3: Exciter and Tool Post Arrangement

The adaptive control schemes are implemented using a digital electronic hardware called EZ-ANC which is designed specifically for active noise cancellation application. To drive the device, a 600 mA power supply with 12V is attached. The ground is also designed for noise reduction. The inputs to the EZ-ANC board are analog signals, including the reference and error signals. The output from the EZ-ANC board is an analog control signal. The EZ-ANC has PCB-mounted BNC sockets arranged so that all inputs are on one side of the PCB, and all the outputs on the other side. The power, serial, and analog signal connections are shown in Figure 5.4.

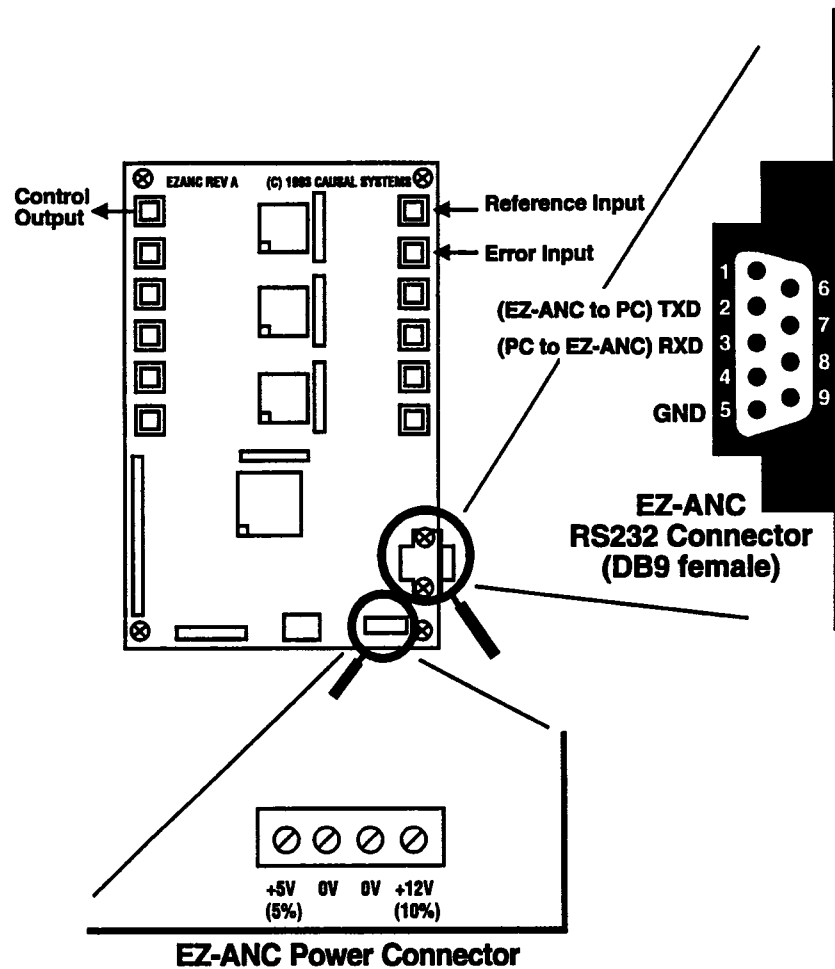


Figure 5.4: EZ-ANC Power, Serial, and Analog Signal Connections

The communication protocol between EZ-ANC and its host computer uses ASCII characters, VT100 escape sequences for text, and TEK4010 escape sequences for graphics. Communication is handled through a software tool called Kermit which can emulate both VT100 and TEK4010. The disturbance signal is produced by using LabVIEW. A HP signal analyzer is used to analyze the signal in the time and

frequency domains. In Figure 5.5, a picture depicting the whole experimental setup is shown.

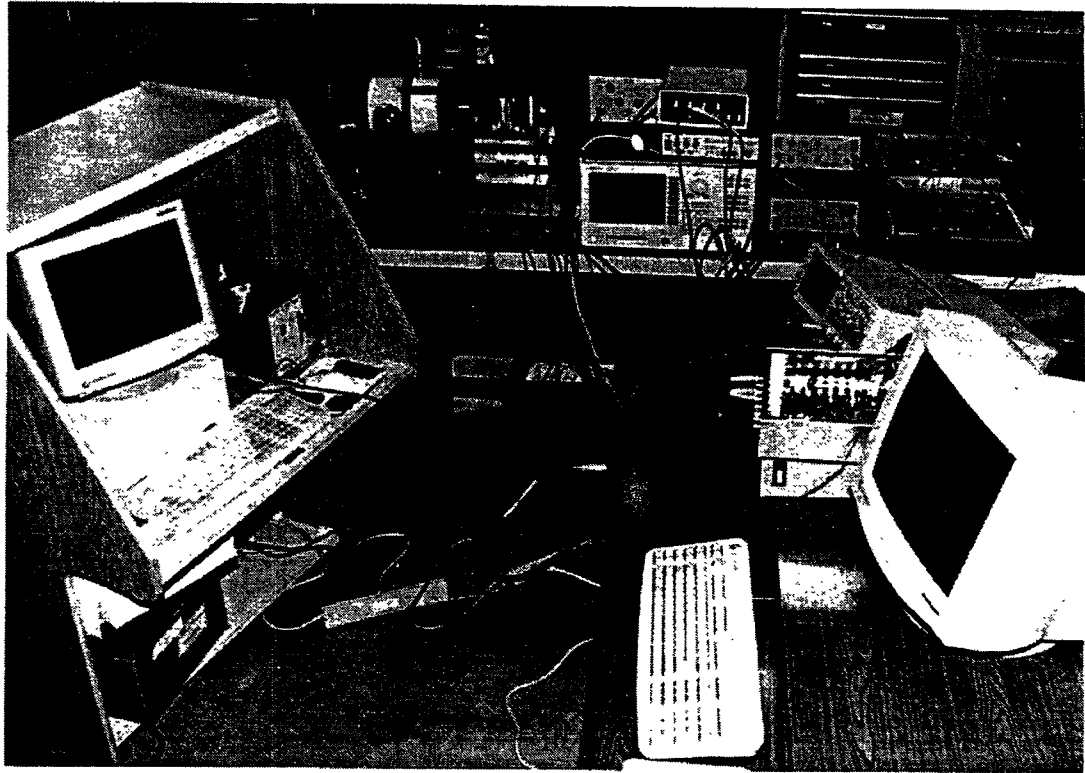


Figure 5.5: Experimental Setup

An adaptive vibration control strategy is applied in order to cancel out the tool post vibration caused by the vibration exciter. Here, two cases are studied. In the first case, the system identification is performed on-line, whereas in the second case, the system identification is performed off-line.



## 5.2.2 Control with On-line System Identification

In the first case study of system identification, the system identification and the adaptation algorithm are performed on-line.

### 5.2.2.1 Design of Experiment

A harmonic disturbance with the application of feedforward control scheme is selected for analysis. The same signal is used as a disturbance signal and a reference signal.

In order to find appropriate values for the weight structures and the adaptation coefficients of system identification and control processes, a series of experiments were conducted. In order to arrive at the system parameters that work for the disturbance within the bandwidth of the cutting process (0-400 Hz), a systematic approach is designed as shown in Figure 5.6. The approach can be classified into three parts: determination of the values for the gains, filter types and filter sizes of the controller and emulator, and determination of the values for the tuning parameters which refer to the adaptation coefficients.

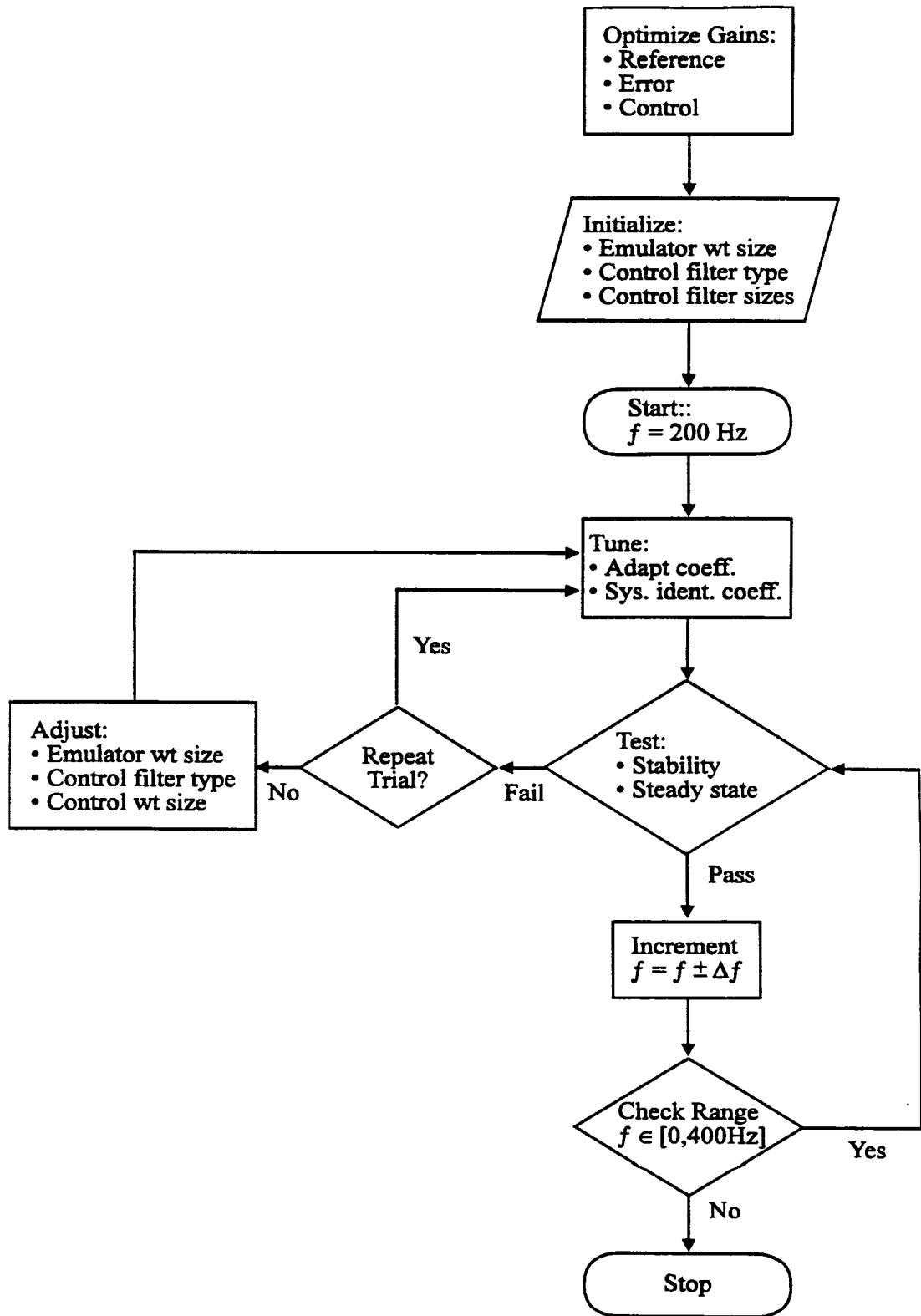


Figure 5.6: Control Design Approach

## 1. Gains

The values of the gains for reference signal, error signal, and control signal are determined and set for the bandwidth of interest. The gains for the reference signal and the error signal are selected in such a way that the signal inputs to the controller are kept close to the limits of the working range of the circuit board in order to utilize the full capacity of the controller. For that the auto-scale feature of the software is utilized. The attenuation gain for the controller output signal is set to 0 dB in the software and an amplifier is used to find the appropriate gain for the working conditions.

When the amplifier gain is too low, the controller will try to produce a higher control signal to compensate for the primary disturbance. When the control signal passes the upper limit of the working range, say 2.8 volts peak to peak, the electronic circuit becomes saturated and the software terminates the control action accordingly. Therefore, the amplifier gain should be set in such a way that the control signal will remain within the working range of the circuit. For the frequency of interest in this thesis work, an amplification of 14 dB gives the right working range for the control signal.

## 2. Filter Types and Sizes

FIR filters are characterized by the number of forward taps, whereas an IIR filter is characterized by both the number of forward taps and the number of backward

taps. Figure 3.10 and Figure 3.11 in Chapter 3 are illustrative of the direct realization of these filters.

It has been said that the gradient of the control mechanism output with respect to the control signal is required for the adaptive algorithm. This knowledge takes the form of an emulator. As a result, the error is filtered through the emulator, before it is used to adjust the weights of the control filter. Here, a FIR filter is used as an emulator to emulate the control mechanism, and both FIR and IIR filters are investigated to serve as a control filter. The number of taps required for the emulator is dependent upon the characteristics of the cancellation path and the modeling signal. The cancellation path includes the amplifier, the PMN actuators, and the mechanical structure of the tool post. This cancellation path introduces a time delay between the sensor and the application of cancellation disturbance. Moreover, the cancellation path can also introduce a gain and phase change.

When using the control output signal for system identification, the performance of the controller deteriorates when the frequency of the reference signal is changed. It also becomes unstable when being operated in wider ranges of frequencies. This occurred due to the fact that the derived model is valid for the frequencies contained within the control signal, and hence the reference signal. Therefore, the modeling signal implemented is a pseudo random signal (PRS) to capture the characteristic of the control mechanism for a wide range of frequency. When PRS is used as a modeling signal, a pseudo random noise is added to the control

signal for the purpose of modeling the control mechanism. Injecting additional noise into a system targeted for active control at a very low level provides a model of suitable accuracy over time while not significantly affecting the performance of the system. The amplitude selected is a compromise between a large amplitude for modeling accuracy and speed, and a small amplitude which does not significantly increase the ambient noise level in the targeted system. After conducting several trials, a tap length of 40 is found to be the right starting point for the emulator.

There are two options for the control filter, FIR and IIR. Where possible, it is advisable to start with FIR filters rather than IIR filters for two reasons. The first and most important reason is the inherent stable architecture of FIR filters. The lack of inherent stability characteristics in the IIR filters, unlike FIR filters, is due to the presence of the feedback section of the filter. If the feedback loop gain becomes too great the system becomes unstable, whereas in the case of FIR filters, the output cannot reinforce itself to drive the system into an unstable mode of operation.

The second reason for selecting FIR filters first, instead of IIR filters, is due to the behavior of the gradient descent algorithm. There is always a single global optimal set of weight values for FIR filters. However, if an IIR filter is used, there can be several local optimal sets of weight values due to the feedback involved. As a result, the gradient descent algorithm used to adapt the IIR control filter weights could be trapped in a local minima which may give quite poor performance, compared to what could have been obtained with the global optimum.

Nevertheless, FIR filters may not always serve the purpose and IIR becomes the appropriate choice. FIR filters do not have poles in their transfer function, and as a result are not good at realizing transfer functions that do have poles. In order to represent a discrete transfer function with zeros and poles with an FIR filter, it often requires a very large weight structure. The computational load associated with an extremely long filter can pose problems for the fastest digital signal processing chips. Since IIR filters are more efficient for realizing a given transfer function with the minimum number of total filter weights, IIR filters should be investigated when the FIR filter weight structure is too high. After several trials, a tap length of 40 was determined to be a good starting point.

### 3. Tuning parameters

The parameter that is used to tune the control parameter is the adaptation algorithm coefficient, while the one used to tune the emulator parameter is the system identification adaptation coefficient. The adaptation algorithm coefficient for the control filter, known as convergence coefficient, is the critical determinant factor of adaptive algorithm stability and convergence speed. For digital implementation, too small a convergence coefficient will result in an increase of the final value of the error criterion due to the quantization error inherent in digital systems. On the other hand, too high a convergence coefficient leads to instability. Therefore, best performance requires a value that is neither too small nor too large. This necessitates the search for an optimum value for the convergence coefficient. Factors that can affect the optimum convergence coefficient include:

- Reference signal frequency: Systems with a low frequency reference signal require small values of convergence coefficient than similar implementation with high frequency reference signals.
- Reference and error signal gains: The convergence coefficient is inversely proportional to the gains, especially a reference signal gain.
- Control filter tap length: The convergence coefficient is inversely proportional to the size of the control filter.

#### 5.2.2.2 Result and Analysis

From the series of experiments, the on-line system identification was determined unstable for lower weight sizes and FIR type control filters. The best results were obtained for a emulator weight of 120, and an IIR control filter with forward tap length of 100 and backward tap length of 100. The adaptation coefficient for the controller was set to 200, the amplitude of the random signal was set at 500, and the adaptation coefficient for the system identification was set at 500. The adaptive algorithm of the emulator was more stable than the control filter adaptive algorithm. The reason for this is the reduction of time delay in the system. The model filter output signal appears directly in the adaptive algorithm error signal, whereas in the control filter case, it must propagate through the model before it is used in the adaptive algorithm.

When the adaptation coefficient for the controller is increased beyond 200, the system becomes unstable. The following steps can be used to increase the speed of convergence while ensuring stability. At this stage for increasing the convergence

speed while maintaining system stability, only two parameter settings need to be changed. The first parameter is adaptation coefficient for system identification from the current value of 500. The second parameter is adaptation coefficient for the controller from the current value of 200. The first run is based on an increment of 100 to both parameter settings, namely, the adaptation coefficient for system identification equal to 600 and the adaptation coefficient for the controller equal to 300. The control system is run for an initial frequency of 200 Hz, as indicated in Figure 5.6. The frequency range is increased by multiples of 25, once to the lower side and then to the higher side. The system may be slow to converge at this time, however, maintaining system stability is the most important outcome desired. After the issue of stability is dealt with for the whole frequency range of interest, in this case 25 Hz to 400 Hz, then the issue of convergence is addressed. The search spaces are set for the adaptation coefficient for system identification (500 - 900) and for the adaptation coefficient for the controller (200 - 600) with an incremental step set to 100. The previous steps are repeated starting from 200 Hz frequency until the frequency range of interest is covered. Slowly, the adaptation coefficients can be raised up to 500 and 800 for control filter and emulator respectively. The improvement in convergence can be noticed at this time. The improvement in convergence speed is noticed for the frequency of bandwidth of interest (0-400 Hz).

At different frequencies two magnitude levels of disturbance were examined to study the effect of the magnitude level of disturbance on the performance of the controller. High level  $[-1 \ 1]$  is applied at frequencies of 50 Hz, 350 Hz, and 400 Hz.



Low level  $[-0.5 \ 0.5]$  is applied at 100 Hz, 150 Hz, 200 Hz, 250 Hz, and 300 Hz. The normalized steady state machine tool vibration with and without control are shown in Figure 5.7.

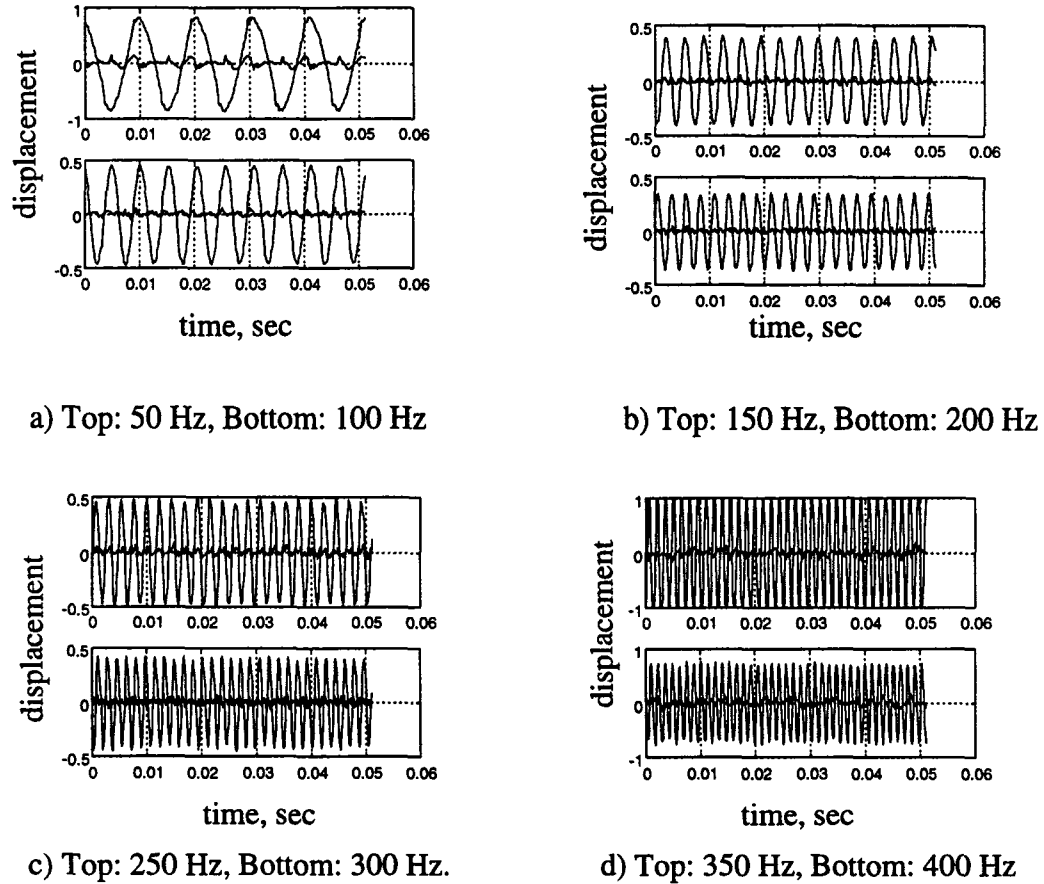
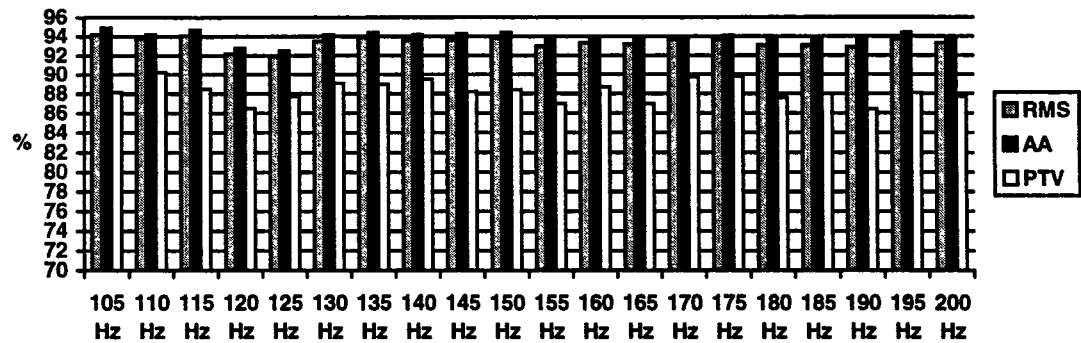
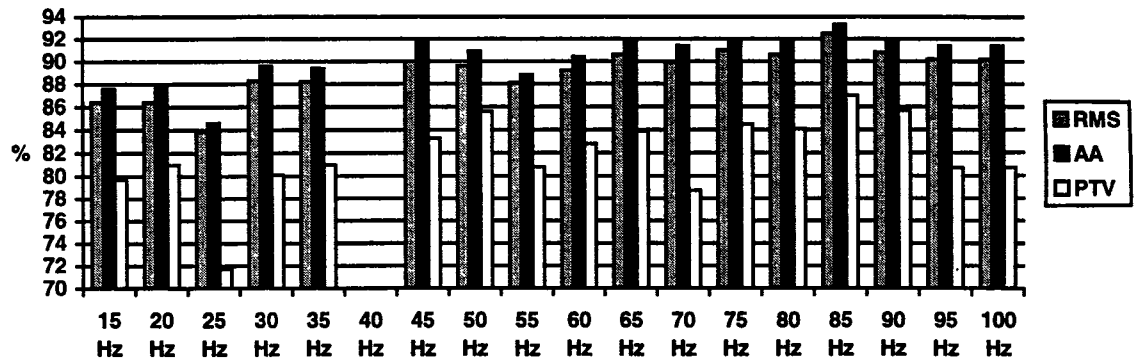


Figure 5.7: Normalized Machine Tool Displacement with and without Controller

Experiments were performed for a harmonic disturbance with frequencies ranging from 15 Hz up to 400 Hz at the interval of 5 Hz. In all cases the controller was able to compensate the machine tool vibration over 70% as shown in Figure 5.8. The percent reduction of the vibration for the three performance indices, Ra, PTV, and RMS, seems to be at the same level, which demonstrates that the vibration reduction

gives the same performance level in all test criteria. The vibration reductions achieved at different frequencies and at two different levels are also comparable. This indicates that the controller can handle a wide range of disturbance frequencies, and also can perform well at different disturbance levels.



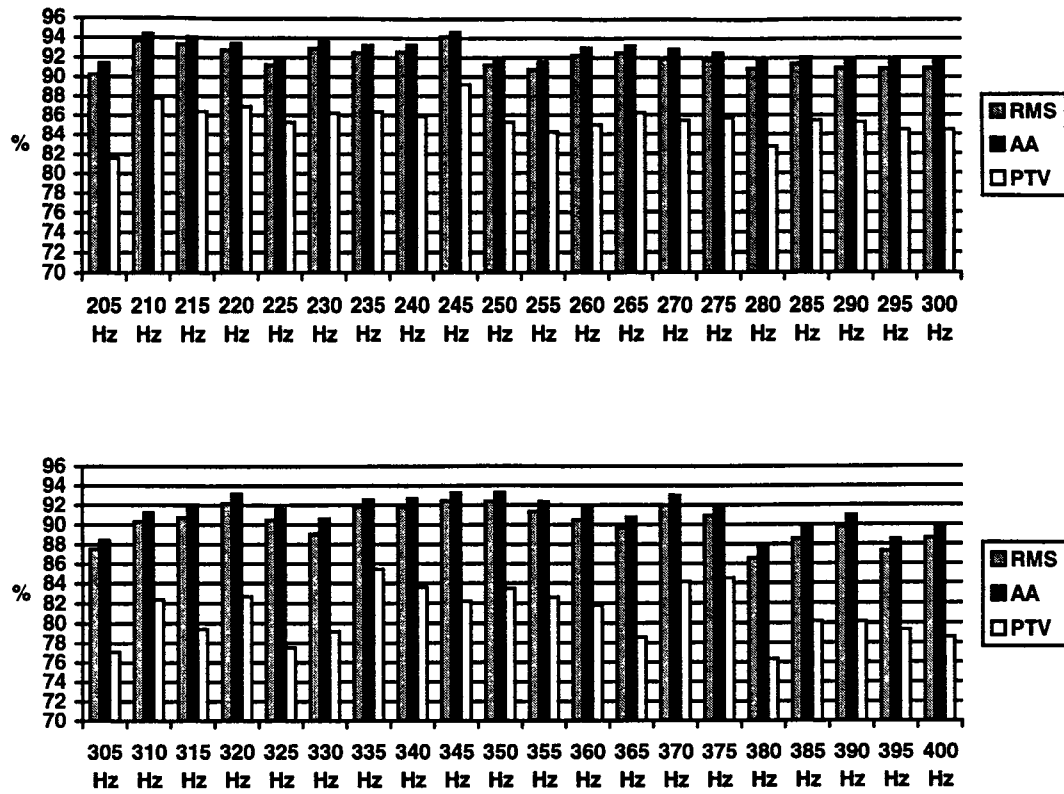


Figure 5.8: Steady State Percent Tool Vibration Reduction

### 5.2.3 Control with Off-line System Identification

In this section, the system identification scheme is run first with the adaptation coefficient of the control filter set to zero. Once the system identification is performed, the adaptation coefficient of the system identification algorithm is set to zero. Therefore, when the system is running with a non-zero convergence coefficient for control filter adaptation, the emulator weight remains unchanged. In this way, the coupling between the system identification and control process is eliminated.

The filter types and filter sizes selected are based on the computer simulation. Accordingly, a FIR filter with 60 tap lengths is selected for the emulator and a FIR

filter with 100 tap lengths is selected for the controller. The same flow chart that was employed in Section 5.2.2 was implemented to find the appropriate adaptation coefficients that work for the entire frequency range. It is found that the adaptation coefficient for the system identification and the amplitude of the modeling signal can be raised from the previous values since the identification process is performed off line. The adaptation coefficient for the control algorithm is found to be 200. Once the control parameters working condition are validated, then further investigation is performed as follows.

#### 5.2.3.1 Design of Experiment I

In order to investigate the effect of the tap length at a fixed multiple frequency disturbance (241 Hz with amplitude of 0.8 V and 185 Hz with amplitude of 0.2 V), the levels listed in Table 5.1 are selected for the weight structures of the emulator and control filters. After carrying out the initial tests, the trials listed in Table 5.2 were selected for trial purposes.

Table 5. 1: Weight Structure Levels

Level	Tap Length
Low [L]	60
High [H]	100

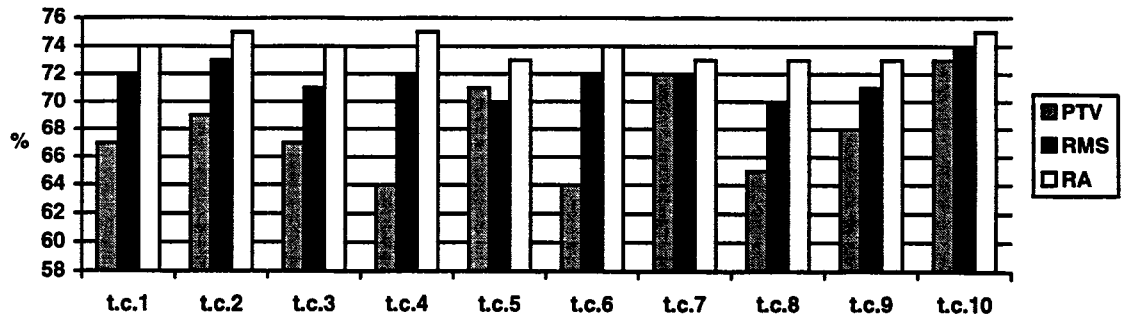
Table 5. 2: Selected Trials

Trial	Emulator forward tap	Controller forward tap	Controller backward tap
1	L	L	0
2	L	H	0
3	L	L	L
4	L	L	H
5	L	H	L
6	H	L	0
7	H	H	0
8	H	H	H
9	H	H	L
10	H	L	H

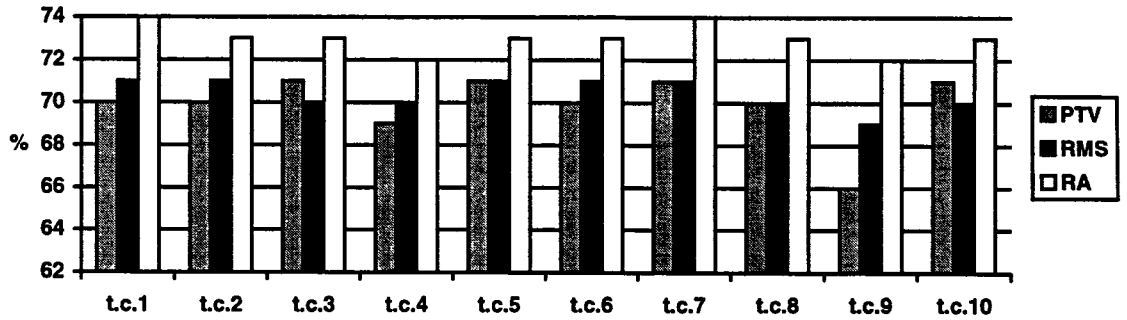
#### 5.2.3.2 Results and Analysis I

Here, feedforward and hybrid schemes are used. The dominant component of the disturbance frequency is assumed known while the other is left unknown. The hybrid control scheme has a problem of instability. It was possible to remedy the stability problem by reducing the adaptation coefficient on-line from 200 down to 100.

The three performance indices used to measure the effect of weight structure on system performance for the two control schemes are shown in Figure 5.9. The steady state performance of the ten trials show that there is no significant difference between them as far as AA and RMS values are concerned. However, for PTV, trial 10 yields the highest vibration reduction with 73% while trial 6 yields the least vibration reduction with 64%.



a) Hybrid control



b) Feedforward control

Fig. 5.9 Machine Tool Vibration Reduction

. The design parameters that work for the desired bandwidth arrived at in the previous experiment were with trial 2. Again here, the same trial gives no sacrifice in performance compared to the other trials. Therefore, the design parameters of trial 2 are validated for this dissertation research work.

### 5.2.3.3 Design of Experiment II

Here, the performance of feedforward and hybrid control schemes at different trial multi-frequency disturbances was tested. The feedforward control scheme can be obtained by keeping the adaptation coefficient constant at 200. However, the adaptation coefficient of the hybrid control is lowered on-line from 200 to 100.

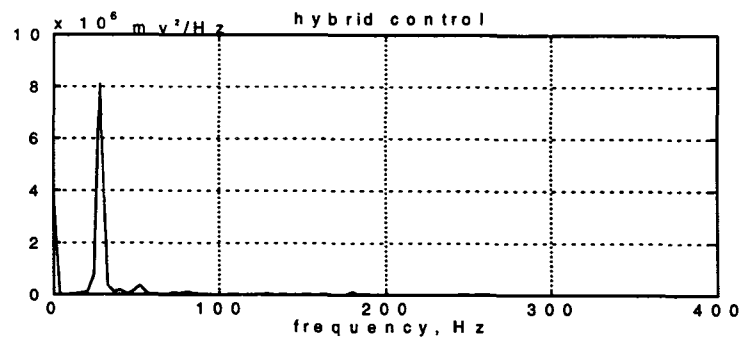
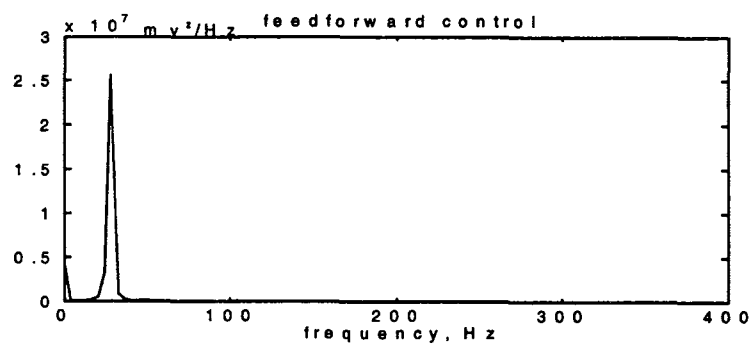
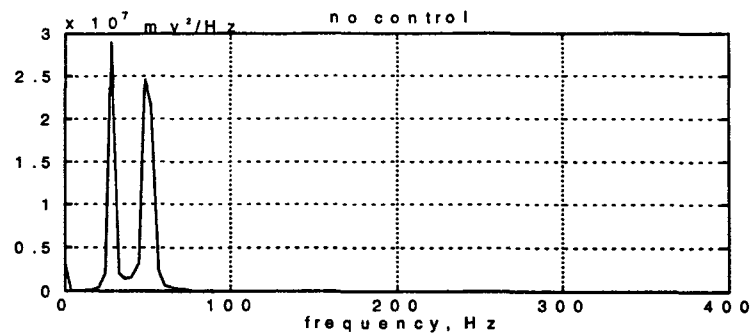
The displacement data are collected with the controller turned off, and also with the controller turned on. The controller is left running for a longer time period after achieving steady state to ensure stability. The driving signal consists of two frequencies with one being the dominant frequency as shown in Table 5.3. The dominant frequency is used as a reference signal in the feedforward control scheme. In the hybrid control scheme, the summation of the dominant frequency and the negative error is used as a reference signal.

Table 5. 3: Frequencies and Amplitudes of Disturbance Signal

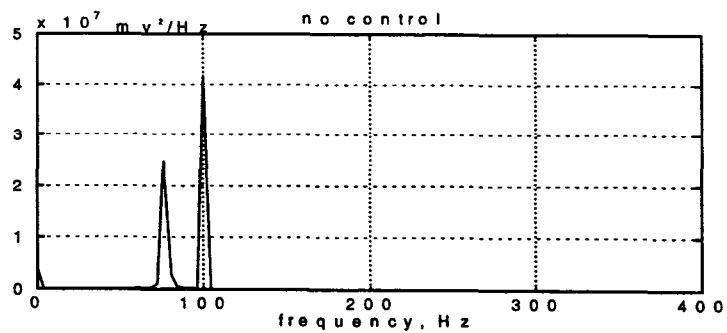
<b>Trial</b>	<b>f<sub>1</sub> Hz</b>	<b>a<sub>1</sub> V</b>	<b>f<sub>2</sub> Hz</b>	<b>a<sub>2</sub> V</b>
1	50	.6	27	.2
2	100	.6	77	.2
3	150	.6	127	.2
4	200	.6	177	.2
5	250	.6	227	.2
6	300	.6	277	.2

### 5.2.3.4 Results and Analysis II

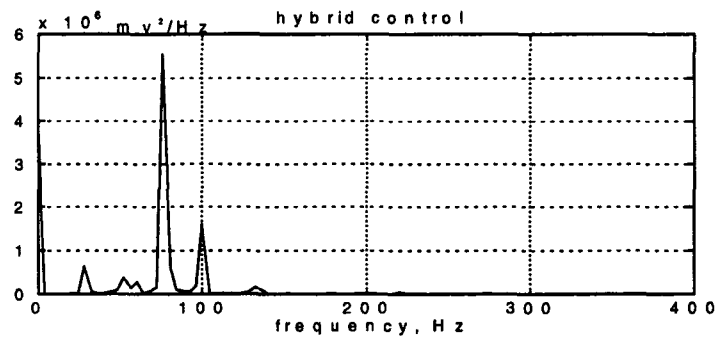
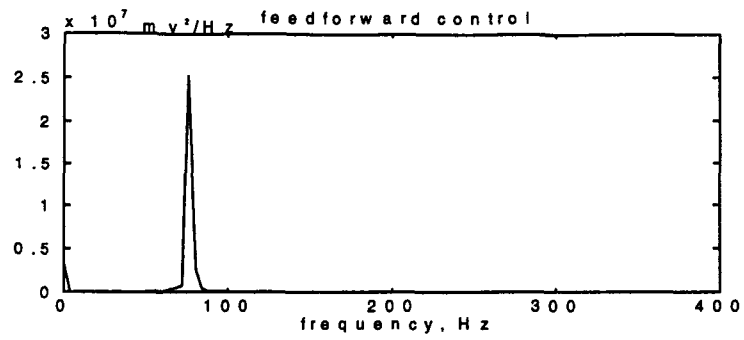
In Figure 5.10, the spectral density of the tool post displacement with no control, with feedforward control, and with hybrid control are shown.



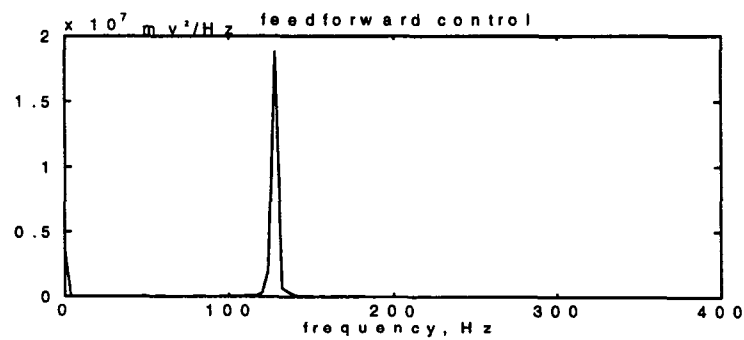
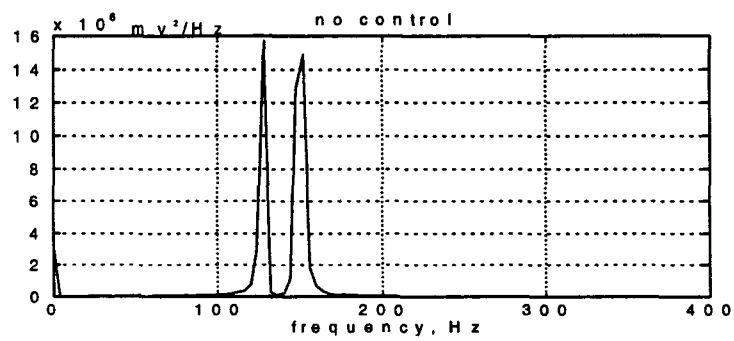
a) Trial #1

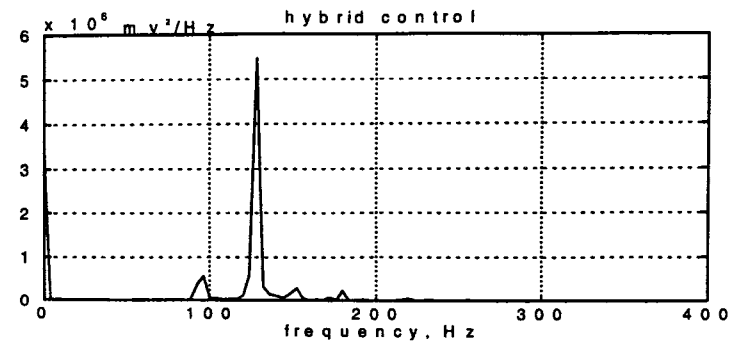




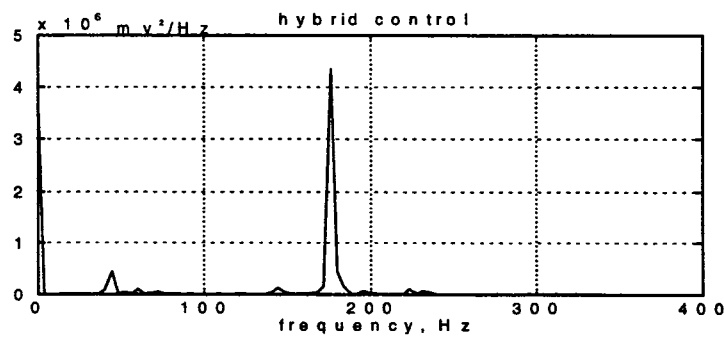
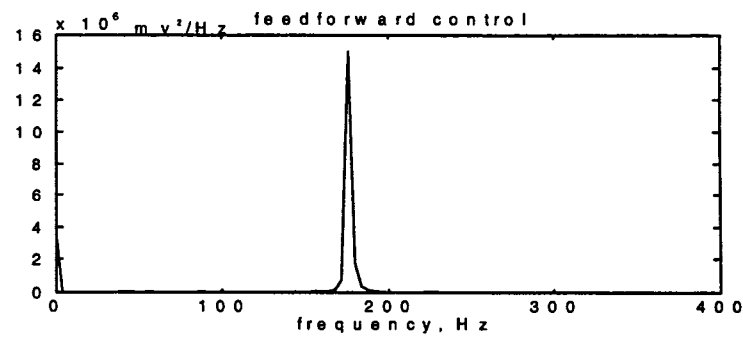
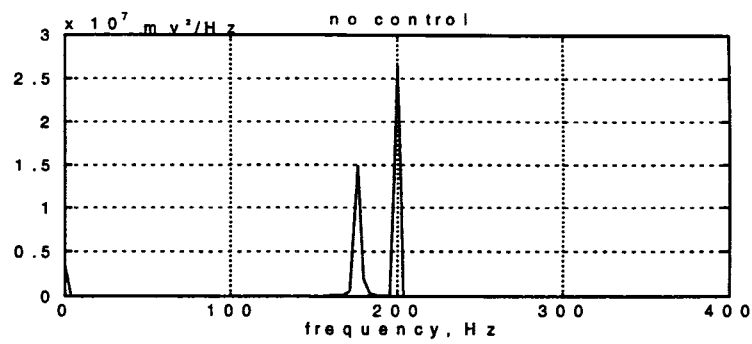


b) Trial #2

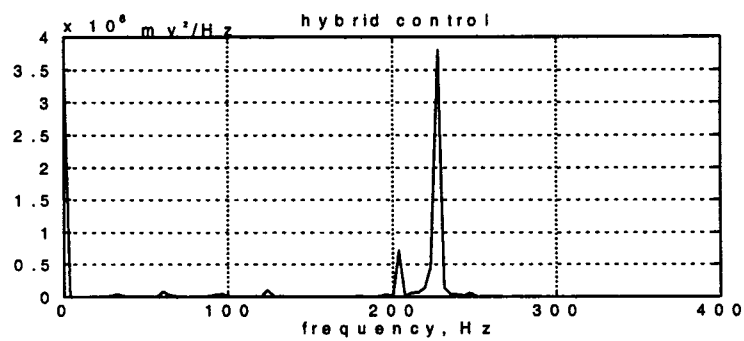
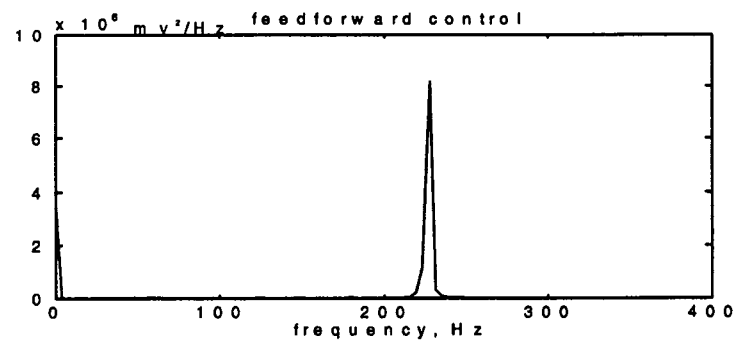
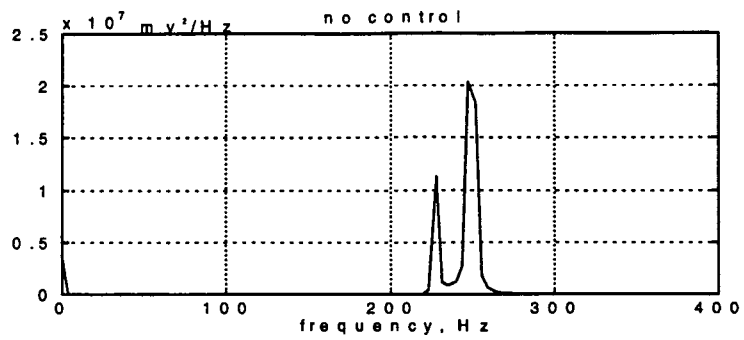




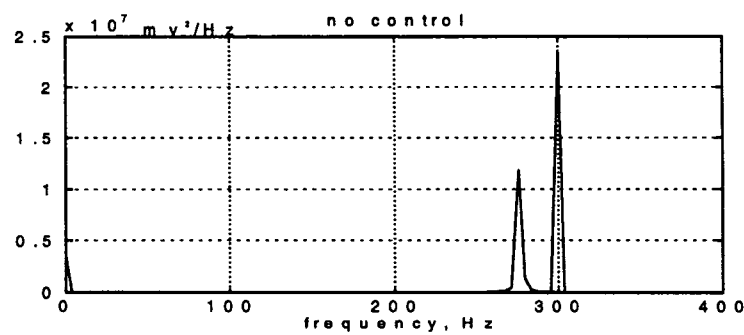
c) Trial # 3

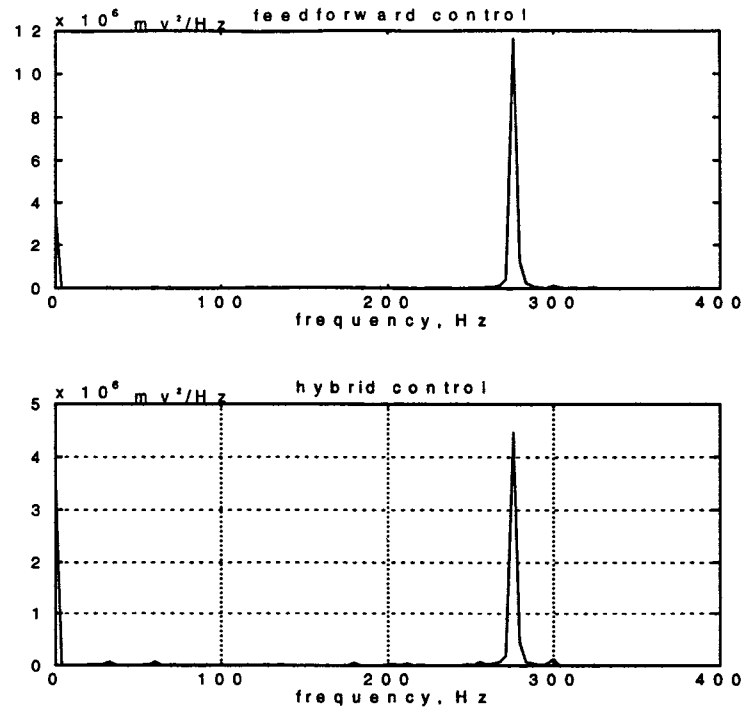


d) Trial # 4



e) trial 5





f) Trial #6

Figure 5. 10: Spectral Density of Tool Displacement

In trial 1, the dominant frequency is completely compensated by the feedforward control scheme. The nondominant frequency that was missing in the reference signal is not compensated at all. The dominant frequency is almost completely compensated by the hybrid control scheme since it is also present in the reference signal of the hybrid control scheme. Compared to the feedforward control, however, there is a small portion of the dominant frequency in the tool displacement which was not compensated with the hybrid control scheme. The major difference between the two schemes is observed on what happens to the frequency component that is missing from the reference signal. In the case of a hybrid control, the spectral

density magnitude for this frequency component is reduced from the order of 3 to the order of 0.8.

In trial 2, the frequency 100 Hz frequency component in the reference signal is completely compensated by the feedforward control, while the other frequency component remains unchanged. In the hybrid control scheme, on top of the dominant frequency, the spectral density magnitude of the other frequency component is dropped from the order of 2.5 to 0.55.

In trial 3, the hybrid control scheme gives the same response. The hybrid control results in a reduction of a spectral density magnitude of the unrepresented frequency from the order of 1.6 to that of 0.55. In trial 4, both control schemes give consistent results. The unrepresented frequency in the hybrid control case is lower in its spectral density magnitude from the order of 1.5 to the order of 0.45.

In trials 5 and 6, the unrepresented frequency showed a slight reduction in the feedforward control case, whereas in the hybrid control scheme, the same rate of reduction as before is observed in the unrepresented frequency. With the exception of trial 6, and possibly trial 1, frequency components other than the driving frequencies are observed in the hybrid control case. This can be attributed to the feedback part of the reference signal.

#### 5.2.3.5 Design of Experiment III

Here, the feedback control scheme is analyzed. However, instability was observed when feedback control is applied in the format of the feedforward control

scheme. Therefore, the adaptation coefficient is lowered on-line from a value of 200 to a value of 50 to avoid instability.

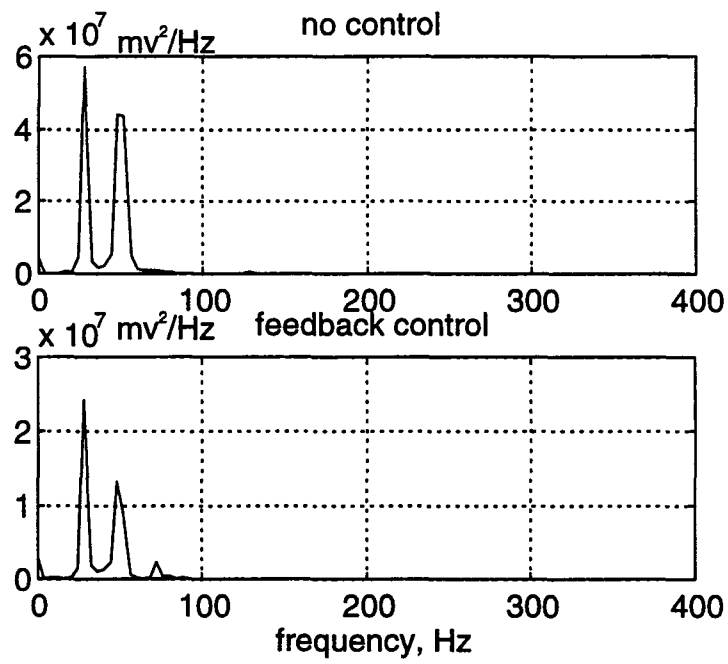
The displacement data are collected with the controller turned off, and also with the controller turned on. The sampling frequency is set to 5.21 kHz. The controller is left running for a longer time period after achieving steady state to ensure stability as before. The negative of the error signal is used as a reference signal in this control implementation. The disturbance signal consists of two frequencies as shown in Table 5.5.

Table 5. 4: Frequencies and Amplitudes (peak) of Distubance Signal

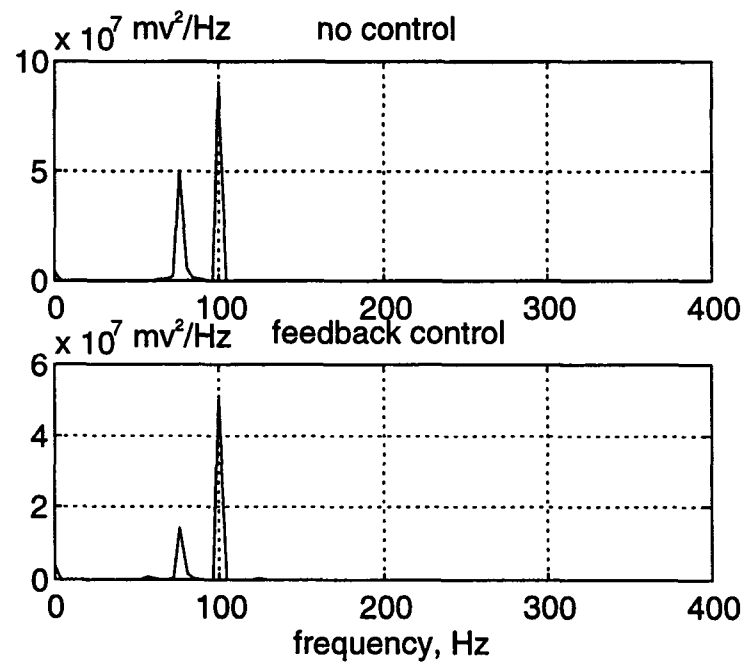
<b>Trial</b>	<b>f<sub>1</sub> Hz</b>	<b>a<sub>1</sub> V</b>	<b>f<sub>2</sub> Hz</b>	<b>a<sub>2</sub> V</b>
1	50	.4	27	.3
2	100	.4	77	.3
3	150	.4	127	.3
4	200	.4	177	.3
5	250	.4	227	.3
6	300	.4	277	.3

#### 5.2.3.6 Results and Analysis III

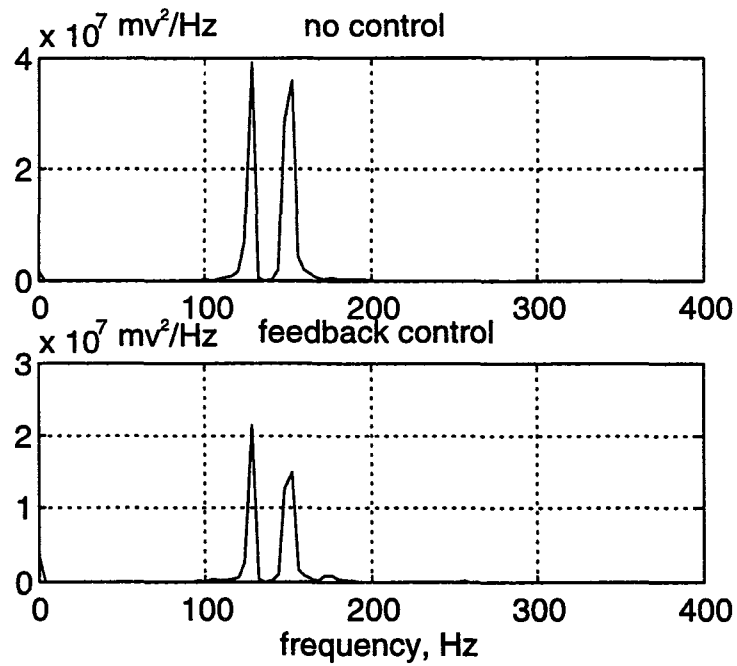
The spectral density for the machine tool displacement without the controller and with the controller are given for the six trials in Figure 5.11.



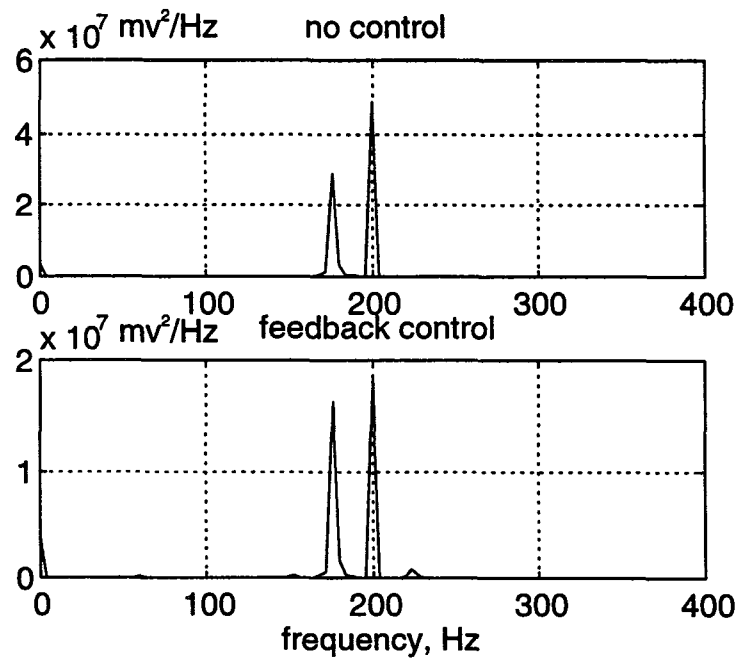
a) trial #1



b) trial #2

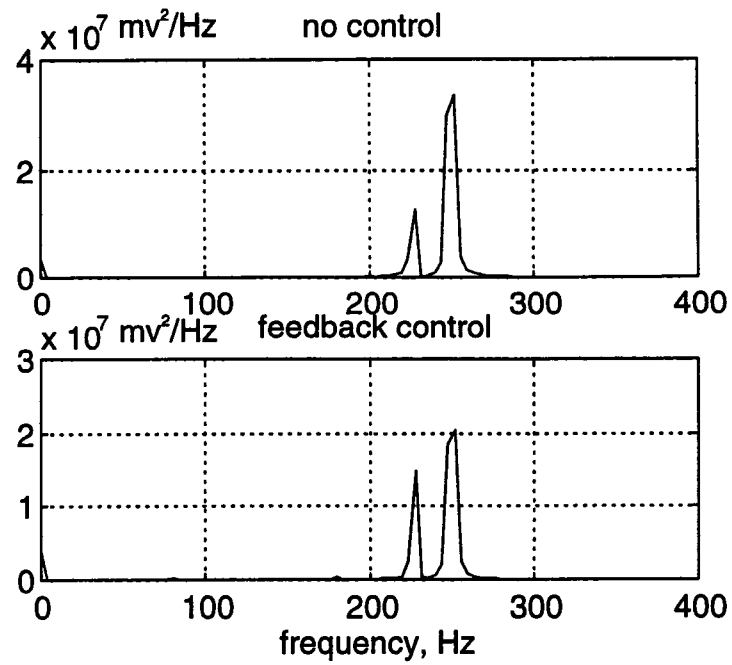


c) trial # 3

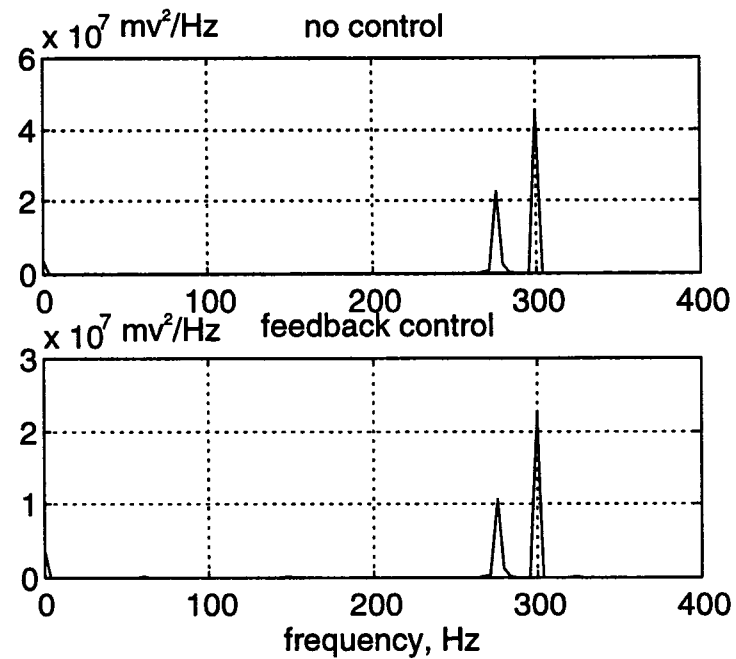


d) trial # 4





e) trial # 5



f) trial # 6

Figure 5. 11: Spectral Density of Tool Displacement

From the figures it is clear that both frequency components are reduced by about one half in most cases. In the previous experiment, the unreferenced signal was reduced from 67% to 75% in the hybrid control system. Here, in the feedback control scheme, the reduction achieved is 50%. The reason in this difference in performance is due to the makeup of the reference signal for the two control schemes. In the hybrid control case, the reference signal was made of the known dominant frequency and the negative feedback signal. Here, only the negative feedback is used.

The following can be deduced from the experiments made so far. For feedforward control, the vibration is almost completely compensated for the frequency component that is available in the reference signal. The unreferenced frequency component will not be compensated at all. For hybrid control, the referenced component is almost completely compensated. In addition, the unreferenced frequency is compensated upto 75%. The feedback control can reduce the vibration for all frequencies in the feedback signal upto 50%. Therefore, the usage of the appropriate control scheme depends on the nature of the problem. Accordingly, the following is the recommendation based on the results obtained from the experiments.

- Where a reference signal that is correlated to the primary disturbance is available, feedforward control scheme is the best one among the alternatives.
- Where only part of the primary disturbance is known as a priori, then hybrid control scheme is the best one among the alternatives.

- When there is no way to determine the signal that is correlated with the primary disturbance, the feedback scheme becomes the only alternative.

#### 5.2.3.7 Design of Experiment IV

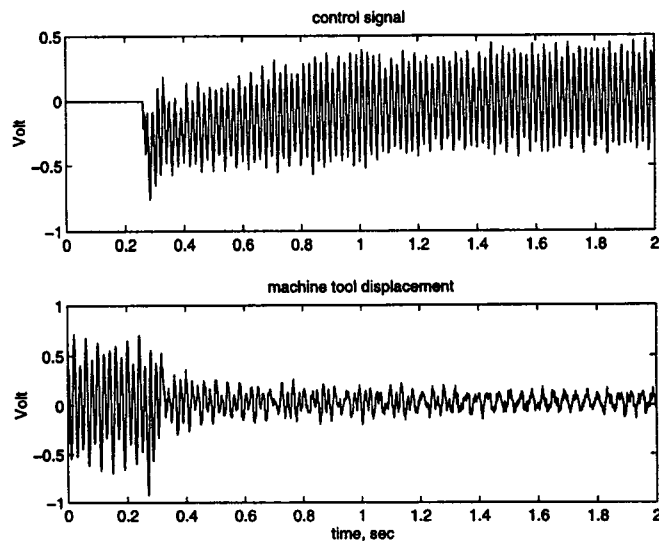
Since hybrid control comprises the other two control schemes, the transient response of hybrid control is analyzed using disturbance signals listed in Table 5.6.

Table 5. 5: Frequencies and Amplitudes of Disturbance Signal

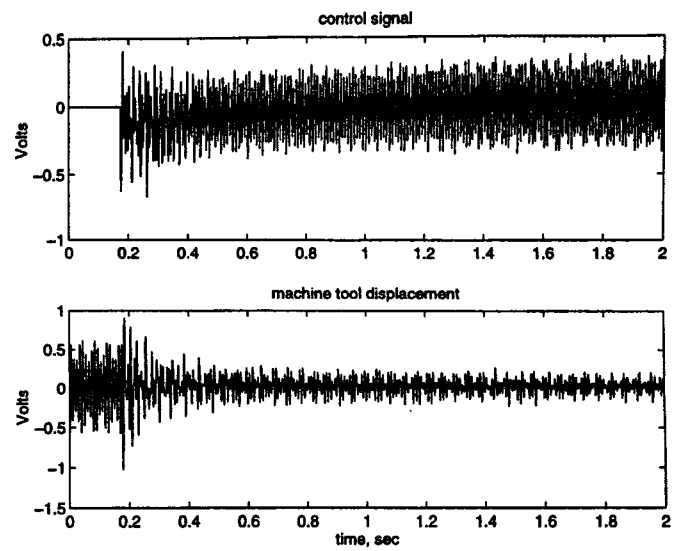
Trial	f1	a1	f2	a2
1	50	.8	27	.2
2	100	.8	77	.2
3	150	.8	127	.2
4	200	.8	177	.2
5	250	.8	227	.2
6	300	.8	277	.2

#### 5.2.3.8 Results and Analysis IV

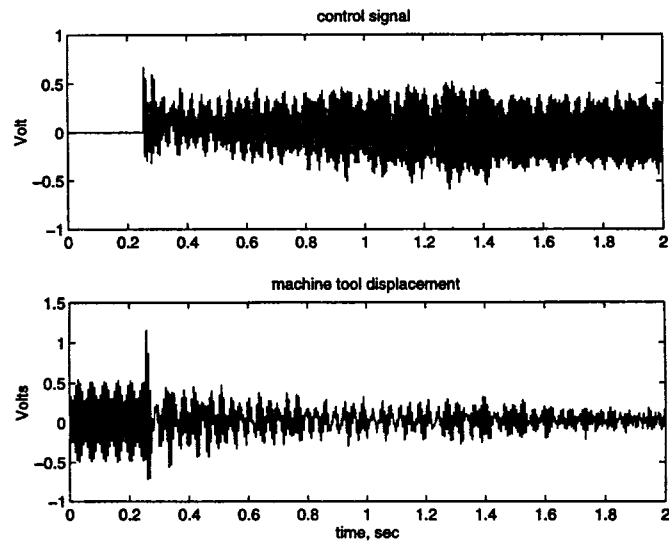
In Figure 5.12, the transient response for each trial is shown.



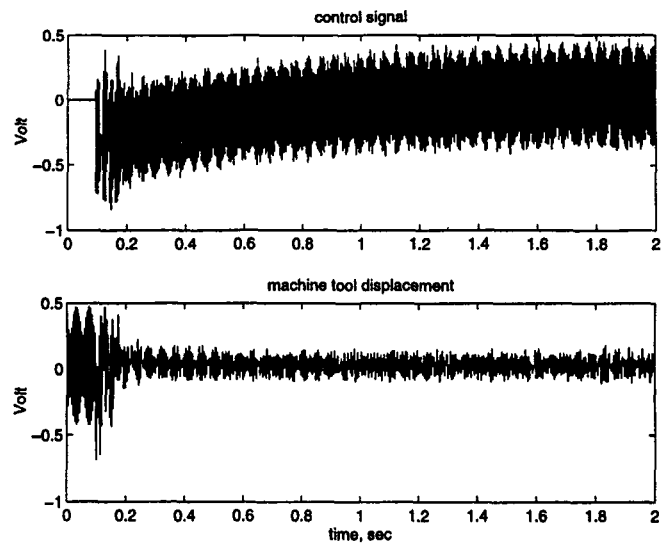
a) trial # 1



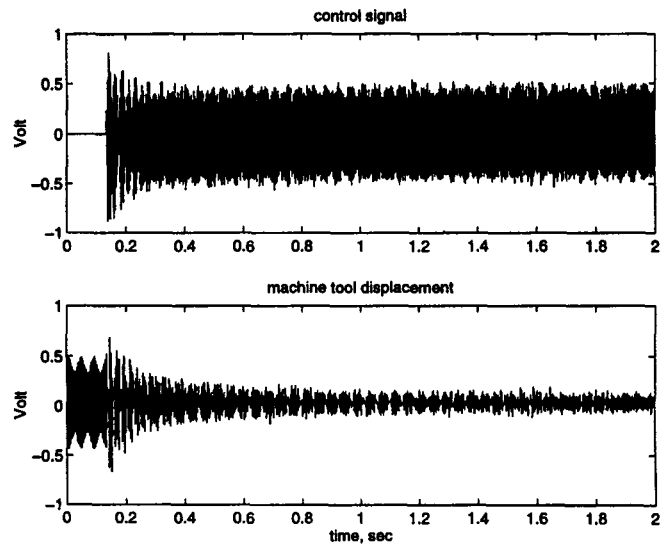
b) trial #2



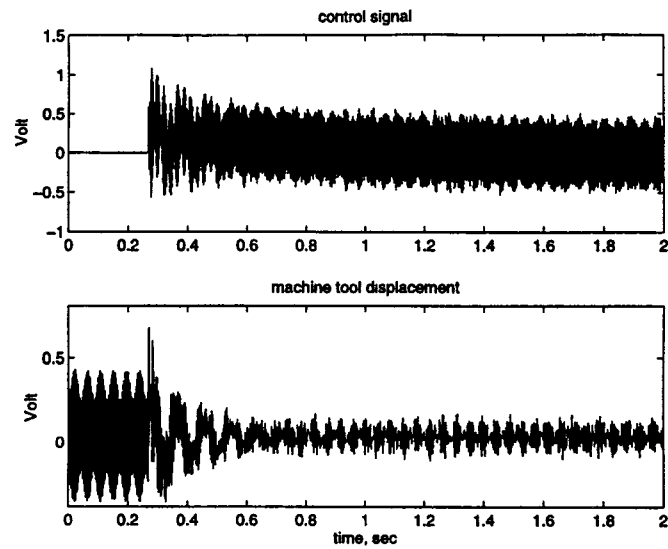
c) trial #3



d) trial #4



e) trial #5



f) trial #6

Figure 5. 12: Transient Response

The transient response shown in the figures above confirm that the selected adaptation coefficient ensures fast convergence speed while maintaining stability.

### 5.3 Machine Shop Experiment

The machining experimentation is performed on the shop floor by using a lathe machine. The experiments are done in two phases. The first case represents a turning operation in which both ends of the workpiece are fixed. One end is fixed with a three-jaw chuck, and the other end is supported by a central head, which rotates with the workpiece during machining. In the wazzu second case, the end supported by the central head is released. This resembles a situation in which the free end of a

cantilever is subjected to a force. The direction of the force remains unchanged while the cantilever is rotating.

In the two types of machining setups, the dynamic characteristics of the machining system are distinguished from each other. In this thesis work, the system disturbance characteristics are analyzed first. This is done by analyzing the frequency content of the machine tool displacement without the application of a controller. This position variation may introduce variation of the vibration modes that are involved during machining. Such a time dependency of the tool position is also considered in this thesis research. Results obtained from this study will form a basis to an appropriate control strategy for vibration compensation.

### 5.3.1 Experimental Setup

In Figure 5.13, the experimental setup for the machine shop experiments is shown. Aluminum bars of two dimensions are used in the experiments. The first test bar is a round bar with 12 inches length and 3 inches diameter. The second test bar is long and slender with a diameter of 2 inches and a length of 24 inches. The round bar is secured in the chuck. In order to avoid the slippage of the workpiece into the chuck due to the thrust force of the cutting process, the end of the workpiece is grooved and secured in the chuck in such a way that longitudinal movement is blocked. Depending on the two types of setup used, one end of the bar is free to vibrate in the cantilever beam setup, and the other end is fixed by the chuck attached to the spindle. For the fixed setup, one end of the test bar is supported by the tail stock and the other end is fixed by the chuck attached to the spindle. In order to avoid over constraining the test

bar, the moving central part of the tail stock is moved slowly to the end of the test bar while the spindle is rotating with the test bar. The central part of the tail stock is locked when it touches the test bar and it rotates with the test bar simultaneously. In this way, the test bar is well positioned and tightened for the machining tests.

The smart tool post is securely tightened into the tool holder of the lathe machine. The tool tip of the smart tool post is aligned with the tip of the lathe spindle. In doing so, the vertical elevation of the tool tip is made at the center line of the workpiece. The actuators are connected in a series similar to the laboratory experiments. The two wires from the actuators are connected to the power supply of the actuators. At the same time the noncontact displacement sensor mounted at the back of the tool post is connected to the sensor electronics.

The displacement signal from the sensor electronics is connected to the oscilloscope for visual observation, to the HP35667 signal analyzer for frequency content analysis and data storage, to the control circuit as an error signal, and as a reference signal for feedback and hybrid control schemes.



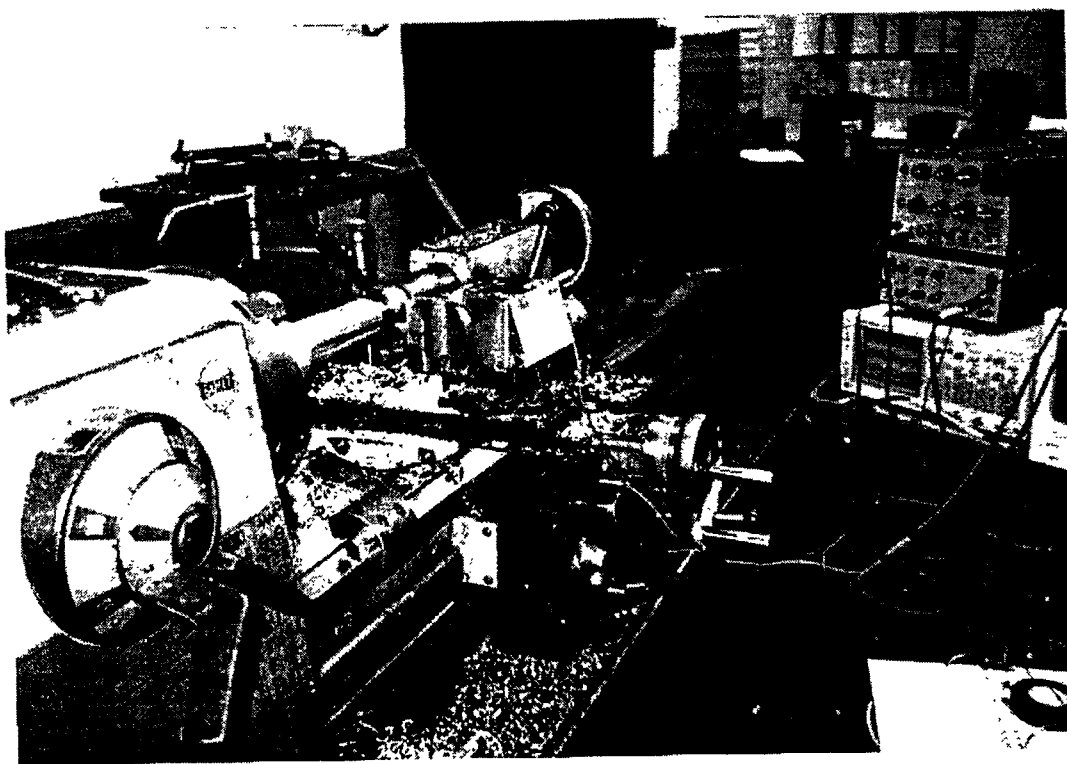
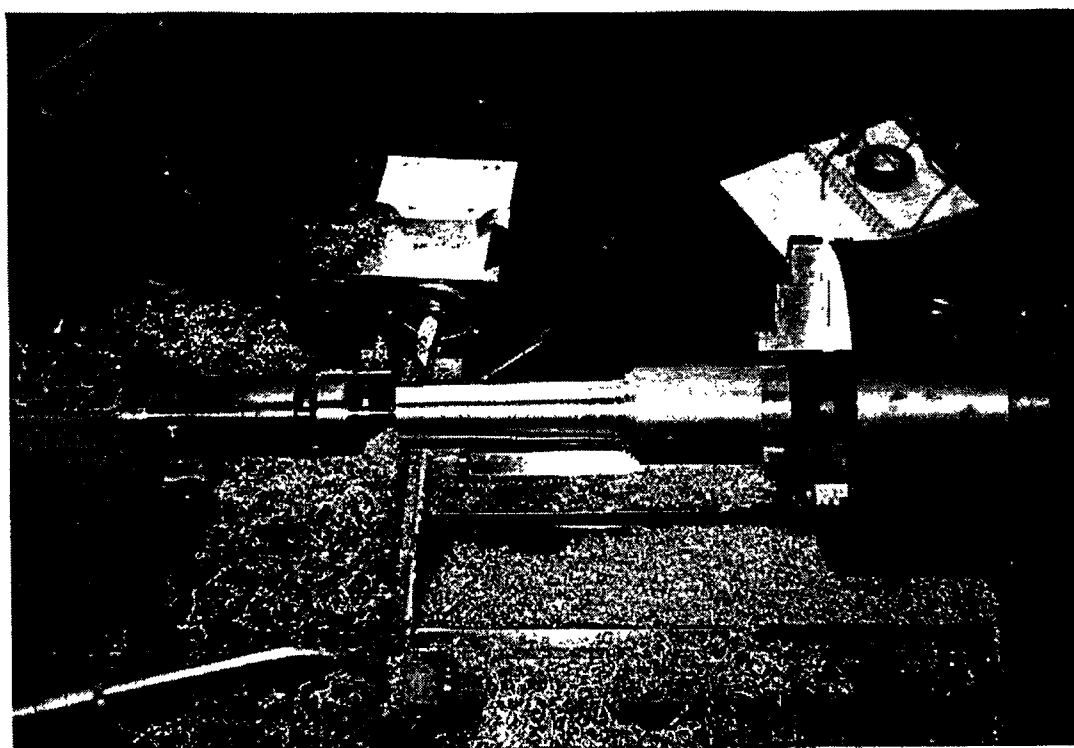


Figure 5. 13: Shop Floor Experimental Setup

### 5.3.2 Turning Operation with both Ends Supported

The both ends supported experiment represents the practice of turning operation in the machining industry. By supporting both ends, the rigidity of the work piece is increased, and thereby, the machine tool vibration is reduced. After the system disturbance is analyzed, the appropriate control scheme is applied and the performance of the controller is ascertained in the next sections.

#### 5.3.2.1 System Disturbance Characterization

In order to study the disturbance nature of the cutting process for this work piece setup, a round aluminum bar with a diameter of 3 inches and a length of 12 inches is selected. The cutting conditions, namely, the depth of cut, the feed, and the spindle speed are considered as variables in this study.

The following levels are selected for the three cutting conditions.

Table 5. 6: Levels for Cutting Conditions

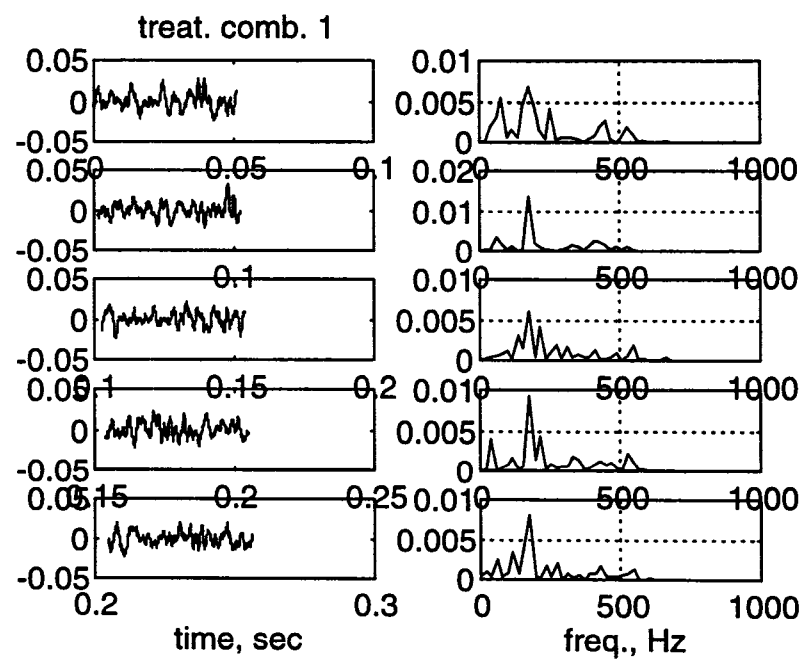
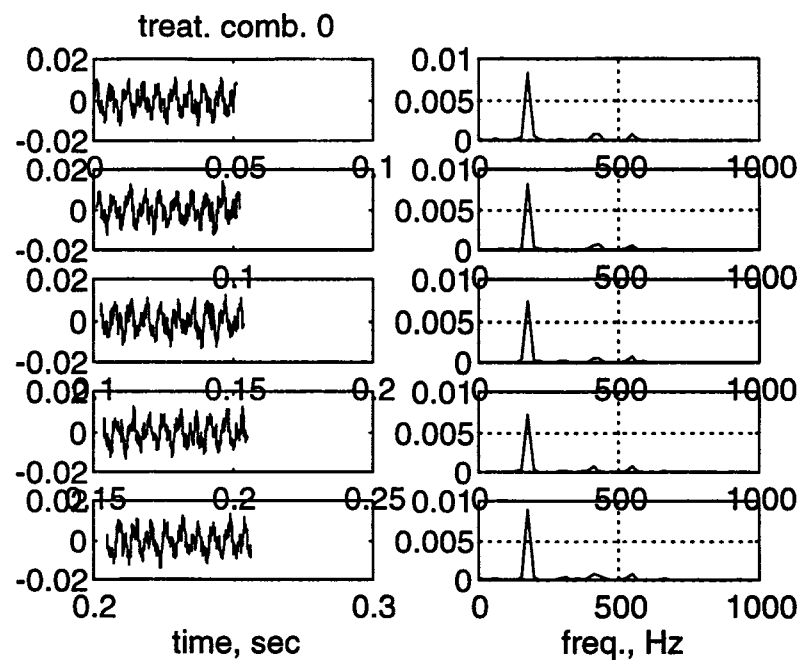
	Depth of cut, in	Feed, in/rev	Spindle speed, rpm
Low [L]	0.02	0.002	190
High [H]	0.04	0.02	470

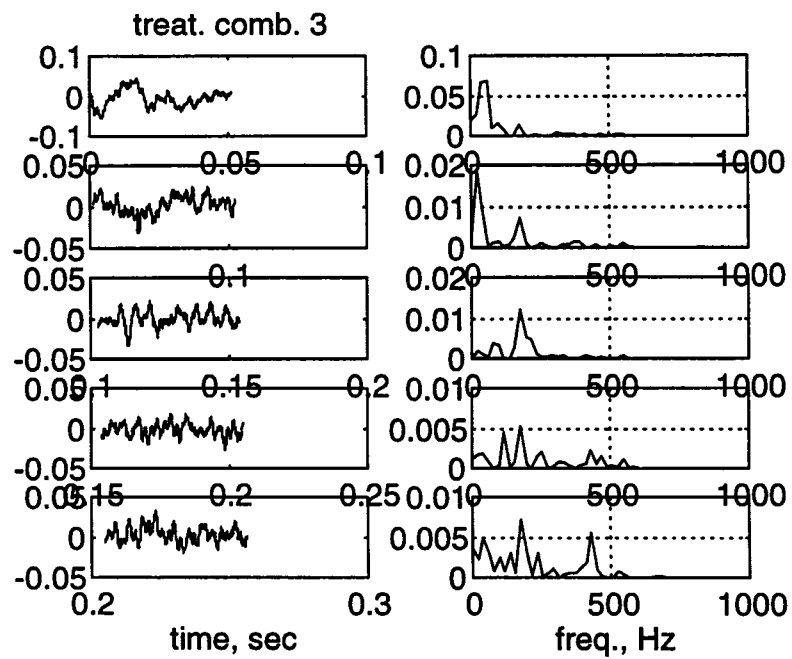
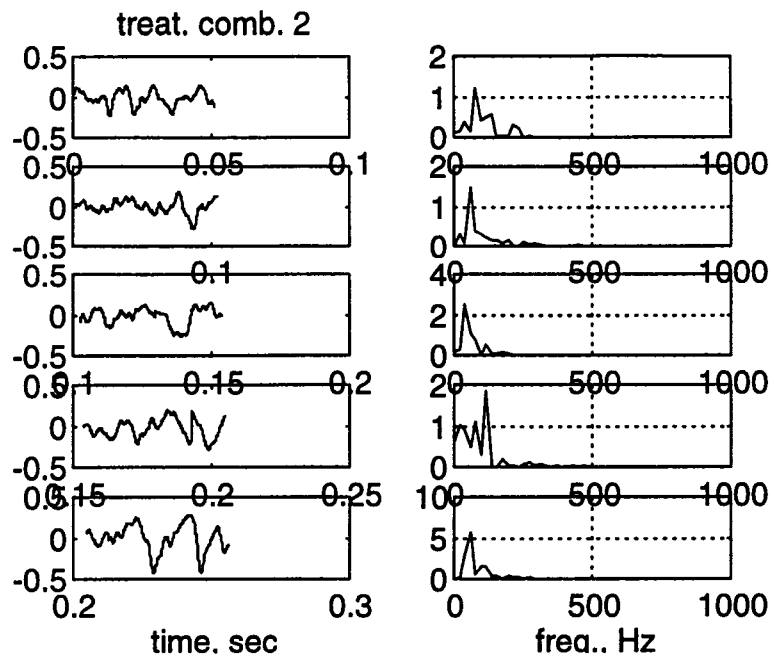
Accordingly, the 2 level factorial design for the three parameters gives the following treatment combinations.

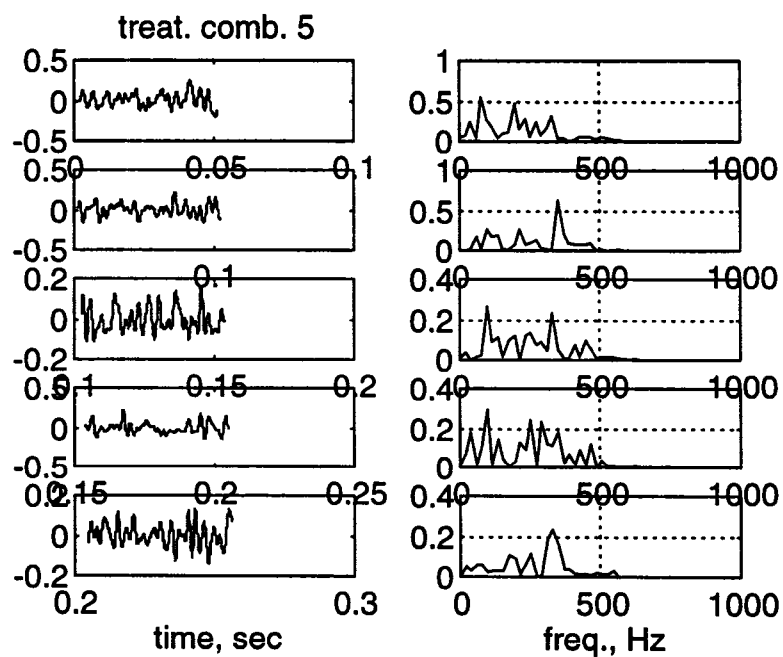
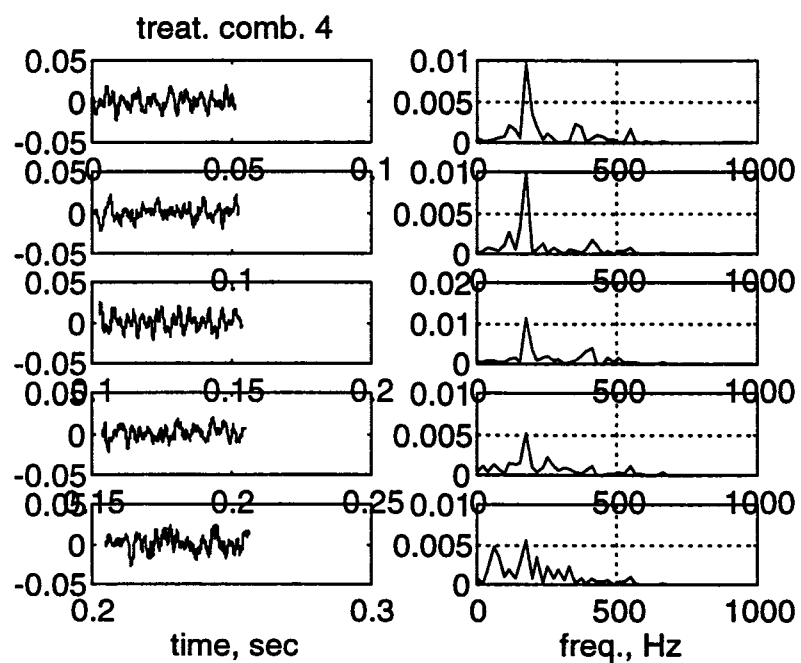
Table 5. 7: Treatment Combinations

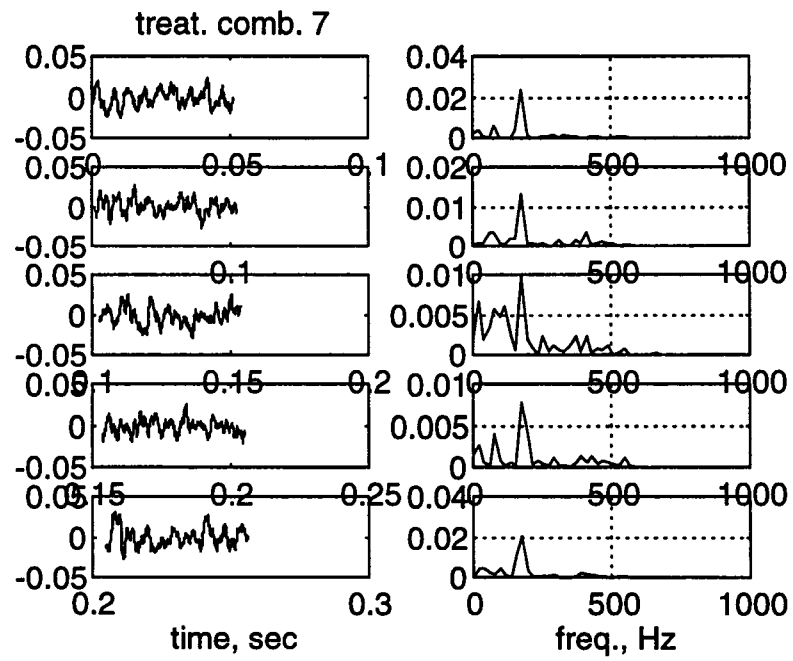
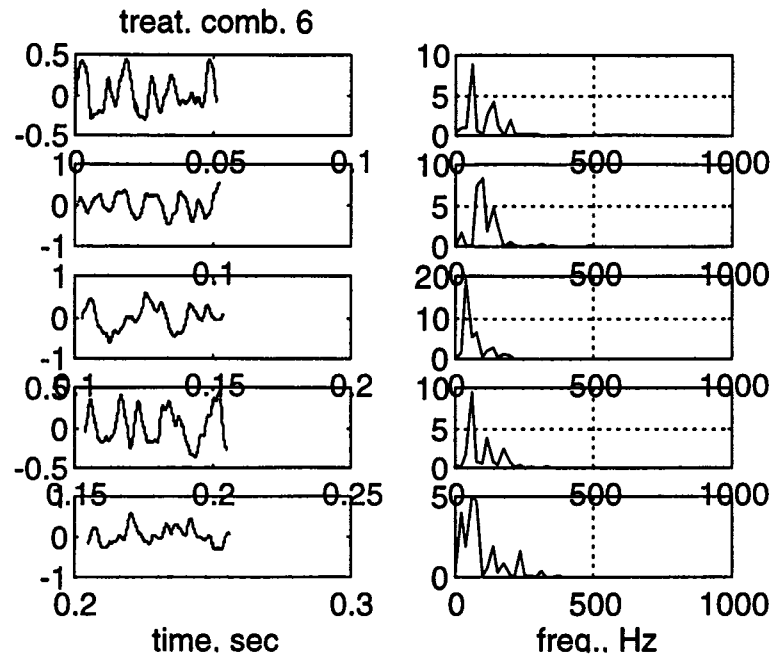
select Treatment combination	Depth of cut	Feed rate	Spindle speed
0	no cut	on	on
1	L	L	L
2	L	L	H
3	L	H	L
4	H	L	L
5	L	H	H
6	H	L	H
7	H	H	L
8	H	H	H

An additional treatment, referred to as the zero treatment combination, is added to study the effect of measurement noise. This is the measurement of the tool vibration with sensor electronics, motor spindle, and feedrate on at the time when the cutting operation has not started.. This allows the disturbance characteristics due to the cutting process to be identified and analyzed more effectively. The collected data are divided into a series of windows of time, and the spectral content of each window is evaluated to find out the disturbance characteristics as a function of time, more specifically as a function of the cutting force position on the test bar. The time and power spectral density of the windows for each treatment combination is shown in Figure 5.14.









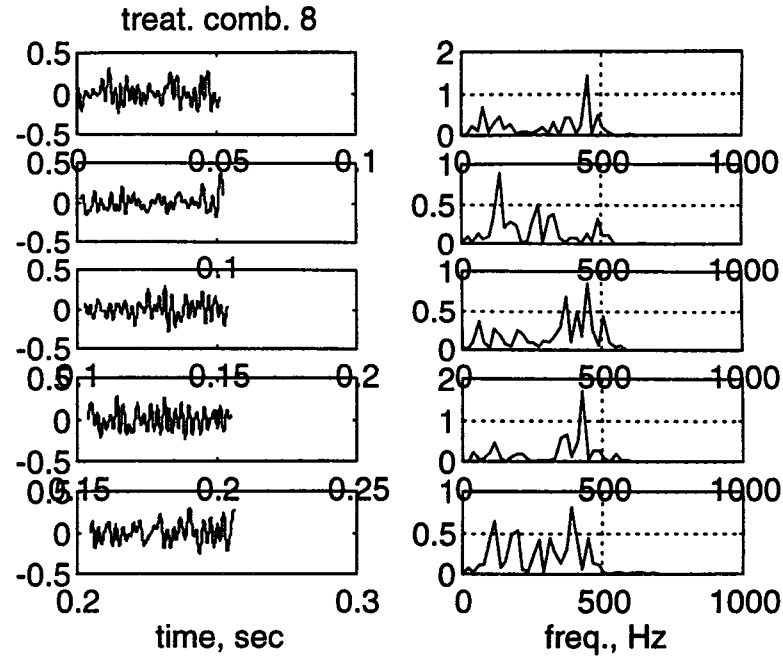


Figure 5. 14: Disturbance Signal Analysis

Examining the results shown in the above figures, the following observations can be made:

1. The case for no cutting, which represents the measurement noise, has a frequency characteristic of 60, 120, 180, 240, 300 Hz, etc. These components can be mainly attributed to the noise and its harmonics.
2. The disturbance, or the tool vibration, is mainly characterized by two frequency peaks which are time dependent. It is to be noted that this characteristic changes for the both ends support machining tests.



### 5.3.2.2 Design of Experiment

Based on the observation, it is clear that the dynamic variation of the cutting force, or the impending disturbance can not be known well in advance to implement feedforward controller. Therefore, two cases are investigated; namely, the negative feedback control scheme and hybrid scheme. The hybrid scheme is implemented with a reference signal composed of a random signal with frequency content in the disturbance frequency range and a negative of the error signal.

After noting the displacement range of the cutting process without the controller, the appropriate gain for the actuator amplifier is determined. This is done by using a signal generator to produce a sinusoidal signal of 1 V amplitude as a control signal. The tool post is left free to vibrate while increasing the actuator amplifier gain. The actuator gain is set at a point where the machine tool vibration is at the same level as the primary disturbance.

Similar to the laboratory experimentation, the control strategy with on-line system identification is found to have stability problems. The instability is pronounced in machining experiments since the shop floor environment is not a controlled environment like the laboratory environment. Therefore, the control strategy with off-line system identification is implemented. The weight structures that were used in the laboratory experiments were implemented. A series of experiments were performed to determine the adaptation coefficients. Based on the insights given through the laboratory experiments, the adaptation coefficient were varied in the range of 50 to 200. Adaptation coefficient reduced on-line from 100 to 50, from 150 to 50,

from 200 to 50 are investigated. The best result is obtained for adaptation coefficient reduced on-line from 150 to 50. An adaptation coefficient of more than 200 causes instability. The vibration reduction due to the controller for this adaptation coefficient is analyzed using the three performance indices, namely, AA, PTV, and RMS.

Three sets of experiments are designed. In the first set the depth of cut and the spindle speed are fixed constant. The feedrate is varied in two levels that correspond to trial 1 and trial 2. In the second set, the spindle speed and the feedrate are kept constant, and the depth of cut is varied in two levels which correspond to trial 3 and trial 4. In the third set, the feedrate is kept constant, and the spindle speed and the depth of cut each assume two levels. Trial 5 and trial 6 pair the low spindle speed level with the high level of depth of cut and vice versa. The first two sets are performed on an aluminum test bar 12 inches in length and 3 inches in diameter. The third set is performed on a long and slender bar measuring 2 inches in diameter and 24 inches in length. Negative feedback is implemented in trials 1, 4, 5,6 and hybrid control scheme is implemented in trial 2 and 3. The values for the cutting conditions for the six trials are listed in Table 5.8

Table 5. 8: Cutting Conditions

Trial	Spindle speed rpm	Feed rate in/rev	Depth of cut in
1	470	0.003	0.01
2	470	0.002	0.01
3	470	0.002	0.04
4	470	0.002	0.02
5	470	0.002	0.02
6	260	0.002	0.03

### 5.3.2.3 Results and Analysis

It has been noticed that the implementation of controller can reduce the vibration during machining. However, the performance obtained in the shop floor experiments is not as good as that obtained in the laboratory experiments, because the laboratory experiments were conducted in a controlled environment.

In order to account for the changing disturbance characteristics, a statistical approach is taken to evaluate the performance of the controller. Since the lowest spindle speed selected is 260 rpm, the smallest frequency component in the cutting process is found by dividing the spindle speed by 60. The result is more than 4 Hz. Experimental data of 25 seconds are collected where the controller is tuned on at about half of the time. The data collected during the first 8 seconds are used to represent the machine tool displacement without the controller, and the data collected during the last 8 seconds are used to represent the machine tool displacement with the application of the controller. Each data set is further divided into 16 samples, thus each sample is for the duration of 0.5 second.

The three performance indices, RMS, AA, and PTV are calculated for the machine tool displacement of each sample of the two sets: one without control and the other with control, as listed in Table 5.9.

Table 5.9: Performance Indices for 16 Samples

a) Trial #1

RMS		AA		PTV	
w/o c	w.c.	w/o. c	w. c.	w/o c.	w. c.
27.1910	20.9230	20.4516	16.6367	215.0000	123.0000
19.7765	21.2975	15.7472	15.9902	113.0000	161.0000
20.0430	16.3241	16.3739	12.7348	108.0000	101.0000
23.6579	17.9846	18.6478	14.5918	142.0000	101.0000
16.6950	21.4043	13.2692	16.7596	101.0000	134.0000
21.3913	15.6078	16.5202	12.1873	151.0000	96.0000
18.9764	18.6661	15.0181	14.7499	118.0000	118.0000
19.5453	21.2277	15.0782	16.7403	128.0000	120.0000
19.3601	18.0737	15.4566	14.2951	114.0000	111.0000
23.8158	18.9885	17.3584	14.9922	199.0000	114.0000
22.2178	19.5858	16.2629	14.8399	171.0000	140.0000
19.1351	18.8329	14.8778	15.0668	119.0000	108.0000
16.8018	17.9011	13.1192	13.9573	103.0000	114.0000
18.7578	15.7823	14.8108	12.7832	116.0000	89.0000
17.9778	17.7515	14.4659	13.9825	95.0000	105.0000
18.2901	18.3607	14.5569	14.8751	106.0000	100.0000

b) Trial #2

RMS		AA		PTV	
w/o c	w.c.	w/o. c	w. c.	w/o c.	w. c.
111.7462	114.5170	89.2422	94.0107	684.0000	695.0000
117.3701	105.6333	95.4312	83.6035	665.0000	702.0000
125.6606	110.8586	100.9692	89.3592	841.0000	595.0000
112.9140	113.5461	91.4096	91.0281	733.0000	697.0000
109.3025	104.0913	88.4746	83.1499	633.0000	623.0000
110.5618	113.1755	88.7446	89.6976	664.0000	719.0000
118.1013	110.6128	93.6081	91.5394	691.0000	574.0000
104.8025	104.7798	83.1292	82.0822	576.0000	594.0000
132.4115	103.1587	108.8172	83.8645	671.0000	539.0000
109.7817	104.1929	89.8250	81.5195	618.0000	661.0000
115.3309	101.2187	93.7101	82.5632	578.0000	536.0000
130.4292	103.6672	106.6370	84.5353	752.0000	553.0000
119.8999	105.3354	95.2830	84.4391	645.0000	603.0000
122.3298	93.6576	101.6581	74.5439	674.0000	551.0000
111.4183	96.6896	92.1605	75.7015	542.0000	654.0000
123.1777	98.2945	100.8296	79.1843	642.0000	531.0000

c) Trial #3 (times 1000)

RMS		AA		PTV	
w/o c	w. c.	w/o. c	w. c.	w/o c.	w. c.
0.1950	0.1586	0.1574	0.1311	1.1560	0.8110
0.1841	0.1621	0.1470	0.1317	0.9550	0.8230
0.1825	0.1652	0.1465	0.1368	0.9350	0.8220
0.1933	0.1985	0.1557	0.1586	1.0470	1.2560
0.2294	0.1607	0.1755	0.1314	1.6310	0.8140
0.1826	0.1559	0.1555	0.1285	0.8680	0.7930
0.1777	0.1621	0.1506	0.1305	0.7900	0.8520
0.1756	0.1822	0.1504	0.1455	0.8370	1.0570
0.1790	0.1657	0.1502	0.1350	0.9850	0.8490
0.1841	0.1531	0.1567	0.1234	0.9240	0.8730
0.1658	0.1594	0.1400	0.1239	0.7860	0.9500
0.1613	0.1569	0.1353	0.1237	0.8660	0.8950
0.1706	0.1644	0.1448	0.1329	0.8530	0.9180
0.1813	0.1479	0.1512	0.1174	0.9220	0.7740
0.1695	0.1941	0.1396	0.1581	0.8770	1.0910
0.1821	0.1851	0.1482	0.1515	0.9620	0.9880

d) Trial #4

RMS		AA		PTV	
w/o c	w. c.	w/o. c	w. c.	w/o c.	w. c.
108.0374	88.8468	87.9120	70.1495	574.0000	553.0000
104.7980	100.0446	83.6640	79.5540	634.0000	605.0000
98.0226	100.0084	79.8162	80.4571	514.0000	636.0000
106.2174	100.5081	86.3106	77.6584	514.0000	631.0000
107.0612	101.4535	86.7209	80.4531	679.0000	535.0000
111.8774	98.3680	90.1798	76.7558	655.0000	526.0000
117.6848	108.9445	94.6643	88.0807	630.0000	621.0000
108.2642	106.5000	89.0256	84.6950	566.0000	623.0000
101.1508	98.8373	82.6660	77.2110	512.0000	577.0000
118.9805	102.2629	94.3629	83.0780	710.0000	573.0000
112.7133	96.0455	92.4687	75.1390	574.0000	628.0000
120.1030	91.7817	98.3396	70.3993	647.0000	700.0000
114.7128	103.0381	90.3396	82.0855	656.0000	556.0000
116.9407	93.3960	90.9909	75.2202	762.0000	490.0000
116.7842	87.9945	94.1721	70.8545	614.0000	545.0000
102.5749	100.3293	82.6620	82.1031	518.0000	592.0000

e) Trial #5 (times 1000)

RMS		AA		PTV	
w/o c	w. c.	w/o c	w. c.	w/o c.	w. c.
0.2327	0.2015	0.1839	0.1597	1.4970	1.1740
0.1962	0.2014	0.1545	0.1604	1.1280	1.1460
0.2165	0.1777	0.1725	0.1394	1.4470	1.0990
0.1970	0.1942	0.1555	0.1539	1.3080	1.1690
0.2191	0.1840	0.1730	0.1429	1.3890	0.9880
0.2115	0.1945	0.1713	0.1470	1.1900	1.3500
0.1832	0.1981	0.1474	0.1583	1.1410	1.0460
0.2062	0.1792	0.1591	0.1428	1.5400	1.1210
0.1912	0.1690	0.1521	0.1375	1.1490	1.0450
0.2284	0.1538	0.1820	0.1200	1.2960	0.8850
0.1825	0.1841	0.1459	0.1409	1.0860	1.0820
0.1864	0.1909	0.1473	0.1490	1.1180	1.1110
0.1875	0.1901	0.1474	0.1501	1.0470	1.2360
0.2206	0.1896	0.1746	0.1518	1.4400	1.1160
0.1951	0.1729	0.1551	0.1342	1.2270	1.1010
0.2075	0.2084	0.1657	0.1642	1.3360	1.4010

f) Trial 6 (times 1000)

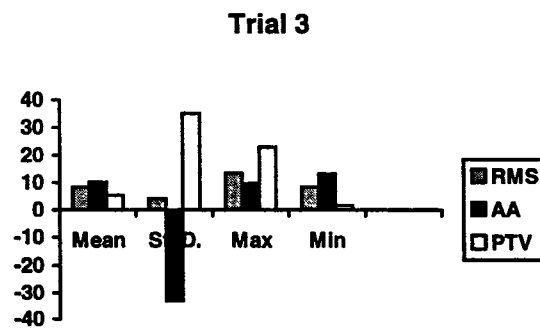
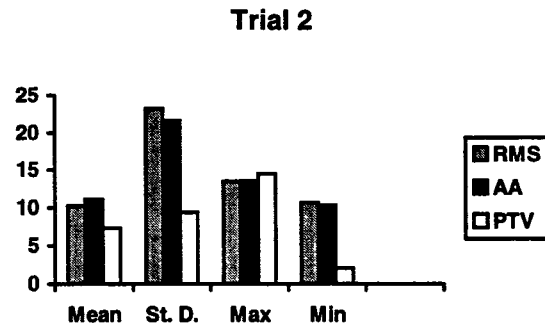
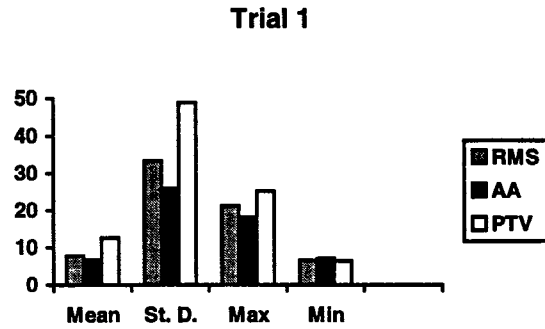
RMS		AA		PTV	
w/o c	w. c.	w/o c	w. c.	w/o c.	w. c.
0.1403	0.1323	0.1072	0.1048	0.9000	0.8830
0.1499	0.1352	0.1165	0.1051	0.9170	0.8860
0.1466	0.1316	0.1136	0.1000	0.8870	0.8660
0.1379	0.1324	0.1073	0.0985	1.0160	0.8720
0.1534	0.1361	0.1200	0.1054	1.0280	0.8540
0.1589	0.1223	0.1245	0.0948	1.2930	0.7850
0.1475	0.1252	0.1131	0.0965	1.2040	0.9980
0.1519	0.1277	0.1166	0.0999	1.1140	1.0640
0.1488	0.1208	0.1163	0.0944	0.9990	0.7810
0.1447	0.1299	0.1131	0.1023	1.0600	1.0000
0.1496	0.1386	0.1167	0.1077	1.0050	1.0080
0.1360	0.1352	0.1040	0.1060	0.8460	0.7980
0.1265	0.1285	0.0943	0.0986	0.8850	0.8980
0.1355	0.1351	0.1003	0.1038	0.8940	0.9610
0.1382	0.1230	0.1051	0.0953	0.8930	0.7960
0.1264	0.1173	0.0954	0.0913	0.8860	0.8500

The statistical measures—mean, standard deviation, maximum, and minimum values—are determined for each performance indices for the six trials and are listed in Table 5.10.

Table 5. 10: Statistical Measures of the Performance Indices

RMS		AA		PTV	
w/o c	w. c.	w/o. c	w. c.	w/o c.	w. c.
mean					
0.0202	0.0187	0.0158	0.0147	0.1312	0.1147
0.1172	0.1052	0.0950	0.0844	0.6631	0.6142
0.1821	0.1670	0.1503	0.1350	0.9621	0.9104
0.1104	0.0986	0.0890	0.0784	0.6099	0.5869
0.2039	0.1868	0.1617	0.1470	1.2712	1.1294
0.1433	0.1295	0.1102	0.1003	0.9892	0.8938
standard deviation					
0.0028	0.0019	0.0019	0.0014	0.0357	0.0183
0.0080	0.0061	0.0071	0.0055	0.0726	0.0658
0.0155	0.0148	0.0093	0.0123	0.2017	0.1309
0.0068	0.0058	0.0052	0.0052	0.0755	0.0527
0.0163	0.0140	0.0130	0.0114	0.1574	0.1254
0.0093	0.0062	0.0087	0.0049	0.1279	0.0883
maximum					
0.0272	0.0214	0.0205	0.0168	0.2150	0.1610
0.1324	0.1145	0.1088	0.0940	0.8410	0.7190
0.2294	0.1985	0.1755	0.1586	1.6310	1.2560
0.1201	0.1089	0.0983	0.0881	0.7620	0.7000
0.2327	0.2084	0.1839	0.1642	1.5400	1.4010
0.1589	0.1386	0.1245	0.1077	1.2930	1.0640
minimum					
0.0167	0.0156	0.0131	0.0122	0.0950	0.0890
0.1048	0.0937	0.0831	0.0745	0.5420	0.5310
0.1613	0.1479	0.1353	0.1174	0.7860	0.7740
0.0980	0.0880	0.0798	0.0701	0.5120	0.4900
0.1825	0.1538	0.1459	0.1200	1.0470	0.8850
0.1264	0.1173	0.0943	0.0913	0.8460	0.7810

In Figure 5.15, the percent reduction due to the controller in the three performance indices for each of the four statistical measures is shown.





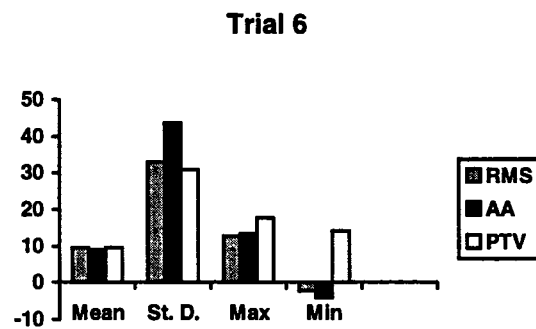
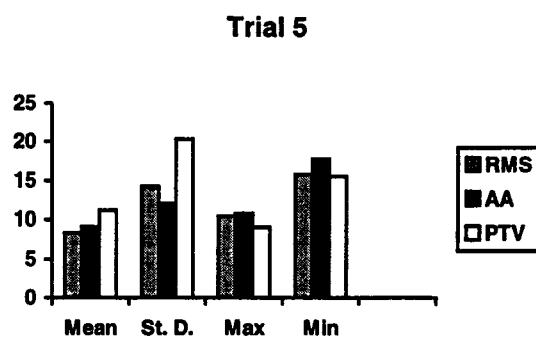
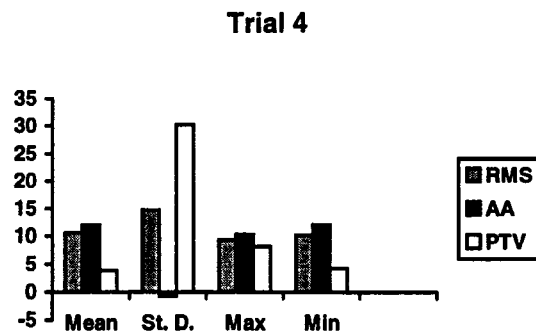


Figure 5. 15: Statistical Measures of Tool Vibration Reduction

The percent reduction of the mean level of the tool vibration for all the six trials is about 10%. The variation is observed in the standard deviation. A close examination at the results shows that there is no significant advantage of one method over the other.

### 5.3.2.4 Roughness Measurements

A set of experiments is performed to determine the roughness average of the 3 test bars. A negative feedback control is implemented. The full detail of experimental results is provided in the Appendix. Here, the four trials that show the best attenuation are discussed. The cutting conditions for these four trials are listed in Table 5.11.

Table 5.11 Selected Trials

Trial	Test bar	Spindle speed rpm	Feed rate in/rev	Depth of cut in
1	long	625	0.002	0.03
2	long	470	0.002	0.02
3	short #1	260	0.002	0.03
4	short #1	190	0.002	0.04

The surface conditions of the machined test bars, mainly, the surface finish, are analyzed by using a profilometer at the National Institute of Standards and Technology, Gaithersburg, Maryland. For each trial, the roughness average  $R_a$  is calculated for the machining performance for the cases either without or with the controller. The  $R_a$  values for the samples taken for each trial are listed in Table 5.12.

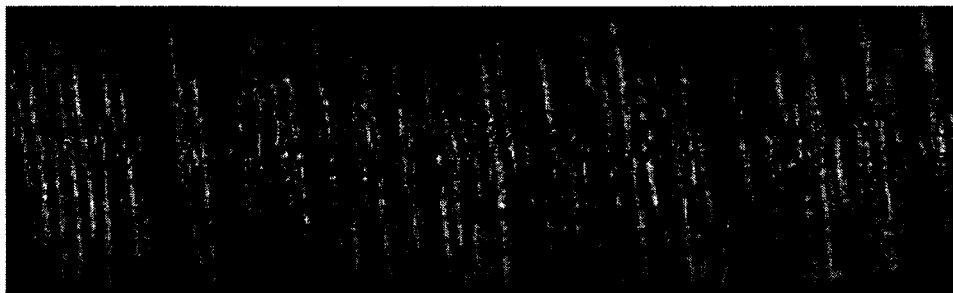
Table 5.12 Roughness Average Measurement

	Trial 1		Trial 2		Trial 3		Trial 4	
	w/o c	w.c.	w/o c.	w.c.	w/o c.	w.c.	w/o c.	w.c.
$R_{a_1}$	1.8600	1.4900	0.6800	0.3900	0.5200	0.4300	0.3900	0.3400
$R_{a_2}$	2.2000	1.1700	0.4500	0.4800	0.4300	0.3200	0.3700	0.3500
$R_{a_3}$	1.7000	1.6300	0.5100	0.3400	0.5400	0.3900	0.4700	0.3500
$R_{a_4}$	2.0100	1.5600	0.6800	0.4700	0.6100	0.3800	0.3500	0.3600
$R_{a_5}$	1.4300	1.4300	0.7000	0.4600	0.6000	0.3900	0.4400	0.3500

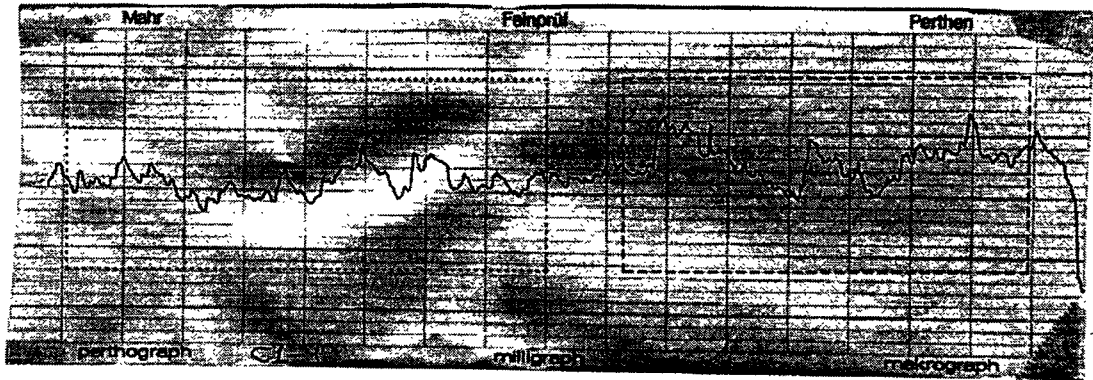
The test bar is further photographed using a CCD camera instrument available at the Advanced Design and Manufacturing Laboratory. In Figure 5.16, the photographic picture of the test bar, the roughness measurement of the test bar, and the statistical measures of the measured Ra values are shown.



Without control



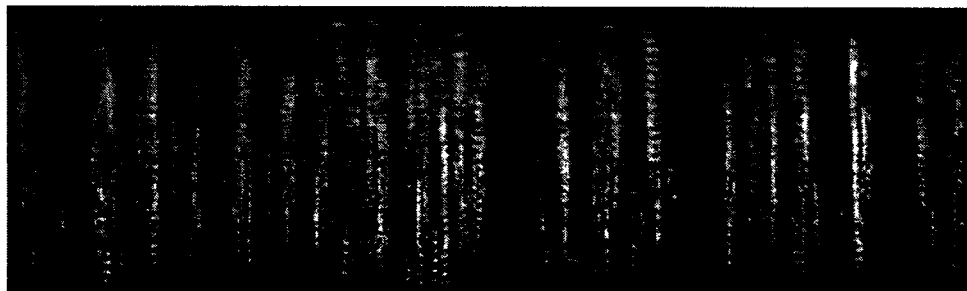
With control



where, the machine tool displacement with the control is in box , while the machine tool displacement without the control is in the box

Roughness Average (Ra)	no control	with control
Mean	1.84	1.456
Standard Deviation	0.2944	0.1766
Max.	2.2	1.63
Min.	1.43	1.17

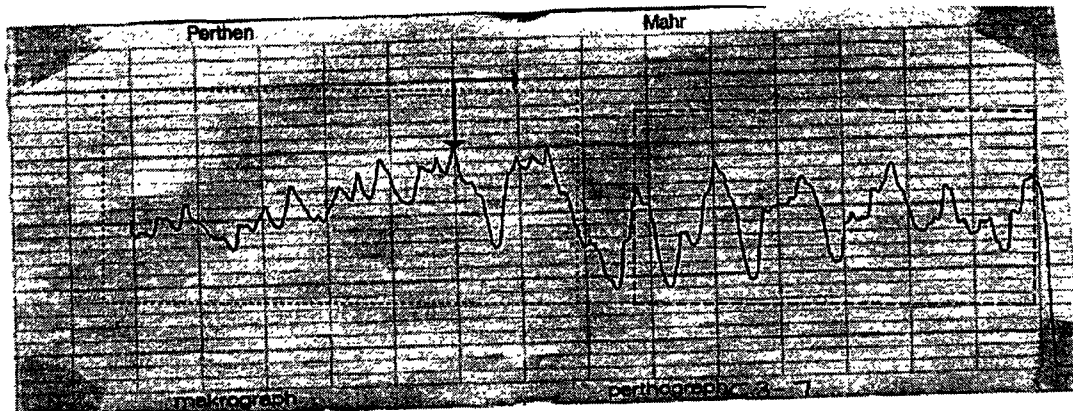
a) Trial #1



Without control



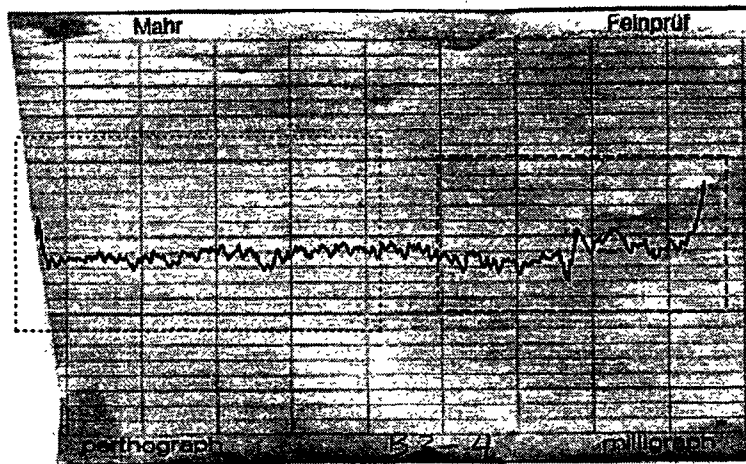
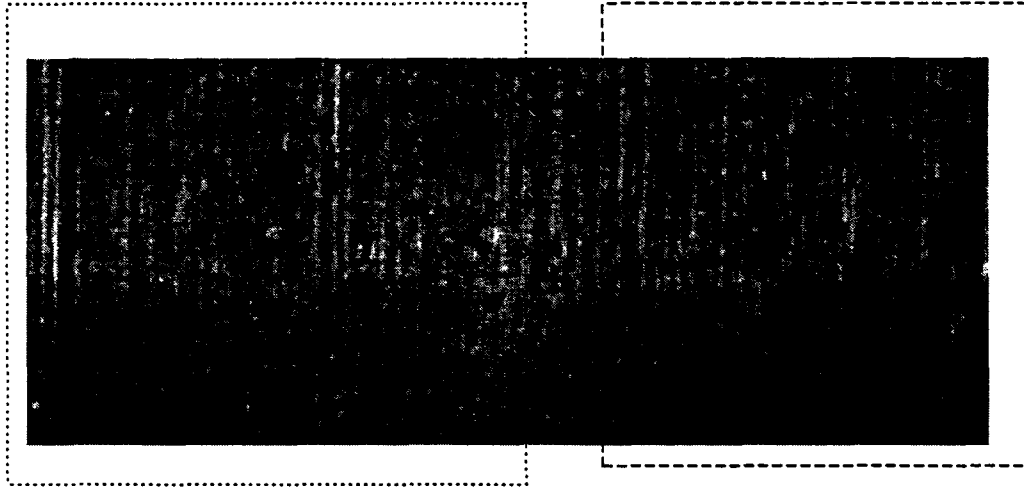
With control



where, the machine tool displacement with the control is in the box ,  
while the machine tool displacement without the control is in the box .

Roughness Average (Ra)	no control	with control
Mean	0.604	0.428
Standard Deviation	0.1155	0.0606
Max.	0.7	0.48
Min.	0.45	0.34

b) Trial #2

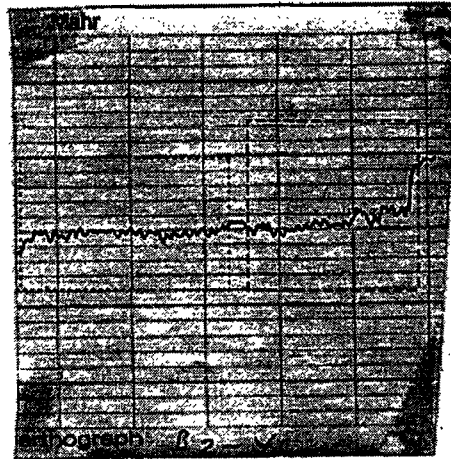
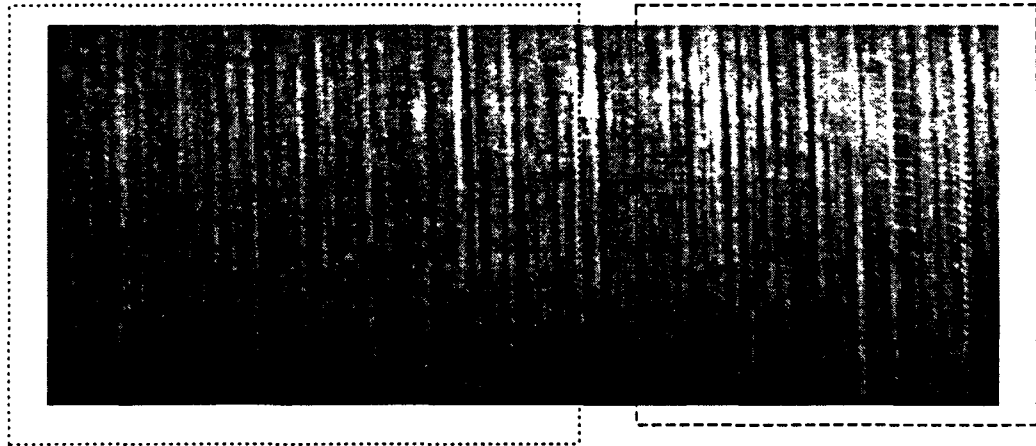


where, the machine tool displacement with the control is in the box  ,

while the machine tool displacement without the control is in the box .

Roughness Average (Ra)	no control	with control
Mean	0.404	0.35
Standard Deviation	0.0498	0.0071
Max.	0.47	0.36
Min.	0.35	0.34

d) trial #3



where, the machine tool displacement with the control is in the box  ,  
 while the machine tool displacement without the control is in the box .

Roughness Average (Ra)	no control	with control
Mean	0.54	0.382
Standard Deviation	0.0725	0.0396
Max.	0.61	0.43
Min.	0.43	0.32

d) trial #4

Fig. 5.16 Surface Roughness Measurement Data

The percentage reduction in the Ra value when the controller was applied is calculated for the statistical measures and it is shown in Figure 5.17.

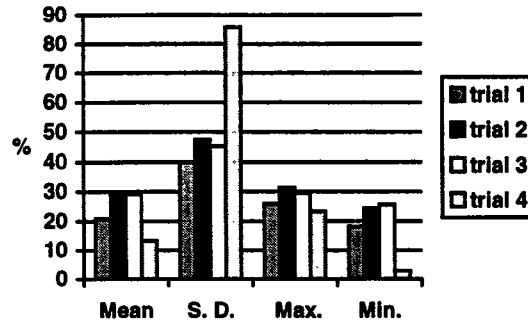


Figure 5.17: Statistical Measures of Tool Vibration Reduction

### 5.3.3 Turning Operation with one End Supported

In order to explore the capability of the designed controller in compensating tool vibration, a special case study is carried out in this thesis research. The test bar, instead of being supported at both ends, is suspended at the tail stock end. This special setup resembles a cantilever beam structure. When the cutting force is generated and is acting on the test bar, the test bar will vibrate following the dynamic characteristics of a cantilever beam. Such an accelerated tool vibration provides a unique environment to examine the compensation capability. From the previous discussions, it has been seen that the feedforward control scheme yields the highest reduction of tool vibration when the disturbance is known. Therefore, this effort opens a door for a future smart tool post design for machining operations where such a control strategy can be applied.

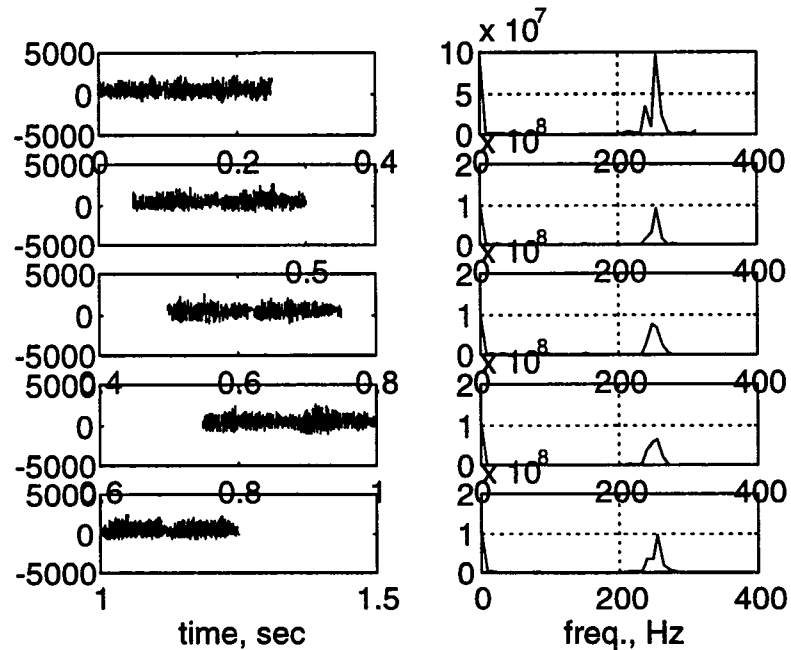


### 5.3.3.1 System Disturbance Characterization

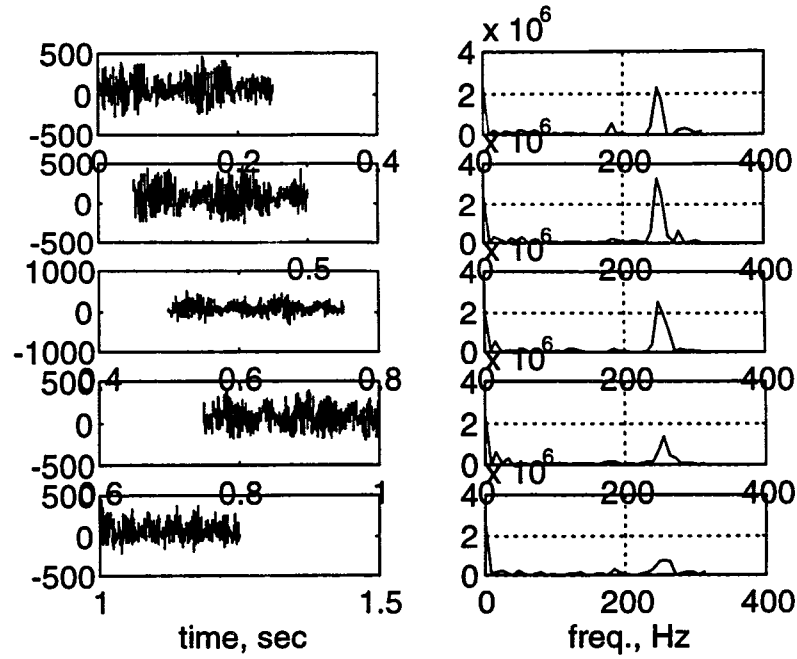
As stated in the previous section, a cantilever setup is used to study the disturbance characteristics. Trials have been conducted for machining conditions with different settings of spindle speed, feedrate, and depth of cut. The main objective is to introduce chatter into the system and then compensate for it.

It has been observed that significant tool vibration may not be present when the spindle speed setting is below 470 rpm. Therefore, a spindle speed of 470 rpm and 625 rpm are selected for the study. The feedrate in the range of 0.0015 to 0.002 in/rev is selected. The depth of cut is selected between 0.0005 to 0.002 in. The signal analyzer is used to detect the frequency peaks. The sampling rate is 3.2 kHz.

Examining the associated frequency spectra, a dominant frequency is evident as shown in Figure 5.18.



a) s.s.=470, fr=0.002, doc=0.001



b) s.s. 470, fr. =0.0015; d.o.c=0.001

Figure 5. 18: Disturbance Signal Analysis

### 5.3.3.2 Design of Experiment

The design parameters identified in the laboratory experimentation are implemented in this experiment. A reference signal with the dominant frequency is used in the feedforward control scheme. The dominant frequency was determined by using the signal analyzer. Experiments are performed from the cutting conditions listed in Table 5.13. Some of the cutting conditions are repeated to gain an estimate of the vibration attenuation while maintaining the cutting condition.

Table 5. 13: Cutting Conditions

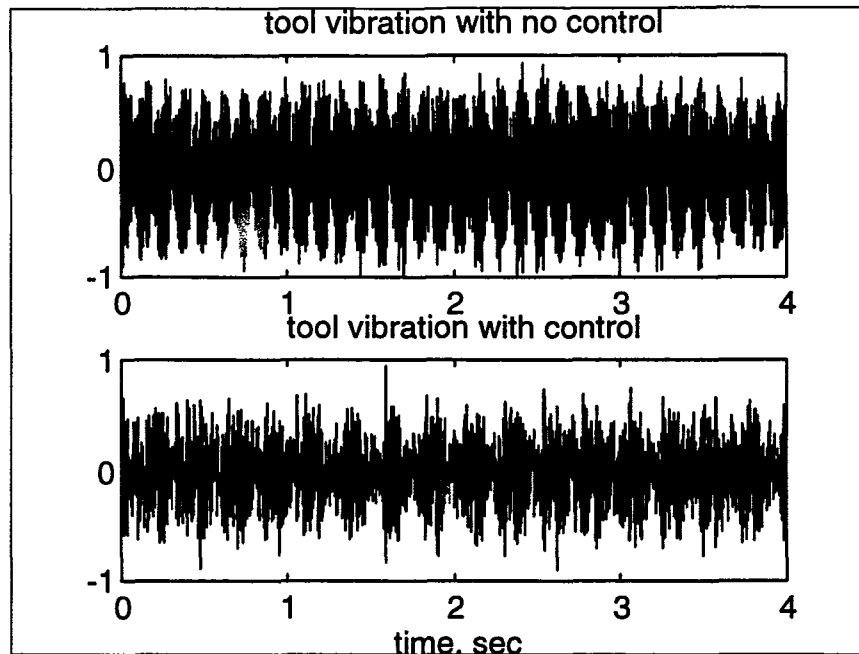
Trial	Spindle speed rpm	Feed rate in/rev	Depth of cut in
1	470	0.002	0.01
2	470	0.002	0.01
3	470	0.002	0.01
4	470	0.002	0.01
5	470	0.0015	0.01
6	470	0.0015	0.015
7	625	0.002	0.01

Trial 1 through 3 are performed by keeping the cutting condition the same to evaluate the vibration reduction for different initial roughness conditions.

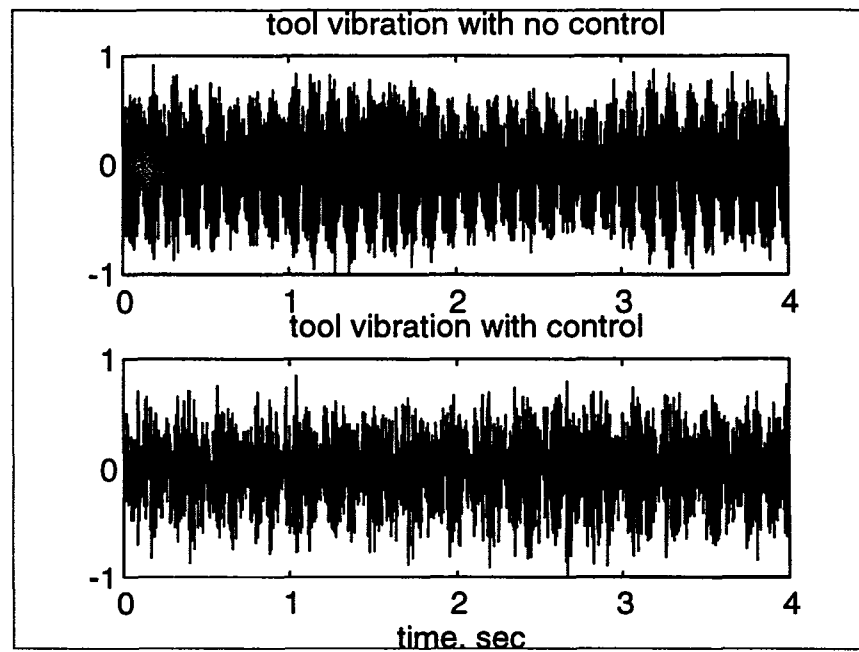
The next four trials are conducted after changing the boundary condition by resetting the tool bar on the lathe. They are selected in such a way that the two cutting conditions are kept constant, and the third cutting condition is varied in two levels. In trials 4 and 5, the spindle speed and the depth of cut is kept constant and the feedrate is varied. In trials 5 and 6, the spindle speed and the feedrate are kept constant and the depth of cut assumes two levels. Finally, in trials 4 and 7, the feedrate and the depth of cut is kept the same while the spindle speed takes two levels of values.

#### 5.3.3.3 Results and Analysis

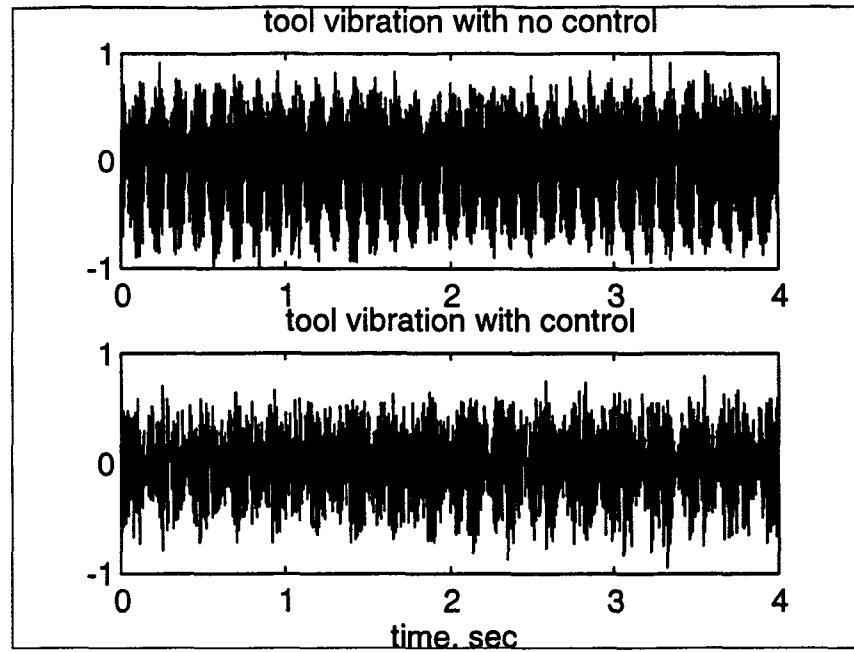
The tool vibration with and without the controller is normalized to a scaling range [-1 1], and the results are depicted in Figure 5.19.



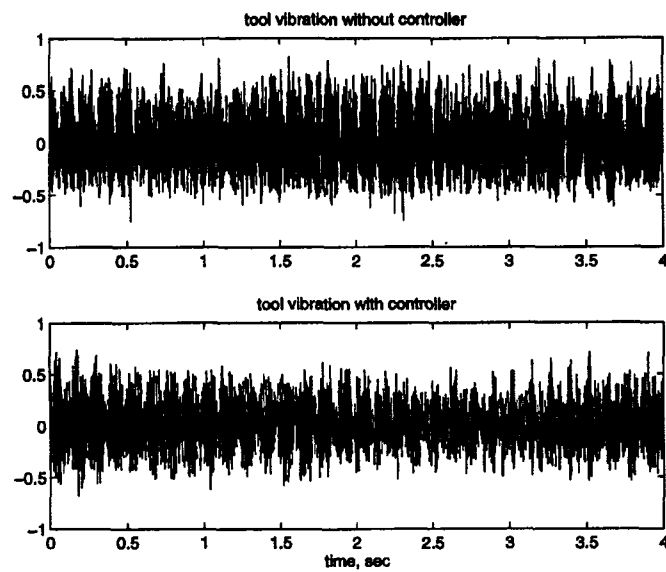
a) trial #1



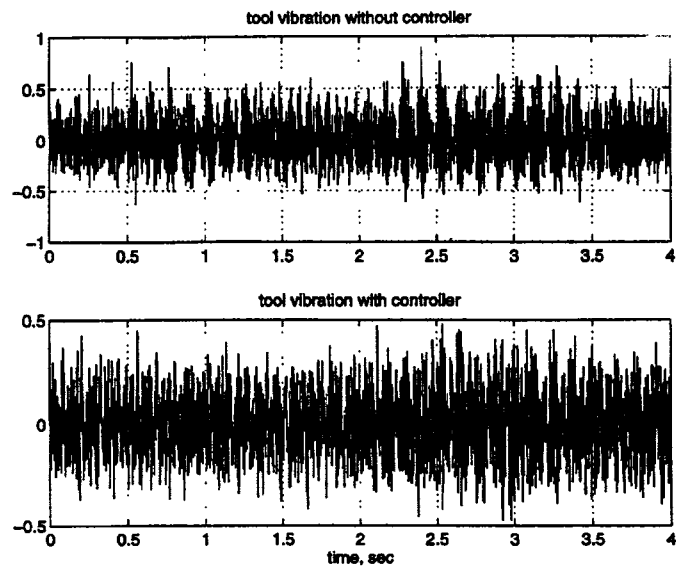
b) trial #2



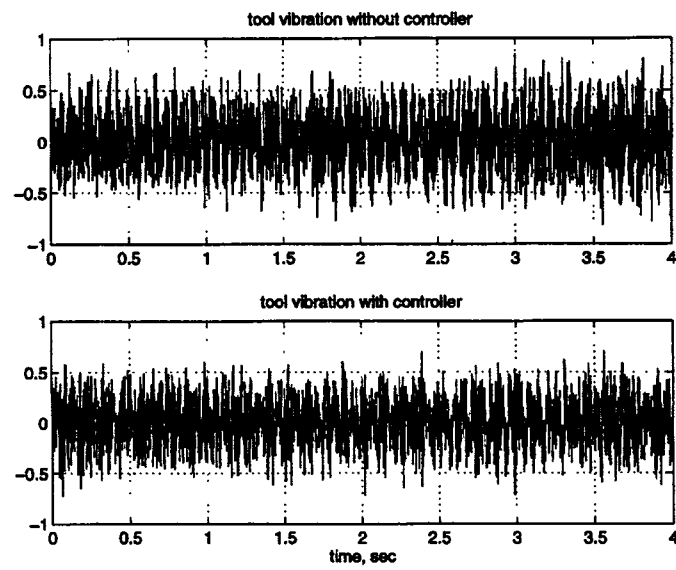
c) trial #3



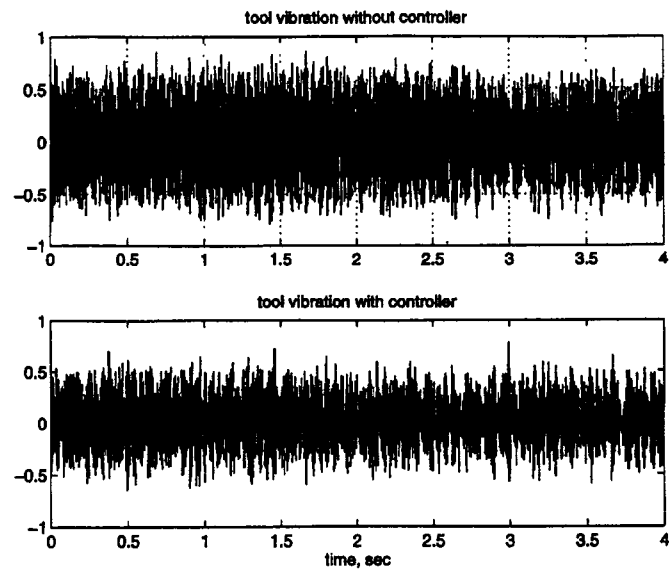
d) trial #4



e) trial #5



f) trial #6



g) trial #7

Figure 5.19: Tool Vibration with and without Control

The percentage reduction is calculated using the three performance indices as shown in Figure 5.20.

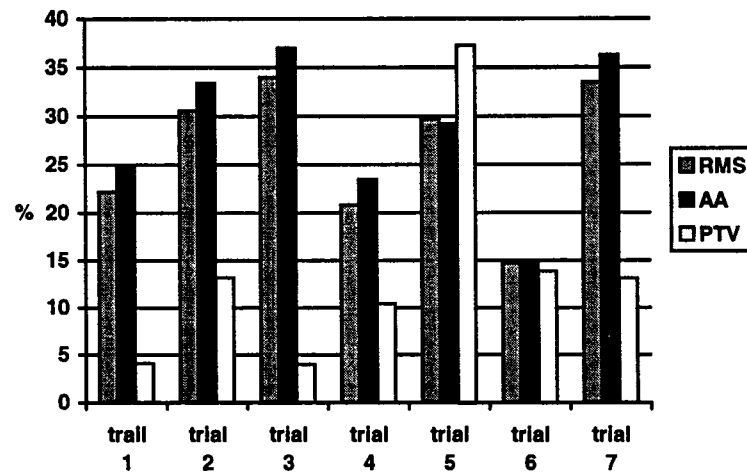


Figure 5.20 Percent Tool Vibration Reduction

The repetition of trial 1 by trial 2 and 3 shows that the tool vibration reduction is getting better and better. Take the AA index as an example, the reduction for trial 1 is 23%. The reduction changes to 31% for trial 2, and it changes to 34% for trial 3. This finding is very important to illustrate that, as long as the cutting condition remains the same, the performance of the controller is enhanced in time. When the boundary condition of the test bar varies, for example, the new clamping condition of the test bar, the reduction magnitude may change.

When the spindle speed is increased in trial 7 from trial 4, reduction of tool vibration is further improved. When the feedrate is reduced from trial 4 to 5, the percentage reduction is getting better. When the depth of cut is reduced to a very low value, the reduction of tool vibration seems not very effective.



## Chapter 6

### CONCLUSIONS AND RECOMMENDATIONS

#### 6.1 Conclusions

The focus of this thesis research is to introduce the advanced neural network control methodology to tool vibration compensation. The goals of this thesis research are successfully met. In all aspects of the studies performed, a significant reduction in tool vibration during machining was achieved for a variety of machining operations. Certainly, reduction in tool vibration was not significant for many other machining settings. This implies the complexity to control tool vibration during machining.

Investigations conducted in this thesis research include mathematical modeling, computer simulation, system implementation, and experimental verification. Significant findings are summarized as follows:

1. The two major parts of a mechatronic system are electrical and mechanical components. The mechanical part lays a foundation for carrying out tool vibration compensation, and the electrical part provides the intelligence to command the PMN actuators to function as desired.
2. Three linear neural network control schemes, feedforward, feedback, and hybrid (a combination of both) have been studied. Results obtained from this thesis research strongly indicate that the feed forward neural network system represents

the best choice among the three for tool vibration reduction. The reasons for its superior performance of the feedforward control are as follows:

- a) The zero delay in actuating the control action. It is a prevention control that generates the system output which counteract the disturbance upon its arrival.
- b) A sizable stability margin. The adaptation coefficient for the feedforward control scheme can be maintained constant while maintaining stability. However, the adaptation coefficient should be reduced on-line for the other two schemes to ensure stability.

3. Experimental results show the reduction of tool vibration during machining. This indicates that smart material made actuators, such as PMN actuators, are good candidates to be used by the machine tool industry. In this thesis research, guidelines to use the linear neural network, namely, digital filters, to drive PMN actuators are developed. These guidelines are listed as follows:

- a) The gain of reference and error signals should be set to the limits of the circuit board to maximize the cancellation capability of the controller. The stability issue due to the reference gain can be handled through the use of the adaptation coefficient. The additional advantage is the reduction of the control variables to play with. This is important in machining operations where the complexity of controlling tool vibration poses more difficulties than what has been encountered in the lab environment.

- b) Characterization of PMN actuator performance is critical to the success of control action. Therefore, an off-line system identification for PMN actuators is essential to define the working range of the power amplifier, including the driving frequency and the magnitude. By using the off-line system identification, the stability of the system can be significantly improved since coupling between the controller adaptation algorithm and the emulator adaptation algorithm, that cause system instability, will be eliminated.
- c) The systematic design approach developed in this thesis work should be used in a controlled environment in order to arrive at the control design parameters for the machining operation
- d) Since it is found that the Finite Impulse Response (FIR) type filters perform well in machine tool vibration reduction, they are most suitable for the control filter for the smart tool post application. The first and most important feature of FIR filters is their inherent stable architecture. The lack of inherent stability characteristics in the IIR filters, unlike FIR filters, is due to the presence of the feedback section of the filter. It creates a way for the output to reinforce itself with high weight gains, leading to an unstable control system.

The main contributions of this thesis research are:

1. A successful implementation of PMN actuators for in-process vibration cancellation in turning operation.
2. A successful implementation of linear neural network methodology for active machine tool vibration cancellation.
3. Development of guidelines for identification of the neural structure of nonlinear neural network.

## 6.2 Recommendations

The complexity of controlling tool vibration has been well recognized for centuries. The effort made in this thesis research, although demonstrating the great promising by using PMN actuators, would be difficult, if not impossible, in accomplishing the journey to conquer the problem of tool vibration control. The following list represents recommendations for future work to control tool vibration and improve machining accuracy:

1. The need to acquire a better sensing system. The sensing system used in this thesis work is the type of variable impedance transducer. Although the accuracy is good, a better accuracy is desired. Such accuracy improvement will increase the accuracy of the control action.
2. When heavy machining duties are required, the tool post is subjected to severe dynamic loading conditions. Control of tool motion and/or compensation of tool vibration become more complex. In order to effectively compensate under heavy

duty machining operations, an optimal working condition for the PMN actuators should be identified. This may lead to a working range which is not linear between the voltage and the displacement. Therefore, a nonlinear neural network control system with parallel processing hardware is highly recommended.

3. A modified design of the tool post which accommodates both displacement and cutting force sensors is desirable to apply the tool post effectively in turning operation where disturbance is unknown. In doing so, the signal from the force sensor can be used as a reference signal, whereas, the signal from the displacement sensors can be used as an error signal. When such capabilities exist, feedforward control can be applied with the superior performance proven in this research.

## Appendix

### SURFACE PROFILE MEASUREMENT

The surface profile of the machined surfaces for different cutting conditions are shown below. The cutting process is performed with and without the controller. The controller is not implemented for the first 40% period of the time. The machining is done on the test bar right to the left. Since the surface profile is measured from left to the right, the first part of the picture represent the case where the controller is not applied.


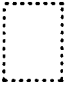
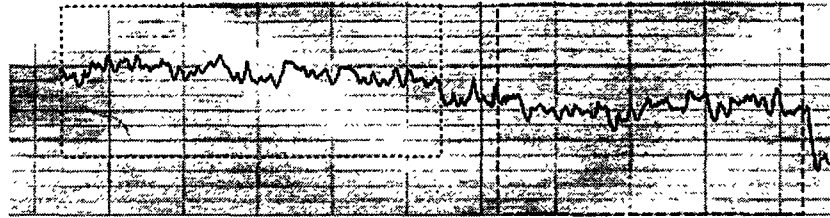
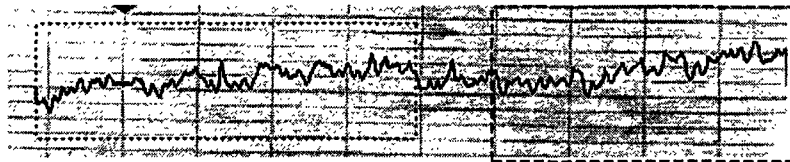
In the figures, the case without the controller is represented by the box, , while the case with the controller is represented by the box, . The cutting conditions for the different trials are given in Table A.1

Table A.1 Cutting Conditions

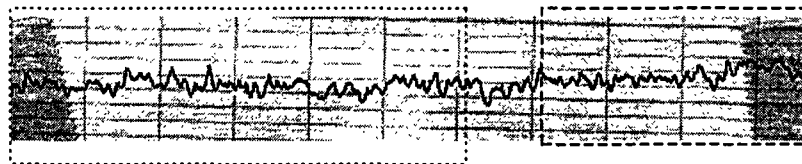
Trials	Spindle speed rpm	Depth of cut in	Feed rate in/rev
1	350	0.004	0.002
2	470	0.02	0.002
3	625	0.03	0.002
4	190	0.04	0.002
5	260	0.03	0.002



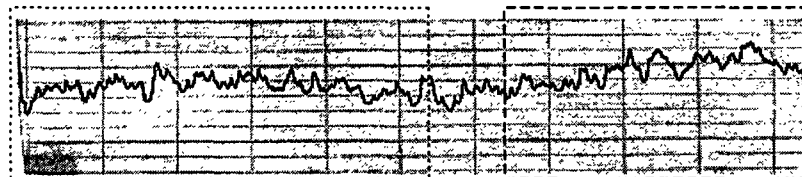
a) adaptation coefficient reduced on-line from 100 to 50



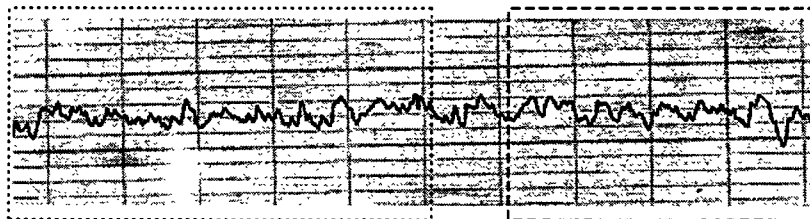
b) adaptation coefficient reduced on-line from 150 to 50



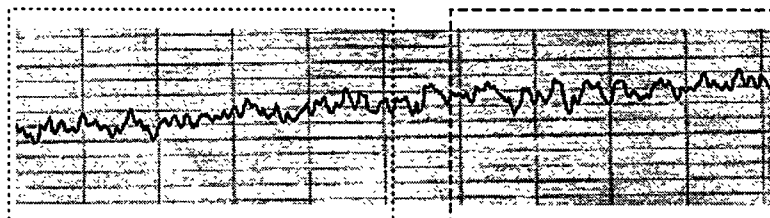
c) adaptation coefficient reduced on-line from 200 to 50



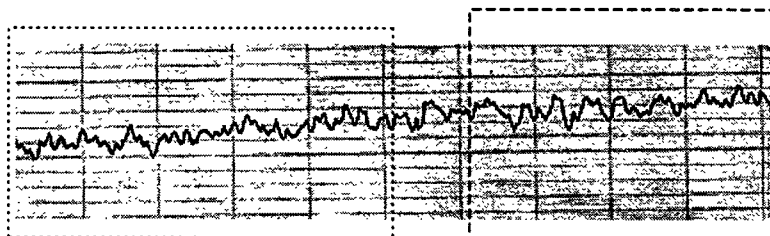
d) adaptation coefficient reduced on-line from 100 to 50



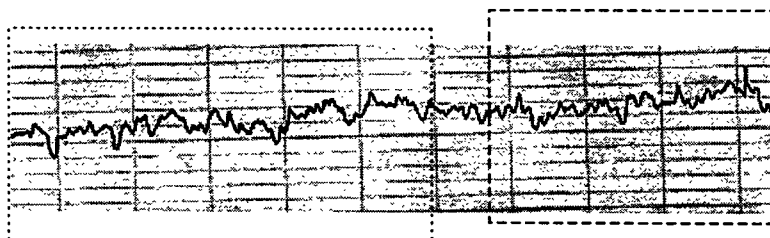
e) adaptation coefficient reduced on-line from 150 to 50



f) adaptation coefficient reduced on-line from 200 to 50

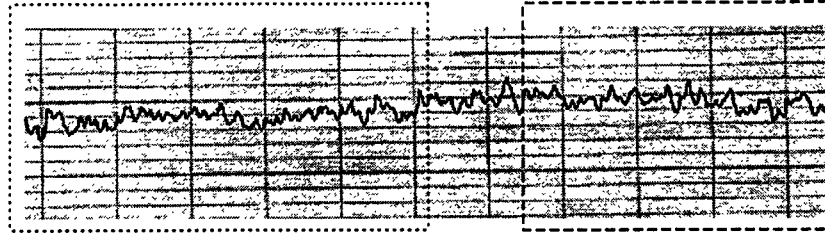


g) adaptation coefficient reduced on-line from 100 to 50



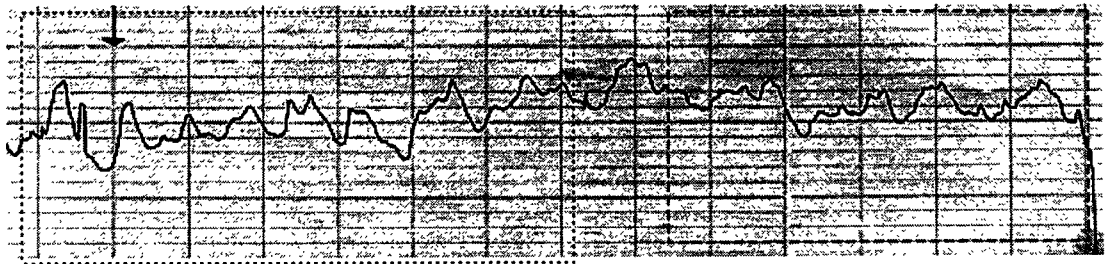
h) adaptation coefficient reduced on-line from 150 to 50



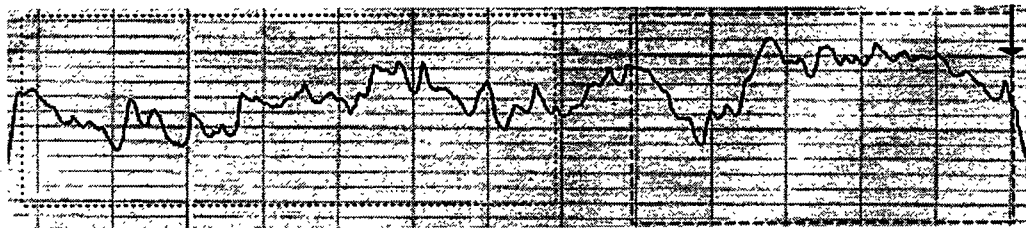


I) adaptation coefficient reduced on-line from 200 to 50

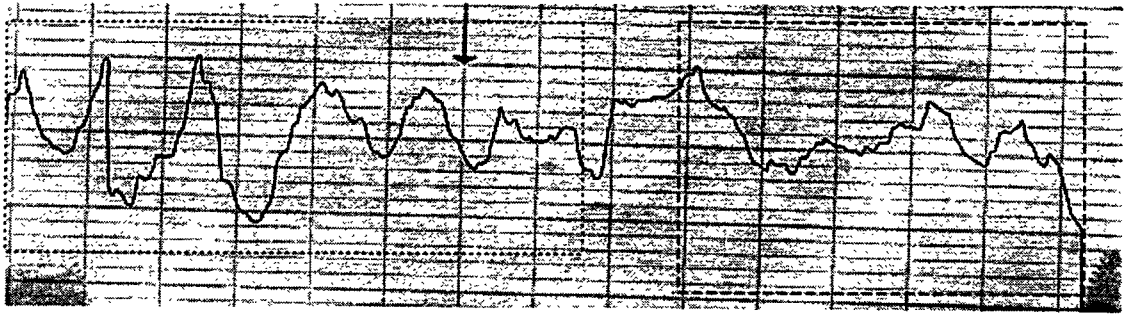
Figure A.1: Surface Profile for Trial 1



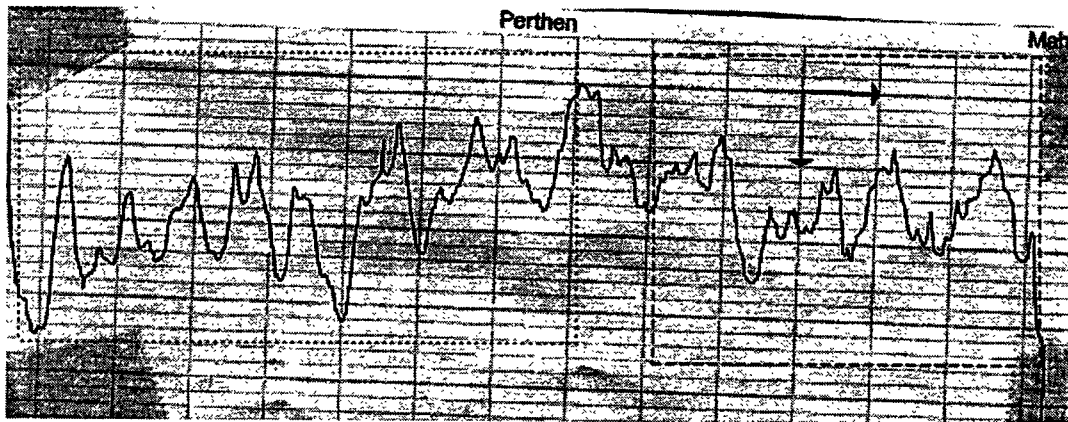
a) adaptation coefficient reduced on-line from 100 to 50



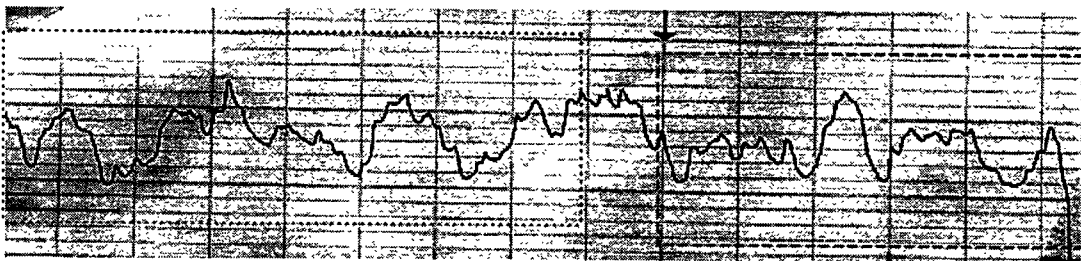
b) adaptation coefficient reduced on-line from 150 to 50



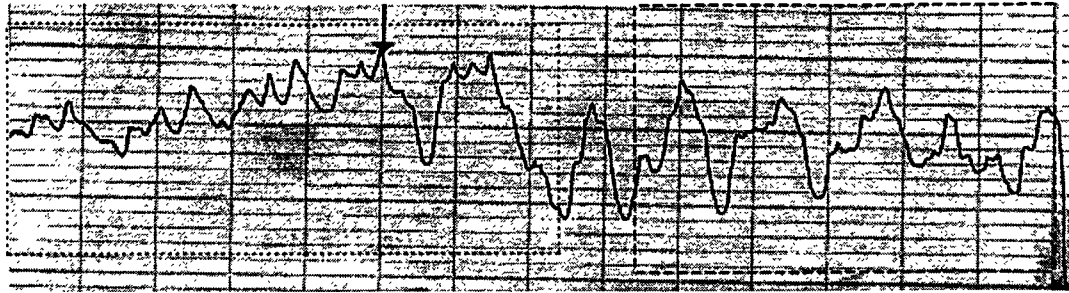
c) adaptation coefficient reduced on-line from 200 to 50



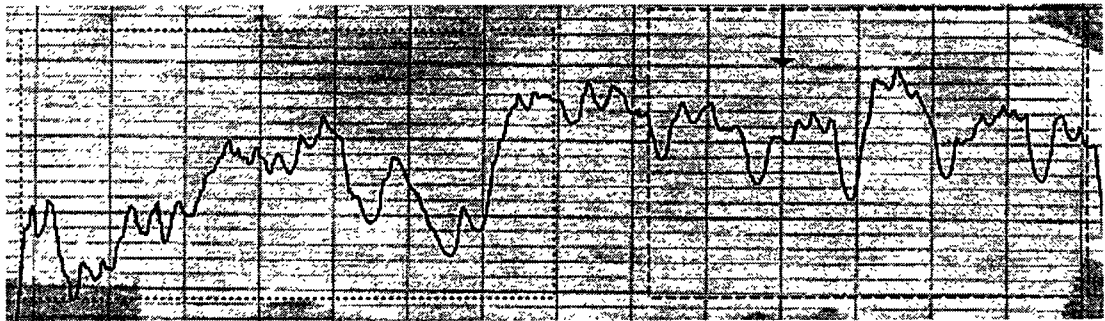
d) adaptation coefficient reduced on-line from 300 to 50



e) adaptation coefficient reduced on-line from 100 to 50

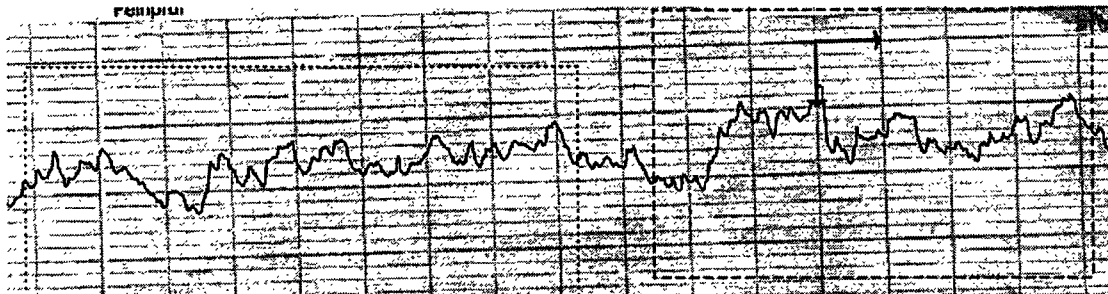


f) adaptation coefficient reduced on-line from 150 to 50

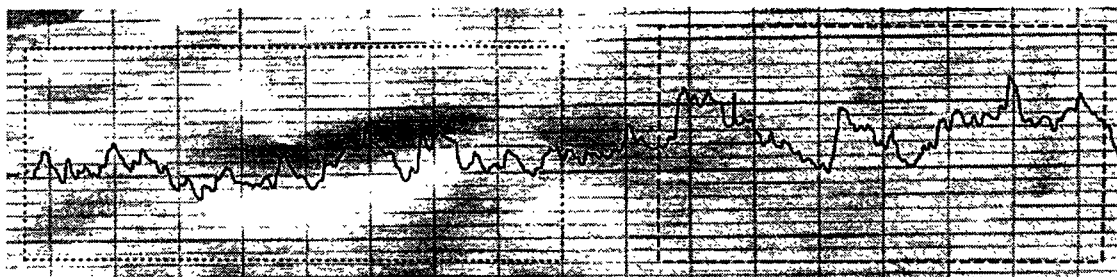


g) adaptation coefficient reduced on-line from 200 to 50

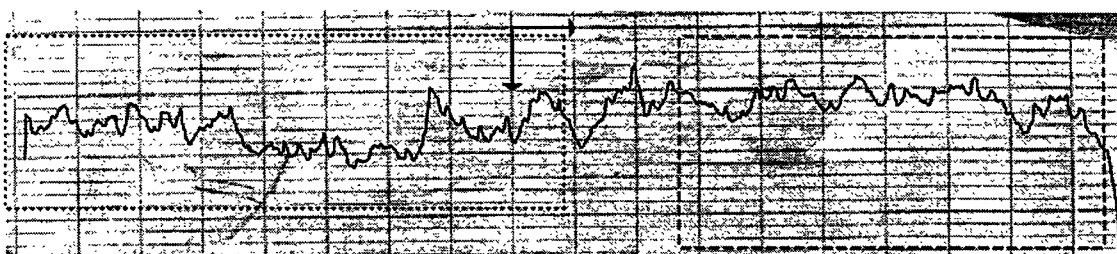
Figure A.2: Surface Profile for Trial 2



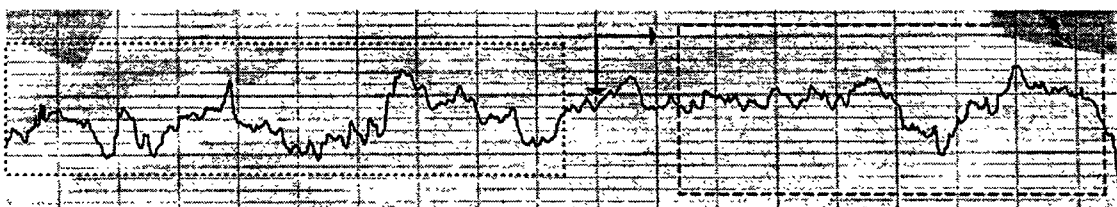
a) adaptation coefficient reduced on-line from 100 to 50



b) adaptation coefficient reduced on-line from 150 to 50

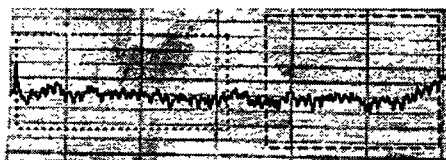


c) adaptation coefficient reduced on-line from 200 to 50

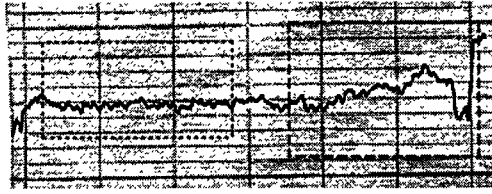


d) adaptation coefficient reduced on-line from 100 to 50

Figure A.3: Surface Profile for Trail 3



a) adaptation coefficient reduced on-line from 150 to 50

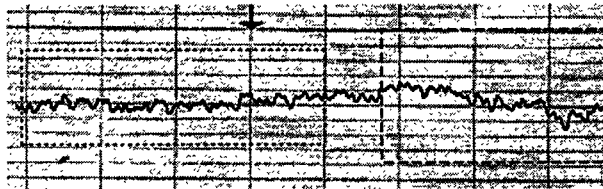


b) adaptation coefficient reduced on-line from 150 to 50

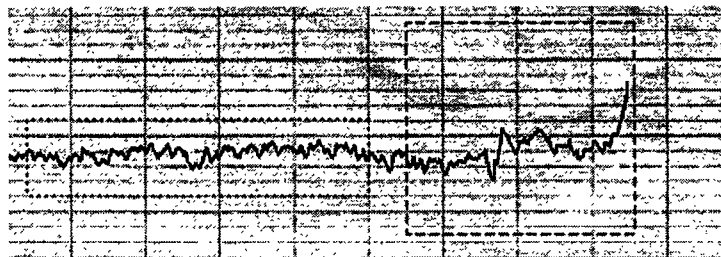


c) adaptation coefficient reduced on-line from 200 to 50

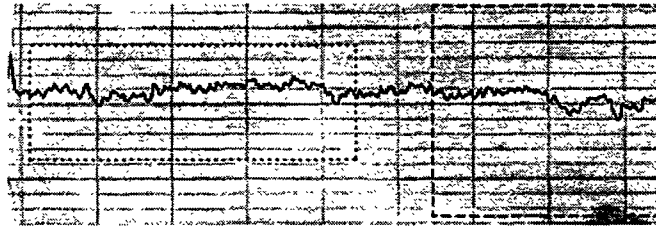
Figure A.4: Surface Profile for Trail 4



a) adaptation coefficient reduced on-line from 100 to 50



b) adaptation coefficient reduced on-line from 150 to 50



c) adaptation coefficient reduced on-line from 200 to 50

Figure A.5: Surface Profile for Trail 5

## REFERENCES

- Aleksander, I., 1991, Introduction to neural nets, Applied Artificial Intelligence, K. Warwick (ed.), Peter Peregrinus Ltd.
- Bedini, R., and Pinotti, P.C., 1982, Experiments on Adaptive Constrained Control of a CNC Lathe, *Transactions of the ASME, Journal of Engineering for Industry*, Vol. 104, pp. 139-149.
- Berger, B.S., Minis, I., and Rokni, M., 1992, "Metal Cutting Dynamics: An Experimental Numerical-Study," *Journal of Sound and Vibration*, pp165-169
- Berger, B.S., Rokni, M., and Minis, I., 1993, "Complex Dynamics in Metal Cutting," *Quarterly of Applied Mathematics*, Vol LI, pp601-612
- Bryson, A.E. and Y.-C. Ho, 1969, *Applied Optimal Control*, New York: Blaisdell.
- Burgess, J.C., 1981, "Active adaptive sound control in a duct: A computer simulation," *J. Acoust. Soc. Am.* 70, pp715-726
- Cook, N.H., Finnie, I. and Shaw, M.C., 1954, "Discontinuous chip formation," *Trans. Amer. Soc. Mech. Engrs.*, 76, pp153.
- Cybenko, G., 1988, Continuous valued neural networks with two hidden layers are sufficient. Technical report, Department of Computer Science, Tufts University.
- Cybenko, G., 1989, Approximation by superposition of a sigmoidal function, *Mathematics of Control, Signals, and Systems* 2: pp.303-314
- Doi, S., 1937, "Chatter of lathe tool," *J. Soc. Mech. Engrs. Japan*, 3, pp94.
- Dold, G., 1996, "Design of a Microprocessor-Based Adaptive Control System for Active Vibration Compensation Using PMN Actuators", M.S. Thesis, Department of Mechanical Engineering, University of Maryland, College Park, MD
- Dowyle E. L., 1953, *Metal Machining*, Prentice-Hall, Inc., Englewood Cliffs, N.J.
- Eman, K., Wu, S.M., 1980, A feasibility study of on-line identification of chatter in turning operations, *ASME Journal of Eng. for Industry*, Vol. 102, pp. 315-321.
- Ferraresi, D., 1960, "Dynamische Schniffkraft messungen beim drehen," *Maschinenmarkt*, 66, pp33.

Field, M., and Merchant, M.E., 1949, "Mechanics of formation of discontinuous chip in metal cutting," Trans. Amer. Soc. Mech. Engrs., 71, pp421.

Funahashi, K., 1989, On the approximate realization of continuous mappings by neural networks, *Neural Networks 2*: pp. 183-192

Hebb, D.O., 1949, *The Organization of Behavior*, Wiley, New York.

Hornik, K., Stinchcombe, M. and White, H., 1989, Multilayer feedforward networks are universal approximators, *Neural Networks 2*: pp. 359-366

Hunt, K. and Sbarbaro, D., 1991, Neural networks for nonlinear internal model control, *IEEE Proceedings-D*, 138 (5), pp. 431-438.

Juneja, B.L., and Sekhon, G.S., 1987, Fundamentals of metal cutting and machine tools, Wiley Eastern Ltd, New Delhi, India, pp392.

Kalpakjian, S., 1991, Manufacturing Processes for Engineering Materials, Addison-Wesley Publishing Company, Inc.

Kegg., R.L., 1965, Cutting dynamics in machine tool chatter, Transactions of ASME, pp. 464-470

Koenigsberger, I. and Thusty, J., 1971, Structures of Machine Tools, Pergamon Press.

Koren, Y., 1983, Computer Control of Manufacturing Systems, Chapter 6 and 8, McGraw-Hill, New York.

Koren, Y., and Masory, O., Adaptive Control with Process Estimation, Annals of the CIRP, Vol. 30, No. 1, 1981, pp. 373-376

Kung, S. Y. , 1993, Digital Neural Networks, Prentice Hall, Englewood Cliffs, New Jersey.

Kuznetsov, V.D., 1966, Metal Transfer and Build-up in Friction and Cutting. (E.H. Freitag, ed.), Oxford: Pergamon Press Ltd.

Kwakernaak, H., and Sivan, R., 1972, Linear Optimal Control Systems, Wiley Interscience.

Landberg, P., 1956, "Vibrations caused by chip formation," Microtechnic, 10, pp 219.

Levin E., Gewirtzman R. & Inbar G., 1991, "Neural Network Architecture for Adaptive System Modeling and Control". Neural Networks, 4, pp. 185-191.



- Ljung, L., and Glad, T., 1994, Modeling of Dynamic Systems, Prentice Hall, Englewood Cliffs, NJ.
- Luu, H., 1996, "Implementation of a Designed Tool Post for Tool Vibration Compensation Using PMN Actuators", M.S. Thesis, Department of Mechanical Engineering, University of Maryland, College Park, MD
- Madhusudan, A.P., 1995, Schemes for Active Vibration Control of Plates, M.S. Thesis, Department of Mechanical Engineering, University of Maryland, College Park, MD
- Masory, O., and Y. Koren, "Adaptive Control System for Turning", Annals of the CIRP, Vol. 29, No. 1, 1980
- Merchant, M.E., "Basic Mechanics of the Metal-Cutting Process," Journal of Applied Mechanics, Vol. 11, Transactions of the ASME, Vol. 66, 1940
- Merritt, H. E., "Theory of Self-Excited Machine-Tool Chatter," Journal of Engineering for Industry, November 1965, pp447-454
- Miller W.T., Sutton, R.S., and Werbos, P.J. (editors), 1990. Neural Networks for Control. MIT Press, Cambridge, Mass
- Milner, D. A., "Adaptive Control of Feedrate in the Milling Process," 1974, Int. J. Mach. Tool Des. Res., Vol 14, pp187-197
- Minis, I., Magrab, E., and Pandelidis, I., 1990, Improved methods for prediction of chatter in turning, Part II: Determination of cutting process parameters, ASME Journal of Eng. for Industry, Vol. 112, pp. 21-27
- Narendra, K.S., and Mukhopadhyay, S., 1994, "Adaptive control of nonlinear multivariate systems using neural networks", Neural Networks, 7 (5), pp. 737-752
- Narendra, K. S. and Parthasarathy, K., 1990, Identification and Control of Dynamical Systems Using Neural Networks, IEEE Transactions on Neural Networks, Vol. 1, No. 1, pp 4-27.
- Nelson, P.A., and Elliott, S.J., 1994, Active Control of Sound, Academic Press.
- Ogata, K., 1990, Modern Control Theory, Prentice Hall.
- Pandit, S.M., Subramanian, T.L., and Wu, S.M., 1975, Modeling machine tool chatter by time series, ASME Journal of Eng. for Industry, pp. 211-215

Park, J., 1995, Active Control of Noise in a Three-Dimensional Enclosure, M.S. Thesis, Department of Mechanical Engineering, University of Maryland, College Park.

Parker, D.B., 1985, Learning Logic, Technical Report TR-47, Center for Computational Research in Economics and Management Science, Massachusetts Institute of Technology, Cambridge, MA.

Psaltis D., Sideris A. and Yamamura A., 1987, "Neural Controllers". Proceedings of IEEE first International Conference on Neural Networks, San Diego, Vol. 4, pp 551-558

Psaltis D., Sideris A. and Yamamura A., 1988, "A Multilayered Neural Network Controller". IEEE Control Systems Magazine, 8 (2), pp. 17-21

Rumelhart, D.E., Hinton, G.E., and Williams, R.J., 1986a, Learning Representations by Back-Propagating Errors, *Nature* **323**, pp533-536

Rumelhart, D.E., Hinton, G.E., and Williams, R.J., 1986b, Learning Internal Representations by Error Propagation. In *Parallel Distributed Processing*, vol. 1, chap. 8

Sampath, A., and B. Balachandran, 1996, Active Structural Acoustic Control of Bandlimited Disturbances, Proceedings of the SPIE 1996 Symposium on Smart Structures and Materials, San Diego, California, Vol. 2717, pp. 422-433

Shteinberg, I.S., 1947, Ustranenie Ibratsii, Vozn Ikayushchikh Pri Rezanii Metallov Na Tokarnom (Elimination of vibrations excited during turning), USSR, Mashgiz.

SMS News, 1993, The SMS Partnership for Synthesis and Processing of Smart Materials.

Spiewak, S., and Szafarczyk, M., 1978, Algorithms of Operation and structures of ACC Controllers for Rough Turning, *Annals of the CIRP*, Vol. 27, No. 1, pp. 413-418

Srinivasan, K., Nachtigal C.L., 1978, Investigation of the cutting process dynamics in turning operations, *ASME Journal of Eng. for Industry*, Vol. 100, pp. 323-331.

Stute, G., Goetz, F.R., Adaptive Control System for Variable Gain in ACC Systems, Proceedings of the Machine Tool Design and Research Conference, 1975, pp117-121

Tobias, S.A., 1965, Machine Tool Vibration, John Wiley & Sons, Inc., New York.

Tomizuka M., Oh, J.H., and Dornfeld, D.A., 1983, Model Reference Adaptive Control of the Milling Process, Annual Winter Meeting of ASME: Control of Manufacturing Processes and Robotic Systems.

Tomizuka, M., and S. Zhang, "Modeling and Conventional/Adaptive Control PI Control of a Lathe Cutting Process," Proceedings of the American Control Conference, Boston, Massachusetts, June 1985

Ulsoy, A. G., Koren, Y., and Rasmussen, F., 1983, "Principal Developments in the Adaptive Control of Machine Tools," ASME Journal of Dynamic Systems, Measurement and Control, Vol. 105, No. 2, pp. 107-112

Warwick, K., Irwin, G. W., and Hunt K.J., 1992, Neural Networks for Control and Systems, IEEE Control Engineering, Ser. 46, New York, N.Y.

Watanabe, T., "A Model-Based Approach to Adaptive Control Optimization Milling," 1983, Control of Manufacturing Process and Robotic Systems, D. Hardt, ed., ASME, New York, pp. 27-46

Weck, M., 1980, "Adaptive Control in Turning", Proceedings of the Machine Tool Task Force Conference, Vol. 4, Sect. 7.15

Weck, M., 1985, Handbook of Machine Tools, Vol. 4, Wiley.

Werbos, P., 1974, Beyond Regression: New Tools for Prediction and Analysis in the Behavioral Sciences. Ph.D. Thesis, Harvard University.

White, D.A. and Sofge, D. (editors), 1992, "Handbook of intelligent control. Neural, fuzzy, and adaptive approaches", Van Nostrand Reinhold.

Widrow, 1971, Adaptive Filters, *Aspects of Network and System Theory*, edited by R. E. Kalman and N. Declaris, (Holt, Rinehart, and Winston, New York), pp. 185-189.

Widrow, B., Shur, D., and Shaffer, S., 1981, "On adaptive inverse control," Proceeding of the 15th Asilomar Conference on Circuits, Systems and Computers, 9-11, Pacific Grove, CA, pp. 185-189.

Widrow, W. and Stearns, S.D., 1985, Adaptive Signal Processing, Prentice-Hall, Englewood Cliffs, NJ, pp. 288

Wilson, G.E., and Wilkinson, A. J., 1981, Adaptive Control for a CNC Lathe, Proceedings of the Twenty-second International Machine Tool Design and Research Conference, pp. 205-213

Wing, F.K., 1995, A Systems Engineering approach to design a smart tool post structure, M.S. Thesis, Department of Mechanical Engineering, University of Maryland, College Park, MD

Wu, D.W., Liu R., 1985, An analytical model of cutting dynamics, Part 1: Model Building, ASME J. of Eng. for Industry, Vol. 107, pp. 107-111

Yabutta, T., and Yamada, 1990, "Possibility of Neural Network Controller for Robot Manipulators", IEEE International Conference on Robotics and Automation, Cincinnati, p1686-1691.